

©Copyright (2006)
Josef D. Dufek

The Ascent and Eruption of Arc Magmas: A Physical Examination of the Genesis,
Rates, and Dynamics of Silicic Volcanism

Josef D. Dufek

A dissertation
submitted in partial fulfillment of the
requirements for the degree of

Doctor of Philosophy

University of Washington

2006

Program Authorized to Offer Degree:
Earth and Space Sciences

UMI Number: 3224211

Copyright 2006 by
Dufek, Josef D.

All rights reserved.

INFORMATION TO USERS

The quality of this reproduction is dependent upon the quality of the copy submitted. Broken or indistinct print, colored or poor quality illustrations and photographs, print bleed-through, substandard margins, and improper alignment can adversely affect reproduction.

In the unlikely event that the author did not send a complete manuscript and there are missing pages, these will be noted. Also, if unauthorized copyright material had to be removed, a note will indicate the deletion.

UMI[®]

UMI Microform 3224211

Copyright 2006 by ProQuest Information and Learning Company.

All rights reserved. This microform edition is protected against unauthorized copying under Title 17, United States Code.

ProQuest Information and Learning Company
300 North Zeeb Road
P.O. Box 1346
Ann Arbor, MI 48106-1346

University of Washington
Graduate School

This is to certify that I have examined this copy of a doctoral dissertation by

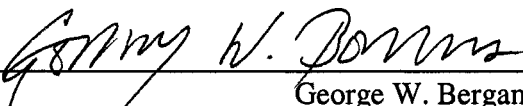
Josef D. Dufek

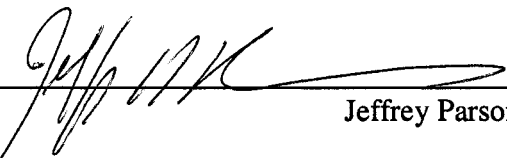
and have found that it is complete and satisfactory in all respects,
and that any and all revisions required by the final
examining committee have been made.

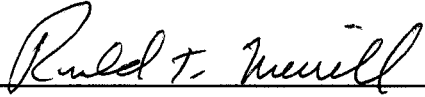
Chair of the Supervisory Committee:


George W. Bergantz

Reading Committee:


George W. Bergantz


Jeffrey Parsons


Ronald Merrill

Date: May 29, 2006

In presenting this dissertation in partial fulfillment of the requirements for the doctoral degree at the University of Washington, I agree that the Library shall make its copies freely available for inspection. I further agree that extensive copying of the dissertation is allowable only for scholarly purposes, consistent with "fair use" as prescribed in the U.S. Copyright Law. Requests for copying or reproduction of this dissertation may be referred to ProQuest Information and Learning, 300 North Zeeb Road, Ann Arbor, MI 48106-1346, 1-800-521-0600, to whom the author has granted "the right to reproduce and sell (a) copies of the manuscript in microform and/or (b) printed copies of the manuscript made from microform."

Signature *Jeff O. O'Neil*

Date *May 24, 2006*

University of Washington

Abstract

The Ascent and Eruption of Arc Magmas: A Physical Examination of the Genesis, Rates, and Dynamics of Silicic Volcanism

Josef D. Dufek

Chair of the Supervisory Committee:
Professor George W. Bergantz
Department of Earth and Space Sciences

The ascent and eruption of magmas in arcs determines the thermal and compositional structure of the crust and shapes the surface landscape. The first section of this study examines the intrusion of mafic mantle melts into the lower crust and thermal and dynamic response of the crust to this input. Distinct melting and mixing environments are predicted as a result of the crustal thickness and age of the arc system. The residence time of arc magmas and their rate of ascent from depth can be constrained by the decay of naturally occurring isotopes of uranium and its daughter products. ^{226}Ra -excesses in arc magmas have been interpreted to result from flux melting of the mantle above subducting slabs and subsequent fast ascent rates from slab to surface, up to 1000 m/yr and higher. However, in this work it is demonstrated that incongruent melting of the lower crust can either maintain or augment mantle-derived ^{226}Ra -excesses and so reduce inferred vertical transport rates.

The second half of this work addresses the explosive volcanic eruption of silicic magmas. Like many other processes nature, volcanic eruptions involve multiple, mechanically distinct phases: for instance, ash particles interacting with a turbulent gas phase in an explosive volcanic eruption. A multiphase numerical model is developed and applied to conduit conditions and pyroclastic flow transport. To

elucidate the role of particle collisions in redistributing momentum after fragmentation in a volcanic conduit, a numerical study was performed comparing the behavior of an inviscid, or collision-less, granular material with a granular material whose viscosity and pressure were modeled using kinetic theory.

The final chapter of this work examines the degree to which particle transport in pyroclastic flows results for bed-load transport or suspended load transport. Numerical leaky and saltating boundaries are developed to examine both over-land and over-water transport of pyroclastic flows. The leaky boundary permits the examination of suspended load in isolation from bed-load transport. A unifying concept is energy dissipation due to particle-boundary interaction: leaky boundaries dissipate energy more efficiently at the boundary than their saltating counterparts and have smaller run-out distance.

TABLE OF CONTENTS

	Page
List of Figures.....	ii
List of Tables.....	iv
Chapter 1: Introduction.....	1
Chapter 2: Lower Crustal Magma Genesis and Preservation:	
A Stochastic Framework for the Evaluation of Basalt-Crust Interaction.....	8
2.1 Introduction.....	8
2.2 Stochastic Dike Intrusion Model.....	15
2.3 Results.....	32
2.4 Discussion.....	60
2.5 Conclusions.....	66
Chapter 3: $^{226}\text{Ra}/^{230}\text{Th}$ -excess Generated in the Lower Crust:	
Implications for Magma Transport and Storage Time Scales.....	68
3.1 Introduction.....	68
3.2 Continuous Dehydration Melting.....	70
3.3 Modeled U-series Disequilibria and Trace Element Signature of Amphibolite Dehydration.....	81
3.4 Discussion.....	86
3.5 Conclusions.....	88
Chapter 4: Transient Two-Dimensional Dynamics in the Upper Conduit of a Rhyolitic Eruption:	
A Comparison of Closure Models for the Granular Stress.....	90
4.1 Introduction.....	91
4.2 Multi-fluid Model for Multiphase Flow.....	96
4.3 Simulation Results.....	107
4.4 Conclusions.....	127
Chapter 5: Suspended Load and Bed-Load Transport of Particle-Laden Gravity Currents:	
The Role of Particle-Bed Interaction.....	129
5.1 Introduction.....	130
5.2 Continuum Multiphase Model.....	133
5.3 Boundary Conditions for Leaky and Saltation Boundaries.....	138
5.4 Particle-Laden Gravity Current Conditions.....	140
5.5 Structure of Particle-Laden Flows.....	145
5.6 Discussion.....	160
5.7 Conclusions.....	165
Chapter 6: Closing Remarks and Future Directions.....	167
Bibliography.....	173
Appendix A: Magmatic Properties.....	198
Appendix B: Derivation of Collisionless Granular Transport.....	206
Appendix C: Granular Constitutive Relations.....	208

LIST OF FIGURES

Figure Number	Page
2.1 Melt Fraction of Amphibolite.....	19
2.2 Amphibolite Dehydration Reaction.....	20
2.3 Melt Fraction of Basalt.....	23
2.4 Modal Abundance of Crystallizing Basalt.....	24
2.5 Schematic of Lower Crustal Conduction Model.....	26
2.6 Steady-State Geotherm.....	28
2.7 The Percent Change in the Mean Volume of Basaltic Melt with Progressive Incorporation of More Realizations.....	30
2.8 Example of a Single Realization of Random Dike Intrusion.....	36
2.9 Crustal and Basaltic Melt.....	38
2.10 Temperature Profiles as a Function of Depth.....	41
2.11 Mean Crustal and Basalt Melt Fractions as a Function of Time and Depth.....	42
2.12 Ratio of Crustal and Basaltic Melt Volumes.....	43
2.13 Effect of Maximum Height of Ascent.....	45
2.14 Effect of Dike Width on Melt Production.....	47
2.15 Melt Fraction as a Function of Depth and Basalt Flux I.....	50
2.16 Melt Fraction as a Function of Depth and Basalt Flux II.....	51
2.17 Surface Heat Flux.....	53
2.18 Mixing and Mingling of Magmas.....	56
2.19 Ductile Creep at the Mantle-Crust Interface.....	58
2.20 Average Basalt Cumulate Density.....	60
2.21 Alumina Saturation Index Plot.....	66
3.1 Isosurfaces of Radioactive Disequilibria.....	82
3.2 Trace Element Enrichment.....	85
3.3 Conceptual Model of U-series Disequilibria in Arc Settings.....	89
4.1 Multiphase Regions in a Volcanic Conduit.....	93
4.2 Schematic Representation of the Conduit Model.....	106
4.3 Particle Velocity Following Initial Shock.....	110
4.4 Pressure at Steady-State.....	111
4.5 Gas Velocities Near the Level of Fragmentation.....	113
4.6 Magma and Particle Velocities Near the Level of Fragmentation.....	114
4.7 Two-Dimensional Cross-Section of Pressure Near Fragmentation.....	115
4.8 Conduit Exit Velocities.....	116
4.9 Volume Fraction of Gas in Conduit for Different Particle Sizes Simulated.....	121
4.10 Two-Dimensional Cross-Section of Gas Volume Fraction Near Fragmentation.....	122
4.11 Granular Viscosity Following Fragmentation.....	123
4.12 Radial Variation in the Vertical Velocity at the Vent.....	125

4.13 Radial Variation of Particle Volume Fraction at the Vent.....	126
5.1 Schematic Representation of Simulation Condition.....	134
5.2 Example of Reconstructed Velocity Probability Distribution.....	139
5.3 Particle Volume Fraction for the Binary Particle Mixtures.....	146
5.4 Vertical Profiles of Flow Conditions.....	148
5.5 Rate of Particle Loss and Development of Suspended and Bed Load.....	149
5.6 Progressive Loss of Particles for Flow Conditions 2 and 4.....	151
5.7 Vertically Averaged Densimetric Froude Number.....	152
5.8 Flow Traversing Leak Boundary.....	154
5.9 Flow Traversing Saltating Boundary.....	155
5.10 The Vertically and Temporarily Averaged Sorting Coefficient.....	157
5.11 The Dissipation Rate of Kinetic Energy.....	158
A.1 Mixture Viscosity as a Function of Melt Fraction.....	199
A.2 Major Element Geochemical Trends for Modelled Basalt.....	202
A.3 Major Element Geochemical Trends for Modelled Amphibolite.....	203
A.4 Density of Amphibolite and Wet Basalt.....	205

LIST OF TABLES

Table Number	Page
2.1 Estimates of Basalt Flux into the Lower Crust.....	11
2.2 Thermal Models of the Lower Crust.....	13
2.3 Key to Nomenclature.....	17
2.4 Selected Conduction Results.....	34
2.5 Selected Conduction Results and Crustal Melting Efficiency.....	35
3.1 Partition Coefficients for Amphibolite Melting Calculations.....	72
4.1 Notation.....	90
4.2 Summary of Conditions in the Upper Conduit at Steady State.....	109
4.3 Summary of Particle Timescales.....	118
5.1 Nomenclature.....	129
5.2 Multifluid Equations.....	135
5.3 Particle Scaling.....	143
5.4 Simulation Conditions.....	145

ACKNOWLEDGEMENTS

I wish to thank Professor George W. Bergantz whose intellectual support greatly helped to shape this work. I have learned much from our discussions, and I have appreciated his suggestions, questions, and encouragement throughout my graduate career. I would also like to thank my committee (Jeff Parsons, Ron Merrill, Kari Cooper, Jim Riley, and Stu McCallum) who have made many suggestions and had the patience to listen and read this work. Many long discussions with Olivier Bachmann who was a post-doc during my first two years of graduate school were greatly appreciated. Funding from the Department of Defense Science and Engineering Fellowship and the NASA Earth Systems Science Fellowship has made much of this research possible. I want to thank my fellow graduate students, especially those in the Physical Petrology group including Glen Wallace, James Loetterle, and Philipp 'Schnittmenge' Ruprecht for all of their help during my time at the University of Washington. Finally, I want to thank my family (Norma, Dave and Eric Dufek) and Carol Paty for their patience and support.

DEDICATION

For my mom who taught me about perseverance, my dad who taught me to always check what was on the other side of the mountain, my brother who taught me patience, and my grandmother who taught me math.

- Chapter 1 -

Introduction

The transit of magma through the crust, and subsequent eruptive dynamics, influences the structure and growth of the crust as well as plays a major role in determining the surface features of the terrestrial planets. The flux of enthalpy and mass associated with ascending mantle melts is one of the most important factors determining the chemical, thermal and rheological evolution of the crust on all rocky planets in the solar system. However, subduction zones (or arcs) and their related magmatic activity are apparently unique to Earth compared to our neighboring planets at the present time. The crustal magmatic systems in arcs are time-dependent and demonstratively open-systems with links to the mantle and atmosphere reservoirs. In fact, it is precisely the recycling of materials from the surface into the mantle (in particular volatile phases on the descending oceanic slab) that initiates magmatism at arcs. Static descriptions of magmatic or eruptive behavior (e.g. measurement of the bulk chemical composition or description of pyroclastic flow deposits) have been useful in detailing the major constituents in these processes. Yet while the conceptual picture of arc systems has been broadly defined over the past four decades, many questions remain concerning the dynamics and rates of both magma intrusion in the lower crust and explosive eruptive dynamics at the surface.

The products of continental arc eruptions routinely show evidence (primarily isotopic) of complex polybaric (at multiple pressures) assimilation and fractionation histories (Hart *et al.*, 2002; Dungan & Davidson, 2004; Davidson *et al.*, 2005), yet the dynamics associated with these processes remains obscured. Assimilation is the process of incorporating preexisting crust into the ascending melt, while fractionation is the process of removing solid phases from the melt either through settling or other

processes. An active debate in modern petrology is the degree to which arc magmas represent primarily fractionates of mafic mantle melts, or melts of preexisting crust initiated by the enthalpy associated with intrusion of mantle magmas (Anderson, 1976; Bergantz, 1989; Grove *et al.*, 2003). The relative proportion of recycled crustal material versus the proportion due to the immediate ascent of mantle materials has a bearing on how quickly material is cycled through the arc and the timescales required to produce more silicic or evolved melts. A model favoring injection of mantle basalts into the crust, fractional crystallization of this material, and then eruption implies relatively fast timescales compared to multiple melt-freeze (or partial melt-freeze) cycles. Regardless of whether erupted magmas are generated primarily by fractionation or assimilation, a mass balance problem arises if the crust is considered to be a closed system. If the range of estimated basalt flux is approximately constant in all arcs, the volume of material predicted to accumulate in mature arcs is substantial. The observation that melts leaving the mantle wedge are likely basaltic in composition and that the bulk crust is andesitic (Kay *et al.*, 1992), places the further constraint that some removal of material from the crust must be weighted toward the more mafic components. Erosion, lower crustal flow and delamination (the process of density foundering of the crust back into the mantle) have all been proposed as mechanisms that foster the enrichment of the crust in incompatible elements (Kay *et al.*, 1992; Lee *et al.*, 2001; Montgomery *et al.*, 2001; Saleeby *et al.*, 2003).

Due to the primarily mafic composition of the lower crust (Rudnick & Taylor, 1987), and elevated geotherms in the lower crust (> 25 km), this region of the crust is a likely site of crustal and mantle magmatic interaction. Previous studies have adopted either one-dimensional conduction approaches to lower crustal interaction or considered very large, but infrequent, injection of mantle melts into the crustal system. In Chapter 2 of this work a stochastic framework is developed to study the intrusion of mantle melts into the crust and to study the thermal and dynamic response of the crust to these intrusions without *a priori* specification of dike geometry. This enables the consideration of the effect of variable intrusion geometry,

depth of the mafic intrusions and the flux of basalt on the melting and mixing environments in the lower crust. The developed model uses a sophisticated approach to accurately partition sensible and latent heat for geologically realistic melt fraction to temperature relationships for both the mantle and crustal material. In particular, the dehydration reaction of amphibolite is considered as a proxy for the lower crust. (Here amphibolite refers to a mafic rock consisting mainly of amphibole and plagioclase). This is an example of an incongruent melting reaction in which multiple phases (minerals) are consumed and produce other mineral phases and a melt phase. Further, the rheological evolution of the melt+solid system is calculated as the injection of mantle material proceeds during the evolution of the arc system. The thermal and phase equilibria criteria for crustal density instabilities is developed and this work demonstrates that the transfer of material in the crust-mantle system need not be only one-way.

The timescale of magma ascent from the source melting zones in the mantle above the subducting oceanic plate to the surface was largely unconstrained until the measurement of radioactive nuclides in arc lavas (Gill & Williams, 1990). Disequilibria between intermediate daughter products in the decay series of ^{238}U provides a useful chronometer for magmatic processes and ascent rates of magma from depth, sensitive to timescales of $\sim 10\text{ ka} - 350\text{ ka}$ (^{238}U - ^{230}Th disequilibria) or $\sim 100\text{ a} - 10\text{ ka}$ (^{230}Th - ^{226}Ra disequilibria). If left unperturbed, the activity ratios of a parent and daughter nuclide should decay to a steady-state ratio of 1 within analytical uncertainty after approximately 5 half-lives of the daughter nuclide. The presence of ^{226}Ra -excesses in arc magmas has been interpreted to result from flux melting of the mantle above subducting slabs and subsequent fast ascent rates from slab to surface, up to 1000 m/yr and higher. The paradigm in U-series interpretation was that only the fluids coming off the subducting slab can enrich radium relative to thorium efficiently to create the very large ^{226}Ra disequilibria found in some arc magmas (Turner *et al.*, 2001). Crustal processes were considered to be primarily transparent to the U-series nuclides. In Chapter 3, I consider the effect of incongruent melting reactions (similar

to those reactions considered Chapter 2) on U-series disequilibria, as well as the effect of melting occurring over a prolonged period of time rather than instantaneous melting. The work in Chapter 3 demonstrates that incongruent melting of the lower crust could either maintain or augment mantle-derived ^{226}Ra -excesses and so reduce inferred vertical transport rates. This helps to reconcile the observation that many arc magmas have likely stalled at depth and assimilated some crustal material during their ascent, and helps reconcile crystal residence time scales of thousands to tens of thousands of years in some arc lavas (Cooper & Reid, 2003; Costa *et al.*, 2003; Turner *et al.*, 2003).

After volatile rich, evolved ($\sim\text{SiO}_2 > 63$ wt. %) magmas reach the shallow crust they are prone to erupt explosively. The combination of high viscosity and high volatile contents in these dacitic to rhyolitic magmas contributes to the generation of some of the most explosive, plinian-style eruptions (eruptions that form buoyant columns that reach the stratosphere) (Carey & Sigurdsson, 1989). After sudden depressurization events the dissolved volatile contents (many in excess of 5 wt. % H_2O) begin to exsolve forming bubbles in the melt (Cervantes & Wallace, 2003). This induces buoyant ascent of the melt+bubble mixture, and this acceleration towards the surface leads to a positive cycle of further depressurization, exsolution and acceleration. After the bubbly magma is strained past its yield strength it can explosively fragment producing ash and pumice pyroclasts in a turbulent gas mixture (Papale, 1999). This is the sort of eruption exemplified by the eruption of Mount St. Helens and larger variants such as the Kos Plateau Tuff in Greece. The velocity, particle size distribution and particle volume fraction that exits the eruptive vent will largely determine the style of eruption. For instance a very dilute and fast mixture is more likely to form a buoyant plinian column and ascend beyond the tropopause (>11 km) in the atmosphere. A dense and (relatively) slow moving mixture of magmatic gases and pyroclasts will entrain less ambient air above the volcanic vent and will likely collapse to form ground-hugging pyroclastic flows.

Volcanic eruptions are time-dependent phenomena with a vast range of relevant length-scales. Understanding the multiple scales of turbulence as well as particle-gas and particle-particle interaction in volcanic eruptions represents a significant challenge. The observation that large-scale structures exist in many turbulent flows (Broadwell and Mungal, 1991), and that particles can become concentrated in these structures (Eaton and Fessler, 1994) and can modulate turbulent intensity (Gore and Crowe, 1989) has led to an increased awareness of possible two-way feedback in particle-fluid systems. In addition to these particle-fluid interactions, particles can also interact with each other (Sommerfeld, 1995). Particles of variable size will respond to the same forcing on different timescales, which promotes segregation of different size and density particles in a flow. Sorting in deposits, elutriation of fine particles in pyroclastic flows by the upward motion of gas (Sparks et al., 1978), and the ballistic trajectories of larger particles while smaller clasts are entrained in the rising plume of hot gas, are all manifestations of the multiphase effect of the relative segregation of particles observed in volcanic eruptions.

Two distinct regions of multiphase flow exist in a developing conduit eruption and are separated by a fragmentation front: magma/bubble flow and gas/particle flow. The momentum transfer between the particles and the gas after fragmentation as well as the velocity and pressure evolution of the system will play an important role in the evolving vent conditions. In Chapter 4, a continuum multiphase model is developed in which the particle, air, magma, and bubble phases are treated as distinct, interpenetrating continua that can move relative to each other. This study addresses whether particles can move with significantly different velocities than the gas phase as a result of explosive conduit conditions. The momentum transfer within the particle phase is considered using kinetic theory and compared to an idealized, inviscid granular material as assumed by several previous one-dimensional conduit models. This study is one of the first to consider two dimensional conduit flow, and shows that radial variations in the magmatic pressure field result from vertical magmatic viscosity gradients. Further the radial distribution of pyroclasts following

fragmentation is enriched near the conduit walls as a result of particle-particle collisions. Relative velocities develop between the gas and particle phases, and this is shown to be important during inefficient fragmentation with particles larger than a centimeter in size.

Following eruption, particle-gas mixtures that are denser than the ambient air form ground-hugging particle-laden gravity currents called pyroclastic flows. Pyroclastic flows represent a special class of particle-laden gravity currents, as their interstitial gas density is less than the ambient air. Hence, when they become dilute (either from entrainment or deposition) they can undergo a buoyancy reversal and ascend from the surface. The internal structure of pyroclastic flows is poorly known; for instance, the degree to which particles in these flows are transported through turbulent suspension relative to saltating (making multiple collisions at the base of the flow) in a particle enriched bed-load region is subject to argument (Sparks *et al.*, 1978; Dade & Huppert, 1995). In Chapter 5 a similar multiphase treatment as used in Chapter 4 is employed to discern the internal structure, energy dissipation mechanisms and run-out distance of pyroclastic flows.

Several deposits and observations indicate that pyroclastic flows can surmount steep topography and even cross large bodies of water. For instance, flows from Krakatau were reported 60 km from the source, and flows from the Kos, Greece eruption produced deposits > 40 km from their source (Carey, 1996; Allen & Cas, 2001). Flows that cross water provide the conceptual framework to study suspended load transport in relative isolation from bed-load transport. A numerical treatment for leaky or over-water flows is developed and compared to a saltating boundary condition. The work in Chapter 5 provides a link between basal energy dissipation and run-out distance and develops this concept as a unifying framework that can be applied to other types of particle-laden gravity currents.

The following chapters describe arc magmatism and eruption processes from a fluid dynamics and rates-based perspective. Chapters 2-5 were originally written for publication as separate manuscripts (for the *Journal of Petrology*, *Geology*, *Journal of Volcanology and Geothermal Research*, and the *Journal of Theoretical and Computational Fluid Dynamics*, respectively) with co-authors Prof. George W. Bergantz on the work from Chapters 2, 4, and 5 and Dr. Kari Cooper on the work from Chapter 3. This work is written at an exciting time in the study of magmatic processes when the computational, field and analytical tools have advanced to a point where there are many opportunities for integrating numerous approaches. It is hoped that the novel multiphase characterization and careful melting calculations presented in this study will foster further inquiry into volcanic processes using an interdisciplinary approach.

- Chapter 2 -

Lower Crustal Magma Genesis and Preservation: A Stochastic Framework for the Evaluation of Basalt-Crust Interaction

2.1 INTRODUCTION

The genesis of new continental crust in arc settings is ultimately driven by mantle melting and injection of basalt into the crust, but the controls on basalt-crust interaction remain poorly understood. Basaltic magma transports both mass and enthalpy, and the petrologic diversity that occurs when basalt reaches crustal depths has been postulated to originate from closed-system fractionation of the primitive basalt (Grove *et al.*, 2003), crustal melting (Fornelli *et al.*, 2002; Saleeby *et al.*, 2003) and intermediate mixtures of the two processes (Anderson, 1976; DePaolo *et al.*, 1992; Feeley *et al.*, 2002). The range of processes reflects a continuum of basalt-crust interactions occurring at different pressure-temperature conditions, and lithological variations, in the crust. However, quantification of the importance of crustal melting as a result of the variable style, flux, location and temporal response of basalt intrusion remains elusive.

Geological and geophysical data provide an incomplete picture of the geological expressions of the interaction of basalt with the lower crust (depths greater than 25 km). Datasets that provide information about basaltic interaction with the lower crust include: A.) seismic velocity changes indicating mafic lower crust (Furlong & Fountain, 1986; Rudnick, 1990; Holbrook *et al.*, 1992; Ducea *et al.*, 2003), B.) mafic xenoliths with mineral assemblages indicative of higher pressure (DeBari *et al.*, 1987; Rudnick & Taylor, 1987; Ducea & Saleeby, 1998; Lee *et al.*,

2001), C.) and outcrops of lower crustal terrains in the Sierra Nevada, California, Fiordland, New Zealand, Kohistan, Pakistan, the Chipman Dikes, Saskatchewan, and in the Penninsular Terrane, Alaska (Jan & Howie, 1981; DeBari & Coleman, 1989; Pickett & Saleeby, 1993; Williams *et al.*, 1995). Additionally, geochemical data from erupted magmas such as the trace element concentrations attributed to residual garnet (Hildreth & Moorbath, 1988), isotopic data (Griffin *et al.*, 2002; Hart *et al.*, 2002), and major element geochemical trends indicative of the suppression of plagioclase crystallization (Green, 1982; Grove *et al.*, 2003) have all been interpreted to imply either crystallization or melting processes occurring at lower crustal pressures. In light of geochemical data from the southern volcanic zone of the Andes, Hildreth & Moorbath (1988) suggested that the lower crust may be a region of enhanced melting and mixing of mantle and crustally derived magmas. The paradigm of lower-crustal melting, assimilation, storage and homogenization (MASH) was proposed to describe the along-arc variability they observed as a function of crustal thickness, and this concept has been applied to other arc settings (Hopson & Mattinson, 1994; Kobayashi & Nakamura, 2001; Hart *et al.*, 2002). Additional support for enhanced melt production in the lower crust are the predictions of steady-state geotherms which approach the solidus of many lithologies in the lower crust (Chapman & Furlong, 1992), making these regions prone to melting with the addition of enthalpy supplied by mafic magmas.

Attempts to generalize basalt-crust interaction are usually presented in terms of two endmembers. The first involves intrusion of large, spatially coherent bodies of basaltic magma, commonly represented in the geologic record as gabbro-diorite-norite plutons. The process of crustal melting and contact metamorphism associated with the stages of intrusion and assembly of this type has been well described (Barboza & Bergantz, 2000). Notably, the most significant thermal impact of this process can be limited to a modest contact aureole (Barboza & Bergantz, 2000), despite the large volumes of basaltic material involved. Hence there is little geological support for the notion that the assembly of mafic complexes into a

contiguous body leads to substantial crustal melting or regionally extensive metamorphism (Barboza *et al.*, 1999). Alternatively, basaltic input as dike swarms, overlapping in space and time, may provide for a more efficient means of crustal melting and magma mingling (Hopson & Mattinson, 1994; Bergantz, 1995). However, a comprehensive, quantitative assessment of this form of basalt-crust interaction has not been done.

The objective of this study is to illuminate some of the thermal and dynamic consequences of basalt intrusion as dike swarms. To address a variety of possible intrusion configurations, we consider the random intrusion of basaltic dikes, and the effect of dike geometry, depth of intrusion and basalt flux on the crustal melting efficiency and the persistence and interaction of both crustal and basaltic melt through time. From this analysis, major element geochemical trends can be predicted for the developing thermal environments. We will further consider the criteria for crustal-scale density instability and stratification in the context of a crust that is actively growing through mafic addition. Lastly, we will evaluate the length and time-scales associated with mixing and mingling that result from different thermal environments in the lower crust in order to quantitatively assess MASH-like processes.

Basalt Flux in Arc Environments

Estimates of basalt flux in arc systems provides a global constraint for models aimed at understanding basalt-crust interaction. Gravity and seismic data have been used to estimate crustal thickness in some island arcs (Crisp, 1984; Dimalanta *et al.*, 2002). These estimates can be divided by the age of the arc system since the initiation of subduction to yield an average volume flux into the crust. These data are presented as volume flux through area per unit time in *Table 2.1*. A second method of calculating basalt flux utilizes estimates of the amount of crustal assimilated in erupted magmas and the enthalpy associated with basalt intrusion required to melt this amount of crust (Grunder, 1995). The two methods of estimating the basalt flux yield

results that are within an order of magnitude of each other from $\sim 1.0 \times 10^{-4} \text{ m}^3/\text{m}^2\text{yr}$ to $\sim 1.0 \times 10^{-3} \text{ m}^3/\text{m}^2\text{yr}$.

Table 2.1: Estimates of Basalt Flux into the Lower Crust

Method	Location	Estimate of Basalt Flux ($\text{m}^3/\text{m}^2\text{yr}$)	References
Gravity/ Seismic	Marianas	4.93×10^{-4}	Dimalanta et al., 2002
	Marianas	1.92×10^{-4}	Crisp, 1984
	Izu-Bonin	4.89×10^{-4}	Dimalanta et al., 2002
	Aleutians	5.46×10^{-4}	Dimalanta et al., 2002
	Aleutians	3.40×10^{-4}	Crisp, 1984
	Tonga	7.41×10^{-4}	Dimalanta et al., 2002
	New Hebrides	1.04×10^{-3}	Dimalanta et al., 2002
	Kuril	4.72×10^{-4}	Crisp, 1984
Geochemical/ Thermal	Eastern Nevada	4.0×10^{-4}	Grunder, 1995

Basalt Flux Range Employed in This Study: 1.0×10^{-4} to $5.0 \times 10^{-3} \text{ m}^3/\text{m}^2\text{yr}$

Both the seismic and gravity estimates, and the enthalpy balance calculations are likely underestimates of the amount of basalt flux. The seismic and gravity studies do not incorporate the loss of mass due to erosion or to the lateral flow of material in the upper-mantle/lower crust. Likewise, the enthalpy calculation assumes near perfect efficiency in the transfer of enthalpy, and as such represents a minimum end-member for the amount of basalt required for melting.

If the range of estimated basalt flux is approximately constant in all arcs, the volume of material predicted to accumulate in mature arcs is substantial. Erosion (Montgomery *et al.*, 2001), lower crustal flow (Meissner & Mooney, 1998), delamination (Kay *et al.*, 1992; Lee *et al.*, 2001; Saleeby *et al.*, 2003), and Rayleigh-Taylor type density instability (Jull & Kelemen, 2001) have all been called upon as

mechanisms to remove crustal material and several of these mechanisms may operate simultaneously. The observation that melts leaving the mantle wedge are likely basaltic in composition and that the bulk crust is andesitic (Kay *et al.*, 1992), places the further constraint that some removal of material from the crust must be weighted toward the more mafic components. Although the details of the mechanisms differ, Bird (1979), Kay & Kay (1993), and Jull & Kelemen (2001) have suggested that garnet-rich assemblages can develop greater densities than mantle material, and Jull & Kelemen (2001) demonstrated that ductile dripping instabilities can form on a timescale of 10^7 years, provided that the underlying mantle temperature exceeds 700°C . Thus any crustal scale model of basalt-crust interaction must address the mass balance relationship between basaltic input and crustal thickness.

Developing a Rationalizing Framework for Assessing the Thermal State of the Lower Crust

The quantitative assessment of basaltic underplating of the crust, and the resulting melting and mixing in the lower crust, have been considered in a number of numerical studies (*Table 2.2*). Analysis of the variety of results associated with these simulations provides motivation for the more general, stochastic approach applied in this study. The models can be divided into two groups: two-dimensional simulations of isolated sections of the crust which allow for convective transport, typically with constant temperature boundary conditions (Bittner & Schmeling, 1995; Barboza & Bergantz, 1996; Raia & Spera, 1997) and one-dimensional conduction simulations (Younker & Vogel, 1976; Wells, 1980; Bergantz, 1989; Petford & Gallagher, 2001; Annen & Sparks, 2002). Other hybrid approaches, such as Huppert & Sparks (1988) use a one-dimensional parameterized convection model.

In order to compare these models that consider different geometric configurations and lithologies, a rationalizing framework was developed to evaluate the efficiency of the melting process.

Table 2.2: Thermal Models of the Lower Crust

Study	Model Type ¹	Magma Intr. Style ²	Intr. Rate (m/yr)	Total Intr. Magma (km)	T _{int} (°C)	Depth Intr. (km)	Lithology ³	Liquidus, Solidus (°C)	Super-Heat (K)	Max. Crust. Melt ⁴	Efficiency (%)
Yunker and Vogel, 1976	1-D, Cond. No Bottom heat loss	Single Intrusion	NA	2.0	500	NA	Basalt-Biotite Granite	L: 1200, S: 1100 L: 1100, S: 800	200.0	H=375 m @ 40,000 yrs	32
Wells, 1980	1-D, Cond. Over-Accretion	Multiple Intrusion	0.004	40.0	200	10.0	Tonalite	L: 1050, S: 800	-25.0	H=1237.5 m @ 1.6x10 ⁶ yrs	8
Huppert and Sparks, 1988	1-D, Param. Conv., No bottom heat loss	Single Intrusion	NA	0.5	500	NA	Basalt Granodiorite	L: 1200, S: 1091 L: 1100, S: 850	0.0	H=220 m @ 100 yrs	44
Bergantz, 1989	1-D, Cond. No bottom heat loss	Single Intrusion	NA	5.0	700	30-35	Basalt Pelite	L: 1250, S: 980 L: 1200, S: 725	0.0	V=500 km ³	NA
Bittner and Schmelting, 1995	2-D, Convection	Single Intrusion	NA	5.0	756	27.0	Basalt Granite	L: 1100, S: 950 L: 1050, S: 760	0.0	NA	NA
Barboza and Bergantz, 1996	2-D, Convection	Fixed Temp. bottom bound. T _v /T _{int} =1.66	NA	NA	600	30-35	Pelite	L: 1200, S: 750	0.0	H=1250 m @ 79,300 yrs	NA
Raia and Spera, 1997	2-D Convection	Fixed Temp. bottom bound. T _v /T _{int} =1.10	NA	NA	1195	NA	(CaAl ₂ Si ₂ O ₈ -CaMgSi ₂ O ₆)	L: 1547, S: 1277	NA	NA	NA
Pedersen, et al. 1988	1-D, Cond. Over-Accretion	Multiple Intrusion	0.002	10.0	650	35	Basalt Granodiorite	L: 1250, S: 1100 L: 1000, S: 710	0.0	H=650 m @ 5.0 x 10 ⁶ yrs	5
Petford and Gallagher, 2001	1-D, Cond. Over-Accretion	Multiple Intrusion	1.0	1.0	650	35.5	Basalt Amphib.	L: 1250, S: 1050 L: 1075, S: 1010	50.0	H=50 m @ 1000 yrs	4
Annen and Sparks, 2002	1-D, Cond. Over-Accretion 50 m sills/10,000 yrs	Multiple Intrusion	0.005	8.0	600	30.0	Basalt Amphib.	L: 1300, S: 620 L: 1075, S: 1010	0.0	H=400 m @ 1.6 x 10 ⁶ yrs	8

¹ Dimension, heat-conduction or convection.² Intruding magma, physical configuration of intrusion (sill, etc.) or specified temperature boundary condition.³ Intruded magma listed first, then country-rock.⁴ Integrated melt volume/basal area, or for 1-D models integrated melt height

A completely efficient melting process is defined such that all of the enthalpy associated with cooling and crystallizing a volume of intruded magma is used to heat and melt only the volume of crust that becomes molten. This is efficient because no heat is 'wasted' heating regions of the crust that do not become molten, and all of the enthalpy is instantaneously applied. A similar approach is described in detail by Grunder (1995).

We define the efficiency of the melting process in these studies with respect to the efficient endmember:

$$E\% = 100 \times V_{crust}^{mod.} / V_{crust}^{eff.}, \quad (2.1)$$

where $V_{crust}^{mod.}$ is the reported melt volume (or length reported in one-dimensional simulations) and $V_{crust}^{eff.}$ is the volume of the efficient end-member predicted using the volume of intruded basalt, and the thermal parameters (liquidus, solidus, thermal diffusivity, latent heat and heat capacities) reported in the respective studies.

The predicted efficiency of the melting process corresponds closely with the geometric configuration assumed by the models. One-dimensional, vertically stacked, over-accretion conduction models that cool on both sides of the intrusions are 4 to 8% efficient (Wells, 1980; Pedersen *et al.*, 1998; Petford & Gallagher, 2001; Annen & Sparks, 2002). One-dimensional conduction simulations that cool on one side only (insulated boundary condition on the other side) are 32 to 38% efficient (Younker & Vogel, 1976). The parameterized convection model (Huppert & Sparks, 1988) with no bottom heat loss is 44% efficient. In light of the predicted melting efficiencies, uncertainty still exists as to which modeling assumptions best represent the melting process in the lower crust, especially considering more complex intrusion geometries likely in natural settings. In order to avoid *a priori* specification of an assumed intrusion configuration, we have adopted the approach of treating the intrusion process as stochastic. Multiple simulations with different dike geometries can be

combined to determine the average melting behavior of the crust for a given flux of basalt.

2.2. STOCHASTIC DIKE INTRUSION MODEL

Conservation Equations

A two-dimensional model has been developed to illuminate the possible progression of thermal and compositional heterogeneities following basalt intrusion as random dikes in the lower crust. Two sets of simulations were performed: one with only heat transfer, but no bulk flow between the basaltic dike intrusions and the crust, and another in which heat transfer, local fluid (melt plus crystals) motion, and ductile creep are considered. The two-dimensional forms of the conservation equations per unit volume are:

Conservation of Enthalpy:

$$\frac{\partial H}{\partial t} + \frac{\partial}{\partial \mathbf{x}_j} (\mathbf{v}_j H) = \frac{\partial}{\partial \mathbf{x}_i} k_{\text{mix}} \left(\frac{\partial}{\partial \mathbf{x}_i} T \right), \quad (2.2)$$

where:

$$H = \rho_{\text{mix}} \int_{T_{\text{ref}}}^T \overbrace{c_{\text{mix}}}^{\text{Sensible Heat}} dT + \overbrace{\rho_{\text{mix}} fL}^{\text{Latent Heat}}. \quad (2.3)$$

Conservation of Mass:

$$\frac{\partial \mathbf{v}_j}{\partial \mathbf{x}_j} = 0. \quad (2.4)$$

Momentum:

$$\frac{\partial}{\partial t} (\rho_{\text{mix}} \mathbf{v}_i) + \frac{\partial}{\partial \mathbf{x}_j} (\rho_{\text{mix}} \mathbf{v}_j \mathbf{v}_i) = -\frac{\partial P}{\partial \mathbf{x}_i} + \mu_{\text{mix}} \frac{\partial^2 \mathbf{v}_i}{\partial \mathbf{x}_j^2} + \rho_{\text{mix}} \mathbf{g}. \quad (2.5)$$

Species Conservation:

$$\frac{\partial \gamma}{\partial t} + \frac{\partial}{\partial x_j} (v_j \gamma) = \frac{\partial}{\partial x_i} D \left(\frac{\partial}{\partial x_i} \gamma \right) \quad (2.6)$$

Side Boundary Conditions:

$$\frac{\partial T}{\partial x_1} = 0; \frac{\partial v_2}{\partial x_1} = 0; v_1 = 0. \quad (2.7)$$

Table 2.3 has a list of symbols and nomenclature used. Einstein summation is implied for repeated vector indices. The advective (second from the left) term in the momentum equation was retained because it is important in describing chaotic advection (at Reynolds number: $\sim 10^{-2} - 10^0$) that may occur in melt-dominated regions.

In multiphase regions of melt and solid, local relative motion between crystals and melt is not considered, and the thermal and physical transport properties of the system are developed as volume-weighted mixtures of material properties using the local composition and melt fraction parameters. Details of this procedure and physical and thermal properties of the magma and solid are described in the *Appendix A*.

Table 2.3: Key to Nomenclature

Symbol	Parameter	units
H	enthalpy	(J)
t	time	(s)
k	thermal conductivity	(W/mK)
c	specific heat	(J/kgK)
T	temperature	(K)
f	melt fraction	
L	latent heat	(J/kg)
g	gravity	(m/s ²)
M	mean value of basalt melt	
N	number of model realizations	
v _i	velocity	(m/s)
CMF	critical melt function	
D	chemical diffusivity	(m ² /s)
μ_m^i	melt dynamic viscosity	(Pa·s)
μ_{mix}	mixture dynamic viscosity	(Pa·s)
$\mu_{param.}$	viscosity parameterization for $f < \text{CMF}$	(Pa·s)
ρ_c^l	amphibolite melt density	(kg/m ³)
ρ_c^s	solid amphibolite density	(kg/m ³)
ρ_b^l	basalt melt density	(kg/m ³)
ρ_b^l	solidified basalt density	(kg/m ³)
γ	composition variable	
$\xi_{\%}$	percent change in mean	

Thermodynamic Closure of Conservation Equations: Melt Fraction to Enthalpy Relationship

The geological complexity of multiphase solidification and melting can be incorporated into the enthalpy model by invoking suitable functions relating the melt fraction to the local enthalpy (Bergantz, 1990; Barboza & Bergantz, 1997).

Appropriate forms of the thermodynamic closure are obtained by parameterizing experimental data that links the melt fraction of a particular lithology to temperature.

Amphibolite Melt Fraction Relationship

A mafic, amphibolitic composition provides one end-member proxy for the composition of the lower crust in arc systems. In response to basaltic thermal input, the amphibolite may begin a dehydration reaction if there is an absence of a free vapor phase (Sen & Dunn, 1994); the so-called damp melting. Several studies have examined this reaction (Beard & Lofgren, 1991; Rapp *et al.*, 1991; Rushmer, 1991; Sen & Dunn, 1994; Wolf & Wyllie, 1994; Rapp & Watson, 1995) and are used to parameterize the melt fraction as a function of temperature (*Figure 2.1*). The melt fraction and the mode of the residuum determine the major element composition of the melts, their physical properties, as well as the partitioning of trace elements (Patiño-Douce & Johnston, 1991; Barboza & Bergantz, 1997; Ducea, 2002).

Amphibolite dehydration reactions are pressure dependent, as reflected in melt fraction and modal abundance of residual phases (Sen & Dunn, 1994). Departure from a linear melt-fraction to temperature relationship in amphibolites during dehydration results from the incongruent melting of amphibole +/- plagioclase (Wolf & Wyllie, 1994), (*Fig. 2*). At greater than ~10 kbar, amphibole and plagioclase generally react in a peritectic relationship to form an increase in the garnet and clinopyroxene mode as well as a tonalitic melt (Wolf & Wyllie, 1994).

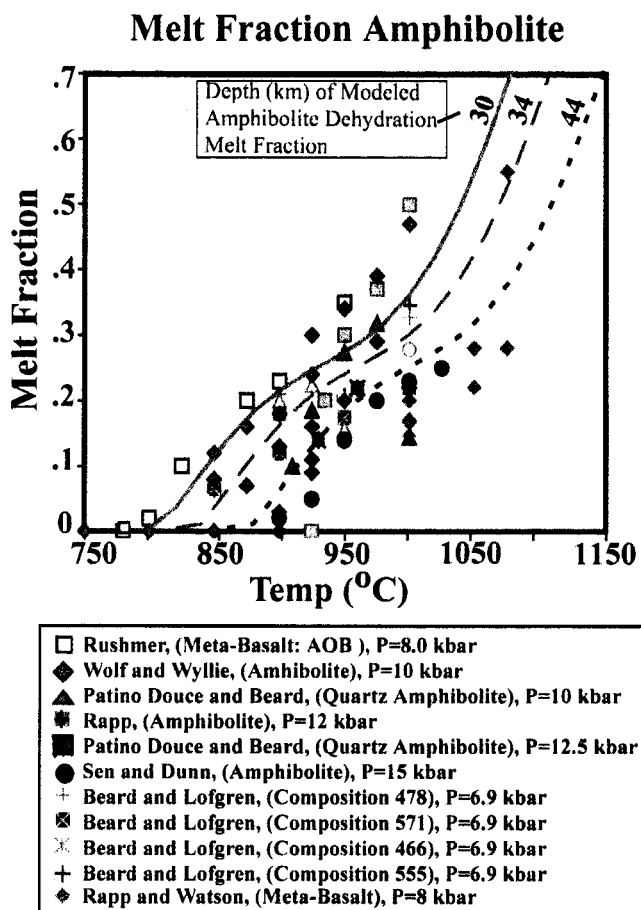


Figure 2.1: Melt fraction of amphibolite. Parameterized melt fraction functions based on the dehydration melting experiments of: (Beard & Lofgren, 1991; Rushmer, 1991; Patiño-Douce & Beard, 1994; Sen & Dunn, 1994; Wolf & Wyllie, 1994; Rapp & Watson, 1995).

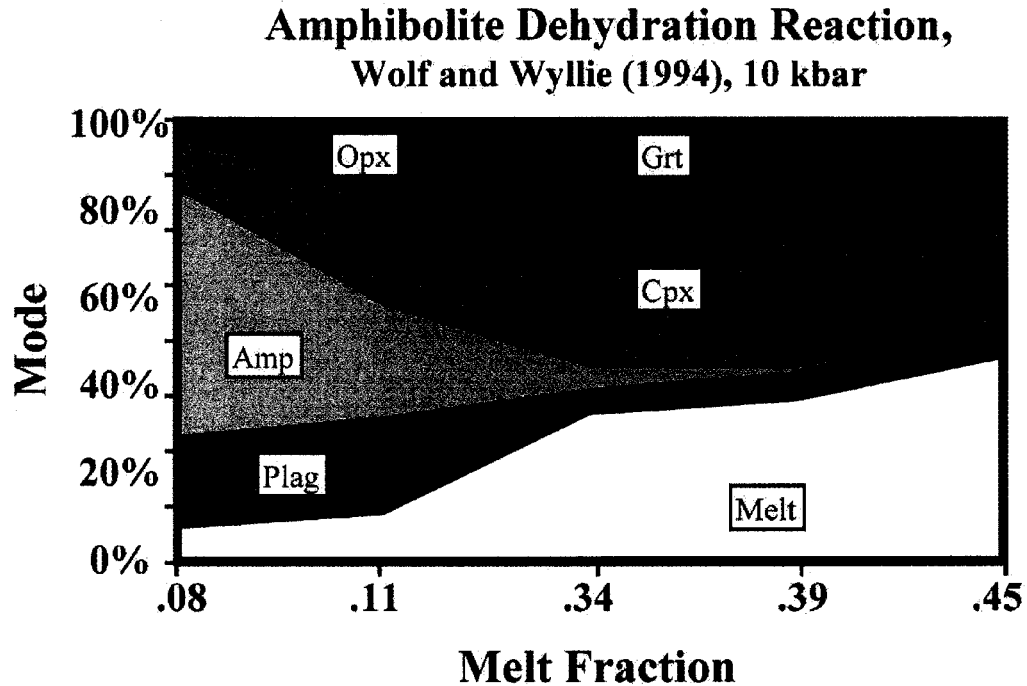


Figure 2.2: Modal abundance (by volume) of an amphibolite undergoing dehydration melting. From the experiments of Wolf and Wyllie (1994).

To obtain a general melt fraction versus temperature relationship appropriate for the modeling of amphibolite melting, we combined experiments with a range of mafic compositions with both calc-alkaline and tholeiitic trends. The functional form of the melt fraction curve was determined by parameterizing the data of Sen & Dunn (1994) at 15 kbar along with the projected liquidus for their composition using the MELTS thermodynamic package (Ghiorso & Sack, 1995):

$$f = -2.0968 \times 10^{-12} (T^*{}^5) + 1.09308 \times 10^{-8} (T^*{}^4) - 2.26718 \times 10^{-5} (T^*{}^3) + 2.33912 \times 10^{-2} (T^*{}^2) - 12.0048 (T^*) + 2451.69, \quad (2.8)$$

where:

$$T^* = T + 12.0(15\text{kbar} - P), \quad [T \text{ in degrees C, } P \text{ in kbar}], \quad (2.9)$$

$$T_{\text{solidus}} \geq T^* \geq T_{\text{liquidus}}, \quad (2.10)$$

$$T_{\text{solidus}} = .1495P^2 + 11.309P + 697.86, \quad (2.11)$$

and

$$T_{\text{liquidus}} = .25P^2 + 35.0P + 1260.0. \quad (2.12)$$

The 'stair-step' form of the melt fraction function corresponds to three stages of reactions (*Figure 2.1*). The initial stage of melting consumes the small amount of quartz present (~2 wt. %) along with plagioclase and amphibole incongruent reaction to produce a significant increase in melt over a 50°C temperature range. This is followed by the continuing reaction of amphibole and plagioclase to form melt, garnet, and clinopyroxene. The final sequence of reactions corresponds to the melting of clinopyroxene and garnet. We acknowledge there is uncertainty due to the lack of experimental data at melt fractions greater than ~.5. However, as the thermal calculations demonstrate, these higher melt fractions are unlikely to occur as a result of anatexis in the lower crust.

For internal consistency, the functional form of the melt fraction was extrapolated to lower pressure using the solidus temperature at 10 kbar (Wolf & Wyllie, 1994) and fitting the data of Rapp & Watson (1995) and the quartz amphibolite data of Patiño-Douce & Beard (1995), both at ~ 12 kbar. Below 10 kbar, garnet ceases to form as a reaction product (Beard & Lofgren, 1991; Rushmer, 1991). In general, the meta-basalts examined by Beard and Lofgren (1991) at 6.9 kbar had lower melt fractions than given by *Equation 2.8* (*Figure 2.1*), although they fall within the range of melt fractions in the other experiments at higher pressure.

This implies that at lower pressures the crust may be slightly less fertile than predicted by these calculations.

Wet Basalt Melt Fraction Relationship

The melt fraction-temperature relationship used for the wet basalt is modified from the experiments of Muntener et al (2001) for a high Mg # basaltic andesite at 12 kbar and 3.8% wt. initial water content (*Figure 2.3*). The solidus of the basalt is constrained by the experiments of Green & Ringwood (1968). Supplemental MELTS calculations have been performed for a similar composition and produce an equivalent melt fraction diagram (Ghiorso & Sack, 1995). Likewise the phases predicted by MELTS are very similar to those reported by Muntener et. al. (2001) for the period from the start of crystallization until the formation of amphibole near the furthest extent of crystallization (.39 melt fraction) reached in these experiments. The order of crystallization and comparison to MELTS calculations is depicted in the mode, *Figure 2.4*, with clinopyroxene being the dominant near liquidus phase followed subsequently by garnet then amphibole. At ~10-12 kbar the solidus of a wet tholeiitic basalt is at minimum at approximately 620°C (Green, 1982) and varies little in the range 8-15 kbar. The liquidus increases with increasing pressure at a rate of approximately 5°C/kbar (Green, 1982).

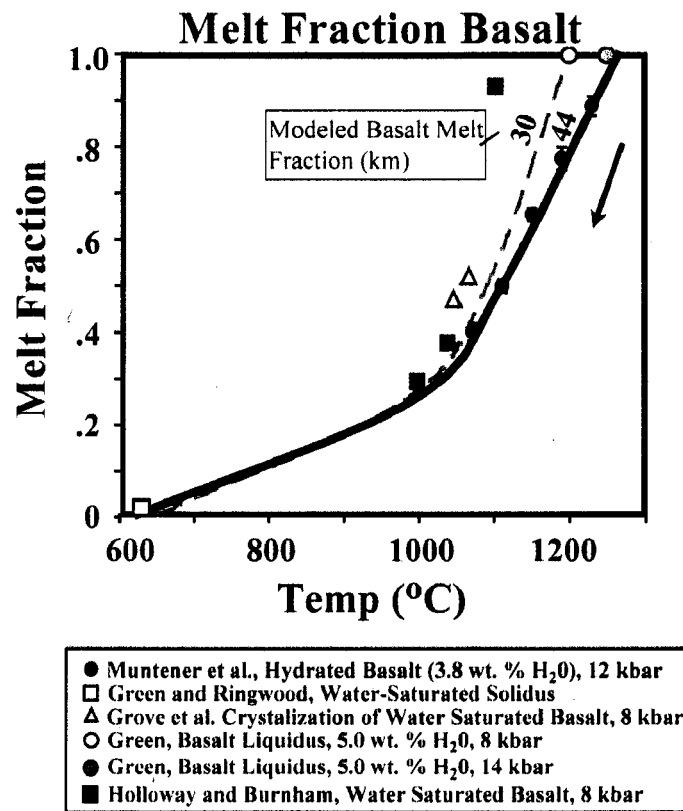
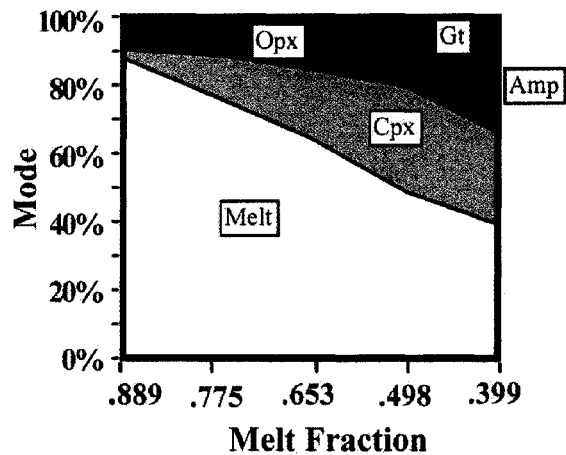


Figure 2.3: Melt fraction of wet basalt. Parameterized melt fraction function based on the experiments of Muntener et al. (2001), Grove et al. (2003), Green (1982), Green (1972), Green and Ringwood (1968), and Holloway and Burnham (1972).

A.) Mode of Basalt+3.8 wt. % H₂O
Muntener et al. (2001) P=12 kbar



B.) Mode of Basalt+3.8 wt. % H₂O
MELTS Calculation, (Ghiorso and Sack, 1995) P=12 kbar

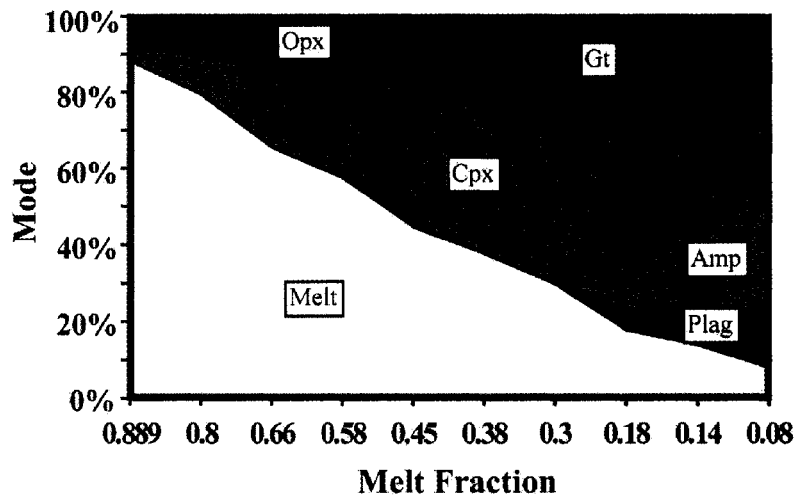


Figure 2.4: Modal abundance of a crystallizing wet basaltic andesite (3.8% wt. H₂O). A) Based on the experiments of Muntener et al., 2001. B) Modal abundance using the same starting composition as A) with the MELTS thermodynamic algorithm (Ghiorso & Sack, 1995).

A Stochastic Dike Intrusion Model: The Framework For Evaluating a Range of Intrusion Geometries

A stochastic, dike-intrusion model was developed to study the thermal, rheological and chemical consequence of basalt/mafic-crust interaction that may occur near the Mohorovicic discontinuity in arc settings. The random nature of the approach provides for a wide range of possible intrusion sequences, while still being constrained by the long-term basalt flux averages (*Table 2.1*). As it is difficult to predict the detailed stress state in the lower crust over long time periods, the stochastic approach tests all possible outcomes. Conduction simulations were performed to explore melt production as a function of crustal thickness and basalt flux. Advection simulations were also performed to examine magma mixing in regions of high melt fraction, the mingling phenomena in the low melt fraction creeping regime, and the formation of density instabilities at the mantle/crust interface (Rudnick, 1990; Kay & Mahlburg-Kay, 1991).

The lower crust is idealized as depicted in *Figure 2.5*. This two-dimensional geometry assumes that there is little variability in the perpendicular dimension to the modeled plane (along arc axis). The side boundaries are “reflecting” so that lateral temperature gradients do not develop. The two dimensional model is linked to a larger scale one-dimensional model that allows the thermal anomaly created by the injection of magma to propagate both above and below the two-dimensional domain. The smallest scales that can be resolved in the two-dimensional grid is 1 m^2 unless otherwise stated, and the one-dimensional domain has a resolution of 10 m.

The initial condition for the numerical simulations is determined by calculating a steady-state geotherm for a generic arc setting. The assumed initial heat flux at the surface is 68 mW/m^2 and the temperature is fixed at 0° C .

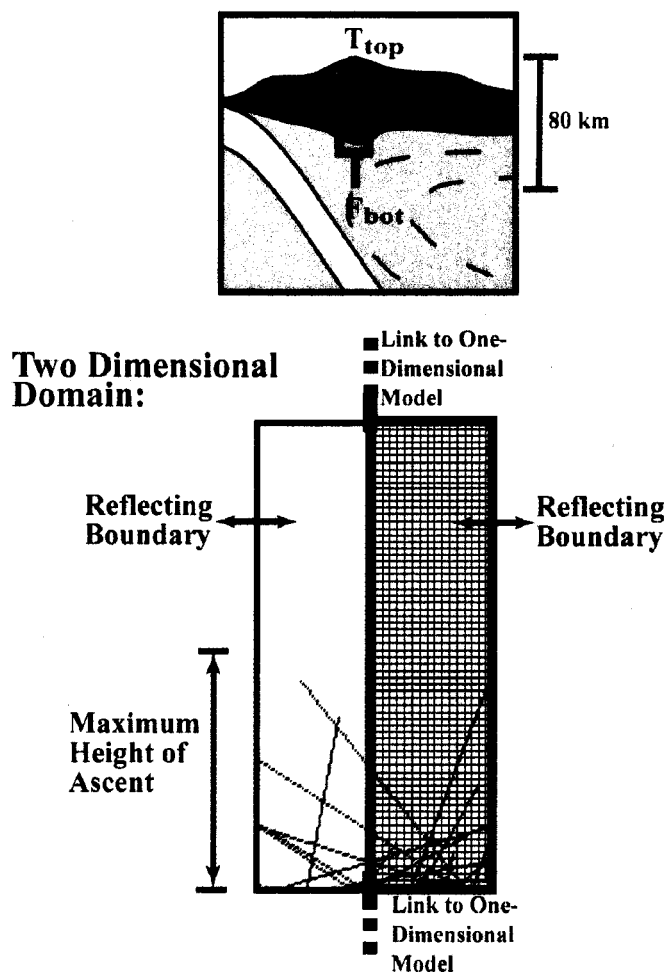


Figure 2.5: Schematic of lower crustal conduction model. A two-dimensional model is linked to a one dimensional conduction model that extends from the surface to the mantle lithosphere. Side boundaries in the two-dimensional domain are reflecting. Dikes can intrude up to the specified maximum height of ascent.

For comparison, this is approximately the current average heat flow in the Washington Cascades (Touloukian *et al.*, 1981) and approximately equal to the global average heat flow of 65 mW/m^2 (Petford & Gallagher, 2001). The initial, steady-state geotherm (Figure 2.6) was calculated by the method of Chapman & Furlong (1992).

Heat production from radioactive elements was assumed to be $.94 \mu\text{W}/\text{m}^3$ at the surface, with exponential decrease with depth with a characteristic length-scale of 15 km. Lower crustal heat production (below 15 km) was assumed to be $.5 \mu\text{W}/\text{m}^3$ and the mantle region had a heat production of $.02 \mu\text{W}/\text{m}^3$ (Chapman & Furlong, 1992).

We have modeled the injection of basalt as small aspect-ratio dikes as exemplified by the Chipman dikes and the Chelan complex (Hopson & Mattinson, 1994; Williams *et al.*, 1995) (*Figure 2.5*). Observations of outcrops with dikes at lower crustal pressures motivate the modeled fracture-assisted intrusion of mantle-derived basalt into a mafic, amphibolitic lower crust (Williams *et al.*, 1995). This implicitly assumes instantaneous emplacement of the basalt as the fracture mechanism is assumed to be much faster than subsequent viscous and thermal relaxation.

We will use the term 'realization' to denote a distinct episode of progressive basalt injection in the lower crust with multiple diking events. Ensemble averages of many different realizations of the model can then be used to describe the average behavior expected for a given flux of basalt into the lower crust, as well as the range of variability. Dike orientation in any particular realization is random to avoid *a priori* designation of dike geometry. There is an equal probability of dike intrusion in any direction (uniform distribution). The maximum height of ascent of a dike is fixed to simulate stress or material property changes that inhibit further dike propagation. Any intrusion up to the height of maximum ascent is possible (*Figure 2.5*).

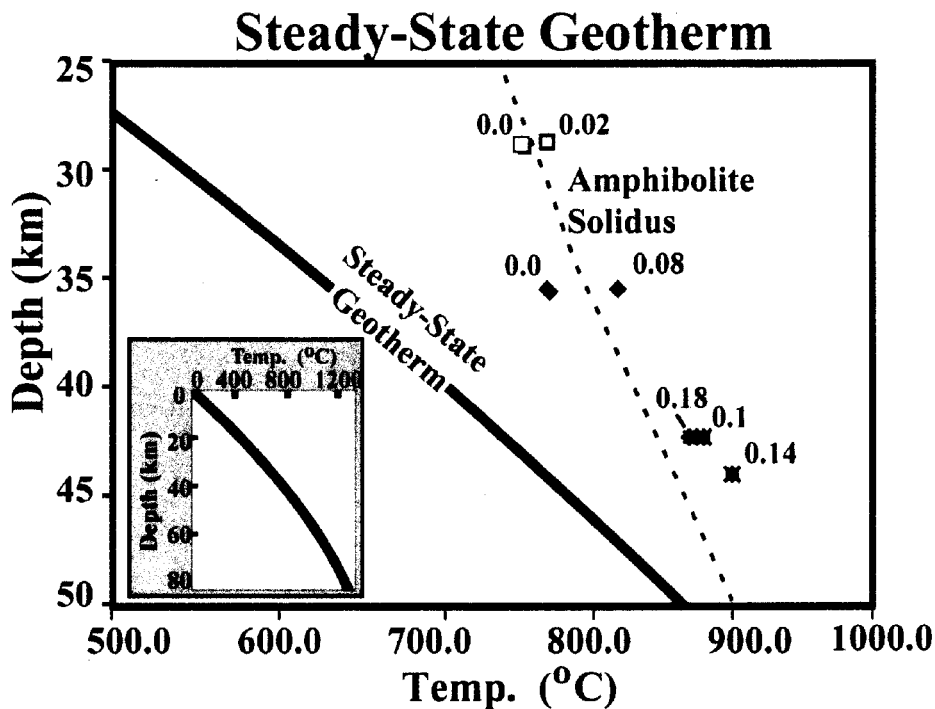


Figure 2.6. The steady state geotherm calculated by the method of Chapman and Furlong (1992). Surface heat flux is 68 mW/m^2 , approximately equal to the average heat flux in the Washington Cascades (Touloukain and Ho, 1981). This calculation is valid if the mechanical boundary layer is significantly thicker than the crustal thickness. Also shown is the inferred solidus of amphibolite from the experiments of Rushmer (1991), Wolf and Wyllie (1994), Rapp & Watson (1995), and Patiño-Douce and Beard (1995). Symbols are the same as in *Figure 2.1*.

The time interval between dike intrusion events is random, up to twice the specified average interval of intrusion, with an equal likelihood of a diking event occurring at any time up to this maximum value. The average flux of basalt is fixed in sets of simulations to facilitate comparison, but any particular realization of the model will have different dike geometries and variable intrusion histories.

The criteria for assessing the number of realizations that adequately describe this variability was defined such that adding another realization changes the mean value of the volume of basalt melt present by less than .01 %:

$$\xi_{\%} = 100 \times \left(\int M(N)dt - \int M(N-1)dt \right) / \int M(N)dt . \quad (2.13)$$

Here $\xi_{\%}$ denotes the percent change between realizations, and M is the mean for a given, N, number of realizations. This is schematically depicted in *Figure 2.7*. For the criteria $\xi_{\%} < .01$, between 25-50 realizations are typically required for the conditions studied.

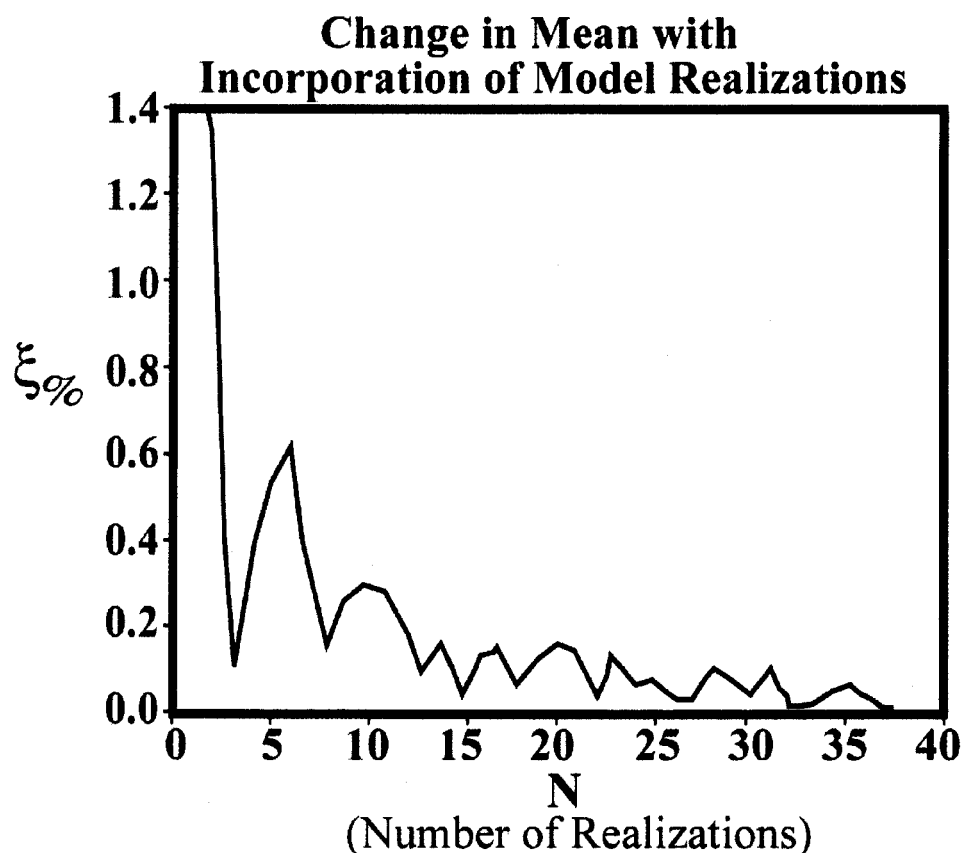


Figure 2.7. The percent change in the mean volume of basaltic melt with the progressive incorporation of more realizations. 25- 50 realizations are typically required to insure $\xi_{\%} < .01$.

Dike Intrusion Parameters

The effect of varying dike width, depth of intrusion, and maximum height of ascent of a propagating dike was accessed in separate suites of simulations. Constraints on the magnitude of these values were provided by outcrop and theoretical arguments. For example, observations of basaltic dike widths commonly less than 10 m motivated our choice of using widths of 1, 5 and 10 m in the simulations. Magma viscosity, magma over-pressure, and stress state of the host rock are all factors contributing to dike width (Fialko & Rubin, 1999). In a survey of dikes

in southwest Japan and Peru, Wada (1994) observed a correlation between the viscosity of the intruding magma and the width of dikes. For dikes with basaltic viscosity, widths of 1 – 10 m were most commonly observed. (A notable exception is the larger width dikes associated with flood basalt volcanism. The 100 m+ dike width observed in these regions have been attributed to greater magma over-pressure and extensive meltback (Fialko & Rubin, 1999).) Other observations suggest that similar controls on dike width operate at lower crustal pressures. The Chipman dikes provide evidence for dikes of tholeiitic basalt 1- 10 m+ width at an inferred pressure of 10 kbar (Williams *et al.*, 1995). Dikes from the upper mantle Balmuccia massif range in size from < 1 cm to 1 m (Mukasa & Shervais, 1999). While these observations do not restrict the possibility of larger width dikes, they do demonstrate that in many settings basalt dikes are limited to less than 10 m.

Crustal thicknesses between 30-50 km were considered in order to constrain the melt production in a range of arc settings. A thicker crust will influence crustal melt production in two ways: A.) the ambient temperature will increase with depth, and B.) the phase diagram, and hence the melt fraction diagram, is also a function of pressure. (For instance, garnet becomes a stable phase in the dehydration of amphibole after the pressure exceeds > 10 kbar (Wolf & Wyllie, 1994).) This will have an important effect on the major and trace element composition as well as potentially altering the volume of melts produced. The crustal thickness range of 30-50 km corresponds to the thickest island arc settings (Dimalanta *et al.*, 2002) as well as many continental arc settings.

Evaluating Melt Productivity

Two principal metrics will be applied to evaluate the degree of melt production. To facilitate comparison to previous one-dimensional simulations (Petford & Gallagher, 2001; Annen & Sparks, 2002) the sum of all melt fractions is normalized by the basal length of the simulations to give a melt length. This is equivalent to the 'melt thickness' reported by Petford & Gallagher (2001) or the

'compaction thickness' of Annen & Sparks (2002). While the total amount of melt is important in determining the overall mass balance of magma entering, residing and potentially exiting the lower crust, the local melt fractions determine the composition of any particular melt. At each time-step, there is a range of residual basalt and crustal melt fractions distributed throughout the modeled section of the lower crust. The basalt melt fractions vary from some minimum melt fraction that reflects basalt that has cooled to ambient conditions, up to a maximum melt fraction of 1.0 when the basalt intrudes at its liquidus. Similarly, a range of crustal melt fractions can coexist in one time-step from unmelted crust up to a maximum crustal melt fraction in regions in proximity to voluminous or recent basalt intrusion. For both the basalt and crustal material, the respective mean melt fraction is calculated by averaging the melt fractions of all areas that exceed their solidus.

2.3 RESULTS

Depth of emplacement, maximum height of ascent of the intrusions, and basalt flux were varied in the conduction simulations to elucidate the range of residual basalt and crustal melt fractions and the amount of melt produced (*Table 2.4*). A second set of simulations also considering advective transport were conducted using the temperatures from conduction simulations as the initial and boundary conditions. Dynamic simulations over short (5.0×10^3 yr) and long (10^7 yr) timescales examined magma mixing and ductile creep, respectively.

Single Realizations and Stochastic Ensemble Behavior

The progress of a single realization illustrates the spatial distribution of intruded basalt and crustal melt fractions that can coexist at a single instant in time (*Figure 2.8*). In this example calculation, the zone of intrusion is 100 m thick, the average basalt flux is $.001 \text{ m}^3/\text{m}^2\text{yr}$, and the crustal thickness is 44 km or at approximately 12.5 kbar pressure assuming an overlying crust with an average density of $2900 \text{ kg}/\text{m}^3$. The time after initiation of basalt intrusions is 50,000 years. Each dike is injected as a separate event, and the most recent dike intrusion and

associated temperature perturbation can be identified in the lower left-hand corner of the simulated domain depicted in *Figure 2.8*.

Table 2.4: Selected Conduction Results

Time Flux (yrs) (m^3/m^2yr)	Dike Width (m)	Max. Height of Ascent (m)	Depth (km)	Max. Amp. Melt Frac.	Mean Amp. Frac.	Mean Res. Melt Frac.	Min. Res. Melt Frac.	Norm. Amp. Melt Vol.	Norm. Basalt Melt Vol.	Norm. Ratio Basalt Melt Mantle Melts)	Standard Dev. Basalt Melt	Standard Dev. Crustal Melt	Diff. Lenth -Scale
10^6	0.0005	10	34	0	0	0.03	0.02	0	14.45	0	2.8	0	470
10^6	0.0005	5	34	0	0	0.03	0.02	0	15.6	0	3.1	0	332
10^6	0.0005	1	34	0	0	0.04	0.03	0	18.9	0	3.2	0	148
10^6	0.001	10	34	0	0	0.04	0.02	0	39.5	0	5.8	0	331
10^6	0.0005	10	44	0.08	0.04	0.09	0.06	118.9	43.3	2.74	6.2	10	470
10^6	0.001	5	34	0	0	0.05	0.04	0	44.5	0	6.3	0	234
10^6	0.001	10	34	0	0	0.05	0.04	0	52.1	0	6.8	0	331
10^6	0.0005	1	44	0.19	0.09	0.18	0.13	296.2	90.15	3.28	8.7	31	148
10^6	0.001	10	44	0.19	0.09	0.18	0.14	293.5	179.8	1.63	13.	28	331
10^6	0.001	5	44	0.20	0.10	0.18	0.15	307.6	183.4	1.67	16.	16	234
10^6	0.001	1	44	0.23	0.12	0.19	0.16	392.2	191.3	2.05	15.	22	104
10^6	0.005	10	34	0	0	0.10	0.05	0	492.5	0	44.	0	148
10^6	0.005	1	34	0.07	0.06	0.16	0.15	43.6	795.5	0.054	48.	11	47
10^6	0.005	10	44	0.32	0.22	0.21	0.16	662	1042.5	0.634	72.	42	148
10^6	0.005	5	44	0.33	0.22	0.21	0.16	683	1051.5	0.649	76.	25	105
10^6	0.005	1	44	0.47	0.28	0.23	0.26	1157.9	1139.5	1.016	66.	42	47

Table 2.5 Selected Conduction Results and Crustal Melting Efficiency

Time (yrs)	Flux (m ³ /m ² /yr)	Dike Width (m)	Max. Height of Ascent (m)	Depth (km)	Max.		Mean		Min.		Norm.		Efficiency (%)
					Amp. Melt Frac.	Frac.	Amp. Melt Frac.	Frac.	Basalt Melt Frac.	Basalt Melt Frac.	Amp. Melt Vol. (m)	Basalt Melt Vol. (m)	
10 ⁶	0.001	10	1000	34	0	0	0.02	0.01	0.03	0	0	17.9	0
10 ⁶	0.005	10	1000	34	0	0	0.06	0.03	0.03	0	0	310	0
10 ⁶	0.001	10	1000	44	0.13	0.07	0.12	0.09	0.09	35.8	124	10.4	10.4
10 ⁶	0.005	10	1000	44	0.17	0.10	0.14	0.11	0.11	50.3	715	3.4	3.4
5×10 ⁶	0.001	10	1000	34	0	0	0.08	0.03	0.03	0	402.5	0	0
5×10 ⁶	0.005	10	1000	34	0.15	0.07	0.15	0.08	0.08	242.9	3757.5	0.5	0.5
5×10 ⁶	0.001	10	1000	44	0.35	0.17	0.22	0.08	0.08	693.9	1124.5	7.1	7.1
5×10 ⁶	0.005	10	1000	44	0.45	0.22	0.30	0.19	0.19	1038.6	7437.5	2.3	2.3
10 ⁷	0.001	10	1000	34	0	0	0.10	0.06	0.06	0	1044	0	0
10 ⁷	0.005	10	1000	34	0.18	0.08	0.16	0.12	0.12	532.0	8115	0.6	0.6
10 ⁷	0.001	10	1000	44	0.43	0.21	0.25	0.13	0.13	1044.5	2480	5.7	5.7
10 ⁷	0.005	10	1000	44	0.52	0.27	0.33	0.25	0.25	1479.1	16565	1.6	1.6

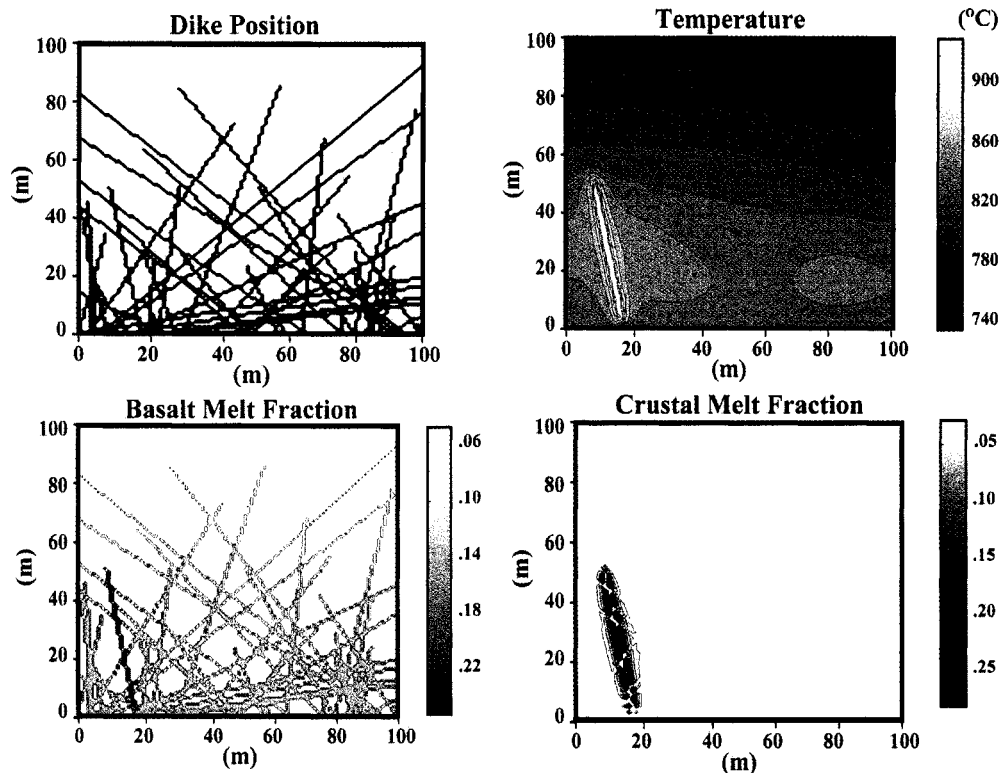


Figure 2.8. Example of a single realization of random dike intrusion. The zone of intrusion is 100 m thick, average basalt flux is $.001 \text{ m}^3/\text{m}^2\text{yr}$, crustal thickness is 44 km, and the time after the initiation of intrusions is 50,000 years. Dike position, temperature, and basalt and crustal melt fractions are shown.

The unique intrusion history of each realization yields a range of melt volumes when an ensemble of simulations are combined (*Figure 2.9*). The mean and standard deviations of melt volumes for the basalt and crustal melts from a selected group of simulations is presented in *Table 4*. The melt volume standard deviations range from 5-40 % of the mean volumes. In general, larger percentage standard deviations occur at lower basalt intrusion rates for timescales less than 10^6 years. At lower fluxes of basalt ($<.001 \text{ m}^3/\text{m}^2\text{yr}$), individual intrusions result in localized, transient thermal anomalies that are primarily responsible for melt production.

Thermal Evolution of the Lower Crust Following Basalt Intrusion

The progressive emplacement of basaltic dikes increases the ambient temperature in the lower crust and a temperature anomaly develops with respect to the steady-state geotherm (*Figure 2.10*). This phenomena has been noted in several other numerical studies of intrusion in the lower crust (Wells, 1980; Pedersen *et al.*, 1998; Annen & Sparks, 2002) and is simply understood as the input of thermal energy associated with successive basalt injection accumulating at a faster rate than the heat can be diffused. Hence, two thermal time-scales are relevant in the heating of the crust through thin intrusions: A.) the time-scale of diffusion for individual intrusions and B.) the time-scale of diffusion for the broader thermal anomaly associated with the amalgamation of successive intrusions. The shorter wavelength, higher amplitude, thermal perturbations associated with the former are primarily responsible for the maximum basalt and crustal melt fractions, but also decay on timescales of $\sim d_w^2/\kappa$, where d_w is the dike width and κ is

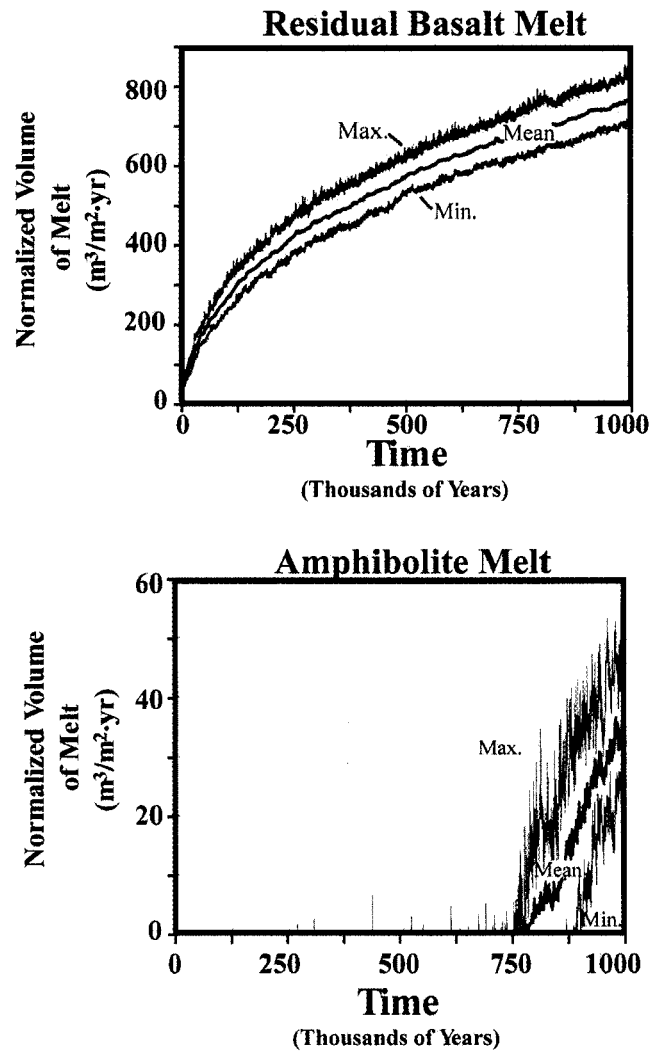


Figure 2.9. The mean, maximum and minimum volume of crustal and basalt melt normalized by the basal area of the simulations (yielding a melt length). Basalt flux is $.005 \text{ m}^3/\text{m}^2\text{yr}$, dike thickness is 1 m, crustal thickness is 34 km, and the maximum height of ascent is 100 m. Other melt volumes and standard deviations are shown in Table 2.4.

the thermal diffusivity. For 1 m wide dikes this timescale is of the order of 10-20 days. The broad, low amplitude thermal anomalies associated with the slow accumulation of basalt through successive intrusions decay on timescales more

closely associated with the zone of active intrusion. For a 100 m thick zone of active intrusion diffusive timescales on the order of 400 years are applicable.

For the basalt fluxes of $.0001-.005 \text{ m}^3/\text{m}^2\text{yr}$ the temperature near the zone of intrusions increases with time, and on average, the temperature following an intrusion does not have sufficient time to relax to the steady-state profile completely before the next intrusion. *Figure 2.10* depicts the width and amplitude of the mean thermal anomalies for several different scenarios. Two different basalt fluxes ($.0001 \text{ m}^3/\text{m}^2\text{yr}$ and $.005 \text{ m}^3/\text{m}^2\text{yr}$) are considered to intrude a crust 34 km thick. In scenario (a) the maximum height of ascent is 1000 m and dike width is 10 m, in scenario (b) the maximum ascent height is 100 m with 10 m wide dikes, and in (c) the maximum ascent height of the dikes is 100 m with 1 m dikes. The mean temperature increases the fastest when the intrusions are narrower and concentrated in the smallest region of the crust. After 10^6 years following the initiation of basalt intrusion, only scenarios b and c with the basalt flux of $.005 \text{ m}^3/\text{m}^2\text{yr}$ produce crustal melts. All model realizations with basalt fluxes of $.0001 \text{ m}^3/\text{m}^2\text{yr}$ create thermal anomalies over 10^6 years with the ambient temperature increased only 20-40 °C over the steady-state geotherm.

The amplitude of the thermal anomalies and the time required to reach the crustal solidus at different crustal depths varies greatly, and is an important constraint in determining the composition of melts from young versus mature arc systems. Whether or not crustal melting can occur depends on the thickness of the crust, the basalt intrusion rate, and the length of time the basalt intrusion rate remains approximately constant. The temperature difference between the solidus of the amphibolite and steady-geotherm decreases with increasing depth (*Figure 2.6*). As a consequence, for a given increase in temperature above the steady-state geotherm, amphibolite crust at depth will have a higher degree of melt. This is demonstrated in *Figure 2.11* in which the basalt flux is held constant at $.001 \text{ m}^3/\text{m}^2\text{yr}$, the zone of intrusion is 100 m thick, and dike widths are 1 m thick. For a crustal thickness of 30

km, the mean crustal melt fraction takes $\sim 1.3 \times 10^7$ years to reach .1. Even after 5.0×10^7 years of basalt intrusions the mean crustal melt fraction does not exceed .4 at this depth. For comparison, the period of time from the initiation of subduction to present in several Pacific island arcs varies between $\sim 2.5 \times 10^7$ years. to $\sim 5.0 \times 10^7$ years (Dimalanta *et al.*, 2002). In contrast, mean crustal melt fractions exceeding .4 at 50 km depth occur after $\sim 1.5 \times 10^6$ years of intrusion for the same basalt flux. These calculations predict that production of significant volumes of crustal melt is much more likely in the thickened crust of mature, continental arcs.

At depths greater than ~ 40 km, immediately following the initiation of intrusions, there will be greater volumes of crustal melt than residual basalt (*Figure 2.12*). This can simply be explained by the greater initial temperatures from the steady state geotherm. As basalt continues to intrude at these depths the volume of residual basalt will become greater than crustal volumes. At shallow depths (< 40 km) the volume of mantle melts is always greater than the crustal melt volume.

Style of Emplacement of Basalt Dikes: Maximum Height of Ascent

The degree to which basalts can penetrate the overlying crust will influence the efficiency of crustal melting. Previous studies have focused on an end-member intrusion geometry where basalt accumulates in sill-like bodies at the base of the crust, and each successive basaltic sill is emplaced on top of the other sills. However, it is clear that primitive magmas reach the surface (Cole, 1982; Muntener *et al.*, 2001), motivating further examination of deviations from the over-accretion assumption as used in previous models (Table 2.2). To assess the sensitivity of the ascent of basaltic magma to different crustal levels, the maximum height of ascent of the dikes was varied while holding the basalt flux constant at $.001 \text{ m}^3/\text{m}^2\text{yr}$ with 5 m wide dikes. The development of crustal melt and residual basalt melt volumes is depicted in *Figure 2.13* after intrusions lasting 10^6 years.

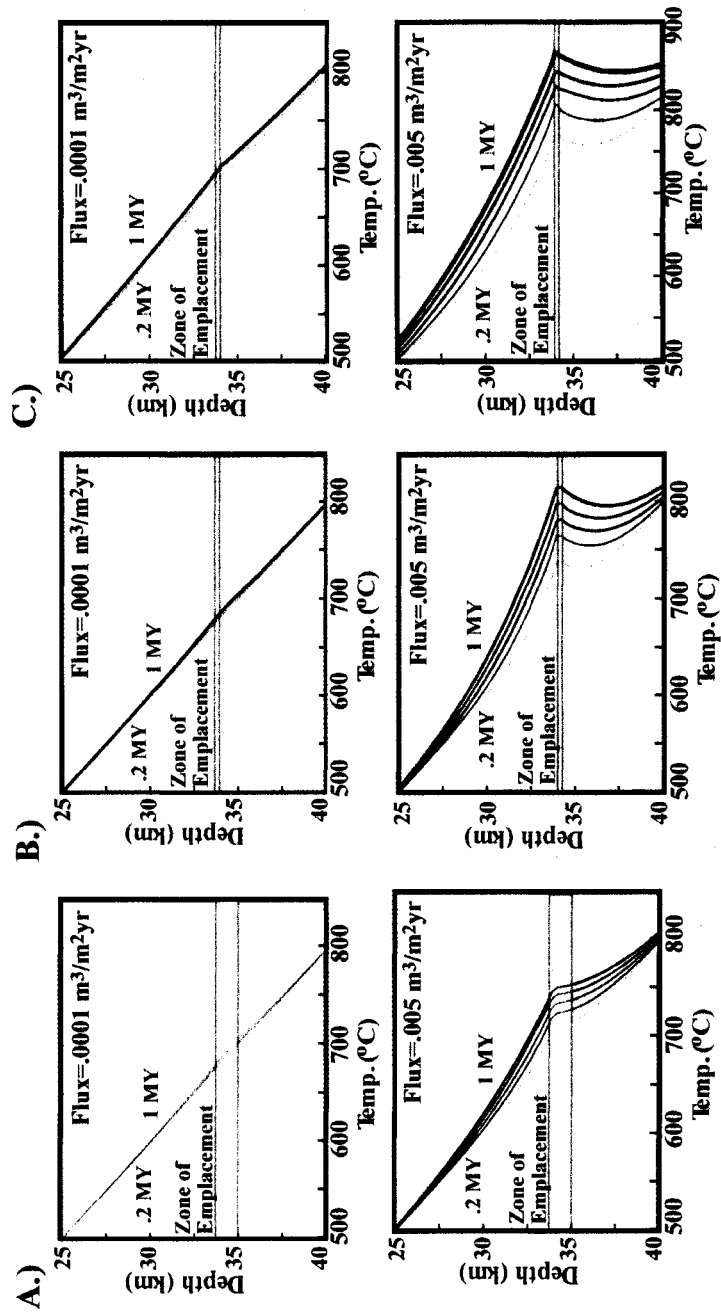


Figure 2.10. Temperature profiles as a function of depth. The shaded region is the domain of the two-dimensional models in which active intrusion is occurring. Extending beyond this domain is the one-dimensional conduction model. In all simulations the crust is 34 km thick, and two basalt fluxes are considered: .0001 and .005. In A.) the maximum height of ascent is 1000 m and dike width is 10 m, B.) the maximum height of ascent is 100 m with 10 m dikes, and in C.) the maximum height of ascent is 100 m with 1 m dikes.

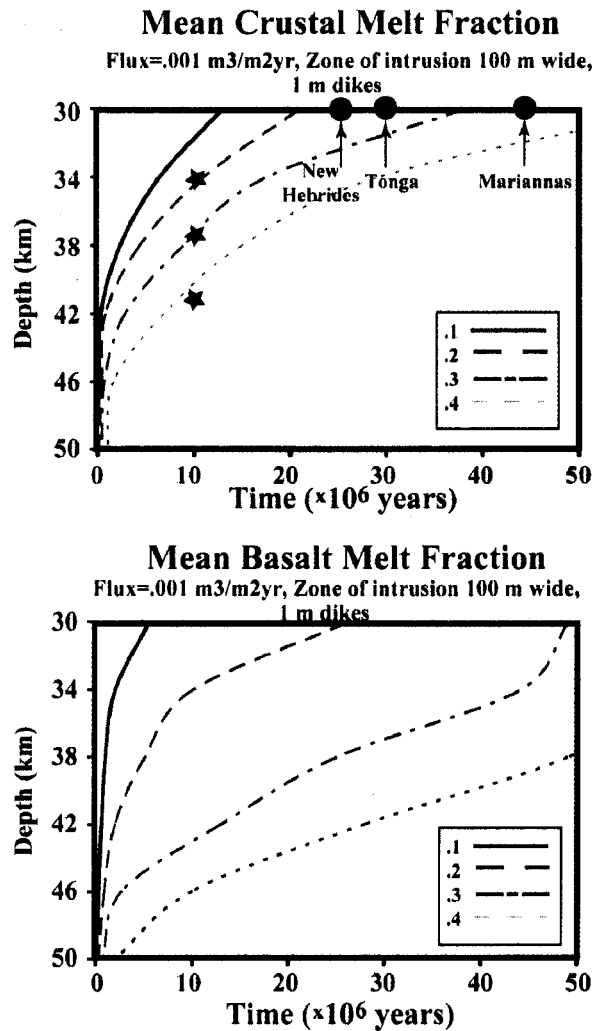


Figure 2.11. Mean crustal and basalt melt fractions as a function of time and depth. All simulations use a flux of .001 m³/m²yr, 100 m maximum height of ascent and 1 m dikes. For comparison, the time since the initiation of subduction for the New Hebrides, Tonga and Mariannas island arcs are shown (all these regions have less than 30 km thick crust (Dimalanta et al., 2001)). The stars mark conditions that were used for the initial conditions of the advection simulations examining magma mixing and mingling.

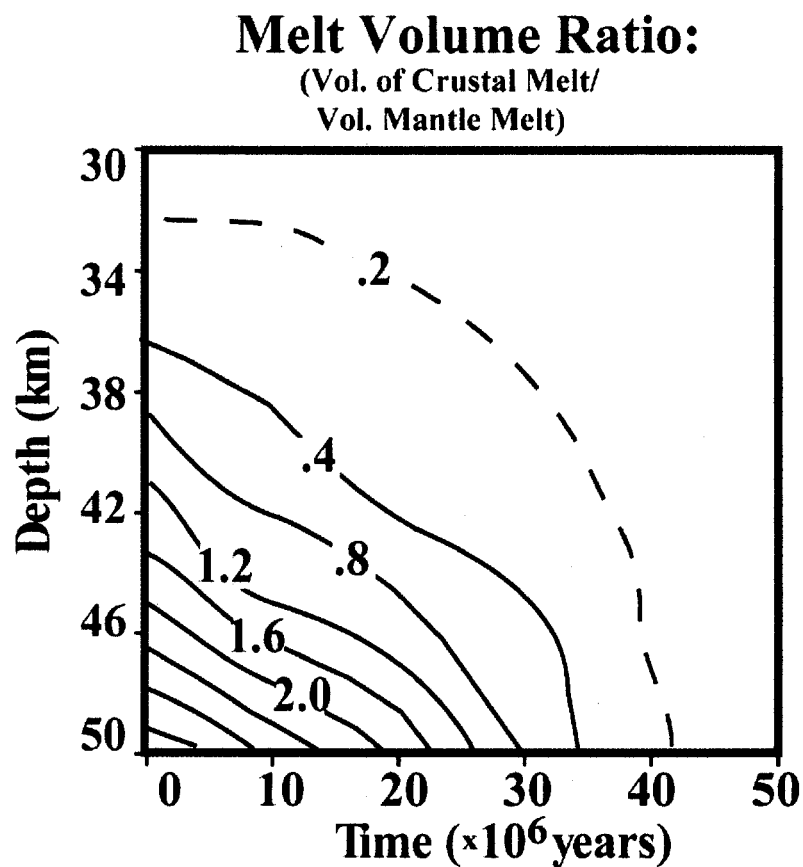


Figure 2.12. Melt volume ratio (volume of crustal melts/ volume of mantle melts). Conditions are the same as in *Figure 2.11*. At greater depths and just following the initiation of intrusions greater volume of crustal melt can be produced, while shallow and long-lived systems favor greater volumes of residual basaltic melt.

The assumption of over-accretion maximizes the volumes of both residual basalt melt and crustal melts. For thick crust (>44 km) some crustal melting will occur if the dikes are intruding up to 5 km from the base of the crust. However, the crustal melt volume produced for such long range propagation decreases 3 orders of magnitude compared with over-accretion (*Figure 2.13*). Basalt injections that propagate less than 100 m from the base of the crust produces a greater volume of crustal melt than residual basalt melt at 44 km depth over 10^6 years of basalt intrusion. However, as the maximum height of ascent increases and the basalt reaches shallower depths, a larger ratio of residual basalt will coexist with crustal melts.

Dikes ascending to shallower levels in the crust are less likely to produce significant crustal melting for three reasons. The greater length of the dikes spreads the flux of enthalpy over greater areas, and hence if the flux of basalt is constant, the cumulative probability that dikes will overlap for a given period of time decreases. Secondly, the average interval of time between dike events is increased to maintain a constant flux, and with this increased time the longer dikes can diffuse their enthalpy over a greater area. A large amount of energy is expended increasing the temperature of a large volume of crust by only a few °C. Finally, dikes that reach shallower regions of the crust also encounter a larger temperature contrast between the basalt liquidus and the surrounding crust, which promotes solidification of the dikes without crustal melting.

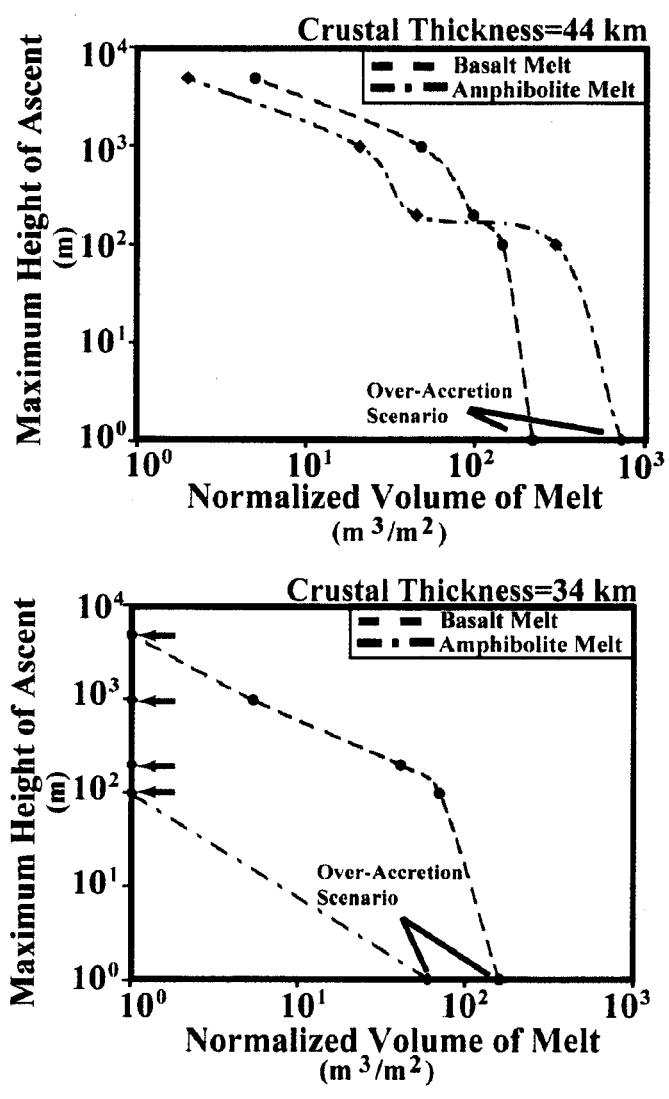


Figure 2.13. Effect of maximum height of ascent. The normalized volume of melt for both the crust and basalt is given as a function of the maximum height of ascent after 10⁶ years of intrusion, basalt flux of .001 m³/m²/yr and dike width of 5 m. Two crustal thicknesses are considered: 34 km and 44 km. Over-accretion maximized the melt volume for the conditions examined.

Thin crust (~34 km) is associated with a much smaller degree of crustal melting, provided that the lithosphere thickness is constant as implied by the steady-state geotherm calculations (McKenzie & Bickle, 1988). For all propagation lengths, the residual basalt volumes are greater than volumes of crustal melt. For maximum heights of ascent greater than 100 m, only isolated patches of crustal melting occurs and no long-term reservoir of crustal melt is developed over 10^6 years. When the basalt dikes extend greater than ~ 5 km from the base of this thinner crust, no residual basalt melt accumulates beyond the timescale to conductively cool single intrusions. These calculations do not rule out dike events extending to the top of the crust and rapidly erupting material from depth. However, for this thermal environment, if dikes stall during their ascent no melt will be retained on timescales on the order of $\sim d_w^2/\kappa$.

The Effect of Intrusion Width on Crustal Melting

The width of the basalt intrusions will be influenced by the basalt magma viscosity, material properties of the surrounding crust and the magma over-pressure. Dike widths of 1, 5 and 10 m were considered at different crustal depths and basalt flux (*Figure 2.14*) to characterize the melt productivity as a function of dike width.

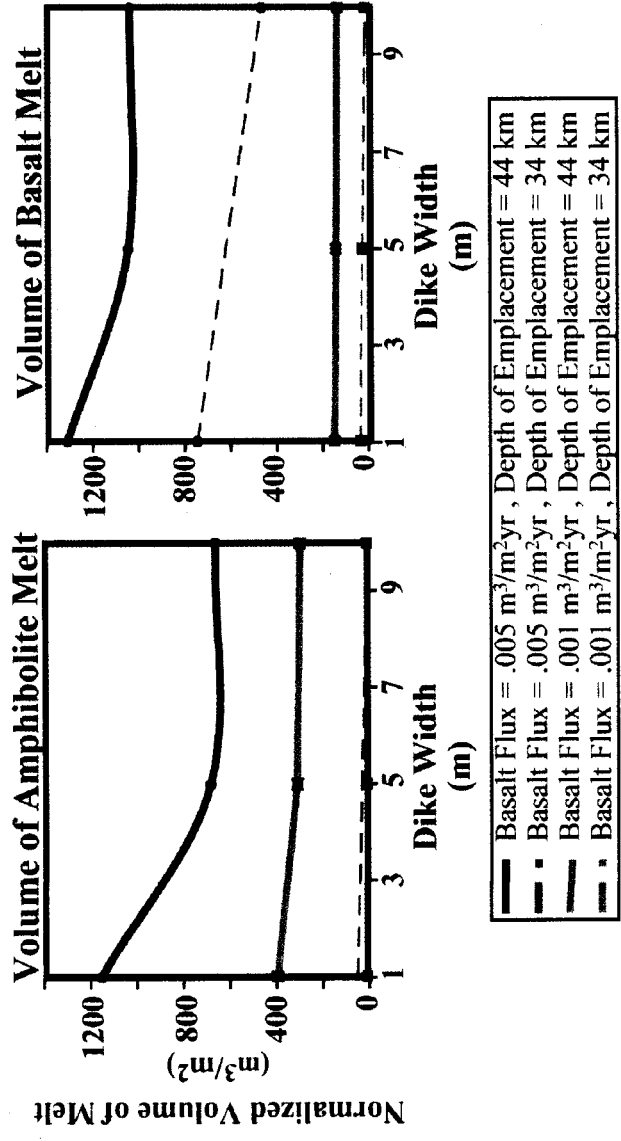


Figure 2.14. Effect of dike width on melt production. Dikes of 1, 5 and 10 m were considered. The smaller width dikes maximized the melt volume in the stochastic simulations.

For a given flux of basalt, smaller width dikes increase the melt volumes for both the residual basalt and the crustal melt. The average time interval between dike intrusions is much less for the 1 m dikes with constant intrusion rate, and consequently the probability of overlapping thermal anomalies of large amplitude is greater. In most scenarios 1 m dikes produced ~ 5 to 15 percent greater melt than 10 m dikes. This effect on crustal melting is particularly pronounced for the highest flux rate ($.005 \text{ m}^3/\text{m}^2\text{yr}$) and 44 km depth.

The more complex intrusion geometry at least partially explains the difference between this dependence on dike width in these simulations compared to the results of one dimensional over-accretion models in which the location of intrusion is prescribed. Petford & Gallagher (2001) report that crustal melting is maximized when the period between intrusions equals the diffusive heat loss timescale of the basalt sills. In their analysis, if heat is lost faster than the timescale for diffusion less crustal melting will result. Annen & Sparks (2002) report little difference in crustal melt production for 10, 50 and 500 m sills at 20 km depth. The crucial difference between the over-accretion condition and our two-dimensional intrusion conditions is the probability of intersection of thermal anomalies. Over-accretion specifies that successive sill intrusions be adjacent to each other, and so the analysis of Petford & Gallagher (2001) applies. However, in the two-dimensional calculations the probability of intersection of dikes and their associated thermal anomalies is less than 1. Hence dike intrusion configurations that promote the greater intersection of dikes, and hence thermal anomalies, will develop greater crustal melting.

Basalt Flux and Crustal Thickness: Primary Controls on the Crustal Melting Process

The two most important factors controlling the growth of thermal anomalies in response to the intrusion of magma are the depth of emplacement and the flux of the intruding magma. Flux was varied in this suite of simulations between $.0001$ and $.005 \text{ m}^3/\text{m}^2\text{yr}$ to simulate the estimated range of basalt flux into the crust in arc

settings (Table 1). The crustal thickness was varied between 30 and 50 km. A summary of crustal melt fractions and the residual basalt melt fractions at 10^6 years for 100 m intrusion zone and 1 m dikes is presented in *Figure 2.15*. Similar results are produced after 10^7 years for 10 m wide dikes and a maximum ascent height of 1000 m (*Figure 2.16*). Crustal melt fractions vary from 0 to the maximum crustal melt fraction in the upper left columns of *Figures 2.15* and *2.16*. Likewise basalt melt fractions are bounded by their intruded melt fraction, 1.0, and their minimum melt fraction shown in the lower left of *Figures 2.15* and *2.16*.

The simulations predict that for a thin crust (~30 km) of mafic composition, and the specified initial condition of 68 mW/m^2 surface heat flow, very little to no crustal melting can be expected for geologically constrained basalt fluxes. At 10^6 years the intrusive zones of 100 m and 1000 m fail to produce mean crustal melt fractions above .1 even at the highest basalt flux. Except for the very lowest basalt fluxes, a small amount of residual melt from the basalt will remain after reaching ambient conditions. However, the basalt ensemble average melt fractions do not exceed .2 following 10^6 years since the initiation of intrusions for shallow depths. Residual basalt magma compositions in these melt fraction ranges are generally dacitic to rhyo-dacitic, and the crustal melts are dacitic (tonalitic) and have ~65 wt. % SiO_2 .

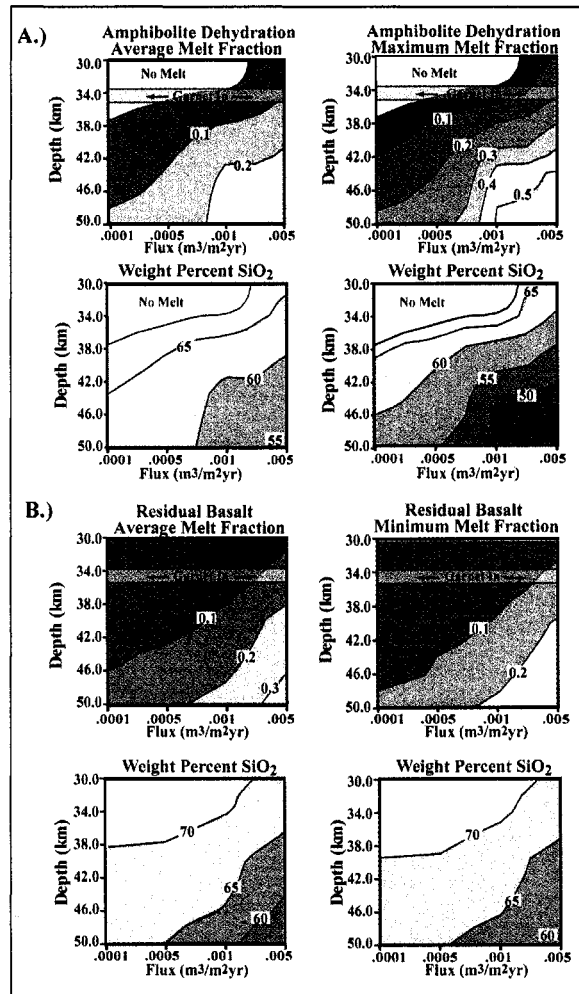


Figure 2.15. Melt fraction of A.) crustal and B.) basaltic material as a function of depth and flux of basalt. The maximum height of ascent was 100 m, dike width was 1 m and the information was extracted 10^6 following the initiation of modeled intrusions. For the amphibolite composition both the average and maximum melt fractions are shown. Melt fractions of the amphibolite in the simulations will vary from 0 to the maximum melt fraction. The mean and minimum basalt melt fractions are shown. Basalt melt fractions will vary from their intruded melt fraction of 1 to the minimum melt fraction. The predicted wt. % SiO₂ is given for the amphibolite and basalt based on the experiments of Wolf and Wyllie (1994) and Muntener et al. (2001), respectively, and from MELTS calculations.

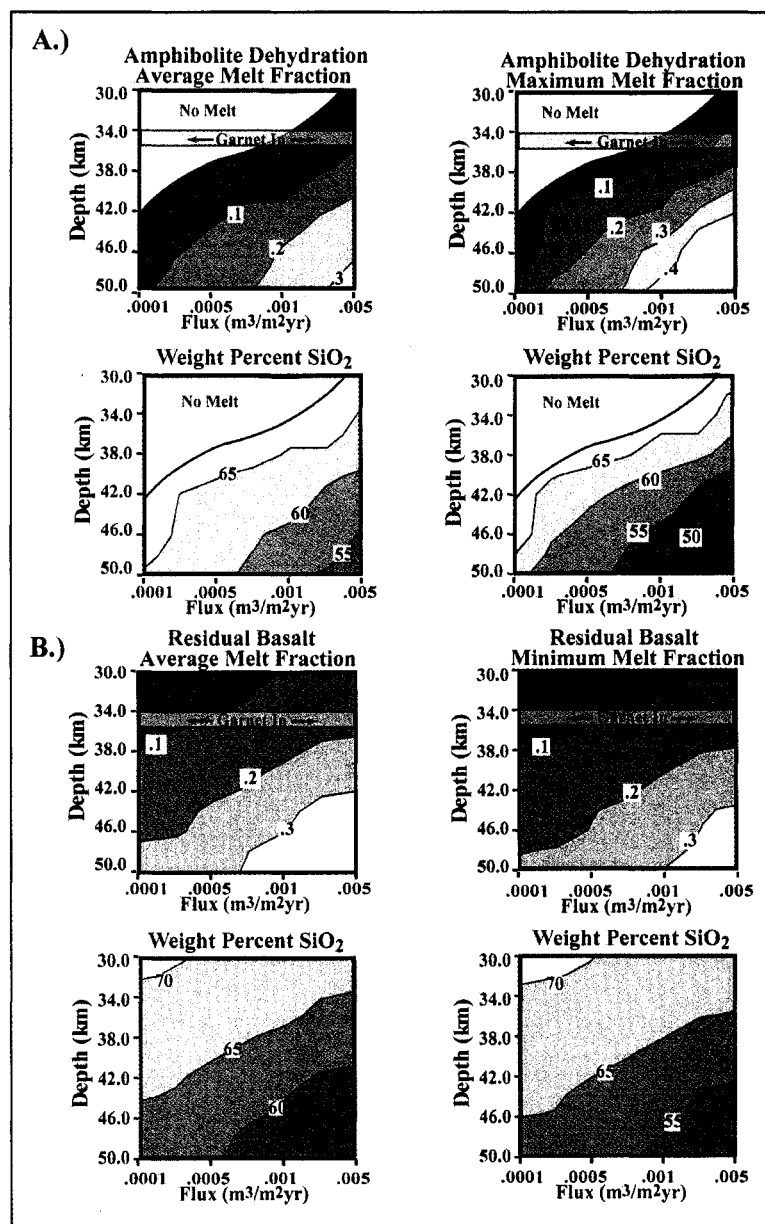


Figure 2.16. Melt fraction of A.) crustal and B.) basaltic material as a function of depth and flux of basalt. The maximum height of ascent was 1000 m, dike width was 10 m and the information was extracted 10^7 years following the initiation of intrusions.

Melting is facilitated with increasing depth, and with a 40 km thick crust, crustal melt fractions exceed .2 for both the 100 and 1000 m maximum heights of ascent after 10^6 years of intrusion. After 10^7 years the crustal melt fractions reach $\sim .3$. Coeval basalt melt fractions have approximately the same range as the crustal melt fractions (.2-.3). At 50 km depths the mean crustal melt fractions are slightly lower than the residual basalt melt fractions. Average crustal melt fractions reach $\sim .35$ at these depths after 10^7 years of intrusion for a maximum ascent height of 1000 m. The coeval maximum basalt melt fraction is approximately $\sim .38$. After 10^7 years of intrusion at depths greater than 40 km and basalt fluxes exceeding $.001 \text{ m}^3/\text{m}^2\text{yr}$, both the residual basalt and crustal melts are andesite to basaltic andesite in composition and can persist as long as basalt flux continues into the lower crust system.

Within the stochastic framework, the efficiency of crustal melting is slightly enhanced relative to the reported one-dimensional over-accretion values (4-8%) for greater depths (>40 km), low basalt flux ($<.0005 \text{ m}^3/\text{m}^2\text{yr}$), and immediately following initiation of intrusion. For instance, after one million years and at 44 km depth, 10 m wide dikes are $\sim 10\%$ efficient at producing crustal melts (*Table 2.4*). However, because the active zone of intrusion remains fixed at the base of the crust, the efficiency of crustal melting decreases with time as more enthalpy is consumed elevating the temperature of recently intruded basalt. After ten million years, 10 m dikes are only 5% efficient at producing crustal melts at 44 km depth. For the assumed initial geotherm, the injection of basalt in dikes is less efficient at all times relative to over-accretion for thin crust.

The Geotherm and Surface Heat Flux

Although the initial steady state geotherm was calculated with a surface heat flux of $68 \text{ mW}/\text{m}^2$, the surface heat flux with the progressive intrusion of basalt increased with time (*Figure 2.17*). After 5.0×10^7 years of simulated time, and a basalt flux of $.001 \text{ m}^3/\text{m}^2\text{yr}$, the surface heat flux from intrusions at 30 km depth exceeds $100 \text{ mW}/\text{m}^2$. For similar conditions, but with intrusions at 50 km depth the

surface heat flux is at approximately 80 mW/m^2 after 5.0×10^7 years of intrusions. As expected, the simulations indicate that the thicker crust produces a greater amount of crustal melting, but has a lower surface heat flux than the thinner crust with the same flux of basalt.

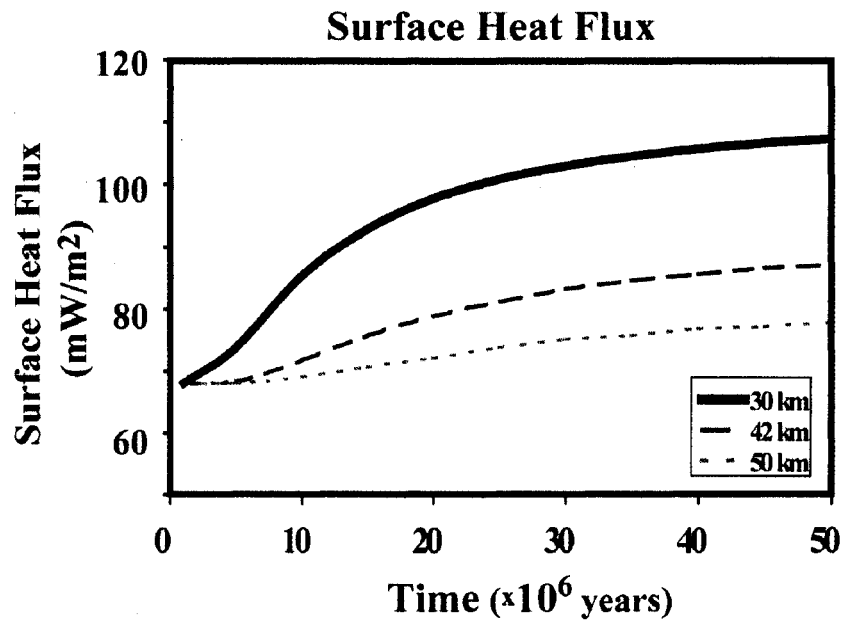


Figure 2.17. Average surface heat flux as a function of time. Three simulated conditions are considered: $.001 \text{ m}^3/\text{m}^2/\text{yr}$ basalt flux with 30 km, 42 km and 50 km thick crust. Basalt dikes are 10 m thick and the maximum height of ascent is 1000 m. After 5.0×10^7 years surface heat flux exceeds 100 mW/m^2 for the 30 km thick crust, while the 50 km crust has a surface heat flux of $\sim 80 \text{ mW/m}^2$ for the same period of intrusions.

Advection Simulations: Mixing and Mingling in the Lower Crust

The intrusion of basaltic magma into the crust creates a hybrid thermal and compositional framework that may facilitate mixing of mantle derived basalts with crustal melts. Additionally, subsolidus creep in the ductile lower crust may mingle mantle and crustal material, and may give rise to density instabilities where portions of the dense lower crustal material is transferred into the mantle (Jull & Kelemen, 2001; Lee *et al.*, 2001; Ducea, 2002). Both hyper-solidus mixing and sub-solidus mingling are potentially important in determining the mass balance and chemical nature of the crust, although they operate on much different timescales. Two sets of simulations were performed to illuminate A.) magma mixing under different thermal conditions, B.) subsolidus creep and mingling of basalt and crust as well as the conditions required for a density instability and crustal delamination.

Magma Mixing

The homogenization of mantle basalts with partially molten crust was modeled in a suite of simulations that used the conduction results for initial and boundary conditions. The mixing calculations simulated 5000 years of elapsed time, and the same intrusion configuration was used in all simulations with an average basalt flux of $.001 \text{ m}^3/\text{m}^2\text{yr}$. The initial conditions for the advection simulations were extracted from the conduction simulations for depths of 34 km, 38 km and 42 km after 10^7 years of simulated time (shown as stars in *Figure 2.11*). While this is not an exhaustive assessment of the possible outcomes, it does illustrate the potential mixing conditions for a variety of melt fractions. In these simulations, the mixture density of the magma and solid was used.

In keeping with the rheological model (*Appendix A Eqns. 4 and 5*), an abrupt transition in the ability to mix magmas was observed at conditions in which the mean crustal melt fraction was greater than .3 and maximum melt fractions of both the intruded and crustal material exceed the critical melt fraction in close juxtaposition.

For the three conditions considered, only the 42 km depth simulations produced conditions conducive to rapid mixing (*Figure 2.18*). However, it is reasonable to extrapolate the ease of mixing to greater depths and greater flux of basalt as these conditions would likely also produce high melt fractions. Maximum crustal melt fractions exceed .4 in the 38 km depth simulations, however adjacent regions of basalt are generally quenched, impeding mixing. Also these regions of melt above the CMF are also short-lived, typically decaying on the order of 100 days with length scales of 1-5 m. For both the 34 and 38 km depth simulations, isolated pods of basalt melt are separated by crustal material with melt fractions less than .2. This impedes large scale commingling of material on these timescales.

In the 42 km depth simulations, mixing is driven by the crystallization of the basalt that yields a crystal-melt mixture density greater than the partially molten surrounding crust, and the basalt mixture will begin to 'sink' back to a level of neutral buoyancy. This flow may trap isolated patches of crustal melt, and initiate low Reynolds number mixing. Likewise, partial melting will generate tonalitic melts from the amphibolite that will be buoyant. This is exemplified when a pool of crustal melt accumulates below a dike. Provided that portions of the dike have greater melt fraction than .4, the crustal melt can 'tunnel' into the overlying dike, and mix in the interior. The Reynolds number in the interior of the dikes ranges from 1.0×10^{-4} to 1.0. Upon reaching the interior of the dike, mixing occurs on timescales of 1-100 days, providing a mechanism for relatively rapid mixing and mingling in the vicinity of the intruded dikes. In these simulations, the buoyancy reversals that provided the potential energy driving mixing operated mostly on lengthscales of less than 10 m, which suggests that for dike swarm intrusions in the lower crust the MASH-process is fast and local in the thermally mature portions of a thickened crust.

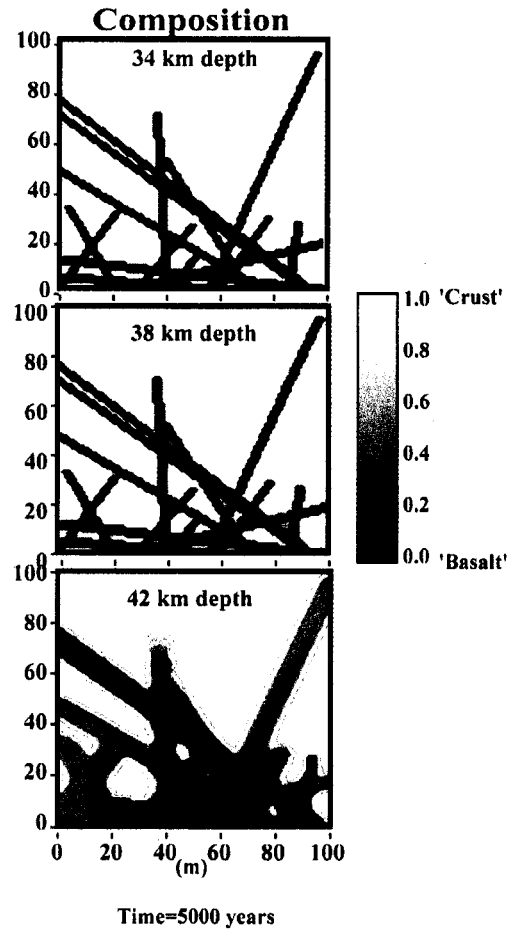


Figure 2.18. Mixing and mingling calculation. Initial condition for these 5000 year simulations are given in Fig. 2.11 (stars) and are for a basalt flux of $.001 \text{ m}^3/\text{m}^2\text{yr}$, 10^7 years following the initiation of intrusions. Depths of 34 km, 38 km and 42 km were examined. Following 5000 years only the 42 km simulation produced extensive mixing/mingling.

As the melt fractions of both the crustal melts and the residual mantle melts are often similar for any given thermal condition, their compositions and viscosity will also be similar, and magma mixing may be expected provided the magmas are closely juxtaposed. The simulations predict that mixed magmas will be volumetrically weighted toward the mantle contribution in shallow systems and in arc

systems with a high flux of basalt (*Figure 2.12*). A low flux of basalt, and especially thicker crust (~50 km) produces the greatest ratio of crustal melt to mantle melt. While the ratio of crustal melt in erupted magmas would be difficult to discern on the basis of major element geochemistry alone, the isotopic signature of the arc melts will be impacted, provided there is sufficient isotopic contrast between the crustal and mantle magmas (Hart *et al.*, 2002).

Gravitational Instability and Ductile Creep

Density differences between the crystallizing basalt, melting amphibolite, and mantle peridotite may also produce subsolidus creep. Jull & Kelemen (2001) demonstrated that ultra-mafic cumulates with densities greater than typical mantle lithologies can form and, at temperatures greater than 700°C, produce crustal density instabilities on timescales of 10^7 years. We expand on their model by invoking two end-member density models: For one end-member, crustal and residual basaltic melt is assumed to be completely removed from the solid matrix leaving a dense cumulate, and, at the other extreme, no melt is removed and the mixture density is calculated for the magma and solid.

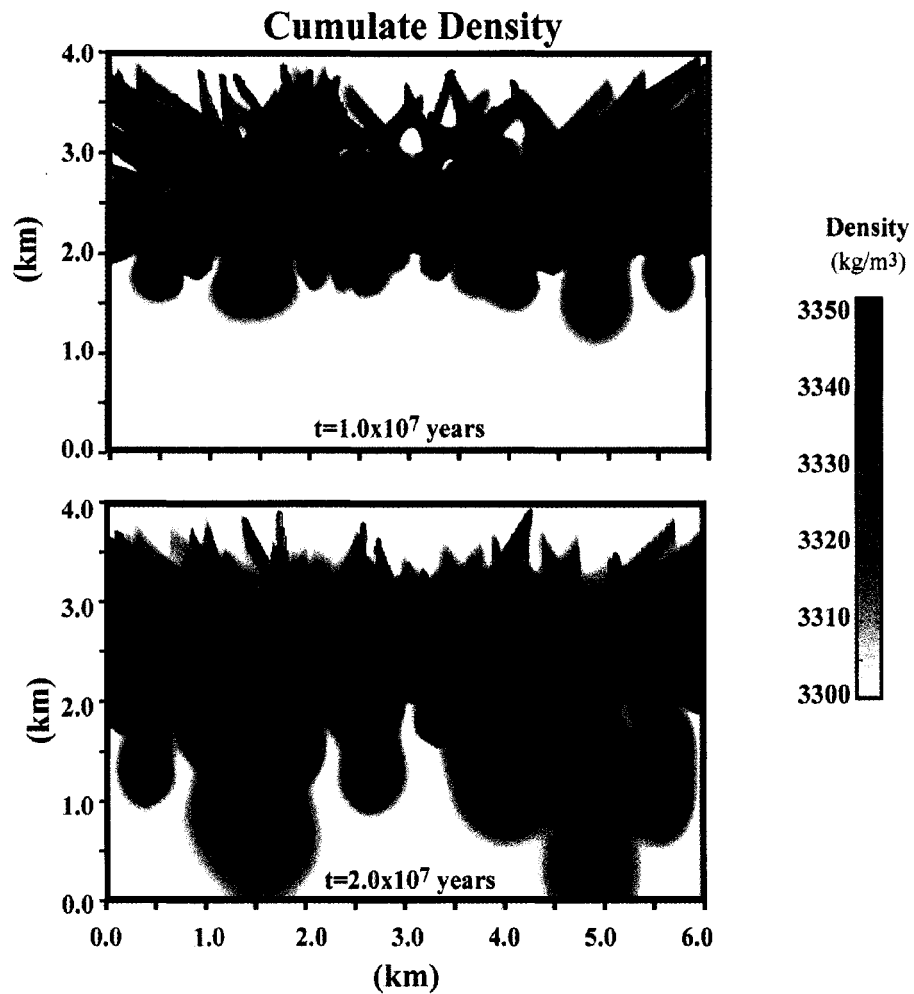


Figure 2.19. Ductile creep at the mantle-crust interface. Shown is the time evolution of the cumulate density (all melt has been extracted). The cumulate density conditions are for flux conditions of $.0002 \text{ m}^3/\text{m}^2\text{yr}$, 10 m wide dike and 50 kilometers crustal depth, after 1×10^7 and 2×10^7 years of intrusions. The cumulate density exceeds the mantle peridotite density creating convective instabilities. Instabilities the scale of individual dike intrusions coalesce as they descend. (Resolution 10 m^2).

Only in the simulations in which melt was removed did the lower crustal cumulates (both residual material from the intruded magma and crustal solids) become more dense than mantle peridotite (*Appendix A Figure 4*). When mean crustal and intruded

melt fraction is low (<0.2 melt fraction), the removal of melt was not sufficient to produce cumulates that had greater density than the mantle. The lower density of the plagioclase component, which remains a residual phase for small melt fractions, lowers the total cumulate density below the density of peridotite.

Density contrasts created by the web of basaltic dikes initiates the instabilities for melt fractions greater than ~.2. These instabilities coalesce as they descend into the mantle (Fig. 19). The constitutive relations used in these simulations is similar to the weak, dense layer considered by Jull & Kelemen (2001), however, the random orientation of the dikes and the progressive addition of mass complicates using the scaling formulated by these authors for the Rayleigh-Taylor instability of the dense layer. Our results for the initiation of density instabilities are consistent the results of Jull & Kelemen (2001) and the conceptual model of Ducea (2002), and adds additional constraints concerning the formation of instabilities in a crust where melting of amphibolite and/or the crystallization of wet basalts is occurring. The process requires: A.) the stability of garnet that necessitates pressures greater than 9 kbar and average melt fractions less than 0.5, B.) most of the plagioclase component must be removed, which requires melt fractions typically greater than ~.2, and C.) efficient segregation of melt leaving dense cumulates. To illustrate the basalt intrusion conditions that can produce a density instability the average cumulate density from the simulations given in *Figure 2.16* (10 m dikes, 1000 m maximum ascent, 10^7 years after the initiation of intrusion) is shown in *Figure 2.20*. Densities that exceed $\sim 3300.0 \text{ kg/m}^3$ are sufficient to initiate an instability. If melt is efficiently segregated, lower flux ($.0005 \text{ m}^3/\text{m}^2\text{yr}$) and a crustal thickness of 50 km is required to produce crustal density greater than the mantle. However an order of magnitude greater flux can melt most of the plagioclase component at shallower depths and if the melt is removed this crust may also become unstable at depths just below the garnet stability field. The trace element concentration of melts in this range should distinctively show the presence of residual garnet with little residual plagioclase. For instance, elevated La/Yb and Sr/Y ratios would be expected (Tulloch & Kimbrough,

2003; Bachmann *et al.*, 2004). Furthermore, seismic velocity variations in the upper mantle for such a process may be discerned such as the inferred 'density drip' beneath the Sierra Nevada (Saleeby & Foster, 2004).

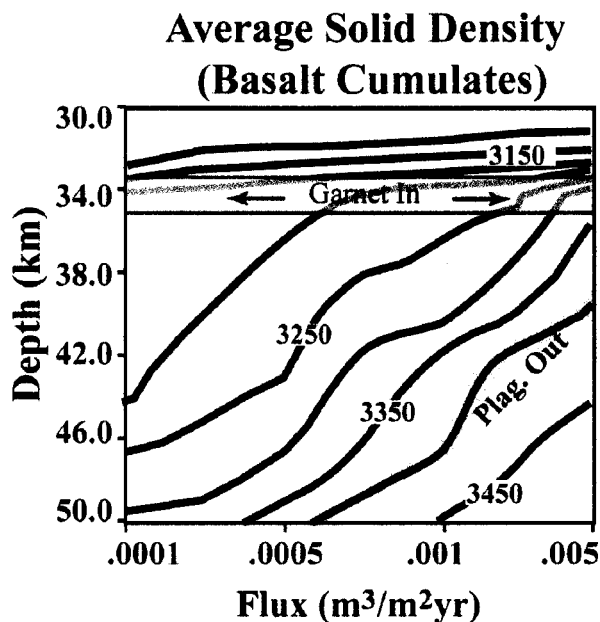


Figure 2.20. Average basalt cumulate density as a function of crustal thickness and flux of basalt. (Simulation conditions are the same as those in *Figure 2.16*: 10 m dikes, 1000 m maximum ascent, 10^7 years after the initiation of intrusions). The cumulate density becomes greater than the mantle peridotite ($\sim 3300 \text{ kg/m}^3$) if the melt fraction is sufficiently high that little plagioclase is in the solid assemblage ($>.2$), pressures are great enough that garnet is stable ($>9 \text{ kbar}$), the melt fraction is below $\sim .5$ so that garnet is a residual phase, and the melt is efficiently segregated from the crystalline residuum.

2.4. DISCUSSION

Predictions of Melt Compositions Based on Thermal Modeling

The genetic relationship between tonalitic-andesitic melt and amphibolite-pyroxenite residuum predicted by dehydration experiments at lower crustal pressures is expressed in the geologic record. Observations of tonalite, amphibolite, and pyroxenite in close juxtaposition have been noted in several lower crustal terrains.

The amphibolite Chipman dikes in Saskatchewan have dominant hornblende and plagioclase and minor clinopyroxene and garnet in dikes that have intruded a tonalitic body. The emplacement of these dikes has been interpreted to be ~10 kbar at the base of an Archean island arc (Williams *et al.*, 1995). Reheating conditions have produced pods of tonalitic melt, commonly associated with strain shadows associated with garnet. The Kohistan arc, Pakistan, interpreted as the exposed base of a Jurassic island arc at 12-14 kbar, has pyroxenitic, amphibolitic and tonalitic assemblages, although multiple stages of deformation have hindered the reconstruction of the relationship between units (Jan & Howie, 1981). Similarly, pyroxenites are common in the 9.5-11 kbar Tonsina assemblage, Alaska, in yet another basal zone of an interpreted mid-Jurassic island arc (DeBari & Coleman, 1989).

The geochemical and modal trends of distinct melting regimes established by the depth, basalt flux, and duration of intrusion in the melting zone can be determined by combining an assumed starting lithology, compositional information from melting experiments, and the melt fractions predicted in the conduction simulations. We focus on the silica, potassium, and the alumina saturation index (ASI) in order to compare the experiments and simulations with observed arc magmas.

For most basalt flux conditions (*Figures 2.11, 2.15 and 2.16*) crustal melt fractions and residual basalt melt fractions are less than .1 for a 30 km thick crust subjected to random diking, even after several million years of intrusion. At small crustal melt fractions (<0.1) dehydration of amphibolite, as considered by Wolf & Wyllie (1994), produced a tonalitic melt with ~65 wt. % SiO₂ at 10 kbar. The maximum SiO₂ content in the partial melting of amphibolite is dependent on the mode of the protolith. The Wolf & Wyllie (1994) experiments represent a primitive, high-Mg number end-member with mostly amphibole and high-anorthite plagioclase in the starting composition. Experiments with greater amounts of plagioclase, more albitic plagioclase, and with small amounts of quartz will all increase the SiO₂ wt % of the melt. For instance, the quartz amphibolite composition examined by Patiño-

Douce & Beard (1995) produced a melt with ~76 wt. % SiO₂ at 10 kbar and 0.1 melt fraction. Regardless, tonalitic melts (essentially low K₂O dacitic to rhyolitic melts) are predicted to be produced at the low melt fractions predicted to form in the modeled thin crust environment. Even crust of intermediate thickness (30-40 km) will have crustal melts that are dacitic after 10's of millions of years of intrusion. The SiO₂ content of the amphibolite dehydration melt stays at or above 60 wt % until about 0.3 melt fraction, or at approximately the amphibole-out phase boundary. Only after reaching ~.4 melt fraction are andesitic to basaltic-andesitic crustal melts produced. For the thin crust (~30 km), more typical of island arcs, such high melt fractions were not achieved in the simulations even after 50 million years of intrusion with a basalt flux of .001 m³/m²yr. However, crustal melts up to .4 were produced in a 50 km thick crust in a few million years for a range of basalt fluxes, and basaltic andesitic crustal melt was predicted to have a long residence time provided the crust continued to be fluxed with mantle magmas. It should be stressed that this trend applies to the baseline compositions due to lower crustal magma processing, and subsequent fractionation in the upper crust may be responsible for the production of some of the silicic magmas that are observed in thick crustal settings. This may be particularly true of magmas that have trace element patterns indicative of extensive plagioclase fractionation that is largely inhibited at higher pressures.

The SiO₂ trend of a crystallizing wet basalt is essentially the reverse of the melting experiments. For the 12 kbar, 3.8 % wt. H₂O experiments of Muntener et al., the crystallization of pyroxene dominates the phase assemblages to ~.4 melt fraction, and does not alter the SiO₂ content significantly (*Figure 2.4*). Extrapolation with MELTS predicts ~65 wt. % SiO₂ for the crystallizing magma at .2 melt fraction (*Appendix A Figure 2*). Again, the thermal conditions in a thin crust or with a very low basalt flux will produce dacitic to rhyo-dacitic magma if these mantle basalts stall for a protracted period of time, whereas the thermal conditions produced with a thicker crust or a greater basalt flux will drive the residual magmas toward an andesitic composition.

At low melt fractions (0.1-0.3) the Wolf & Wyllie (1994) amphibolite dehydration experiments have potassium concentrations of 0.3-0.4 wt. %. Extrapolation of the experiments of Muntener et al. (2001) used to parameterized the crystallization of the intruded wet basalt predicts potassium concentrations from .8 to 1.1 wt. % in the same melt fraction range. At higher melt fractions, the more mafic intruded magma has even lower potassium content (*Appendix, Figure 3*). The low potassium content (< 1.0 wt. %) produced in several amphibolite melting experiments (Beard & Lofgren, 1991; Rapp, 1991; Rushmer, 1991; Wolf & Wyllie, 1994) corresponds to many island-arc magmas (Bryan *et al.*, 1979; Zellmer *et al.*, 2003) and some TTG suites (Arth *et al.*, 1978), but is too low when compared to many continental arc dacites and rhyolites (Anderson *et al.*, 2000; Bachmann *et al.*, 2002), suggesting a prolonged multi-stage process involving fractionation is required to produce continental arc compositions rather than a singular melting event. The low potassium produced in these melting experiments is the result of low initial potassium composition because potassium is incompatible in the residual phases produced in the dehydration reaction (Rapp & Watson, 1995; Sisson *et al.*, in press). In the few experiments (Sen & Dunn, 1994; Sisson *et al.*, in press) with initial potassium at higher concentrations, potassium contents more typical of calc-alkaline granites are produced. Dehydration melting experiments on an amphibolite performed by Sen & Dunn (1994) at 15 kbar produced andesite-dacite composition melts with ~2.5-5.0 wt. % K₂O. The experiments of Sisson et al. (in press) have demonstrated that small amounts of partial melting (0.1-0.3 melt fraction) of a mafic source at 8 kbar can produce similarly high potassium content in dacitic to rhyolitic liquids if the initial potassium content of the protolith is ~1-2 wt. % K₂O. These results indicate that if enough potassium can be introduced in the basalt as it leaves the mantle wedge or accumulates in this melt while it stalls at the base of the crust, and then crystallizes to form an amphibolite, subsequent partial melting can directly produce the elevated potassium content observed in continental arc settings.

Mantle melting processes, recycling of weathered exogenous sediments (McCarthy & Patiño-Douce, 1997), and repeated melting-solidification cycles (igneous distillation), have all been invoked to produce the high potassium content in lower crustal settings. The high potassium in melts in settings such as Costa Rica (Lidiak & Jolly, 1996; Hannah *et al.*, 2002) and the Philippines (Vogel, *per. comm.*) where a thick crust of meta-sediments is absent, appears to imply that in some settings incorporation of weathered material isn't necessary for the production of high-K suites. Igneous distillation can produce elevated incompatible concentrations, but the accumulation of cumulates may create a mass balance problem. However, the model calculations demonstrate that crustal instability is a likely consequence of basalt intrusion and melt extraction, especially in thick crustal regions. A prolonged intrusion history with multiple melt-solidification cycles, coupled with the development of lower crustal instabilities that remove some of the mafic cumulates may produce a lower crust that is a repository for the incompatible-enriched melt, but still produce crustal thickness observed seismically. Such an environment is predicted in these simulations for a relatively steady flux of basalt intruding the crust over millions of years in several stages of intrusion. For instance after several million years of simulated basalt intrusion, a variety of basalt fluxes are capable of generating multiple melt-solidification cycles as well as generate density instabilities (*Figure 2.20*, densities greater than 3300 kg/m^3), although at different depth-time combinations. After removal of the garnet and pyroxene rich residuum, the remaining lithologies will be tonalitic-andesitic-dacitic, and subsequent melting processes will further increase the incompatible element concentration, including their potassium content.

Low melt fraction dehydration melting of amphibolite, as predicted by the thermal modeling, typically produces moderate to mildly peraluminous melts (*Figure 2.21*). As the melt fraction increases the aluminum content decreases, and the melts become meta-aluminous near the amphibole-out boundary (Rapp *et al.*, 1991). In the simulations these meta-aluminous conditions are achieved in thicker, and more

mature crust. The alumina saturation index throughout the melting experiment of Wolf & Wyllie (1994) are at or slightly more peraluminous than the average range observed in calc-alkaline andesites, dacites and rhyolites (Ewart, 1982).

The shallow and young arc systems investigated in the conduction simulations produced low melt fraction crustal melts and fractionated mantle melts; both of which are predicted to be dacitic-rhyodacitic and mildly peraluminous. Residual modes for amphibolite melt fractions less than 0.2 are amphibolite>plagioclase>clinopyroxene +/- garnet and orthopyroxene. Similar trends are predicted for the cumulates of crystallizing wet basalt at low melt fraction. Regions of greater crustal and intruded magma melt fraction, such as at the base of thickened crust, will produce metaluminous magmas that are generally andesitic. Residual modes will be dominated by pyroxene +/- garnet depending on the pressure. In the conduction simulations, the continued input of enthalpy and mass from the basalt intrusions will create a lower crust with greater melt fractions and melt that is more mafic with time.

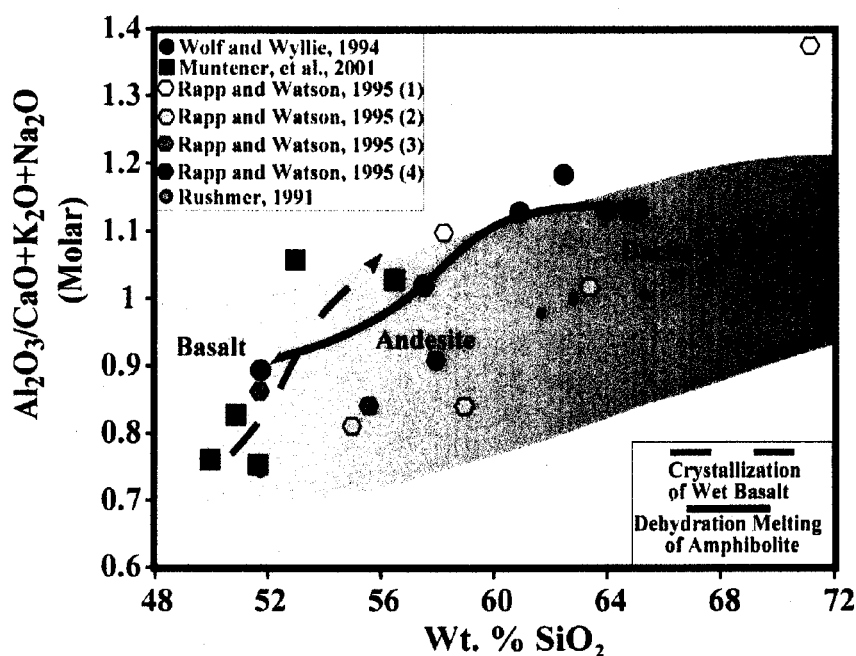


Figure 2.21. Alumina saturation index plot of the dehydrating amphibolite and fractionating wet basalt. Also shown is the ASI range of calc-alkaline magmas reported in the database of Ewart, 1982 (shaded area).

2.5. CONCLUSIONS

The stochastic simulations of basalt dike demonstrate that crustal melting in the lower crust is maximized when basaltic intrusions are confined to a relatively narrow vertical zone at the base of crust; basaltic dikes that ascend several kilometers from the base of the crust are inefficient at producing voluminous crustal melting. This suggests that if lower crustal melting is widespread, density or rheological barriers inhibiting the propagation of basaltic melt are required.

The conduction simulations indicate that shallow, young crust may be a repository for residual basalt melt fractions from ~.1-.3 and amphibolite dehydration melts from 0-.1 melt fraction. The coupled cooling of intruded basalt and melting of crust can lead to a convergence in compositions that will be dacitic to rhyolitic in composition. Except for very young arc systems or very low basalt flux, the amount of residual melt from the basalt will be more voluminous than the crustal melts and linear mixtures of the two will be dominated by the crystallizing basalt. However, the dynamic simulations suggest that the low melt fractions present may inhibit the rapid mixing of these melts and distinct pockets of isolated melt may form. At these low melt fractions, the residuum includes amphibole and plagioclase, and even with efficient segregation of melt, the density of lower crustal material will be positively buoyant relative to mantle peridotite. Although little crustal melting occurs, surface heat flow may reach elevated values due to the thin crust.

Mature arc systems with thicker, and ultimately hotter crust at depth yield greater melt fractions from both crustal melting and residual material from the intruded basalt at the base of the crust. For crustal depths of 50 km melt fractions exceeding 0.4 for both the residual basalt liquids and crustal melts can coexist for thousands of years. Individually, these melts will be andesitic to basaltic andesite. The long period of time that these liquids are at high melt fraction promotes homogenization as demonstrated by the advection simulations. Coexisting with the andesitic meta-aluminous melts, will be a garnet pyroxenitic residuum. If the melt can be extracted efficiently from this residuum, the densities of this material will likely be great enough to initiate convective instabilities, providing a mechanism to remove the mafic material from the base of thickened crust

- Chapter 3 -

$^{226}\text{Ra}/^{230}\text{Th}$ -excess generated in the lower crust: Implications for magma transport and storage time scales

3.1 INTRODUCTION

Arc magmas have compositions that reflect an integrated history of melt generation processes in the mantle and variable extents of polybaric assimilation and fractionation within the crust, and many continental arc magmas in particular have trace-element and isotopic signatures consistent with significant contributions from crustal material (Davidson et al., 2005). Although assimilation can potentially occur at any stage during transit through the crust, the thermal environment of the lower crust makes it particularly prone to melting with the progressive input of enthalpy from mafic intrusions. Numerous lines of evidence are consistent with significant lower crustal assimilation by mantle-derived magmas, including the observation of lower crustal outcrops that preserve evidence of crustal melting (Pickett & Saleeby, 1993; Williams *et al.*, 1995), the trace element signature of residual garnet in some continental arc magmas (Hildreth & Moorbath, 1988), isotopic data consistent with crustal assimilation (Hart et al., 2002), and thermal models that predict enhanced melting in thickened continental crust (Dufek & Bergantz, 2005).

Disequilibria between intermediate daughter products in the decay series of ^{238}U provides a useful chronometer for magmatic processes and ascent rates of magma from depth, sensitive to timescales of ~10 ka – 350 ka (^{238}U - ^{230}Th disequilibria) or ~100 ka – 10 ka (^{230}Th - ^{226}Ra disequilibria). A combination of $(^{238}\text{U})/(^{230}\text{Th}) > 1$ (^{238}U -excess) and $(^{226}\text{Ra})/(^{230}\text{Th}) > 1$ (^{226}Ra -excess) is usually observed in arc settings, distinguishing arc lavas from MORB and OIB sources (e.g., Lundstrom, 2003). Typical arc lavas have ^{226}Ra -excesses of ~200-300% (i.e.,

$(^{226}\text{Ra})/(^{230}\text{Th}) = 2-3$), although extremely large ^{226}Ra -excesses have been observed in a few island arc lavas (up to $(^{226}\text{Ra})/(^{230}\text{Th}) = 6.2$; (Turner *et al.*, 2000)). ^{226}Ra -excesses in arc lavas have predominantly been explained by fluid-induced partial melting deep in the mantle and/or addition of Ra-enriched aqueous fluids to such melts of the mantle wedge (e.g., (Turner *et al.*, 2003). Where interaction of melts with the crust beneath volcanic arcs has been considered, it is assumed to decrease mantle-derived ^{226}Ra -excesses due to decay of ^{226}Ra during transport. Because ^{226}Ra -excess will decay to secular equilibrium within ~8-10 kyr, this interpretation implies that the magma has not stalled at any depth for long periods of time. These very short transit times may be difficult to reconcile with crystal residence time scales of thousands to tens of thousands of years in some arc lavas (Cooper & Reid, 2003; Costa *et al.*, 2003; Turner *et al.*, 2003).

Other interpretations of Ra-excesses in arcs are emerging, for example diffusion-induced disequilibria created in the mantle beneath arcs (Feineman and DePaolo, 2003), or a combination of flux melting and daughter ingrowth during melting (Thomas *et al.*, 2002). However, these mechanisms still focus on processes operating within the mantle, and the degree to which crustal melting and wallrock interactions can impact U-series disequilibria during storage and ascent of magmas has yet to be fully explored. Recently Berlo *et al.* (2004) examined the case of batch melting of lower-crustal material at high melt fraction (0.15 – 0.40) and concluded that U-series activity ratios of these melts were near equilibrium. However, the assumption of congruent, batch melting may be inappropriate under many crustal melting conditions (Rushmer, 1995). For example, mafic, amphibolitic lower crust at pressures of ~ 10 kbar will undergo incongruent dehydration melting in which amphibole and plagioclase react to form garnet, pyroxenes and melt (Wolf & Wyllie, 1994). As is now well-accepted in the case of mantle melting, ingrowth of radioactive nuclides can occur during the melting process, and the final activity ratios in the melt will be a function of the melting rate and the critical porosity above which melt is

segregated. Under lower-crustal conditions, disequilibria may also be affected by the progress of the melting reaction and its impact on bulk partition coefficients.

With this geological motivation, we develop an incongruent, continuous melting model for lower crustal conditions to further investigate the role of crustal processes on the U-series nuclides. The combination of incongruent melting, partition coefficients appropriate for crustal pressures and bulk compositions, and daughter ingrowth during melting, lead to significant ^{226}Ra -excesses (> 3) and modest ^{230}Th - ^{238}U disequilibria ($(^{230}\text{Th})/(^{238}\text{U}) = 0.7-1.12$) in melts produced during dehydration melting of the lower crust. When mixed with mantle-derived magmas, the ^{226}Ra -excesses generated in melts of deep continental crust may augment preexisting disequilibria and can relax the ascent timescales inferred for arc magmas. Although the most extreme ^{226}Ra -excesses observed in primitive island arcs basalts cannot be explained by this mechanism, it can generate $(^{226}\text{Ra})/(^{230}\text{Th})$ up to 3, comparable to the disequilibria measured in the majority of arc lavas. This melting process also impacts other trace elements that can be used to deconvolve the trace-element signatures of crustal melting from those of mantle melting and slab fluids.

3.2 CONTINUOUS DEHYDRATION MELTING

We developed a model to examine the trace element and U-series consequences of incongruent dehydration melting in the lower crust. Here, we follow Williams and Gill (1989) in their definition of continuous melting: the melting process occurs at a constant rate in a static (i.e., not upwelling) residue and the melt fraction below a critical porosity is in equilibrium with the residue, and the melt fraction in excess of this critical porosity is instantaneously extracted and aggregated. The continuous melting model is a more physically plausible representation of melting of a static lower crust that is being fluxed with mafic intrusions than is dynamic, batch or fractional melting. Here, we extend the work of Zou and Reid (2001) and McKenzie (1985) to incongruent melting with ingrowth of radioactive nuclides for the case of amphibolite dehydration. The full derivation of the

incongruent continuous melting model for both stable elements and radioactive nuclides is included in the supplemental material.

We applied this model to lower-crustal melting using the specific phase proportions and compositions from the 10 kbar amphibolite dehydration melting experiments of Wolf and Wyllie (1994), appropriate for melting occurring at the base of ~30 km thick crust. The general form of the incongruent melting reaction is $\text{Amp} + \text{Plag} \rightarrow \text{Opx} + \text{Cpx} + \text{Gt} + \text{Melt}$. We used partition coefficients (Ds) relevant to the phases, pressures and compositions in the lower crust (*Table 3.1*), which in some cases are significantly different from those relevant to melting in the deep mantle. Solid solution (primarily anorthite content of plagioclase) affects these partition coefficients. Here we focus on mineral compositions similar to the experimental material used by Wolf and Wyllie (1994), although we also assess the effect of changing anorthite content on the U-series disequilibria.

Table 3.1. Partition Coefficients for Amphibolite Melting Calculations

Phase	Ba	Ra	Th	U	Nb	La	Ce	Sr	Nd	Sm	Zr	Eu	Ti	Gd	Dy	Y	Er	Yb	Lu
Amp. [†]	1.2x 10 ⁻¹	9.6x 10 ⁻³	1.7x 10 ⁻²	8.0x 10 ⁻³	1.9x 10 ⁻¹	1.2x 10 ⁻¹	2.4x 10 ⁻¹	2.8x 10 ⁻¹	6.2x 10 ⁻¹	1.4x 10 ⁰	2.3x 10 ⁻¹	1.1x 10 ⁰	2.0x 10 ⁰	1.5x 10 ⁰	1.8x 10 ⁰	1.7x 10 ⁰	1.5x 10 ⁰	1.2x 10 ⁰	1.1x 10 ⁰
Plag. [§]	5.6x 10 ⁻²	8.0x 10 ⁻³	3.0x 10 ⁻³	6.0x 10 ⁻⁴	1.2x 10 ⁻¹	1.2x 10 ⁻¹	7.0x 10 ⁻²	1.1x 10 ⁻²	8.0x 10 ⁻²	5.0x 10 ⁻²	1.0x 10 ⁻⁴	7.0x 10 ⁻²	2.0x 10 ⁻²	3.0x 10 ⁻²	2.0x 10 ⁻²	1.2x 10 ⁻²	2.0x 10 ⁻²	4.0x 10 ⁻³	9.0x 10 ⁻³
Opx. [#]	7.4x 10 ⁻⁴	7.4x 10 ⁻⁶	2.1x 10 ⁻²	1.8x 10 ⁻²	1.0x 10 ⁻³	1.0x 10 ⁻³	1.2x 10 ⁻¹	7.0x 10 ⁻²	2.7x 10 ⁻¹	4.6x 10 ⁻¹	2.7x 10 ⁻²	3.5x 10 ⁻¹	2.4x 10 ⁻¹	1.0x 10 ⁻²	1.5x 10 ⁻²	8.6x 10 ⁻²	1.0x 10 ⁻¹	1.7x 10 ⁻¹	1.8x 10 ⁻¹
Cpx. ^{**}	9.6x 10 ⁻³	9.6x 10 ⁻⁵	8.2x 10 ⁻¹	7.7x 10 ⁻¹	1.7x 10 ⁻²	1.7x 10 ⁻²	1.3x 10 ⁻¹	9.2x 10 ⁻²	3.1x 10 ⁻¹	6.0x 10 ⁻¹	2.3x 10 ⁻¹	6.9x 10 ⁻¹	1.3x 10 ⁰	8.2x 10 ⁰	9.9x 10 ⁰	1.2x 10 ⁰	1.1x 10 ⁰	8.4x 10 ⁰	9.2x 10 ⁰
Gt. ^{††}	1.0x 10 ⁻⁵	1.0x 10 ⁻⁹	1.0x 10 ⁻¹	3.7x 10 ⁻¹	4.5x 10 ⁻³	2.5x 10 ⁻²	4.0x 10 ⁻²	2.0x 10 ⁻¹	8.6x 10 ⁻²	8.3x 10 ⁻¹	5.2x 10 ⁻¹	7.4x 10 ⁻¹	7.9x 10 ⁻¹	1.1x 10 ⁰	4.4x 10 ⁰	1.0x 10 ⁰	9.4x 10 ⁰	1.4x 10 ⁰	1.6x 10 ⁰

*Ra partition coefficients determined using lattice strain parameters with Ba partition coefficients.

† (Brenan et al., 1995; Klein et al., 1997)

§ (Bindeman et al., 1998; Bindeman & Davis, 2000; Blundy & Wood, 2003)

(Beattie, 1993; McDade et al., 2003)

** (Klein et al., 2000; Barth et al., 2002)

†† (Klein et al., 2000; van Westrenen et al., 2001; Barth et al., 2002; Beattie, 2003)

3.2.1 Incongruent Continuous Melting Derivation

Continuous melting is similar to dynamic melting (commonly applied in the case of adiabatic melting of upwelling mantle), but with the difference that the solid residue in continuous melting is static (i.e., has no upwelling velocity). In the case of stable elements, dynamic melting and continuous melting are mathematically equivalent (Williams and Gill, 1989), and equations describing incongruent dynamic melting of stable elements have been presented previously (Zou and Reid, 2001). In this section we present the derivation of equations describing U-series nuclide behavior during incongruent, continuous melting. We first derive equations describing the behavior of stable elements (section 3.2.2), which are mathematically identical to those obtained by Zou and Reid (2001) although derived in a somewhat different manner. We then expand these equations to account for the effects of ingrowth and decay during the melting process (section 3.2.3). In this paper, we apply these equations to modeling of ^{226}Ra - ^{230}Th and ^{230}Th - ^{238}U disequilibria during incongruent melting of amphibolite, but the equations are general and can be applied to any parent-daughter pair and to any incongruent melting reaction.

3.2.2 Stable Element Calculation

During continuous melting, initial melt fractions remain in equilibrium with the solid residue (batch melting) until a critical porosity is reached. Any additional melt produced beyond this critical porosity is instantaneously extracted and pooled elsewhere and the extracted melt fraction is referred to as X . As the critical mass porosity (Φ) approaches 0, the continuous melting process approaches incongruent fractional melting. We derive in this section equations describing the concentration of stable trace elements in the melt phase as a function of the extracted melt fraction and the critical porosity.

During incongruent melting some solid phases are consumed while others are produced along with the melt. Hence the bulk partition coefficient of element i (D_i) becomes a function of the melt fraction. Those phases which are consumed or produced in different proportions from their initial modal abundance are termed “incongruent” phases, whereas those which contribute to the melting reaction in their initial modal proportions are termed “congruent” phases. Phase proportions are governed by an incongruent reaction that can be written as:



where α_i are the incongruently melting phases, θ_i are the congruently melting phases and β_i are the incongruently produced phases (Zou & Reid, 2001). For the case of amphibolite dehydration melting, only incongruently consumed and produced phases are present.

A general conservation equation for a stable element i (neglecting advective and diffusion terms) is given by:

$$(1 - \phi)\rho_s \frac{\partial c_s^i}{\partial t} + \rho_f \phi \frac{\partial c_f^i}{\partial t} = (c_s^i - c_f^i)M , \quad (3.2)$$

where ϕ is the critical volume porosity, ρ_s is the solid residue density, ρ_f is the magma density, c_s^i is the concentration in the residue, c_f^i is the concentration in the magma and M is the melting rate, assumed to be constant. Note that the concentration of stable trace elements depends on the melt fraction but not on the timescale of melting and therefore is independent of the melting rate; we include M here to make the derivation parallel to that of the derivation of equations relevant to radioactive nuclides (section 3.2.3). We can replace time with extracted melt fraction as a

variable using the following relationship between extracted melt fraction X and time (McKenzie, 1985):

$$X = 1 - \exp\left[\frac{-M_e}{\rho_f\phi + \rho_s(1-\phi)}t\right], \quad (3.3)$$

where M_e is the melt extraction rate. As pointed out by Zou (1998) the melt extraction rate is not strictly the melt production rate, but they are related as:

$$\frac{M}{M_e} = 1 - \Phi, \quad (3.4)$$

where Φ is the critical mass porosity rather than the critical volume porosity and is related to the critical volume porosity by:

$$\Phi = \frac{\rho_f\phi}{\rho_f\phi + \rho_s(1-\phi)}. \quad (3.5)$$

As the stable element concentration is ultimately related to reaction progress rather than strictly to time, it is advantageous to write the differential equation in (3.2) in terms of extracted melt fraction rather than time. Using (3.3) we can perform a change of variables in (3.2), and using (3.4) and (3.5) and noting also that $c_f^i = D^i c_s^i$ we get the following expression:

$$(1-\Phi)(1-X)\frac{\partial D^i c_f^i}{\partial X} + (1-X)\Phi\frac{\partial c_f^i}{\partial X} = (1-\Phi)c_f^i(D^i - 1). \quad (3.6)$$

During incongruent melting D^i is not constant and remains inside the differentiation operator. To perform this differentiation we first need to express D^i as a function of

the melt progress through the extracted melt fraction variable. Both Zou (2001) and Hertogen and Gijbels (1975) give essentially the same expression for D^i in incongruent melting situations based upon mass balance arguments. Using the notation of Zou:

$$D^i = \frac{1}{1-F} [D_0^i - Q_0^i F], \quad (3.7)$$

where

$$D_0^i = \sum x_0^j K_i^j, \quad (3.8)$$

and

$$Q_0^i = \frac{\sum_{\alpha} (p_{\alpha}^j K_i^j) - \sum_{\beta} (t^j K_i^j)}{t^i}. \quad (3.9)$$

F is the total melt fraction (which is related to the extracted melt fraction by $F = \Phi + (1 - \Phi)X$), K_i^j is the partition coefficient of i in the j th phase (here the partition coefficient is assumed constant through the melting range), x_0^j is the fraction of the j th phase originally present, and t^j is the fraction of the j th solid incongruently produced phase, t^i is the fraction of melt produced, and p_{α}^j is the fraction of the j th incongruently melting phase (Note that for the dehydration reaction modeled here $\sum_{\alpha} (p_{\alpha}^j) = 1$ since there are no congruently melting phases). D_0^i is the initial bulk partition coefficient and Q_0^i is a constant related to the rate of change of the partition coefficient as a result of reaction progress as t^j phases are being produced. Note that (3.9) would have to be modified if congruently melting phases were also present (Zou & Reid, 2001). Substituting (3.9) in (3.7), and using the chain rule gives the simplified expression:

$$\frac{\partial c_f^i}{c_f^i} = \left(\frac{Q_0^i + \Phi(1-Q_0^i) - 1}{D_0^i + \Phi(1-Q_0^i) - X[Q_0^i + \Phi(1-Q_0^i)]} \right) \partial X \quad (3.10)$$

Integrating and using the fact that $c_{f0}^i = \frac{c_0^i}{D_0^i + \Phi(1-Q_0^i)}$ (Zou & Reid, 2001) gives us

the following expression for c_f^i as a function of critical mass porosity and extracted melt fraction:

$$c_f^i = \frac{c_0^i}{D_0^i + \Phi(1-Q_0^i)} \left[1 - \frac{Q_0^i + \Phi(1-Q_0^i)}{D_0^i + \Phi(1-Q_0^i)} X \right]^{\frac{1}{Q_0^i + \Phi(1-Q_0^i)} - 1} \quad (3.11)$$

To get the concentration of element i in the aggregate melt this expression must be integrated over X and then divided by X to give:

$$\bar{c}_f^i = \frac{c_0^i}{X} \left(1 - \left[1 - \frac{Q_0^i + \Phi(1-Q_0^i)}{D_0^i + \Phi(1-Q_0^i)} X \right]^{\frac{1}{Q_0^i + \Phi(1-Q_0^i)}} \right) \quad (3.12)$$

This is identical to the expression given in Zou and Reid (2001) equation 16 although derived in a somewhat different manner.

3.2.3 Radioactive Nuclides

The same general solution procedure is followed for the U-series nuclides, although in this case there is an added source term in the conservation equation that complicates the calculation. The half-life of ^{238}U is much longer than the melting

timescale considered, therefore it can be treated as a stable element and equations (3.11) and (3.12) can be used to determine the concentration. However, for ^{230}Th and ^{226}Ra a new conservation equation must be used:

$$(1-\phi)\rho_s \frac{\partial c_s^D}{\partial t} + \phi\rho_f \frac{\partial c_f^D}{\partial t} = (c_s^D - c_f^D)M + \lambda^P [\rho_s c_s^P (1-\phi) + \rho_f c_f^P \phi] - \lambda^D [\rho_s c_s^D (1-\phi) + \rho_f c_f^D \phi] \quad (3.13)$$

Here the superscripts D and P refer to daughter and parent nuclide, respectively, and λ is the decay constant. The first term on the right-hand side accounts for transfer of daughter atoms from the solid to the liquid through melting, the second term accounts for ingrowth of the daughter due to decay of the parent during the melting process, and the third term accounts for decay of the daughter. Using (3.3) and changing the independent variable from time to extracted melt fraction gives:

$$(1-\phi)\rho_s \frac{M_e(1-X)}{\rho_f\phi + \rho_s(1-\phi)} \frac{\partial c_s^D}{\partial X} + \phi\rho_f \frac{M_e(1-X)}{\rho_f\phi + \rho_s(1-\phi)} \frac{\partial c_f^D}{\partial X} = (c_s^D - c_f^D)M + \lambda^P [\rho_s c_s^P (1-\phi) + \rho_f c_f^P \phi] - \lambda^D [\rho_s c_s^D (1-\phi) + \rho_f c_f^D \phi] \quad (3.14)$$

We can express this equation in terms of the concentration of daughter in the magma

by dividing (14) through by M, using $\frac{M}{M_e} = \frac{\rho_s(1-\phi)}{\rho_s(1-\phi) + \rho_f\phi}$, defining

$\rho_{avg} = \rho_s(1-\phi) + \rho_f\phi$, and using the partition coefficient expression

$$(D^D = D_0^D + \Phi(1 - Q_0^D) - X[Q_0^D + \Phi(1 - Q_0^D)]):$$

$$\begin{aligned} & \frac{\partial c_f^D}{\partial X} \left[\frac{D_0^D + \Phi(1 - Q_0^D) - X[Q_0^D + \Phi(1 - Q_0^D)]}{(1-\Phi)\rho_{avg}} \right] + \\ & c_f^D \left[\frac{D_0^D - Q_0^D}{(1-\Phi)(1-X)\rho_{avg}} - \frac{D_0^D + \Phi(1 - Q_0^D) - X[Q_0^D + \Phi(1 - Q_0^D)] - (1-X)}{(1-\Phi)(1-X)\rho_{avg}} + \frac{\lambda^D}{M} \left(\frac{D_0^D + \Phi(1 - Q_0^D) - X[Q_0^D + \Phi(1 - Q_0^D)]}{(1-X)} \right) \right] = \\ & c_f^P \left[\frac{\lambda^P}{M} \left(\frac{D_0^P + \Phi(1 - Q_0^P) - X[Q_0^P + \Phi(1 - Q_0^P)]}{1-X} \right) \right] \end{aligned} \quad (3.15)$$

To simplify the expression, we define $A = D_0 + \Phi(1 - Q_0)$ and $B = Q_0 + \Phi(1 - Q_0)$:

$$\begin{aligned} & \frac{\partial c_f^D}{\partial X} \left[\frac{A^D - X[B^D]}{(1 - \Phi)\rho_{avg}} \right] + \\ & c_f^D \left[\frac{D_0^D - Q_0^D}{(1 - \Phi)(1 - X)\rho_{avg}} - \frac{A^D - X[B^D] - (1 - X)}{(1 - \Phi)(1 - X)\rho_{avg}} + \frac{\lambda^D}{M} \left(\frac{A^D - X[B^D]}{(1 - X)} \right) \right] = \\ & c_f^P \left[\frac{\lambda^P}{M} \left(\frac{A^P - X[B^P]}{1 - X} \right) \right] \end{aligned} \quad (3.16)$$

This equation cannot be solved by separation of variables but can be written in the form,

$$c_f^{D'} + P c_f^D = L \quad (3.17)$$

where P and L are constants. The solution is:

$$c_f^D = e^{-I} (T + c_0^D A^D \frac{1}{B^D}), \quad (3.18)$$

where

$$T = \int L e^I dX, \quad (3.19)$$

and

$$I = \int P dX \quad (3.20)$$

P and L can be simplified to:

$$P = \frac{(1 - B^D)}{(A^D - B^D X)} + \frac{\lambda^D (1 - \Phi)\rho_{avg}}{M(1 - X)}, \quad (3.21)$$

and

$$L = \frac{c_f^p \lambda^p \rho_{avg} (A^p - B^p X)(1 - \Phi)}{M(1 - X)(A^D - B^D X)}. \quad (3.22)$$

So,

$$e^l = (A^D - B^D X)^{\frac{B^D - 1}{B^D}} (1 - X)^{\frac{-\lambda^D (1 - \Phi) \rho_{avg}}{M}} \quad (3.23)$$

and,

$$T = \frac{\lambda^p \rho_{avg} (1 - \Phi)}{M} \int c_f^p (A^p - B^p X)(A^D - B^D X)^{\frac{1}{B^D} - 1} (1 - X)^{\frac{-\lambda^D (1 - \Phi) \rho_{avg} - 1}{M}} \partial X. \quad (3.24)$$

c_f^p is also a function of X. The abundance of ^{238}U can be computed with (3.18), but since there is no parent nuclide $T=0$, the solution simplifies to that obtained by separation of variables. The abundance of ^{238}U can then be used to compute the abundance of ^{230}Th using (3.18). The integral in T is difficult to solve analytically because in general $A^D \neq A^p \neq B^D \neq B^p$, and in this study T was evaluated numerically using the trapezoidal method. With this strongly non-linear function care must be taken that the integration steps are sufficiently small so that errors are small. This required iterative refinement until activity ratios changed by less than 0.01. Once $c_f^{230\text{Th}}$ is determined as a function of X we can use it as the parent in (3.18) to determine $c_f^{226\text{Ra}}$. Equation (3.18) gives the concentration of the daughter nuclide in the melt at any point in the melting process (the instantaneous melt), but the concentration in the aggregated extracted melt is more relevant to this work. This is again calculated using:

$$\bar{c}_f^i = \frac{1}{X} \int c_f^i \partial X. \quad (3.25)$$

3.2.4 Amphibolite Dehydration Reaction

The phase proportions from the amphibolite dehydration experiments of Wolf and Wyllie (1994) were used to form the incongruent melting reaction: .703 Amp + .297 Plag → .031 Opx + .378 Cpx + .355 Gt + .236 Melt. The exact coefficients of this reaction will change as a function of solid solution and P-T conditions (Beard & Lofgren, 1991; Rapp *et al.*, 1991), but this reaction serves as a reasonable proxy for melting occurring at the base of ~30 km thick crust. After the amphibole and plagioclase have been exhausted the residue is assumed to melt congruently.

3.3 MODELED U-SERIES DISEQUILIBRIA AND TRACE ELEMENT SIGNATURE OF AMPHIBOLITE DEHYDRATION

As incongruent melting proceeds, the production of phases in which radium is highly incompatible (garnet and pyroxene) combined with the consumption of phases in which Ra is only moderately incompatible (plagioclase and amphibole) act in concert to elevate $(^{226}\text{Ra})/(^{230}\text{Th})$ in the melt well beyond what would be predicted based on congruent melting models (*Figure 3.1*). A further increase over batch melting occurs due to ingrowth of ^{226}Ra during the melting process when the melting timescale becomes approximately equal to or greater than the half-life of radium (τ_{melt} in *Figure 3.1*). A competing effect is dilution of incompatible elements in the aggregate liquid as melting proceeds. While the increase in incompatibility of radium is outpaced by dilution effects in the aggregate melt at high melting rates ($> 1 \text{ kg/m}^3\text{yr}$) and low critical mass porosity (< 0.001), the model disequilibria are still comparable to or higher than those produced during congruent batch melting with similar residual mineralogy (cf. Berlo *et al.*, 2004).

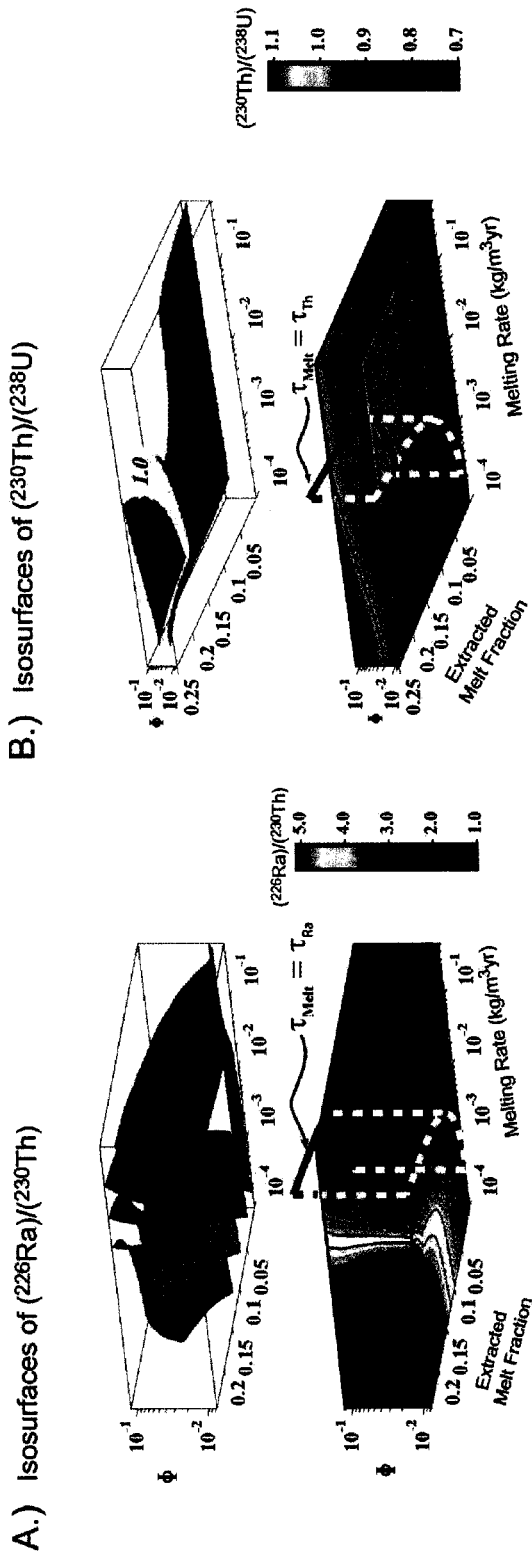


Figure 3.1. Isosurfaces of A.) $(^{226}\text{Ra})/(^{230}\text{Th})$ and B.) $(^{230}\text{Th})/(^{238}\text{U})$ in the aggregate melt from the continuous melting of amphibolite. Activity ratios are shown for a range of critical mass porosity (Φ), extracted melt fraction, and melting rate. Aggregate fractional melting is approached at high melting rates and low critical porosity (extreme right corner of the figure). The dashed lines delineate the melting timescale that equals the daughter nuclide half-life. (The melting time scale is given by: $\tau_{melt} = \frac{\rho_{avg}}{M_e} \ln(1 - X)$, where M_e is the melt extraction rate, ρ_{avg} is the average density, and X is the extracted melt fraction.) To the right of this surface the melting timescale is less than the half-life and dilution effectiveness dominate, but for longer timescales ingrowth effects become important.

At slower melting rates (approaching $\sim 1.0 \times 10^{-4}$) the degree of disequilibrium becomes a weak function of melting rate and - as with dynamic melting calculations applied to mantle upwelling - $(^{226}\text{Ra})/(^{230}\text{Th})$ is principally determined by the critical mass porosity, with ratios up to ~ 5 produced at melting rates of 1.0×10^{-4} and critical mass porosities of 0.01. Mixtures of mantle-derived magmas with lower-crustal melts can thus retain substantial ^{226}Ra -excesses, even if transport times through the mantle wedge were significant.

It should be noted that even the low mass porosities considered here are an order of magnitude larger than those used in many mantle melting calculations (e.g., (Sims *et al.*, 1999; Lundstrom, 2003), but are consistent with observations that melt segregation during lower-crustal melting experiments occurs at porosities of a few percent to 15 % (Rushmer, 1995). Note that if we apply bulk partition coefficients and melting conditions appropriate for mantle melting to this model, we recover the results of previous calculations (for instance melting of garnet peridotite at small porosities ($\sim 1.0 \times 10^{-3}$) and melting rates of order 1.0×10^{-4} (Zou & Zindler, 2000).

The incongruent continuous melting model also has implications for ^{230}Th - ^{238}U disequilibria. Both uranium and thorium become less incompatible as the dehydration reaction progresses and the critical porosity has a modest control on the degree of $(^{230}\text{Th})/(^{238}\text{U})$ disequilibria. At small critical porosities (< 0.001) and low extracted melt fractions (< 0.02), $(^{230}\text{Th})/(^{238}\text{U}) = \sim 0.75$ and is controlled primarily by residual plagioclase and amphibole. As the dehydration reaction proceeds, the amount of residual garnet increases and uranium becomes increasingly more compatible in the residue. This, combined with ingrowth of ^{230}Th during melting, drives $(^{230}\text{Th})/(^{238}\text{U})$ toward higher values, and ^{230}Th excesses ($\sim 12\%$) develop at high critical porosities and extracted melt fractions greater than 0.2.

The application of continuous melting to stable trace elements predicts an enrichment of light rare earth elements (LREE) relative to heavy rare earth elements

(HREE) in the melt, due in large part to the formation of garnet, as well as enrichment of barium and strontium in the melt due to the melting of plagioclase. For example, at a critical porosity of 0.1, La/Yb values are ~ 18-20 throughout the melting range: 0 - 0.2. Amphibolites present in the lower crust are likely to have formed by stalling and solidification of earlier intrusions of mantle-derived hydrous basalts. Hence we use the trace element concentration of primitive island arc basalts as a model initial concentration for the continuous melting process (*Figure 3.2b*), although the general trace-element behavior (*Figure 3.2a*) will remain the same for a reasonable range of compositions of amphibolite. When normalized to primitive mantle, the trace element pattern follows the same general trend as many continental andesites and dacites (*Figure 3.2b*). Mixtures of mantle-derived magmas and amphibolite melts will lie between primitive arc basalts and the model amphibolite melt curves; because lower-crustal amphibolites will be enriched in incompatible elements relative to mantle rocks, the amphibolite melts will dominate the trace-element budget of mixtures even when they represent a smaller percentage of the mixed melts (see *Figure 3.2b*).

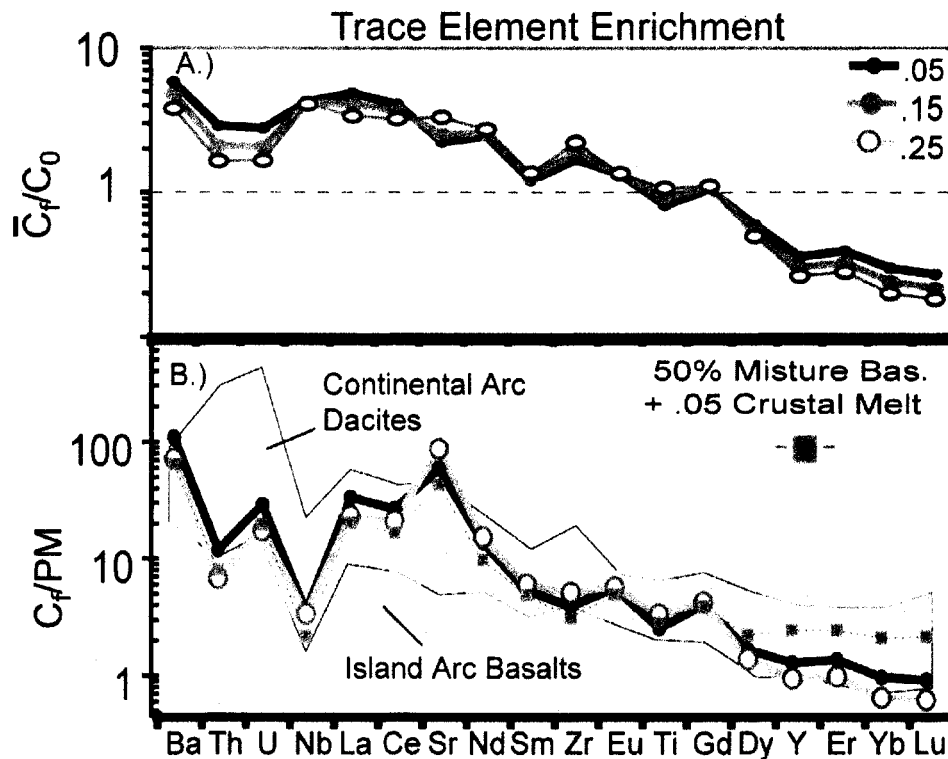


Figure 3.2. A.) Trace element enrichment and B.) trace element concentration relative to primitive mantle for amphibolite dehydration at .1 critical melt fraction (Sun & McDonough, 1989). Initial composition for the amphibolite is assumed to be equal to primitive island arc basalt (Basaltic_Volcanism_Study_Project, 1981). Trace element fields for island arc basalts (Basaltic_Volcanism_Study_Project, 1981), and continental arc dacites are shown in shaded regions (Trumbull *et al.*, 1999; Conrey *et al.*, 2001). For reference, a 50-50 mixture of crustal melt (melt fraction .05) and island arc basalt is shown (dashed line with square symbols).

A notable difference between model results and arc lavas is that the modeled amphibolite melts have positive Eu anomalies whereas arc lavas commonly have negative Eu anomalies. Therefore, some upper crustal fractionation (involving

plagioclase) of amphibolite derived and/or mixed melts would be required to match the general trend of many continental arc magmas.

Any mixing model must also satisfy major element constraints. Melts from amphibolite dehydration are nominally andesitic to rhyodacitic. Melts of quartz amphibolites would have the highest SiO₂ concentration (Patiño-Douce & Beard, 1994) whereas amphibolites with more primitive compositions - like those used the Wolf and Wyllie experiments - produce melts that vary little in SiO₂ and at melt fractions less than 0.2 have 60-64 wt. % SiO₂. Mixtures of these crustal melts with mantle derived basalts will produce intermediate magmas of basaltic andesite to andesite composition.

3.4 DISCUSSION

The non-modal melting calculations presented here demonstrate that incongruent melting of amphibolite at lower crustal pressures can produce ²²⁶Ra-excesses of a magnitude typical for many arc lavas and that these excesses will be coupled with elevated LREE/HREE. Therefore, crustal processes need not act solely to decrease mantle-derived ²²⁶Ra-excesses, and U-series disequilibria measured in arc lavas may reflect the influence of multiple processes (*Figure 3.3*). In particular, mixtures of mantle-derived basalt with amphibolite melts can retain significant ²²⁶Ra-excesses and trace-element patterns similar to those observed in arc lavas.

A notable feature of the continuous melting calculations is that large ²²⁶Ra-excesses are produced over a range of melting rates. There are appreciable uncertainties in the melting rate of the crust and at any specific time or location the melting rate will be determined by timing and geometry of intrusions as well as the lithology and thickness of the crust. Numerical models of crustal melting predict that

melting rates can locally vary from $1.0 \times 10^0 \text{ kg/m}^3\text{yr}$ to $1.0 \times 10^{-4} \text{ kg/m}^3\text{yr}$ depending on the flux of basaltic magma and style of intrusion in the crust (Annen & Sparks, 2002; Dufek & Bergantz, 2005), suggesting that melting rates of the lower crust can be slow enough for ingrowth of ^{226}Ra to be significant (cf. mantle melting rates of $10^3 - 10^5 \text{ kg/m}^3\text{yr}$ for intraplate basalts produced by decompression (Bourdon & Sims, 2003)). Even assuming instantaneous melting (i.e., aggregate fractional melting) significant Ra-excesses can develop.

The solid solution of plagioclase does have some leverage on modeled ^{226}Ra -excesses, where melting of anorthitic plagioclase produces larger Ra-excesses than melting of low-An plagioclase. Aggregate fractional melting of amphibolite with An_{50} plagioclase produces $(^{226}\text{Ra})/(^{230}\text{Th})$ of 1.21 – 1.55 for the melting range of 0 to 0.15 melt fraction, similar to the modest excesses predicted by Berlo et al. (2004). However, if melt extraction rates are less than $\sim 10^{-2} \text{ kg/m}^3 \text{ yr}$, ingrowth effects will result in Ra-excesses exceeding 2.0 at melt fractions of 0.15 even with these lower-An plagioclase compositions.

Stable element patterns can be used to constrain the overall degree of melting for the model. As an example, the La/Yb for Mt. St. Helens lavas are consistent with modeled melt fractions of $\sim 5\text{-}10\%$ (with $\Phi=0.1$) which yields initial $(^{226}\text{Ra})/(^{230}\text{Th})$ excesses of 3.0-4.0 if melting is slow enough for ingrowth effects to develop. Age-corrected $(^{226}\text{Ra})/(^{230}\text{Th})$ in recent Mount St. Helens lavas are 1.46-1.9 and the time to reach $(^{226}\text{Ra})/(^{230}\text{Th}) = 1.5$ from an initial disequilibrium of 3.0-4.0 is approximately 3000 to 4000 yrs, similar to plagioclase ages in these lavas (Cooper & Reid, 2003). Assuming a crustal thickness of 35 kilometers, this would imply average crustal ascent rates of $\sim 8\text{-}10 \text{ m/yr}$, compared to ascent rates exceeding an order of magnitude greater if the disequilibrium were generated entirely in the mantle (Turner et al., 2001). Moreover, since the modeled ^{226}Ra - ^{230}Th disequilibrium is generated as a result of melting processes in the lower crust, it is insensitive to the time spent traversing the mantle wedge. Therefore, the ^{226}Ra -excesses of arc magmas could potentially be

decoupled in time from stable trace-element or long-lived isotopic signatures of slab fluids that are carried by older mantle-derived magmas that formed lower-crustal amphibolites.

3.5 CONCLUSIONS

Ra-excesses observed in island arcs and continental arcs need not be produced exclusively as a result of slab dewatering and resulting flux melting. The exposed roots of arcs show ample evidence for garnet amphibolite compositions that are capable of melting to produce magmas with significant ^{226}Ra -excesses and with either ^{230}Th or ^{238}U excesses. Mixtures of mantle and crustal melts in the lower crust will most likely be weighted toward ^{238}U -excesses as will crustal melts with melt fractions less than ~ 0.15 . These mixed magmas can have significant ^{226}Ra -excesses regardless of the transit time through the mantle wedge, and therefore extreme transport rates in arcs are required only in the case of primitive arc basalts where $(^{226}\text{Ra})/(^{230}\text{Th})$ in arc lavas exceeds 3-5.

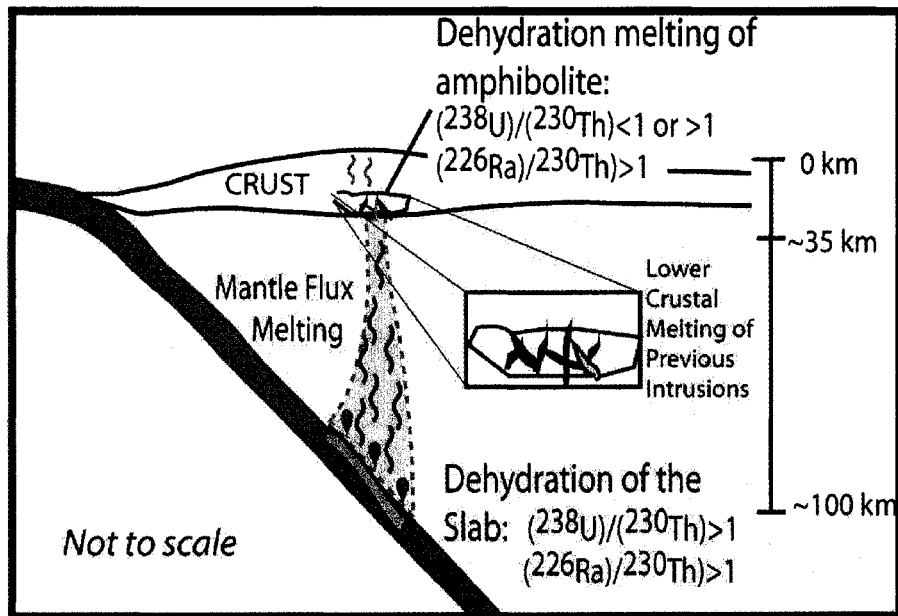


Figure 3.3. Conceptual model of U-series disequilibria produced by different arc processes. Slab dehydration releases fluids enriched in uranium and radium relative to thorium. These fluids initiate flux melting in the mantle. Melts that reach crustal levels can potentially stall, and solidify (producing amphibolite or pyroxenite lithologies), and/or initiate heating and remelting of previous mafic intrusions (amphibolite dehydration) producing melts with either $(^{238}\text{U})/(^{230}\text{Th}) < 1$ or $(^{238}\text{U})/(^{230}\text{Th}) > 1$ and $(^{226}\text{Ra})/(^{230}\text{Th}) > 1$.

- Chapter 4 -

**Transient Two-Dimensional Dynamics in the Upper Conduit of a
Rhyolitic Eruption:
A Comparison of Closure Models for the Granular Stress**

Table 4.1: Notation

c_i	Instantaneous Velocity (m/s)
C_i	Fluctuating Velocity (m/s)
C_{eq}	Equilibrium Solubility of Water (wt. %)
C_D^s	Particle Drag Function (Syamlal)
C_D^w	Particle Drag Function (Wilson)
D_{ij}	Strain Rate Tensor (s^{-1})
d_p	Particle Diameter (m)
d_{bub}	Bubble Diameter (m)
e	Coefficient of Restitution
f	Velocity Frequency Distribution
f_{coll}	Frequency Distribution of Particle Collisions
g	Gravitational Acceleration (m/s^2)
g_0	Radial Distribution Function
I_1	Inter-phase drag (N/m^3)
l	Mean Free Path (m)
m_p	Mass of particle (kg)
M	Momentum Flux ($kg \cdot m/s$)
P	Pressure (Pa)
R	Exsolution rate ($kg/m^3 \cdot s$)
Re_p	Particle Reynold's Number
S_{ij}	Stress tensor (Pa)
t_p	Particle time-scale (s)
T	Temperature (K)
u_1	Average velocity (m/s)
V_r	Ratio of the terminal velocity of a group of particles to a single particle
ΔV_g	Volume Fraction of water exsolved during one time-step ($kg/m^3 \cdot s$)
Δt	Time-step (s)
ε	Volume fraction
δ_{ij}	Kronecker delta

Table 4.1 (Continued)

λ	Second Viscosity Coefficient (Pa-s)
ξ	Bulk Viscosity (Pa-s)
μ	Shear viscosity (Pa-s)
θ_p	Granular Temperature (m^2/s^2)
ρ	Density (kg/m^3)
τ_{ij}	Deviatoric stress tensor (Pa)

Subscripts

g	gas phase
m	magma
p	particles
gp	gas-particle interaction
gm	gas-magma interaction
$\langle \rangle$	Average

4.1 INTRODUCTION

The combination of high shear viscosity and high volatile contents in rhyolitic magmas contributes to the generation of some of the most explosive, Plinian-style eruptions (Carey & Sigurdsson, 1989). The eruption sequence of depressurization, vesiculation, and fragmentation is often generalized to the setting of a high aspect-ratio conduit. This geometry is based upon the observation of relatively stationary central vents often associated with this class of eruption (Dobran, 1992; Dobran, 1993; Slezin, 2003).

Two distinct regions of multiphase flow exist in a developing conduit eruption and are separated by a fragmentation front: magma/bubble flow and gas/particle flow (*Figure 4.1*). Regions of the conduit that have become supersaturated in a volatile species in response to rapid depressurization will begin to form and grow bubbles. The high viscosity of the rhyolitic magma inhibits the formation of significant differential velocities between these phases, provided a permeable network of

interconnected bubbles has not formed (Melnik *et al.*, 2003). However, the net buoyancy force of the bubbles accelerates the magma/bubble flow. Thus the continuous depressurization during the rise of the magma provides a positive feedback as the bubbles continue to grow, and the magma/bubble mixture accelerates until reaching fragmentation.

The precise mechanism of fragmentation remains poorly understood with little unambiguous data to differentiate between ductile and brittle mechanisms (Dingwell, 1996; Mader, 1998). Sparks (1978) initially suggested that fragmentation is associated with .75 gas volume fraction, due to many observations of vesicularity in this range and due to the close correspondence of this value with the maximum packing limit of spheres of a single diameter. Observations of much lower vesicularity (Thomas *et al.*, 1994; Bachmann *et al.*, 2000) in some silicic pumices motivates further scrutiny of the fragmentation limit. It has been proposed that there is a correlation between vesicularity and viscosity of the host magma, with more viscous magma fragmenting at lower gas volume fraction (Gardner *et al.*, 1996; Papale, 1999). However, we treat fragmentation by a static model assuming that it occurs at a gas volume fraction of .75. This facilitates comparison of the granular stress differences by reducing the degrees of freedom in the study; a dynamic fragmentation model will be the subject of future studies. Following fragmentation the multiphase mixture consists of a turbulent gas with dispersed particles or melt droplets. Two principle interactions are responsible for the redistribution of momentum in this regime: particle-particle interaction and particle-gas interaction. Particles transmit momentum to each other directly through either elastic or inelastic collisions. Particle-fluid interaction occurs chiefly as a result of the drag force between a particle and the fluid when the two are moving relative to each other. The aerodynamic response time of a particle is the characteristic time-scale by which a particle responds to these changes in the flow field. This timescale can be developed by considering the equation of motion for the particle in a fluid. For situations in which the density of the particle is much greater than the density of the fluid, such as

in the gas/particle flow following fragmentation, and neglecting particle collisions, gravity and wall interaction, the equation of motion for a particle with small particle Reynolds number reduces to (Maxey & Riley, 1983):

$$\frac{dc_i^s}{dt} = \frac{-6\pi d_p \mu_g}{m_p} (c_i^s - c_i^g), \quad (4.1)$$

where c_i^s is the instantaneous velocity of the particle, c_i^g is the instantaneous velocity of the gas, μ_g is the gas viscosity, m_p is the mass of the particle and d_p is the particle diameter.

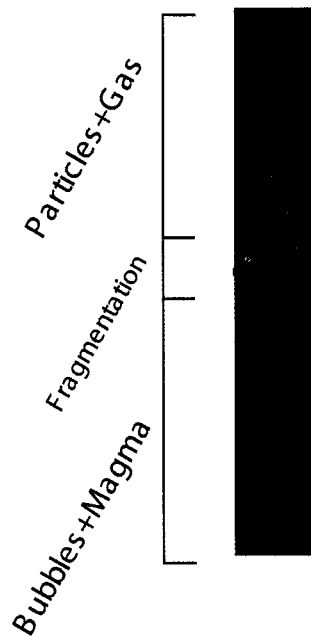


Figure 4.1. Schematic representation of multiphase regions of the conduit: Below the fragmentation level the continuous phase is a rhyolitic magma with dispersed bubbles. At the critical gas fraction of .75 fragmentations occurs, creating a turbulent gas phase with dispersed particles.

(The decomposition of the instantaneous velocity into an average and fluctuating component will be used throughout the paper, $\mathbf{c}_i = \langle \mathbf{c}_i \rangle + \mathbf{C}_i = \mathbf{u}_i + \mathbf{C}_i$. For a given differential velocity between the particle and the gas, the timescale by which the particle accelerates to match the velocity of the gas is given by the reciprocal of the leading coefficients on the right-hand side of equation (4.1). Rearrangement so that this timescale is expressed in terms of the particle density yields:

$$t_p = \frac{\rho_p d_p^2}{6\pi\mu_g}. \quad (4.2)$$

If the density of the particle and the shear viscosity of the gas remains constant, then the aerodynamic response time-scale increases as the square of the particle diameter. The ratio of the aerodynamic timescale to the characteristic time scale of the gas motion is typically referred to as the Stokes number (Eaton & Fessler, 1994). Larger Stokes number particles are slow to respond to gas motion whereas small Stokes number particles behave as tracers to the fluid motion.

The calculation of numerous individual particle paths along with a turbulent flow field is computationally intractable. Hence, work in both the volcanological and industrial community has aimed to try to develop better constitutive models to predict the macroscopic manifestations of the particle-particle and particle-fluid interactions (Lun *et al.*, 1984; Dobran, 1992; Gidaspow, 1994).

In the context of conduit flow, two multiphase theories have been applied: homogenous (single-fluid simulations) and non-homogenous (multi-fluid simulations). Homogeneous conduit flow models (Wilson & Head III, 1981) average the phase properties to create one effective fluid with bulk properties such as density. The particle-particle and particle-fluid interactions are approximated through the designation of shear and bulk viscosity terms to relate stress to strain rates in the bulk material. The implicit assumption in these models is that the aerodynamic time-scale of the dispersed phase is close to zero. This assumption applies well for

bubble/rhyolitic magma flow with low permeability, because there is little relative velocity between phases (Mader, 1998). Above the level of fragmentation a homogenous model should perform well provided that the particles remain tracers of all scales of fluid motion (Dobran, 2001), i.e. the particle size is small enough that the Stokes number approaches zero for any given eddy size.

However, Dobran (1992) demonstrated that significant mechanical non-equilibrium effects (differential velocities between phases) are important in viscous conduit flow, and developed a one-dimensional, steady state, two-phase flow model. This model has been subsequently modified for different magma viscosity relationships accounting for variable magma composition and crystal content (Papale & Dobran, 1994; Papale *et al.*, 1998), different volatile effects (water and carbon dioxide) (Papale & Polacci, 1999), different fragmentation criteria (Papale, 1999) and fragmentation efficiency (Papale, 2001). These models have produced results consistent with quasi steady-state behavior of Mt. St. Helens and Vesuvius (Papale & Dobran, 1994).

Previous non-homogeneous multi-fluid numerical simulations (Dobran, 1992; Papale & Dobran, 1994) have treated the particle phase as inviscid. That is, in one-dimensional simulations where viscosity appears in the drag relations, the particle-wall drag is set to zero. However, the viscosity of the gas is adjusted using mixture theory to account for the distortion of the flow field created by the particles and the apparent increase in viscosity that this creates (Dobran, 1992). Papale (2001) modified this model by introducing a parameterized normal collisional stress (analogous to the granular pressure described here) that provided a repulsive force for high particle concentrations and viscosity for the system was developed using mixture theory.

The inviscid granular phase assumption is appropriate in regions of the flow where there is no collisional redistribution of momentum, or in a fully fluidized bed

far from boundaries (Gidaspow, 1994; Appendix B). However, the magnitude of collisional redistribution of momentum following fragmentation remains an open question. All the phases in a multiphase system are coupled to each other through drag force relationships, and consequently changes in the constitutive relations of one phase affects the other phases. This, in turn, may result in a counter-intuitive feedback in the conduit system. In order to examine the effect of particle collisions in the conduit, a suite of numerical simulations were performed in which the constitutive equation for the granular phase was varied to reflect the collisional and collision-less counterparts. Our approach differs from that of Papale (2001) in that the terms of the granular stress tensor are developed using kinetic theory with the granular viscosity and pressure linked to the local velocity field of the particles through the granular temperature.

4.2 MULTI-FLUID MODEL FOR MULTIPHASE FLOW

4.2.1 Multi-fluid Theory

Our parameterization study of the granular constitutive relationship was performed in the context of a transient, 2-D, isothermal, multi-fluid simulation of conduit dynamics. The multi-fluid treatment of multiphase phenomena has been implemented in a range of volcanological and industrial problems (Gidaspow, 1986; Dobran *et al.*, 1993; Neri & Macedonio, 1996; Neri *et al.*, 2002). The multi-fluid methodology treats each phase as a separate continuum with differential velocities between phases. The particle phase(s) are averaged to form continuum conservation equations. The ‘true’ fluid and particle fluids are interpenetrating continua; that is, the volume fraction of each phase is calculated at individual grid points. The sum of the volume fractions at any one point is required to be unity:

$$\varepsilon_g + \varepsilon_s = 1. \tag{4.3}$$

Additionally, the conservation equations for the different fluids are:

Below the level of fragmentation

Continuity:

$$\frac{\partial}{\partial t}(\epsilon_g \rho_g) + \frac{\partial}{\partial x_i}(\epsilon_g \rho_g u_i^g) = R_g, \quad \text{gas} \quad (4.4)$$

$$\frac{\partial}{\partial t}(\epsilon_m \rho_m) + \frac{\partial}{\partial x_i}(\epsilon_m \rho_m u_i^m) = R_m, \quad \text{magma} \quad (4.5)$$

Conservation of Momentum

$$\frac{\partial}{\partial t}(\epsilon_g \rho_g u_i^g) + \frac{\partial}{\partial x_j}(\epsilon_g \rho_g u_i^g u_j^g) = \frac{\partial}{\partial x_j}(S_{ij}^g) + \epsilon_g \rho_g g - I_j^{gm}, \quad \text{gas} \quad (4.6)$$

$$\frac{\partial}{\partial t}(\epsilon_m \rho_m u_i^m) + \frac{\partial}{\partial x_j}(\epsilon_m \rho_m u_i^m u_j^m) = \frac{\partial}{\partial x_j}(S_{ij}^m) + \epsilon_m \rho_m g + I_j^{gm}, \quad \text{magma} \quad (4.7)$$

Above the level of fragmentation

Continuity:

$$\frac{\partial}{\partial t}(\epsilon_g \rho_g) + \frac{\partial}{\partial x_i}(\epsilon_g \rho_g u_i^g) = 0, \quad \text{gas} \quad (4.8)$$

$$\frac{\partial}{\partial t}(\epsilon_p \rho_p) + \frac{\partial}{\partial x_i}(\epsilon_p \rho_p u_i^p) = 0, \quad \text{particles} \quad (4.9)$$

Conservation of Momentum

$$\frac{\partial}{\partial t}(\epsilon_g \rho_g u_i^g) + \frac{\partial}{\partial x_j}(\epsilon_g \rho_g u_i^g u_j^g) = \frac{\partial}{\partial x_j}(S_{ij}^g) + \epsilon_g \rho_g g - I_j^{gp}, \quad \text{gas} \quad (4.10)$$

$$\frac{\partial}{\partial t}(\epsilon_p \rho_p u_i^p) + \frac{\partial}{\partial x_j}(\epsilon_p \rho_p u_i^p u_j^p) = \frac{\partial}{\partial x_j}(S_{ij}^p) + \epsilon_p \rho_p g + I_j^{gp}. \quad \text{particles} \quad (4.11)$$

Here ϵ is the volume fraction of either particles, magma or gas, S_{ij} are the stress tensors, I_j are the inter-phase momentum transfer terms, and R are the exsolution rates for the magmatic case (Jackson, 1983; Syamlal, 1987). The subscript (g) refers to the gas phase, (m) refers to the magma below fragmentation, and (p) to the particles above fragmentation.

4.2.2 Constitutive Relations Below the Level of Fragmentation

The magmatic stress tensor, \mathbf{S}_{ij}^m , is given by:

$$\mathbf{S}_{ij}^m = -P_m \delta_{ij} + \boldsymbol{\tau}_{ij}^m, \quad (4.12)$$

where P_m is the pressure and $\boldsymbol{\tau}_{ij}^m$ is the deviatoric component of the magmatic stress tensor. The gas and magmatic pressure are assumed to be equivalent for these calculations (Papale & Dobran, 1993). The deviatoric component is closed using the experimental compilation of Hess and Dingwell (1996) for the viscosity of hydrous leucogranitic melt:

$$\boldsymbol{\tau}_{ij}^m = 2\mu_m \varepsilon_m \mathbf{D}_{ij}^m, \quad (4.13)$$

where:

$$\log(\mu_m) = [-3.545 + .833 \ln(w)] + [9601 - 2368 \ln(w)] / \{T - [195.7 + 32.25 \ln(w)]\}. \quad (4.14)$$

where w is the weight percent of water, and T is the temperature in Kelvin. The density of the magma is held constant at 2300 kg/m^3 . The viscosity of the gas phase is held constant at $5.0 \times 10^{-5} \text{ Pa} \cdot \text{s}$, and its density derived from the ideal gas relation both below and above the fragmentation front. As a first approximation, no turbulent viscosity model was used in these simulations. The simulations of Agrawal et al. (2001) suggest that provided $\rho_p \varepsilon_s \gg \rho_g \varepsilon_g$ riser dynamics are relatively insensitive to the use of a turbulence model. This condition is satisfied in most of the computational domain for this problem, although further investigation of turbulence models in this parameter space is needed.

Below the level of fragmentation, it is assumed that the high viscosity of the magma will inhibit large velocity differences between the bubbles and the magma. Hence a simple Stokes drag relation is used:

$$\mathbf{I}_i^{\text{gm}} = \frac{6\pi\mu_m}{\rho_m d_{\text{bub}}^2} (\mathbf{u}_i^g - \mathbf{u}_i^m) - \varepsilon_g \frac{\partial}{\partial \mathbf{x}_i} P_g + \mathbf{R}_g \mathbf{u}_i^m. \quad (4.15)$$

The first term is the Stokes drag term and the second is the buoyancy term. The last term accounts for the mass transfer from the magma to the bubbles. In equation (4.15) the bubbles are assumed spherical and non-deforming.

Volatile Exsolution Model:

The equilibrium solubility of water has been modeled as:

$$C_{eq} = P_g^{.5} \left(0.4874 - \frac{608.0}{T} + \frac{489530}{T^2} \right) + P_g \left(-0.06062 + \frac{135.6}{T} - \frac{69200}{T^2} \right) + P_g^{1.5} \left(0.00253 - \frac{4.154}{T} + \frac{1509.0}{T^2} \right) \quad (4.16)$$

[The equation is reparameterized and simplified from the solubility model of Zhang (1999) by Y. Zhang.] P_g is the gas pressure in MPa, T is the temperature in Kelvin, and C_{eq} is the equilibrium solubility in weight percent (Zhang, 1999). Immediately following depressurization the dissolved water content will be greater than the equilibrium dissolved water content for the lower pressure state. This supersaturation will drive bubble formation and growth. Water is the only volatile phase used here. While this is oversimplified compared with the natural case, it was considered adequate from the standpoint of comparing the dynamics of the granular viscosity phase versus an inviscid granular phase.

Bubble nucleation and growth is considered almost instantaneous upon supersaturation. This is also a simplification, as bubble growth has been demonstrated to be primarily diffusion controlled and some time is required to diffuse water from the melt into the bubbles (Lyakhovskiy et al., 1996). Subtracting the equilibrium solubility from the initial dissolved water content gives the weight percent of water exsolved. This can then be converted to the volume fraction of exsolved water through the equation of state. In practice, this was accomplished by setting the reaction rates in equations (4.4) and (4.5) such that the exsolution of supersaturated water was accomplished over the duration of one time-step, which for these simulations was on the order of 1.0×10^{-4} s.

$$R_g = \Delta V_g \rho_g / \Delta t, \quad (4.17)$$

and

$$R_s = -\Delta V_g \rho_g / \Delta t, \quad (4.18)$$

where ΔV_g is the volume fraction of gas exsolved in one time step.

The volume fraction of exsolved gas can also be converted into an effective bubble diameter using the prescribed bubble number density, 10^{15} m^{-3} based upon the experiments of Hurwitz and Navon (1994). The bubble diameter d_{bub} is needed to compute the interphase drag between the bubbles and the magma (*equation 4.15*).

4.2.3 Constitutive Relations for the Granular Material: Kinetic Theory

The binary collision of particles represents a possible means of redistributing momentum in a particle dense region following fragmentation. On macroscopic scales this momentum diffusivity can be modeled using a granular viscosity to close the deviatoric component of the granular stress-strain rate relationship, and a granular pressure for the isotropic component (Lun et al., 1984; Syamlal, 1987). To develop the properties of the collisional regime, kinetic theory, very similar to that used in the estimation of gas viscosities from molecular collisions, is employed (Gidaspow, 1994). Lun et al. (1984) and Syamlal (1987) developed the method implemented in these calculations, and the reader is referred to these sources for a more detailed accounting of the procedure. The following set of equations results from their analysis considering binary, inelastic collisions of particles:

$$\mathbf{S}_{ij}^p = -P_p \delta_{ij} + \boldsymbol{\tau}_{ij}^p, \quad (4.19)$$

where \mathbf{S}_{ij}^p is the granular stress tensor, P_p is the granular pressure, and $\boldsymbol{\tau}_{ij}^p$ is the viscous stress tensor. The granular pressure is given by:

$$P_p = 2(1+e)\rho_p g_0 \varepsilon_p^2 \theta_p, \quad (4.20)$$

and the granular viscous stress tensor is given by:

$$\boldsymbol{\tau}_{ij}^p = 2\mu_p \mathbf{D}_{ij}^p + \lambda_p \mathbf{D}_{ii}^p \delta_{ij}. \quad (4.21)$$

Here \mathbf{D}_{ij}^p is the rate of strain tensor:

$$\mathbf{D}_{ij}^p = \frac{1}{2} \left[\frac{\partial \mathbf{u}_i^p}{\partial \mathbf{x}_j} + \frac{\partial \mathbf{u}_j^p}{\partial \mathbf{x}_i} \right], \quad (4.22)$$

and g_0 is the radial distribution function (Lebowitz, 1964):

$$g_0 = \frac{1}{\varepsilon_s} + \frac{3\varepsilon_p}{2\varepsilon_p^2}, \quad (4.23)$$

δ_{ij} is the Kronecker delta, and the Einstein summation convention is applied for repeated indices. These relations are often cast in terms of the coefficient of bulk viscosity, which is defined as:

$$\xi_p \equiv \lambda_p + \frac{2}{3} \mu_p. \quad (4.24)$$

The viscous stress tensor is composed of the second viscosity coefficient component (λ_p) and the shear viscosity component (μ_p):

$$\lambda_p = d_p \rho_p \sqrt{\theta_p} \varepsilon_p \left[\frac{4(1+e)\varepsilon_p g_0}{3\sqrt{\pi}} - \frac{\sqrt{\pi}}{9(3-e)} - \frac{2\sqrt{\pi}(1+e)(3e-1)\varepsilon_p g_0}{45(3-e)} - \frac{8\varepsilon_p g_0(1+e)}{15\sqrt{\pi}} \right],$$

(4.25)

$$\mu_p = \frac{d_p \rho_p \sqrt{\theta_p}}{2} \varepsilon_p \left[\frac{\sqrt{\pi}}{3(3-e)} + \frac{2\sqrt{\pi}(1+e)(3e-1)\varepsilon_p g_0}{15(3-e)} + \frac{8\varepsilon_p g_0(1+e)}{5\sqrt{\pi}} \right]. \quad (4.26)$$

An important parameter in these calculations is the granular temperature (θ_p). It is a measure of the fluctuating component of the particle velocity and is defined as

$$\theta_p \equiv \frac{1}{3} \langle \mathbf{C}_i^p \mathbf{C}_i^p \rangle \quad (4.27)$$

Here the instantaneous velocity (\mathbf{c}_i^p) for the solid phase has been decomposed into the average velocity or 'hydrodynamic' velocity \mathbf{u}_i^p and a fluctuating component \mathbf{C}_i^p .

To solve for the granular temperature a transport equation for the granular energy must be developed similar to the momentum equation above. An algebraic approximation was developed by Syamlal, (1987) and is used in these calculations:

$$\theta_p = \left\{ \frac{-K_1 \epsilon_p \mathbf{D}_{ii}^p + \sqrt{(K_1 \mathbf{D}_{ii}^p \epsilon_p)^2 + 4K_4 \epsilon_p [K_2 (\mathbf{D}_{ii}^p)^2 + 2K_3 (\mathbf{D}_{ii}^p)^2]}}{2\epsilon_p K_4} \right\}^2 \quad (4.28)$$

where:

$$K_1 = 2(1+e)\rho_p g_0, \quad (4.29)$$

$$K_2 = \frac{4d_p \rho_p (1+e)\epsilon_p g_0}{3\sqrt{\pi}} - \frac{2}{3} K_3, \quad (4.30)$$

$$K_3 = \frac{d_p \rho_p}{2} \left[\frac{\sqrt{\pi}}{3(3-e)} (1 + 4(1+e)(3e-1)\epsilon_p g_0) + \frac{8\epsilon_p g_0 (1+e)}{5\sqrt{\pi}} \right], \quad (4.31)$$

$$K_4 = \frac{12(1-e^2)\rho_p g_0}{d_p \sqrt{\pi}}. \quad (4.32)$$

This equation assumes that the granular energy is dissipated locally, and is most appropriate for fully developed, simple shear flows (Syamlal, 1987; Gidaspow, 1994). Non-steady forcing in the conduit may give rise to advective transport of granular energy that is not treated with this assumption.

The expression for the granular stress shown above is complex but some intuition can be gained from examining a simpler, non-rigorous treatment as demonstrated by Gidaspow (1994). Assuming a Taylor expansion can be performed, the momentum flux yields the expression:

$$\mathbf{M}(x+l)\langle \mathbf{c} \rangle = \mathbf{M}(x)\langle \mathbf{c} \rangle + l\langle \mathbf{c} \rangle \frac{d\mathbf{M}}{dx}, \quad (4.33)$$

where

$$\mathbf{M} = (mc). \quad (4.34)$$

Here l is the mean free path. Gidaspow (1994) assumes in this simple case that the particle velocity distribution is Maxwellian. That is, the particle velocities vary randomly around a mean velocity. Rearrangement, assuming constant density, and

using the observation that the change in momentum flux equals the product of a viscosity and the strain rate yields the expression:

$$\mu = \lambda \rho \langle c \rangle, \quad (4.35)$$

or that the viscosity is simply the product of the mean free path, the density, and the average velocity. Using the Maxwellian distribution to determine the average velocity, this expression yields:

$$\mu = \left(\frac{1}{3\sqrt{\pi}} \right) \rho_p d_p \sqrt{\theta_p}. \quad (4.36)$$

In both the expression of Lun et al. (1984) and in the simplified Gidaspow (1994) example, the granular viscosity is proportional to the square root of the granular temperature and diameter of the particle, and motivates the examination of the different particle sizes in this study.

Another parameter is the restitution coefficient (e), which is a measure of the inelasticity of particle collisions ($e = 1$ is for a perfectly elastic collision). In general, the coefficient of restitution is a function of the material and velocity of collision, with higher velocity impacts having lower coefficients of restitution (Johnson, 1985). It is difficult to parameterize the restitution coefficient for pumice and droplet materials. In this study a value of .8 was used and a sensitivity analysis is presented below.

For the particle-gas momentum transfer above the level of fragmentation the relation of Syamlal et al. (1993) was used which is based on correlations from terminal velocity measurements:

$$\mathbf{I}_i^{sp} = \frac{3\epsilon_p \epsilon_g \rho_g}{4V_r d_p} C_D^s |\mathbf{u}_i^g - \mathbf{u}_i^p| (\mathbf{u}_i^g - \mathbf{u}_i^p) - \epsilon_p \frac{\partial}{\partial x_i} P_g, \quad (4.37)$$

where V_r is the terminal velocity correlation (the ratio of the terminal velocity of a group of particles to that of a single, isolated particle) given by the expression :

$$V_r = .5(A - .06Re_p + \sqrt{(.06Re_p)^2 + .12Re_p(2B - A) + A^2}) . \quad (4.38)$$

In this relation,

$$A = \epsilon_g^{4.14} , \quad (4.39)$$

$$B = \begin{cases} .8\epsilon_g^{1.28} & \text{if } \epsilon_g \leq .85 \\ \epsilon_g^{2.65} & \text{if } \epsilon_g > .85 \end{cases} . \quad (4.40)$$

The single-sphere drag function and particle Reynold's number are given by:

$$C_D^s = \left[.63 + \frac{4.8}{\sqrt{Re}} \right]^2 , \quad (4.41)$$

and

$$Re_p = \frac{d_p |\mathbf{u}_s - \mathbf{u}_g| \rho_g}{\mu_g} . \quad (4.42)$$

4.2.4 Conduit Parameters

Conduit flow requires that a large region of the conduit be represented in the model even though the phenomena of interest to this study are isolated to the post-fragmentation region. This requirement arises because the behavior at fragmentation is altered by conditions deeper in the conduit such as mass-flux and pressure. The idealized conduit geometry is depicted schematically in *Figure 4.2* and is 24 m in radius and 8 km from base to vent. Symmetry about the centerline is assumed. At the bottom boundary the pressure is fixed at the lithostatic pressure at a depth of 8 km (~212 MPa assuming a crustal density of 2700 kg/m³). At the top of the idealized vent the cross-sectional area increases to permit choked flow conditions. An outlet boundary at atmospheric pressure is specified 4 km above the vent. Sidewall boundaries were designated no-slip below the level of the conduit vent. All simulations were solved on a regular grid with numerical resolution of 4x4 meters. Radial changes in the volume fraction of different phases through time can be examined in these two-dimensional simulations. However, the resolution and imposed symmetry at the center-channel may inhibit the development of meso-scale

structures in these simulations (Neri & Gidaspow, 2000; Agrawal *et al.*, 2001). The conduit was considered isothermal at 850°C, and initial water concentration was assumed to be 4.5 wt. % water and is in rough agreement with the water concentration of many rhyolitic eruptions (Anderson *et al.*, 1989). At the start of the simulations all the water is assumed to be dissolved in the magma and the pressure is magma-static. Under natural conditions such an initial condition is unlikely because a significant component of gas would likely have already exsolved before reaching these depths. Hence, the details of the initial shock are probably unrealistic. However, these simulations proceed to a steady state quickly and this behavior will be examined in detail. Fragmentation is assumed to take place at the critical gas volume fraction of .75. Although the parameters selected for the numerical simulations shown below were chosen with guidance from natural constraints, we stress that this study does not aim to model a particular eruption, but rather to evaluate the sensitivity of the different granular constitutive relations in a general sense for rhyolitic eruptions.

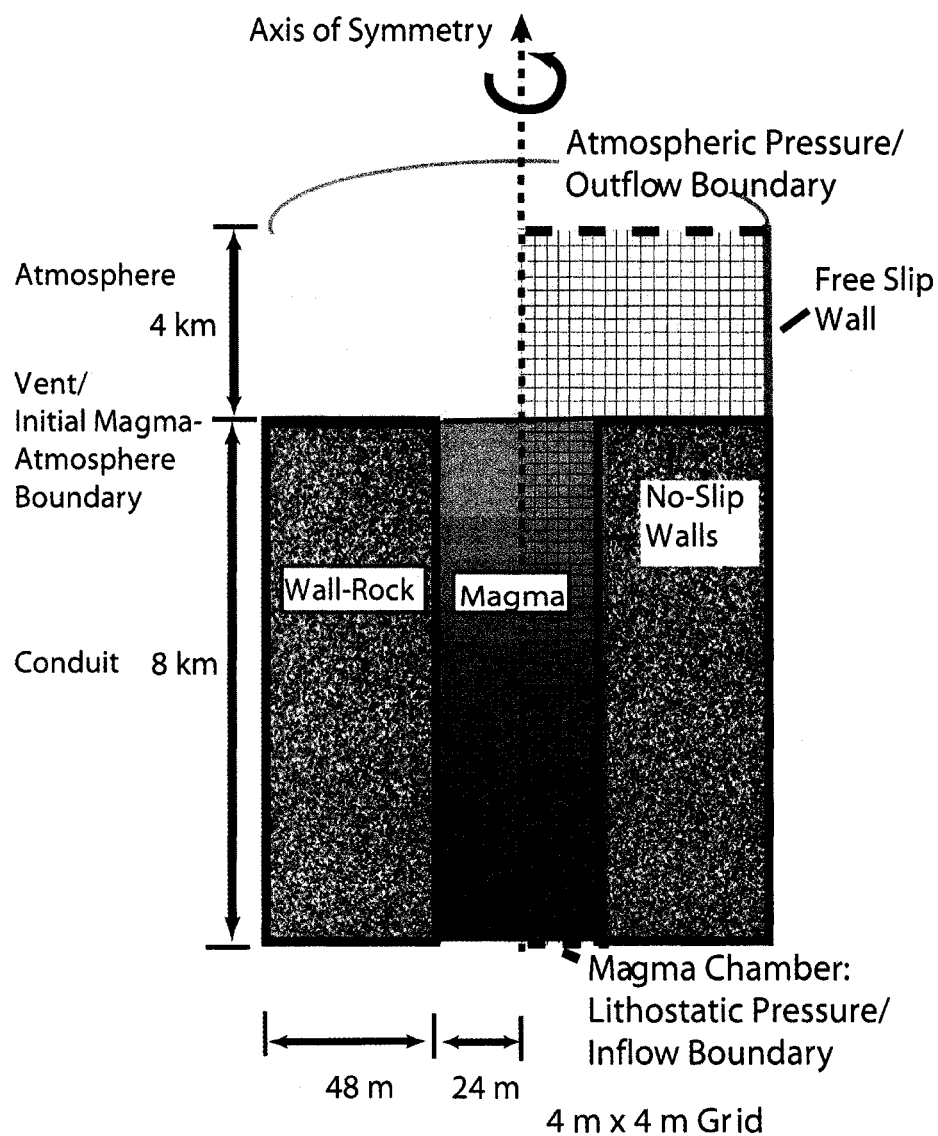


Figure 4.2. Schematic Representation of the Conduit Model: The bottom boundary is specified as the lithostatic pressure at a depth of 8 kilometers. Sidewalls are assumed to be no-slip and the cross-sectional area expands at the vent to permit choked flow. An outflow boundary condition is specified 4 km above the vent. The modeled conduit region is 8 kilometers high and 24 m in radius. Symmetry is assumed about the centerline. The numerical grid is regular (square) and resolution is 4 m x 4 m. This schematic is horizontally exaggerated ~100:1.

4.2.5 Numerical Treatment of the Multi-fluid Equations

The previous set of equations were solved using a modified form of the MFIX (Syamlal et al., 1993) multi-fluid code adapted for volcanic conduit conditions. This code was validated for the industrial fluidized bed application through comparison with experimental results (O'Brien & Syamlal, 1991). A switching function was incorporated to handle the magma/solid particle transition. Below the critical volume fraction the magmatic viscosity of Hess and Dingwell (1996) is applied. Above the level of fragmentation, in the atmosphere, the viscosity of the particle phase is either a.) calculated from kinetic theory or b.) assumed inviscid. The model was run on a single processor with a 18×3000 grid ($4 \text{ m} \times 4 \text{ m}$ resolution). Small timesteps of $\sim 1.0 \times 10^{-4}$ s were required for convergence. The model was tested on a Beowulf multi-processor system, but the geometry and node configuration of this problem scaled poorly.

4.3 SIMULATION RESULTS

Three different particle sizes (.0002 m, .002 m and .02 m) were examined in order to compare the collisional granular stress to the collision-less inviscid granular approximation. To reduce the degrees of freedom, all other variables were held constant between the simulations. *Table 4.2* summarizes some of the relevant results.

4.3.1 Initial Shock

Immediately following rapid depressurization of the magma, a shock develops that propagates up the conduit. An exsolution front propagates back into the conduit and the fragmentation zone develops. The velocity of the multiphase mixture immediately following the shock (both particles and gas) is slightly greater in the simulations using kinetic theory for the granular stress (*Figure 4.3*). This pattern of

greater velocities in the initial shock for the kinetic theory calculations was observed for the .0002 m, .002 m, and .02 m grain sizes. This is likely the result of the greater over-pressure that develops in these calculations in the initial stages of the eruption. As the simulation proceeds, a quasi-steady state pressure is approached that resembles similar results achieved through the calculations of Papale and Dobran (1994) with about 12% over-pressure with respect to the lithostatic gradient immediately below the fragmentation level (*Figure 4.4*). The velocity following the shock for the case of the .0002 m particles calculation was ~410 m/s (kinetic) and ~390 m/s (inviscid) above the level of the vent. These velocities, however, are not sustained and the steady state velocities are approximately half these values.

Table 4.2: Summary of conditions in the upper conduit at steady state^a

Sim. Name	d_p (m)	S_{ij}	$u_g^{exit,max}$ (m/s)	$u_g^{exit,avg}$ (m/s)	$u_p^{exit,max}$ (m/s)	$u_p^{exit,avg}$ (m/s)	P_g^{exit} (Pa)	μ_p^{max} (Pa s)	Mass-Flux (kg/m ³ s)	D_F (m)
I (Visc.)	.0002	C	220.5	206.5	220.5	205.5	2.23×10^6	2.52×10^{-5}	3.66×10^7	1620
II (Visc.)	.002	C	194.5	166.2	188.1	157.7	1.82×10^6	1.45×10^{-3}	3.09×10^7	1440
III (Visc.)	.02	C	172.6	145.1	162.5	137.8	1.60×10^6	1.36×10^{-1}	3.04×10^7	1280
I (Inv.)	.0002	C-L	220.7	216.3	220.6	214.1	2.22×10^6	0.0	3.71×10^7	1576
II (Inv.)	.002	C-L	204.8	195.1	197.2	185.3	1.80×10^6	0.0	3.63×10^7	1416
III (Inv.)	.02	C-L	182.4	171.9	170.1	163.3	1.59×10^6	0.0	3.60×10^7	1256

^a The conduit diameter is 24 m and the height is 8 kilometers in all simulations. d_p is the particle diameter, S_{ij} is the granular stress tensor approximation used: C-collisional, C-L – collision-less, $u_g^{exit,max}$ and $u_p^{exit,max}$ are the exit gas and particle centerline velocities, respectively, $u_g^{exit,avg}$ and $u_p^{exit,avg}$ are the average exit gas and particle velocities, P_g^{exit} is the exit pressure, μ_s^{max} is the maximum granular shear viscosity, the mass flux is recorded at the vent, and D_F is the depth of fragmentation.

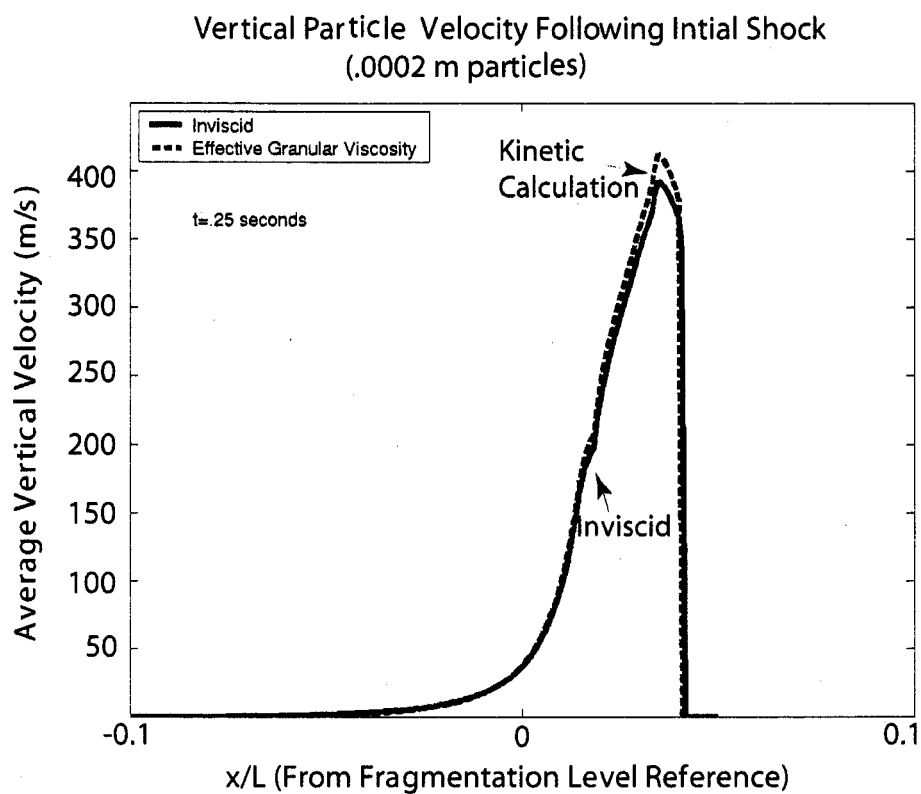


Figure 4.3. Particle velocity following initial shock (~.25 s after start of simulation): Dashed line refers to particle velocity where the effective granular stress tensor has been computed using kinetic theory, and the solid line denotes the particle velocity in a simulation using an inviscid granular material. Both curves refer to simulations with .0002 m diameter particles. The length axis has been non-dimensionalized by dividing by the conduit length and is referenced to 0.0 at the point of fragmentation.

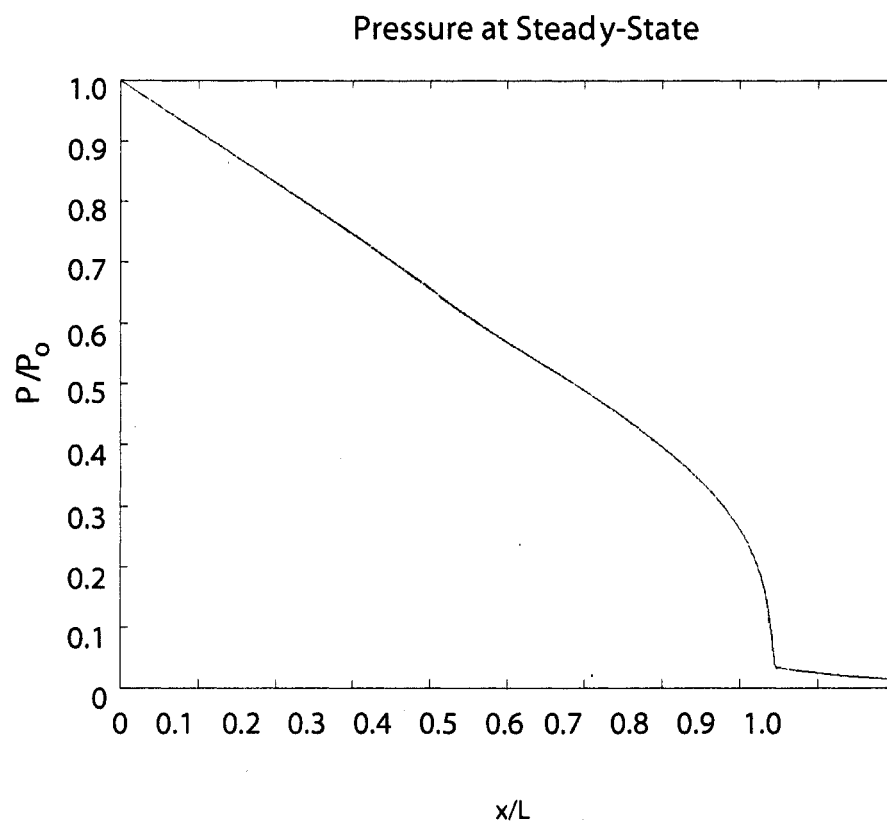


Figure 4.4. Non-Dimensionalized Pressure at steady state: The pressure was normalized by the lithostatic pressure at 8 km depth and the height was normalized by the conduit length. Both the inviscid and effective granular viscosity calculations produce pressure greater than lithostatic below the fragmentation level.

4.3.2 Quasi-Steady State

Steady state conditions were reached on the order of ~10 simulated seconds. Since the diffusion of volatiles wasn't accounted for, this time should not strictly be comparable to eruptive time-scales.

Below the Fragmentation Level

All the simulations produced similar results in the portion of the conduit below the fragmentation level. The fragmentation process for centimeter size particles, especially when the granular viscosity was calculated, was less efficient in moving material away from the fragmentation zone, and hence magma lower in the conduit was at slightly elevated pressures. This inhibited exsolution and consequently resulted in slightly lower velocities (*Figure 4.5,4.6*). There was little differential velocity ($\ll 1\%$) of bubbles and magma below the fragmentation level in any of the simulations. However, there was higher pressure in the center of the conduit, so that at any particular depth there was greater exsolution at the edges of the conduit. This process may have implications for gas loss from the conduit walls as was pointed out by Wilson (1998). Using an analytical calculation, Wilson demonstrated that the effect of increasing viscosity with height was sufficient to produce small lateral pressure variations in the conduit. This apparently is the same mechanism at work in the present calculations as the regions of the greatest vertical viscosity gradient (just below fragmentation) have the largest horizontal pressure gradients (*Figure 4.7*). The vertical increase of viscosity with height is a result of volatile exsolution at lower pressure (Hess & Dingwell, 1996). In these calculations the horizontal pressure variation below fragmentation accounted for about a 3% drop from center-conduit to sidewall.

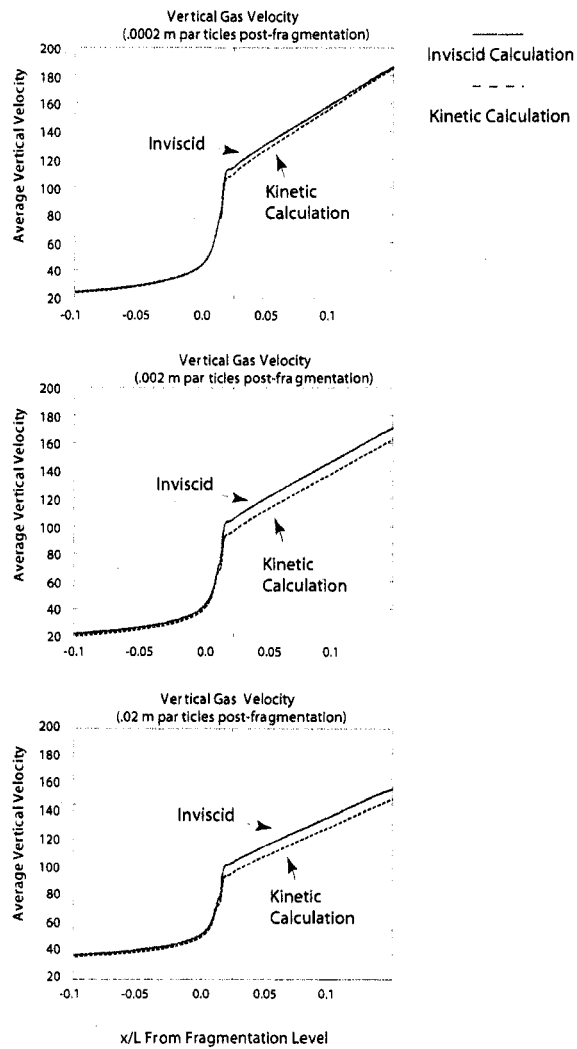


Figure 4.5. Centerline gas velocities near the level of fragmentation: Gas velocities for both the inviscid (solid line) and granular effective viscosity (dashed line) calculations are shown for the simulations using .0002 m, .002 m and .02 m particles.

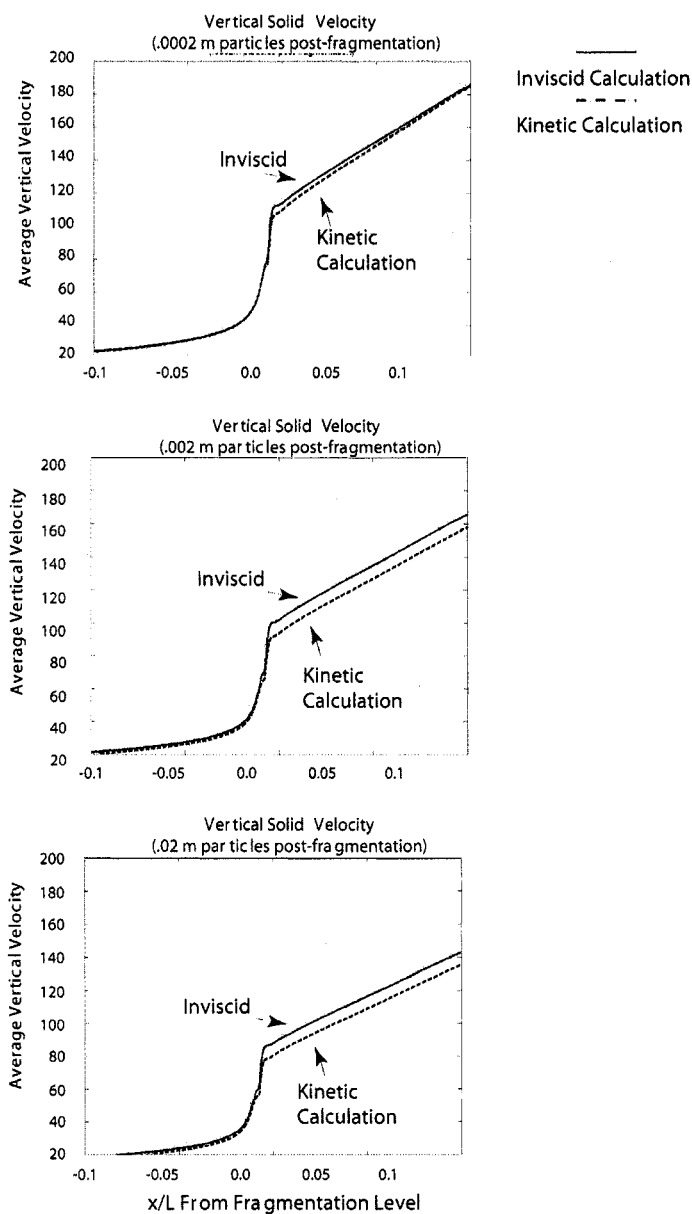


Figure 4.6. Centerline magma and particle velocities near the level of fragmentation: Magma and particle velocities for both the inviscid (solid line) and granular effective viscosity (dashed line) calculations are shown for the simulations using .0002 m, .002 m and .02 m particles. Below the 0.0 point the magmatic rheology applies and above this level either kinetic theory or the inviscid assumption is applied.

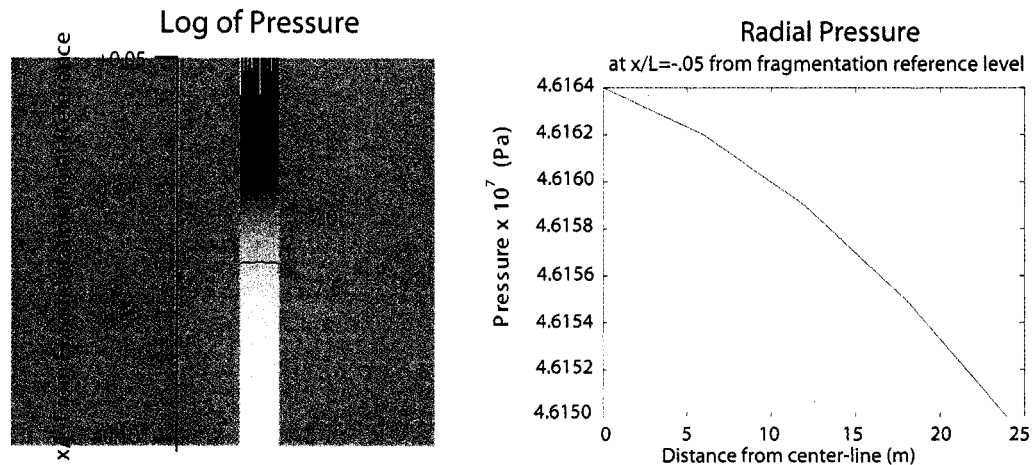


Figure 4.7. Two-dimensional cross-section of pressure near fragmentation: Pressures are displayed on the left as log of Pa. The right panel shows the radial distribution of pressure from the center of the conduit to the edge of the conduit. Both illustrate the higher pressure in the center of the conduit.

Above the Fragmentation Level

Figure 4.8 shows the centerline conduit exit velocities for gas and particles during these simulations. Both the inviscid and granular viscosity calculations show that the relative gas-particle velocity increases with increasing particle size. The eruptions with .0002 m particles have particle and gas velocities that are virtually indistinguishable, whereas the .02 m particles, for the inviscid calculation, have center-line vertical velocities of 182.4 m/s and 170.1 m/s for the gas and particles respectively.

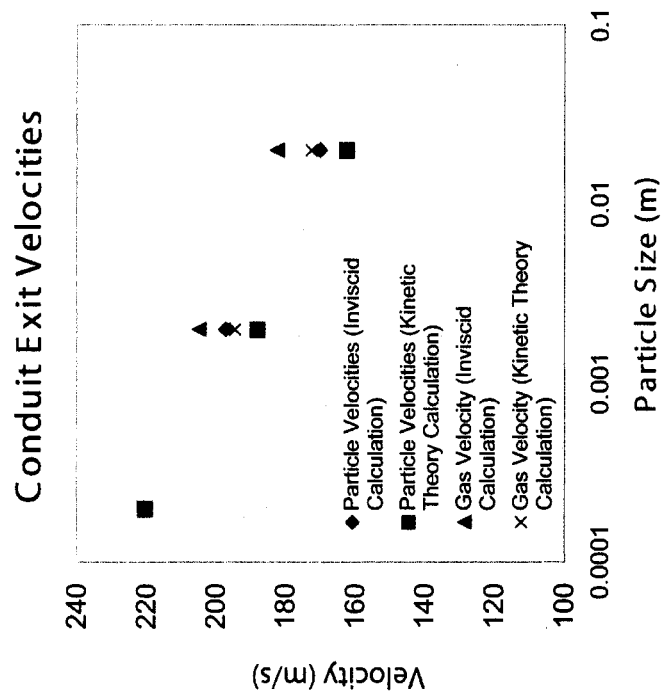


Figure 4.8. Centerline conduit exit velocities: Gas and particle velocities are shown for .0002 m, .002 m and .02 m particle calculations. Both the effective granular viscosity calculations and inviscid calculations are shown.

The greater gas-particle differential velocity observed for the larger particles can be interpreted in terms of the aerodynamic response timescales of the different particles. The particle response times can be estimated from equation (4.2) and are 5.31×10^{-1} seconds for the .0002 m particles, 5.31×10^1 seconds for the .002 m particles and 5.31×10^3 seconds for the .02 m particles. Equation 2 applies for smooth, spherical particles with small particle Reynolds numbers. The larger particles considered here, .002 m and .02 m, have significant differential gas-particle velocity and have particle Reynolds numbers in excess of 100 (equation 4.42). Therefore, a more sophisticated approach is warranted to estimate their response timescales. An aerodynamic timescale can be developed from the drag relation used in this multi-fluid study (*Syamlal formulation, equation 4.37*) that is based on terminal velocity correlations and accounts for the volume fraction of particles present. Neglecting the buoyancy term, this equation recast is:

$$\frac{m_p \frac{d\mathbf{u}_i^s}{dt}}{V} = \frac{3\epsilon_p \epsilon_g \rho_g}{4V_r^2 d_p} C_D^s |\mathbf{u}_i^g - \mathbf{u}_i^p| (\mathbf{u}_i^g - \mathbf{u}_i^p), \quad (4.43)$$

where m_p is the total mass of the solid phase in a control volume (V). Velocities in this equation are the fluid, or average velocities of the gas and particles. The macroscopic density of the particles (m_p/V) can be written in terms of the single particle density, ρ_p , using the volume fraction of the particles in the control volume. Then rearrangement of the terms gives:

$$\frac{d\mathbf{u}_i^s}{dt} = \frac{3\epsilon_g \rho_g}{4V_r^2 d_p \rho_p} C_D^s |\mathbf{u}_i^g - \mathbf{u}_i^s| (\mathbf{u}_i^g - \mathbf{u}_i^s), \quad (4.44)$$

and a timescale of:

$$t_p^s = \frac{4V_r^2 d_p \rho_p}{3\epsilon_g \rho_g C_D^s |\mathbf{u}_i^g - \mathbf{u}_i^s|}. \quad (4.45)$$

Assuming an average volume fraction of particles of 0.1 that is typical in these simulations, the corresponding timescales are .36 s, 6.6 s, and 56 s for .0002 m, .002

m, and .02 m particles, respectively (assumptions used in these calculations listed in *Table 4.3*). These timescales can be compared to the single-particle drag formulation of Wilson (1999) that considered particle roughness and yielded timescales of .56 s, 8.7 s and 36 s, respectively.

$$t_p^w = \frac{4d_p \rho_s}{3\rho_g C_D^w |\mathbf{u}_i^g - \mathbf{u}_i^s|} \quad (4.46)$$

The Wilson relation (*equation 4.46*) and the Syamlal relation (*equation 4.45*) are equivalent in form for dilute conditions ($\epsilon_g \rightarrow 1.0$) and if $C_D^w = C_D^s/V_r^2$. The formulation for these timescales and particle Reynolds number is summarized in *Table 4.3*. The drag correlation developed by Syamlal was used in this study, and hence these timescales are of the most relevance in interpreting our results, although qualitatively any of the drag formulations would have produced differential particle-gas velocities for the .02 m particles for this conduit geometry.

Table 4.3: Summary of particle timescales^b

Particle size (m)	Average Differential Velocity (m/s)	Particle Reynold's Number Re_p	C_D^w	C_D^s	C_D^s/V_r^2	Low Re aero. Time-scale t_p (s)	Wilson Form. Time-scale t_p^w (s)	Syamlal Form. Time-scale t_p^s (s)
.0002	.05	.25	96	70	166	.53	.55	.36
.002	2.5	125	1.22	.99	1.79	53	8.7	6.6
.02	6.0	300	1.22	.50	.87	5300	37	56

Assuming an average transit time on the order of 10 seconds from fragmentation to conduit exit gives equivalent Stokes numbers of approximately .036, .66 and 5.59 for

^b Average differential velocity between the gas and solid phase is estimated as the difference in the centerline velocities at the conduit exit divided by 2. Calculation of C_D^w is given by $24/Re_p$ for $Re_p < 100$ and 1.22 for higher Reynold's number (Wilson, 1999).

.0002 m, .002 m, and .02 m particles. Only the .0002 m particles have sufficient time to respond completely to the gas velocity by the conduit exit.

One key finding from our work is that including the granular viscosity calculation decreases the velocities of the particle and gas phases in simulations with particles greater than about a millimeter. At the conduit exit, this results in centerline velocities of 172.6 m/s for the gas phase and 162.5 m/s for the particle phase when .02 m particles are considered. Again, the calculation with .0002 m particles shows little difference in velocities when the granular stress is considered. It should be noted that the constitutive equations for the gas phase remained the same during all of the simulations. When collisions produced a granular viscosity, the particle phase was slowed, created a greater magnitude drag force between the gas and the particles, and, as a result, slowed the gas. *Figures 4.5 and 4.6* show the centerline vertical velocities of the gas and particles in the near fragmentation area. Immediately following fragmentation the particle phase with the granular viscosity is slowed compared to the inviscid particle phase for even the .0002 m particles. However, as the conduit exit is reached the velocity difference is diminished for the .0002 m particles. For both the .002 m and .02 m particle sizes the viscous particle phase remains slower than its inviscid counterpart from the point of fragmentation to the conduit exit.

The centerline velocities are the maximum velocities in the conduit for both the inviscid and granular viscosity calculations. However, the radial velocity profile at the vent of the conduit varies with the assumption used for the granular stress. For example, *Figure 4.12* shows the velocities at the vent for the .002 m particles for both the inviscid and granular viscosity cases. In general, the velocities are greater in the inviscid case, and decrease less rapidly in the annular flow region than do the velocities in the granular viscosity case. This has a subtle effect on the mass flux calculations given in *Table 4.2*, and results in greater flux of material for the inviscid calculations. In many industrial riser flows a negative annular velocity is often

detected (Miller & Gidaspow, 1992; Neri & Gidaspow, 2000) which is not observed here. However, in the experiments reported by Miller and Gidaspow (1992) the negative velocity disappears for large magnitude vertical velocities. Another mitigating factor is the use of no-slip boundary conditions for the gas and particle phase; one avenue of future research will be to examine the effect of partial slip boundaries on the particle phase (Neri & Gidaspow, 2000).

The spatial distribution of the volume fraction of gas is also changed as a result of modifying the particle size. The larger particles diminish the vertical gradient of volume fraction of gas (*Figure 4.9*) so that fragmentation occurs at a higher level in the conduit for the larger particle sizes. As a result, a greater volume fraction of particles leave the conduit exit when larger particles are considered, although with a lower velocity. The granular viscosity calculation lowers the vertical gradients in the volume fraction of gas in the near fragmentation zone as is depicted in *Figure 4.10*. The calculation of granular stress also increases the near wall concentration of particles compared to the inviscid simulations (*Figure 4.13*). This result is consistent with the observation of core-annular granular flow in industrial risers (Miller & Gidaspow, 1992).

Volume Fraction of Gas for Different Particle Sizes
(Kinetic Theory Calculation)

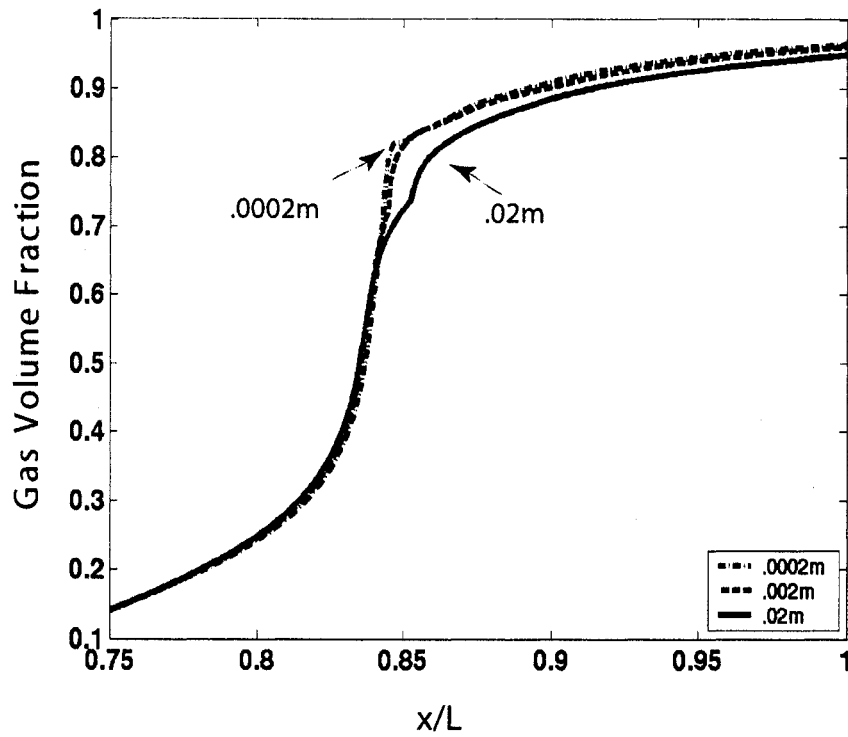


Figure 4.9. Volume fraction of gas for different particle sizes: Conduit height is non-dimensionalized by the length of the conduit and is referenced from the bottom of the conduit (8 km). The larger particles decrease the gradient of volume fraction near fragmentation (.75). A larger volume fraction of the centimeter scale particles exits the conduit.

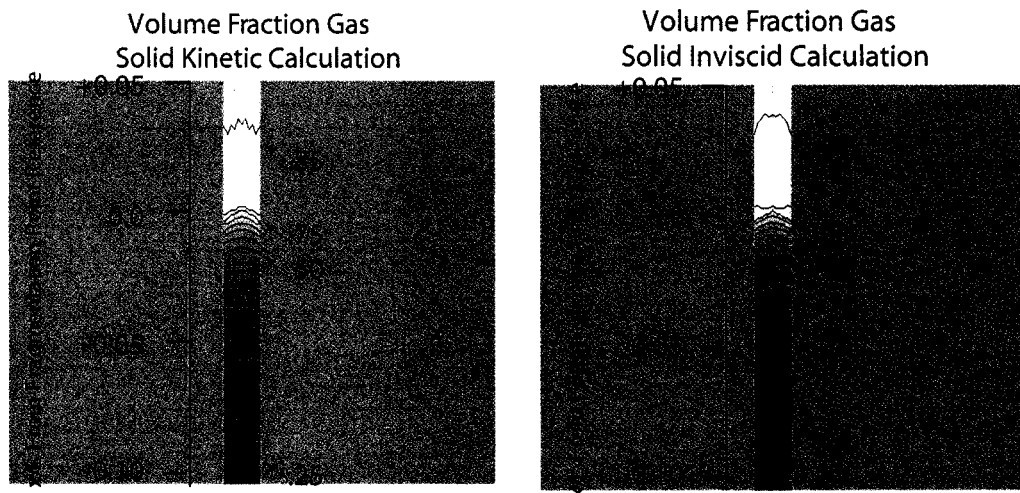


Figure 4.10. Two-dimensional cross-section of gas volume fraction near fragmentation: The granular viscosity (kinetic theory calculation) and the inviscid calculation volume fractions are shown for .002 m particles. The particle volume fraction above fragmentation is slightly more focused in the granular viscosity calculation than in the inviscid calculation.

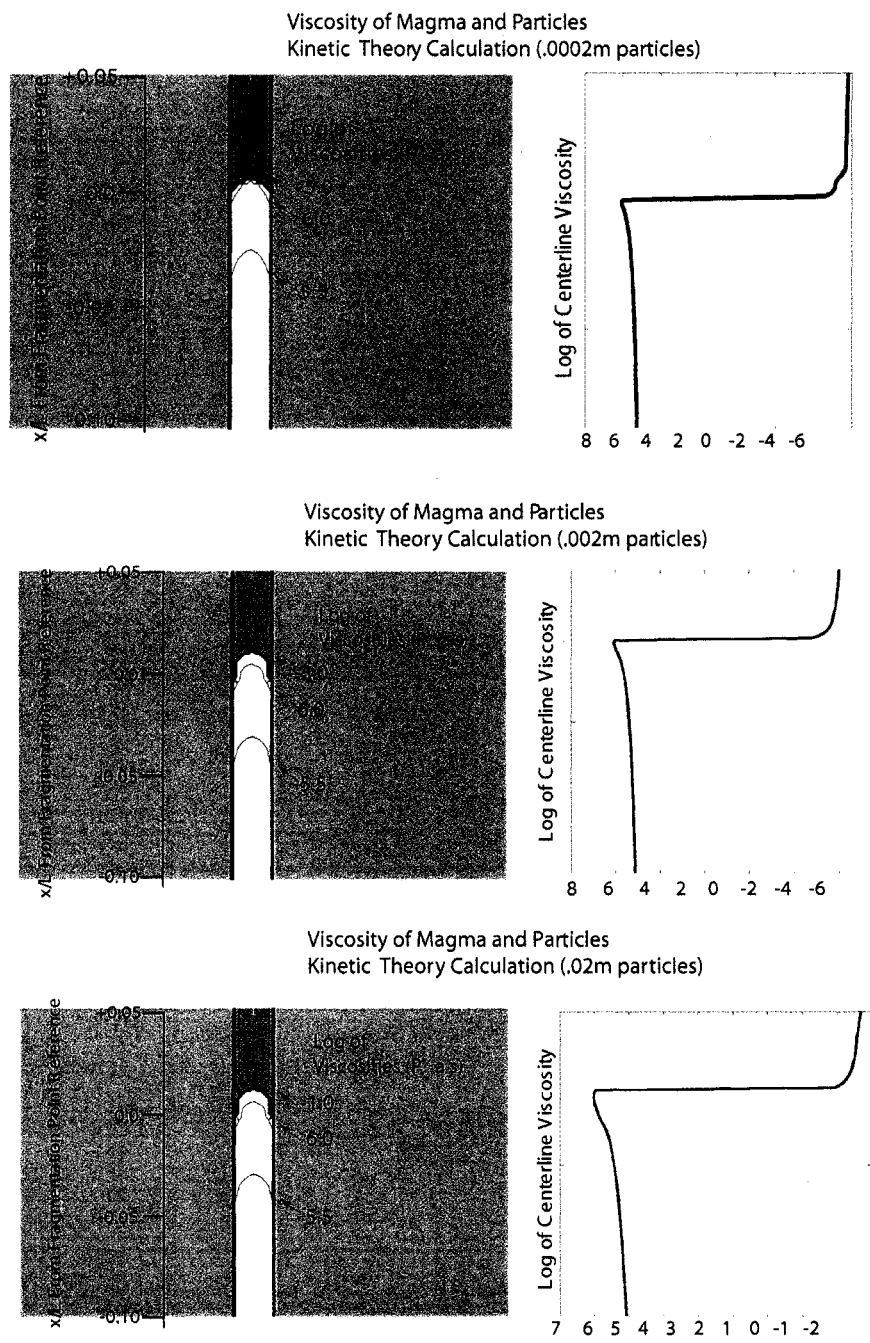


Figure 4.11. Granular viscosity following fragmentation: Effective granular viscosity calculations are shown corresponding to the three particle sizes .0002 m, .002 m, and .02 m. Viscosity is given as the log of Pa-s.

The viscosities that result from the kinetic theory calculation are depicted in *Figure 4.11*. The sub-millimeter particles have viscosities after fragmentation that are approximately 10^{-5} Pa·s which is very near to the viscosity of a gas phase at these elevated temperatures. However, the .02 m particles produce viscosities after fragmentation of about 10^{-1} Pa·s. The granular viscosity is highest immediately following fragmentation and also near to the sidewall boundaries. This is primarily a result of the slightly higher volume fraction of particles in these regions. Examination of equations (4.26) and (4.28) shows that as the volume fraction of particles goes to zero, the granular viscosity must also go to zero. The correlation of volume fraction to granular viscosity has also been noted in the riser experiments (Miller & Gidaspow, 1992). Modifying the coefficient of restitution from .8 to .5 changed the granular viscosity to ~15% lower values.

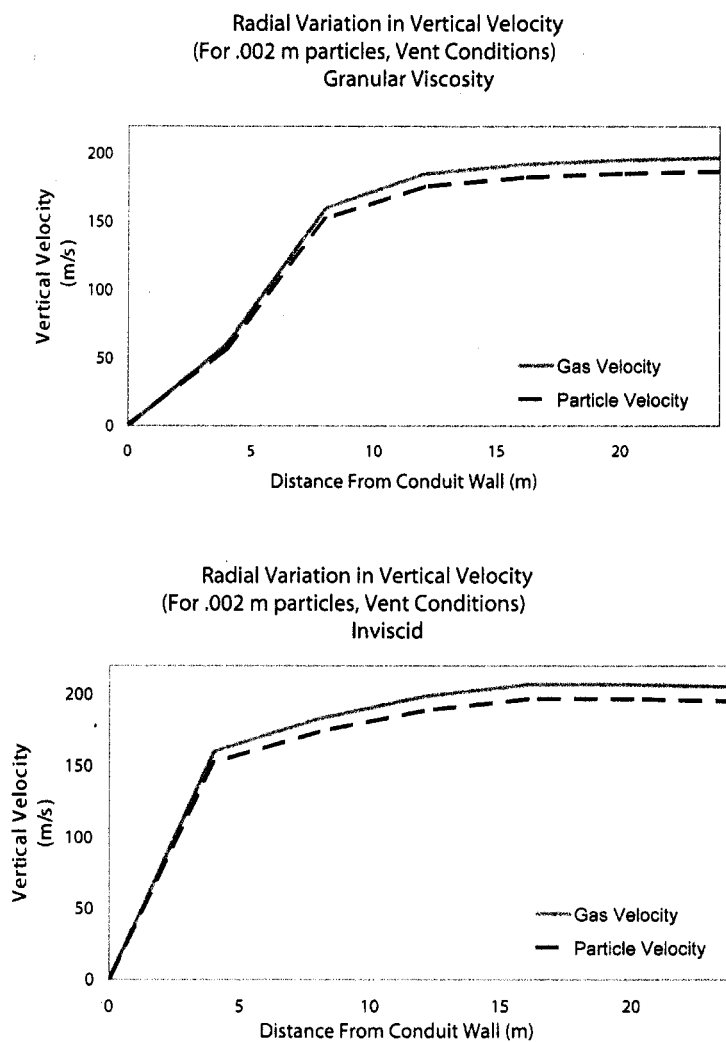


Figure 4.12. Radial variation in the vertical velocity at the vent: Velocity of the gas (solid grey lines) and particles (dashed black lines) are shown for the granular viscosity (top) and inviscid (bottom) calculations using .002 m particles. In both cases the gas exits the conduit with greater velocity, and the relative velocity is greatest in the center of the conduit. In the annular or near-wall region, the velocity of both phases decreases more rapidly further from the wall in the granular viscosity calculation.

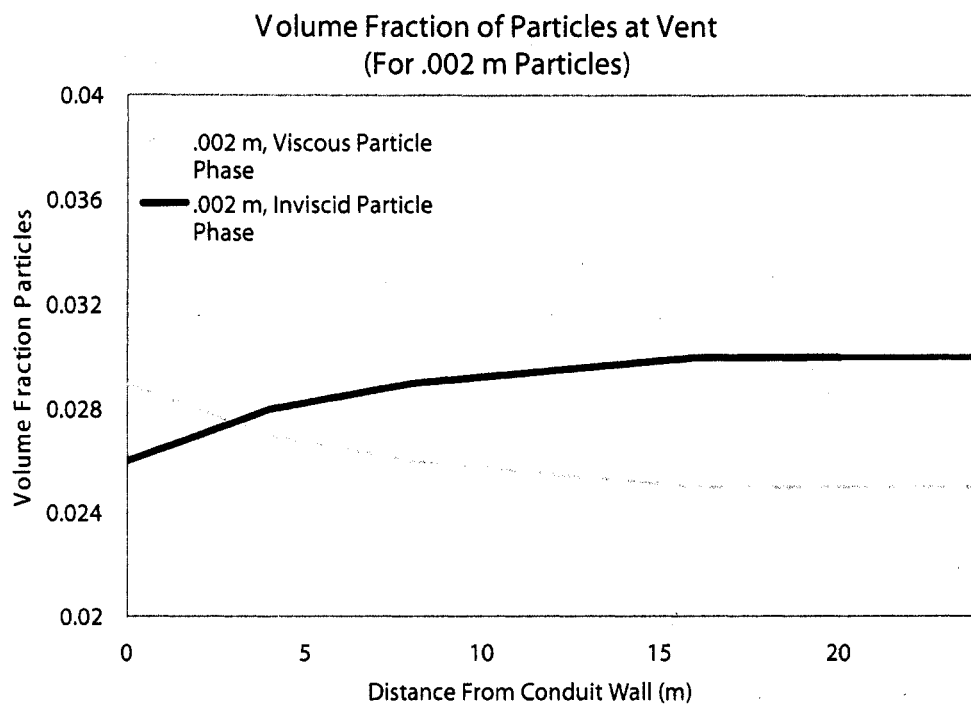


Figure 4.13. Radial variation in the particle volume fraction at the vent: The volume fraction for the granular viscosity (grey line) and inviscid (black line) calculation for .002 m are compared. The calculations using granular viscosity show slightly greater volume fraction in the near-wall region than in the center-conduit.

4.4 CONCLUSIONS

The results from this parametric study of the granular stress in the context of a rhyolitic conduit eruption show that the inclusion of a granular viscosity calculation is probably not necessary for particles of the order .0002 m or smaller. These sub-millimeter particles have granular viscosities on the order of 10^{-5} Pa·s in the conduit setting. However, .002 m and .02 m particles have ~5% differences in the particle centerline velocity and maximum granular viscosities of the order of 10^{-3} Pa·s and 10^{-1} Pa·s, respectively, when collisions are considered.

The use of a two-dimensional model permitted the calculation of radial variations in volume fraction and velocity of gas and particles exiting the conduit. The granular viscosity calculation predicted a greater volume fraction of particles in the near wall region at the conduit vent than did the inviscid calculation. The velocities at the vent for the inviscid calculations were in general higher than the granular viscosity calculations, and had a larger gradient ($\frac{\partial v}{\partial x}$) in the near-wall region. When fragmentation is less efficient and larger particles are produced, as often happens in large silicic eruptions, the results shown here suggest that significant mechanical disequilibria will develop between the gas and particles phases. As the outlet velocity and mixture density of particles and gas will ultimately determine whether an eruption will collapse and form destructive pyroclastic flows, this mechanical disequilibria may play an important role in influencing the evolving eruptive style. Two-dimensional conduit models, such as the one used in this study, may be implemented in the future to determine the structure of more complex flows, evaluate the speed of mixtures of gas/particles for irregular vent geometries, and to evaluate phase distribution in conduits. To extend this approach several aspects of the numerical modeling deserve closer inspection including grid refinement, lack of an imposed symmetry axis or fully three-dimensional simulations, use of a turbulence model, and exploration of partial slip boundaries for conduit flow.

The majority of previous conduit models have used smaller particles as part of the complete atomization assumption (Papale, 2001). That is, magmatic foam is assumed to be completely destroyed in the fragmentation process. The grain size distributions of many volcanic eruptions, however, have abundant pumice clasts much larger than the .0002 m limit (Bursik, 1998; Bachmann *et al.*, 2000). Papale (2001) demonstrated that this inefficient fragmentation could significantly alter conduit exit conditions by lowering velocities and pressures. The results of this parametric study show that inefficient fragmentation may also produce larger pumices that are significantly slowed through particle-particle interaction as well as having a larger aerodynamic response time (Eaton & Fessler, 1994; Burgisser & Bergantz, 2002). The viscous particle phase will slow both phases relative to an inviscid calculation. Future conduit modeling efforts may include modeling multiple size fractions of pumices in a multi-fluid effort similar to the work of Neri *et al.* (2002) for pyroclastic flows. This study suggests that the size fractions greater than a millimeter will produce at least a ~5% change in the vertical centerline velocity, and up to ~10% change in the average vertical velocity if particle collisions are considered. The lower velocities may then modify the eruptive behavior of the conduit system by altering velocities and pressure of the different phases through particle-particle and particle-gas interaction.

- Chapter 5 -

Suspended load and bed-load transport of particle-laden gravity currents: The role of particle-bed interaction

Table 5.1: Nomenclature

Preceding Superscripts:

$m=1,2,3$ (1 is gas phase and 2 and 3 are particle phases)

$p=2$ and 3 (particle phases)

Subscripts:

$i,j=1,2$ (indices for spatial direction)

${}^m c_i$	Instantaneous Velocity of m th phase [m/s]
${}^m C_i$	Fluctuating Velocity of m th phase [m/s]
$C_{1\mu}$	Constant in fluid turbulence model (.09)
$C_{1\epsilon}$	Constant in fluid turbulence model (1.44)
$C_{2\epsilon}$	Constant in fluid turbulence model (1.92)
$C_{3\epsilon}$	Constant in fluid turbulence model (1.22)
C_D^s	Drag coefficient
${}^m c_p$	Heat capacity [J/kg K]
${}^p d$	Particle diameter [m] (1.0×10^{-4} m and .01 m)
e	Restitution Coefficient (.65)
${}^m e_{ij}$	Strain Rate [s^{-1}]
F_c	Coefficient of Friction (.62)
g_i	Gravitational acceleration [m/s^2] (9.81 m/s^2)
g_0	Radial distribution function
H_{gp}	Interphase heat transfer [W/m^3]
H_1	Hindrance coefficient in particle-particle drag (0.3)
${}^m I_i$	Interphase momentum transfer [$kg/m^3 s$]
${}^p I_{2D}$	Second Invariant of rate of strain tensor [s^{-2}]
${}^l k$	Fluctuating kinetic energy of the gas phase [m^2/s^2]
${}^m P$	Pressure [Pa]
${}^m q$	Thermal heat flux [$J/m^2 s$]
R_{km}	Ratio thermal conductivities

Table 5.1 (Continued)

${}^m T$	Thermal temperature [K]
${}^m U_i$	Average velocity [m/s]
${}^m \alpha$	Volume fraction of m th phase
${}^m \varepsilon$	Dissipation rate of fluctuating kinetic energy [m^2/s^3]
${}^p \kappa$	Granular conductivity [$J s / m^3$]
${}^p \theta$	Granular temperature [m^2/s^2]
${}^m \mu$	Dynamic viscosity [Pa s]
${}^m \lambda$	Bulk viscosity [Pa s]
${}^p \varphi$	Angle of Internal Friction (32°)
Π	Turbulence exchange terms
${}^m \rho$	Density of m th phase [kg/m^3]
σ_k	gas turbulence constant (1.0)
σ_ε	gas turbulence constant (1.3)
${}^m \tau_{ij}$	stress tensor [Pa]

5.1 INTRODUCTION

Particle-laden gravity currents are generated in a number of natural settings including volcanic eruptions, avalanches, and turbidity currents. Industrial accidents and explosions also have the potential of generating small-scale particulate flows. Hence, understanding the dynamics of these flows is essential in mitigating a wide range of environmental hazards. These flows are mixtures of particles with a carrier fluid (water or gas), and the mixture has a greater density than the surrounding, particle-less, ambient fluid. Consequently, these flows spread horizontally from their source, close to the ground. However, the interstitial fluid in many particle-laden gravity currents is less dense than the ambient fluid (i.e. interstitial hot gas in pyroclastic flows or fresh water in hyperpycnal turbidity currents). Hence, portions of the flow that become sufficiently dilute in the particle phase will undergo a buoyancy reversal. A substantial amount of research has been conducted on gravity currents (Middleton, 1966; Benjamin, 1968; Britter & Simpson, 1978; Bonnecaze *et al.*, 1993; Hartel *et al.*, 2000; Necker *et al.*, 2002) although much of it has focused on

homogenous fluids of two densities to create the current. The Lagrangian, or local physics of particulate multiphase flows cannot be resolved by this approach. For example, the heterogeneous concentration of particles during an ongoing flow, the phase relative motion, and dilution from particle deposition, are added complications that lead to emergent time and length scales in particle-laden flows.

An important class of particle-laden gravity currents are those that traverse a much denser *fluid*. Examples include pyroclastic flows from volcanic eruptions and avalanches (granular and powder-snow) that encounter lakes or oceans. A number of volcanic events near large bodies of water have resulted in numerous eruptions producing over-water pyroclastic flows (Fisher, 1993; Carey, 1996; Allen & Cas, 2001; Branney & Kokelaar, 2002). Real-time accounts of a few of these eruptions (Carey, 1996) and deposits of others (Allen & Cas, 2001) indicate that a substantial amount of material can be transported great distances over-water. For instance, flows from Krakatau were reported 60 km from the source, and flows from the Kos, Greece eruption produced deposits > 40 km from their source (Carey, 1996; Allen & Cas, 2001). Understanding the frequency and dynamics of these events is hampered due to the fact that deposits from these eruptions are often submerged, and observations are sparse.

Analogue experiments (Freundt, 2003) have elucidated some features of over-water particulate gravity currents, including the bifurcation of some flows into below-water turbidity currents and more dilute over-water flows. However, there are a number of scaling issues that hinder the application of these experiments to natural events. For example, it is difficult to produce high Reynolds number experimental flows. The particle response time due to fluid forcing observed in natural flows (i.e. Stokes number) is also rarely matched in experimental flows (Burgisser *et al.*, 2005). In addition, detailed optical measurements of real-time particle concentration in analogue experiments are limited to dilute flows (less than ~3 volume percent (Parsons, 1998)).

The controls on the partitioning of particle mass into the dilute upper regions of a flow versus dense basal regions are poorly known in particle-laden gravity currents. The relative importance of bed-load (where particles make multiple contacts with the bottom boundary) and suspended-load (where particles are suspended primarily due to turbulence) is difficult to distinguish from deposits generated by flows that have traversed opaque boundaries (over-land). However, most (if not all) of the bed-load of flows that traverse a 'leaky' (over-water) boundary will be removed. Hence this natural filter enables the study of suspended load transport in relative isolation and should allow for estimates of the relative proportion of over-land pyroclastic flows that are being transported by suspension due to grain collisions and turbulence.

Due to the experimental scaling difficulty, we have adopted a multiphase numerical approach to elucidate the spatial and temporal heterogeneity that develops in particle-laden gravity currents. In this Eulerian-Eulerian approach, multiple particle species are treated as distinct, but interpenetrating, continua and grading and segregation of particle size and volume fraction are calculated (Gera *et al.*, 2004). One novel aspect of this work is the development of a 'leaky' boundary condition utilizing a reconstruction of the local particle velocity probability distribution in order to study flows without bed-load. For comparison a 'saltation' boundary condition is developed in which particles interact frictionally and collisionally with the basal substrate. Using these contrasting boundary conditions we evaluate the mass and energy transport of particle-laden gravity currents. In particular we examine the relative importance of bed-load on mass flux and run-out of particle-laden flows.

This paper is organized as follows: In section 2 a multiphase continuum model is developed for a bimodal particle size population. Section 3 derives leaky and saltation boundary conditions using the mean and fluctuating components of the particle velocity field. Section 4 describes the simulation conditions and develops the

scaling analysis employed. Section 5 describes the results of the numerical simulations. These results reveal the consequences of phase relative motion for both saltation and leaky boundaries and resulting instabilities. The relative importance of a basally concentrated zone on flow transport is emphasized. Finally in Section 6 we discuss the dynamics and structure of particle-laden gravity currents in the context of this numerical experiment, and compare the results to previous approximations employed to study their transport.

5.2 CONTINUUM MULTIPHASE MODEL

Continuum multiphase models, initially developed in the fields of chemical and nuclear engineering (Harlow & Amsden, 1975; Drew, 1983; Syamlal, 1987; Agrawal *et al.*, 2001) have shown promise in their ability to predict the meso-scale clustering of particles in turbulent suspensions, and similar approaches have been applied to volcanic eruptions (Neri & Dobran, 1994; Darteville *et al.*, 2004; Dufek & Bergantz, 2005). In the multifluid approach each particle phase and the carrier fluid phase has separate conservation equations for momentum, mass, and energy along with closure assumptions for heat and momentum transfer within and between phases (summarized in *Table 5.2* and in the appendix). Both the mean and fluctuating velocities are calculated for the granular and fluid phases. For the simulations in this study we have adapted the MFX multiphase code for use on saltating and leaky boundary condition flows (O'Brien & Syamlal, 1991).

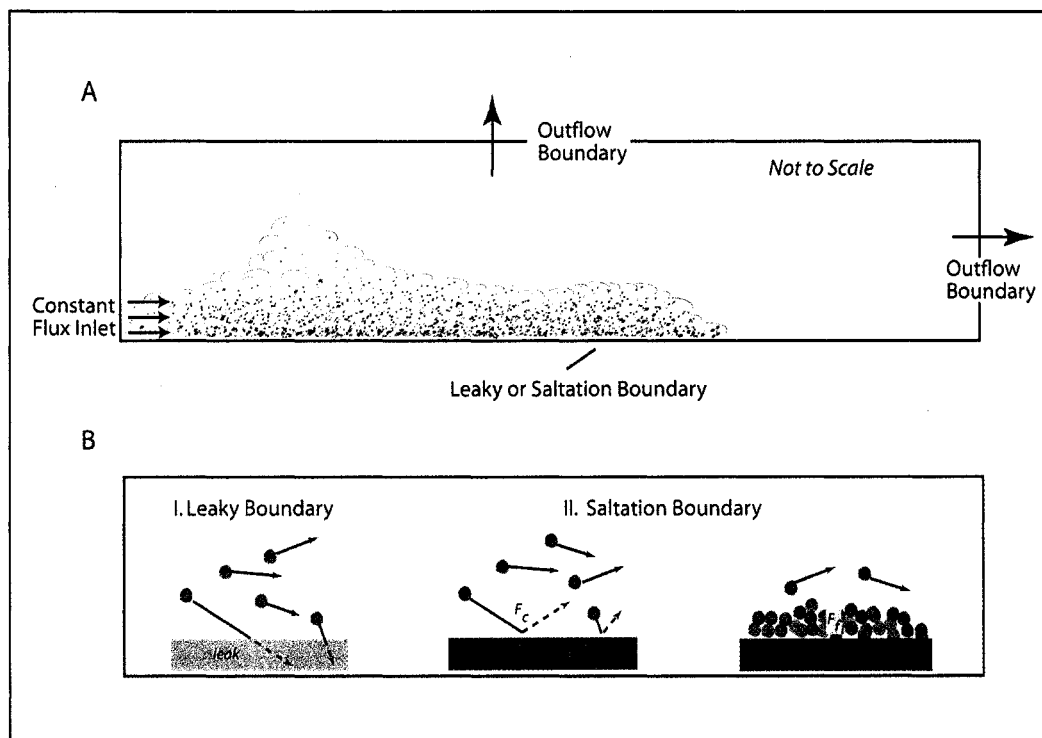


Figure 5.1: Schematic representation of A) simulation conditions and B) boundary conditions. A) The particle-laden gravity currents are introduced at constant flux from the left boundary and propagate to the right. Top and right side are outflow boundaries, and the basal boundary reflects either a leaky condition or a saltating condition. B) For leaky boundaries, the leak flux is calculated at every time-step based on a reconstruction of the local particle velocity probability distribution. Particles interact with the saltating boundaries through inelastic collisions and frictionally.

For collisional transfer of momentum, the constitutive relation for the particle phase is provided by kinetic theory similar to that used in the estimation of gas viscosities from molecular collisions (Lun *et al.*, 1984; Dufek & Bergantz, 2005). This constitutive relation assumes binary, inelastic particle collisions. The collision rate and stress in the granular material depends on the fluctuating particle velocity. A separate transport equation for pseudo-thermal energy is solved in order to determine the granular temperature (covariance of the fluctuating velocity) and close the granular stress in dilute conditions. Pseudo-thermal energy is assumed to be advected by the mean flow and diffuses along gradients in the granular temperature. Locally

pseudo-thermal energy is produced by shear and by the relative velocity between the particle and gas phases (Agrawal *et al.*, 2001) and is dissipated by inelastic collisions and by viscous damping by the carrier fluid. The production of fluctuating motions by gas-particle slip and dissipation by viscous forces ensures that the granular pseudo-thermal energy equation is coupled to the carrier fluid.

At higher particle volume fractions, protracted frictional interaction of particles occurs and the frictional and collisional stresses are assumed to be additive (Syamlal, 1987; Savage, 1998). The frictional stress is developed using the postulate of a yield function and an associated flow-rule to relate stress and strain rate, and has been adopted from theories of soil mechanics. The solids pressure in the frictional regime allows the solid phases to have some compressibility, but provides a resisting force to prevent unphysical void fractions.

Table 5.2: Multifluid Equations

Preceding superscripts:

$m=1,2,3$ (1 is gas phase and 2 and 3 are particle phases)

$s,p=2$ and 3 (particle phases)

Subscripts:

$i,j=1,2$ (indices for spatial direction)

Mean Field Equations

$${}^m c_i = \langle {}^m c_i \rangle + {}^m C_i = {}^m U_i + {}^m C_i \quad (5.1)$$

$$\sum {}^m \alpha = 1, \quad (5.2)$$

Continuity

$$\frac{\partial}{\partial t} ({}^m \alpha {}^m \rho) + \frac{\partial}{\partial x_i} ({}^m \alpha {}^m \rho {}^m U_i) = 0, \quad (5.3)$$

Momentum

$$\frac{\partial}{\partial t} ({}^m \alpha {}^m \rho {}^m U_i) + \frac{\partial}{\partial x_j} ({}^m \alpha {}^m \rho {}^m U_i {}^m U_j) = -\frac{\partial {}^m P}{\partial x_i} \delta_{ij} + \frac{\partial {}^m \tau_{ij}}{\partial x_j} + {}^m I_i + {}^m \alpha {}^m \rho g_i, \quad (5.4)$$

Thermal Energy

$${}^m \alpha {}^m \rho {}^m c_p \left(\frac{\partial {}^m T}{\partial t} + {}^m U_j \frac{\partial {}^m T}{\partial x_j} \right) = -\frac{\partial {}^m q}{\partial x_i} + H_{sp}, \quad (5.5)$$

Table 5.2 (Continued)

Fluctuating Field Equations**Turbulent kinetic energy, fluid phase**

$${}^1k = \frac{1}{2} \langle {}^1C_i {}^1C_i \rangle, \quad (5.6)$$

Turbulent kinetic energy equation, fluid phase

$${}^1\alpha^1\rho \left(\frac{\partial {}^1k}{\partial t} + {}^1U_j \frac{\partial {}^1k}{\partial x_j} \right) = \frac{\partial}{\partial x_i} \left({}^1\alpha \frac{{}^1\mu'}{\sigma_k} \frac{\partial {}^1k}{\partial x_i} \right) + {}^1\alpha^1\tau_{ij} \frac{\partial {}^1U_i}{\partial x_j} + \Pi_{k1} - {}^1\alpha^1\rho^1\varepsilon, \quad (5.7)$$

Dissipation rate of kinetic energy, fluid phase

$${}^1\alpha^1\rho \left(\frac{\partial {}^1\varepsilon}{\partial t} + {}^1U_j \frac{\partial {}^1\varepsilon}{\partial x_j} \right) = \frac{\partial}{\partial x_i} \left({}^1\alpha \frac{{}^1\mu'}{\sigma_\varepsilon} \frac{\partial {}^1\varepsilon}{\partial x_i} \right) + {}^1\alpha \frac{{}^1\varepsilon}{{}^1k} \left(C_{1\varepsilon} {}^1\tau_{ij} \frac{\partial {}^1U_i}{\partial x_j} - {}^1\rho C_{2\varepsilon} {}^1\varepsilon \right) + \Pi_{\varepsilon 1}, \quad (5.8)$$

Pseudo-thermal equation, particle phases

$${}^p\alpha^p\rho \left(\frac{\partial {}^p\theta}{\partial t} + {}^pU_j \frac{\partial {}^p\theta}{\partial x_j} \right) = \frac{\partial}{\partial x_i} \left({}^p\alpha^p\rho^p\kappa \frac{\partial {}^p\theta}{\partial x_i} \right) + {}^p\alpha^p\rho^p\tau_{ij} \frac{\partial {}^pU_i}{\partial x_j} + \Pi_{k2} - {}^p\alpha^p\rho^p\varepsilon. \quad (5.9)$$

In the limit of volume fractions approaching the minimum void fraction both the frictional pressure and granular shear viscosity approach infinity that prevents further circulation of material.

A modified k - ε turbulence model is used to predict Reynolds stresses produced by fluctuating fluid motion. This approach accounts for production and dissipation of turbulent energy due to the presence of a dispersed phase (Peirano & Leckner, 1998). Hence the random, or fluctuating motion of the continuous phase and the dispersed phase are two-way coupled. In this 'two-equation' turbulence model separate transport equations are formed for the turbulent (fluctuating) kinetic energy of the continuous phase and for the dissipation rate of kinetic energy. The standard turbulent kinetic energy equation (Eq. 6) and dissipation rate equation (Eq. 5.7) are modified by source terms to account for production and dissipation of turbulent

energy as a result of particle loading (Peirano & Leckner, 1998). Wall functions and modifications for the near boundary production and dissipation were implemented for the near wall laminar boundary layer. References (Cao & Ahmadi, 1995; Peirano & Leckner, 1998; Benyahia *et al.*, 2005) provide a thorough review of the two-way coupled approach to fluctuating granular and turbulent motion, and the reader is referred to these references for a detailed discussion of this approach. This approach and model constants were validated by Benyahia *et al.* (Benyahia *et al.*, 2005) through comparison with experiments of particle-laden flows (Jones, 2001).

The thermal energy of the flow is described by a transport equation (Eq. 5.4) that includes the effect of advection, conduction and interphase transfer of enthalpy. In order to simplify this analysis viscous dissipation and radiative transfer of heat were not considered (Syamlal *et al.*, 1993). We also assume that heat transfer between different solid phases is negligible. The fluid-solid heat transfer coefficient is a function of the local Nusselt number that reflects the ratio of convective heat transfer to conductive heat transfer. The Nusselt number depends on the local particle volume fraction, Reynolds number and Prandtl number as reflected in the empirical correlation (C57)(Gunn, 1978).

A binary mixture of two different particle sizes was used in the simulations in order to access size sorting in the simplest possible multi-particle system. Drag between particle phases is based on kinetic theory (Syamlal, 1987) but modified by a hindrance term proposed by Gera *et al.* to account for protracted contact between particle phases as close packing is approached (preventing phase relative circulation at close-packing) (Gera *et al.*, 2004). Likewise the radial distribution function must be modified according to the proportion and sizes of the different particle phases (Fedors & Landel, 1979).

5.3 BOUNDARY CONDITIONS FOR LEAKY AND SALTATION BOUNDARIES

In multiphase flows, separate boundary conditions must be specified for the continuous and particle phases. At a rigid, stationary boundary a common approach is to invoke a no-slip boundary for the continuous or gas phase, while the particle phases are modeled as a saltation or partial-slip boundary (Johnson & Jackson, 1987). The shear associated with the particle-wall interactions is a product of the collisional frequency, the tangential momentum transfer per collision, and the concentration of particles near the wall (*Equation 5.9*).

$$F_c = \frac{\overbrace{(3\theta)^{1/2}}^{\text{collisional frequency}}}{s} \times \frac{\overbrace{\phi\pi\rho_p d^3 (U_p - U_w)}^{\text{tangential momentum transfer/collision}}}{6} \times \frac{\overbrace{1}^{\text{number of particles}}}{a_c} \quad (5.9)$$

Where ϕ is the specularity (the fraction of tangential momentum transferred, which depends on the surface roughness), θ is the granular temperature, s is the average distance between the wall and particle, and a_c is the boundary area/particle. In the simulations presented here the specularity coefficient was held constant at 0.02 for consistency (Benyahia *et al.*, 2005), although under natural conditions the specularity coefficient is likely to vary significantly over different surface conditions. Averaged over many particles to form the continua this relation becomes:

$$F_c = \frac{{}^p\alpha g_0 (3\theta)^{1/2} \phi \pi ({}^p\rho) (U_p - U_w)}{6 {}^p\alpha^0} \quad (5.10)$$

Where g_0 is the radial distribution function (A26), and ${}^p\alpha^0$ is the solid volume fraction at close packing. This collisional force is converted into a condition for the particle phase velocity gradient and permits non-zero velocities at the boundary. The fluctuating kinetic energy of the granular phase is also dissipated at the boundary due to inelastic collisions as specified in the granular conductivity equation (A28) (Johnson & Jackson, 1987).

5.3.2 Derivation of a Leaky Boundary Condition from the Velocity Probability Distribution

For the dynamics of a particle-laden gravity current interacting with a leaky boundary, we consider the end-member scenario in which all particles that reach the boundary are removed from the flow. In this way, only transport of the suspended load of the flow is considered. This is similar to considering the particles as being perfectly 'sticky' (i.e. no possibility of saltation at the boundary).

Sedimentation from the flow requires consideration of both the mean and fluctuating component of a particle species' velocity field. The non-zero variance (i.e. granular temperature) of the velocity for a collection of particles can result in a finite sedimentation rate in regions of the flow where the mean vertical particle velocity component is zero or even positive.

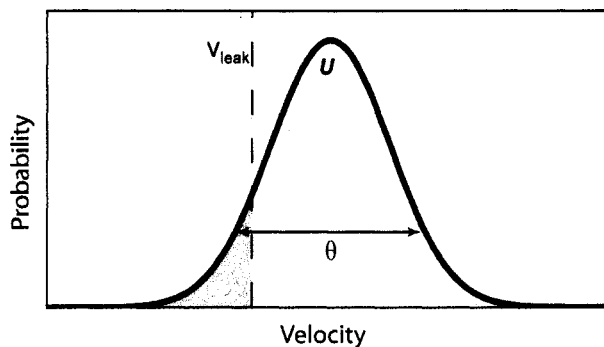


Figure 5.2: Example of reconstructed velocity probability distribution. Both the mean velocity and granular temperature are shown. All velocities below the leak velocity are capable of removing a particle from the flow, and integration of the shading region gives the flux of particles from the system over the given time-step.

As demonstrated in equation (5.8) the granular temperature, and hence the particle velocity probability distribution, is influenced by collisions with other particles and drag with the fluid. Local variation in the sedimentation rate is dependent upon this

velocity distribution and the concentration of particles near the boundary. To examine this effect we can define the leak velocity (v_{leak}) as the velocity sufficient to remove a particle from a given height in the flow during a time interval:

$$v_{leak} = \frac{\bar{l}}{\Delta t}, \quad (5.11)$$

where \bar{l} is the average distance to the boundary in a control volume and Δt is a time interval. In *Figure 5.2* an example leak velocity is plotted along with an example velocity probability distribution. All velocities less than the leak velocity are sufficient to cause sedimentation through the leaky boundary (shaded area in *Figure 5.2*). Integration of the probability distribution from negative infinity to the leak velocity and multiplying this by volume fraction of particles gives the local finite flux of particles from the flow. Again assuming that the particle distribution is Maxwellian this gives the expression:

$$\gamma = \frac{\rho \alpha}{2} \left[1 + \operatorname{erf} \left(\frac{v_{leak} - \bar{v}}{\sqrt{2\theta}} \right) \right], \quad (5.12)$$

Where γ is the volume fraction loss rate over the computational time-step.

5.4 PARTICLE LADEN GRAVITY CURRENT CONDITIONS

5.4.1 Gravity Current and Particle-Fluid Scaling

In order to facilitate comparisons between simulations, the length and timescales were non-dimensionalized. The front condition for many experimental gravity currents reflects a balance between the inertia and potential energy of the flow, and provided that the flow is well mixed, particle-driven gravity currents should also have approximately constant Froude number fronts (Dade & Huppert, 1995; Dade, 2003). Densimetric Froude numbers of approximately 1 to 1.4 have been measured in experiments (Britter & Simpson, 1978; Parsons & Garcia, 1998) where the densimetric Froude number is defined as:

$$Fr_d = \frac{u}{\sqrt{g' H}}, \quad (5.13)$$

where g' is the reduced gravity ($g' = \frac{\rho_{mix} - \rho_{amb}}{\rho_{amb}} g$), u is the velocity and H is the current height. A Froude number of unity will be used for reference in these simulations. Height will be non-dimensionalized using the Froude scaling such that

$$H' = H / H^*, \quad (5.14)$$

where:

$$H^* = u_{inlet}^2 / \langle g' \rangle, \quad (5.15)$$

and u_{inlet} is the initial velocity and $\langle g' \rangle$ is the vertically averaged reduced density. H^* is the height of gravity current with a densimetric Froude number of 1. We define H as the height at which the mixture density (particle+gas) equals the ambient density at 300 K ($\sim 1.29 \text{ kg/m}^3$).

The horizontal length and time scale non-dimensionalization is based on a reference sedimentation rate. If a particle-fluid suspension is well-mixed, and particle-particle interactions are negligible, particle volume fraction in the flow is expected to follow an exponential relation as a result of loss of sedimentation (Hazen, 1904; Martin & Nokes, 1988) with the decay constant reflecting the height of the flow and the settling velocity:

$$\frac{{}^p\alpha}{{}^p\alpha^0} \propto e^{-(w_s/H')t}. \quad (5.16)$$

Where α_p is the particle volume fraction, ${}^p\alpha^0$ is the initial particle volume fraction, w_s is the particle settling velocity, and H' is the scale height of the flow. We define a decay half-life of the flow to be the time at which the concentration in the flow decays to half the initial concentration. We also define $L_{.5}$ as the product of the inlet

velocity and the particle half-life and use this as our reference horizontal length scale so that our dimensionless time and horizontal length scales are:

$$t_5 = \frac{-H * \ln(.5)}{w_s}, \quad (5.17)$$

$$t' = t/t_5, \quad (5.18)$$

and

$$L' = L/L_5. \quad (5.19)$$

The interplay between non-steady acceleration of turbulence and the steady acceleration of gravity will evolve in particle volume fraction, mixture density, sorting, and velocity as a function of space and time. To describe momentum transfer in these flows, and emergent instabilities, we will employ the gradient Richardson number (Ri), the Stokes number (St), and stability factor (Σ_T). The gradient Richardson number is given by:

$$Ri = \frac{-g \frac{\partial \rho_{mix}}{\partial z}}{\left(\frac{\partial u}{\partial z}\right)^2}. \quad (5.20)$$

Flows with gradient Richardson numbers greater than .25 typically are stable (the density gradient is sufficiently great that the shear cannot overcome the stratification), whereas small or negative gradient Richardson numbers have unstable density gradients that promote the development of Kelvin-Helmholtz instabilities, and entrainment of the surrounding ambient fluid. The Stokes number indicates the particle response time-scale relative to the time with which the particle interacts with the flow (Crowe *et al.*, 1985; Raju & Meiburg, 1995):

$$St = \frac{\tau_p}{\tau_f}. \quad (5.21)$$

The fluid timescale is defined by the scale height of the flow divided by its mean velocity:

$$\tau_f = \frac{H}{\langle u \rangle}. \quad (5.22)$$

Although transient eddies are produced on different scales throughout the flow, this scaling is indicative of the characteristic timescale of a particle interacting with the largest eddies in the flow. The aerodynamic response time of a single particle (Wilson, 1976) is given:

$$\tau_p = \frac{4d_p \rho_s}{3\rho_g C_D |u_g - u_s|}, \quad (5.23)$$

where C_D is the drag coefficient . The large-eddy Stokes number for each particle size and for each flow condition is given in *Table 5.3*.

Table 5.3: Particle Scaling

Name	$\langle u^* \rangle^{\S}$	St_1^{\dagger}	St_2	Pn_1^{\ddagger}	Pn_2	Σ_{T1}	Σ_{T2}
1L	1.9	0.0014	7.4	.78	49.60	3.7e-4	1.9
2L	2.8	0.0014	7.4	.53	33.66	3.7e-4	1.9
3L	3.3	0.00065	4.3	.45	28.56	8.9e-5	.58
4L	3.6	0.00065	4.3	.42	26.18	8.9e-5	.58
1S	2.3	0.0014	7.4	.65	40.97	3.7e-4	1.9
2S	3.2	0.0014	7.4	.47	29.45	3.7e-4	1.9
3S	5.4	0.00065	4.3	.28	17.45	8.9e-5	.58
4S	5.6	0.00065	4.3	.27	16.83	8.9e-5	.58

\S Shear velocity

\dagger Particle Stokes Number

\ddagger Particle Rouse Number

The interplay of steady forcing (gravity) and unsteady forcing (turbulent drag and particle-particle interaction) will impact the segregation or dispersal of particles.

The Stokes number is a measure of the unsteady forcing due to particle-fluid drag, and the Froude number scales with the gravitational forcing. The ratio $\frac{St}{Fr^2}$, or stability factor (Σ_T), is a measure of the relative importance of these forcings on the particle phase (Raju & Meiburg, 1995; Burgisser & Bergantz, 2002). As emphasized by Raju and Meiburg (Raju & Meiburg, 1995) steady forcing such as gravity cannot inherently create phase-relative segregation, and particles with large stability factor are more evenly distributed when interacting with vortical structures compared to small stability factor particles. As the smaller stability factor particles couple with vortical structures they are also more readily suspended and sediment at a lower rate (Raju & Meiburg, 1995).

5.4.2 Initial and Boundary Conditions

The simulation conditions are depicted in *Figure 5.1*. A constant flux of particles and gas were introduced in these two-dimensional simulations and was varied to reflect different particle volume fractions and velocities (*Table 5.4*). In all simulations the gas and particles were introduced at 700 K into an atmosphere of 300 K. Gas density was determined using the perfect gas relation assuming a dry atmosphere. Hence the interstitial gas of these flows has a lower density than the ambient air; although the initial particle and gas mixture is denser than surrounding atmosphere. The top and side boundaries are outflow boundaries and the bottom boundary was either a saltation boundary (S) or a leaky boundary (L). Vertical grid spacing is refined at the base of the flow and increases with height (.0125 - .075 H' or 1 - 6 m) and horizontal resolution is ~ .001 L' (6 m). The physical domain of these two-dimensional simulations 573 m x 15 km. Initial solid volume fractions were either .025 or .1 in these simulations. Two grain sizes were used to assess sorting of different grain sizes and densities: 95 % of the flow was comprised of ash with diameter of 1.125×10^{-4} m and density of 2000 kg/m³ and 5% of the flow was comprised of denser particles (lithics) with a diameter of .01 m and density of 2700

kg/m³. The smaller particle size corresponds to stability factors of much less than 1 ($\Sigma_T \ll 1$, $St \ll 1$) whereas the larger and denser particles had stability factors of ~ 1 ($\Sigma_T \sim 1$, $St \geq 1$) (Table 5.3).

Table 5.4: Simulation Conditions

Name	B.C. [§]	α_s [†]	Velocity (m/s)	VF [*]	H*	Fr _d [‡]	Fr ¹
1L	L	.025	50	12.5	66.5	.62	1.95
2L	L	.10	50	50	66.5	.31	1.95
3L	L	.025	100	25	137.9	1.23	2.71
4L	L	.10	100	100	137.9	.62	2.71
1S	S	.025	50	12.5	66.5	.62	1.95
2S	S	.10	50	50	66.5	.31	1.95
3S	S	.025	100	25	137.9	1.23	2.71
4S	S	.10	100	100	137.9	.62	2.72

§ Boundary conditions: L - leaky boundary, S - saltation boundary.

† Solid volume fraction

* Solids volume flux (m³/s)

‡ Densimetric Froude number

5.5 STRUCTURE OF PARTICLE-LADEN FLOWS

Although the size and details of the flow structure are different for every simulation, several generic flow structures are common to all the simulations. The particle-laden gravity currents that traverse leaky boundaries are more dilute on average than the saltation boundary flows. Run-out distance (the furthest extent of the flow) in the leaky boundary flows is marked by the point at which enough particles have been lost that a buoyancy reversal occurs and the flows become lighter than the ambient fluid. In contrast, flows that traverse saltation boundaries develop a bed-load region enriched in particles. Bed-load particles eventually deposit as energy is lost due to inelastic collisions and the shear is insufficient to overcome Coulomb friction. The particle residence time in the saltating flows is greater than in the leaky boundary situation and they produce longer run-out flows. In the following sections

we will examine the heterogeneity that develops for the saltation and leaky boundaries and how sorting, energy content and mass flux are ultimately influenced by transport over the two substrates.

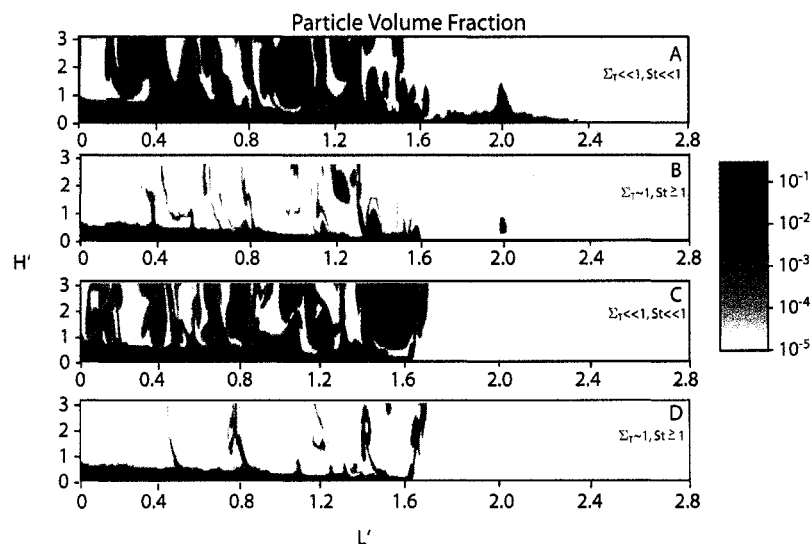


Figure 5.3: Particle volume fraction for the binary particle mixtures with saltating (A & B) and leaky (C & D) boundaries for flow condition 1 (Table 5.3). A and C show the small stability factor particles and B and D show the large stability factor particles. This figure represents the instantaneous particle volume fraction at $t'=4$. The leaky boundary flow has reached its maximum run-out and at $L' \sim 1.6$ where the flow becomes more buoyant than the ambient fluid. The saltating boundary condition flow continues to propagate to the right with a greater amount of large stability factor particles than the leaky boundary counterpart. Shear and buoyancy instabilities generate the eddies that rise above $H'=1$ in these flows.

5.5.1 Density Stratification

Gradients in particle volume fraction develop due to the interaction of gravitational acceleration and the turbulent suspension of different size particles, resulting in a more particle-enriched base as the particle-laden flows continue to propagate away from the inlet (Figure 5.3). The development of particle volume fraction gradients has important implications for entrainment, particle-particle

interaction in the more concentrated regions of the flow, the development of bed-load for the saltating boundaries and particle loss at the leaky boundaries.

Spatially averaged particle volume fractions and horizontal velocity are remarkably similar for both saltating and leaky boundaries in the upper regions of the flow ($>10\%$ of the scale height of the flow). In this region particle-bed interaction has little direct influence on the dynamics of the flow. In the upper regions of the flow particle settling results in portions of the flow becoming more buoyant than the ambient atmosphere as the interstitial fluid is less dense than the ambient fluid (*Figure 5.3*). Likewise shear instabilities (Kelvin-Helmholtz) are promoted as density gradients between the flow and the ambient atmosphere decrease resulting in smaller Richardson numbers (*Figure 5.4*). Both plumes and shear instabilities preferentially remove the fine-grain, small stability factor particles from the flows (*Figure 5.3*). The larger grain sizes ($\Sigma_T \sim 1$) that do rise above the scale height of the flow are typically confined to the core of the plumes where the vertical velocity is the greatest or are centrifuged to the edge of the Kelvin-Helmholtz eddies. However, the average volume fraction of particles above the neutral buoyancy height of the flow is less than 10^{-4} and the total volume fraction of particles above the scale height remains below 5% of the total flow.

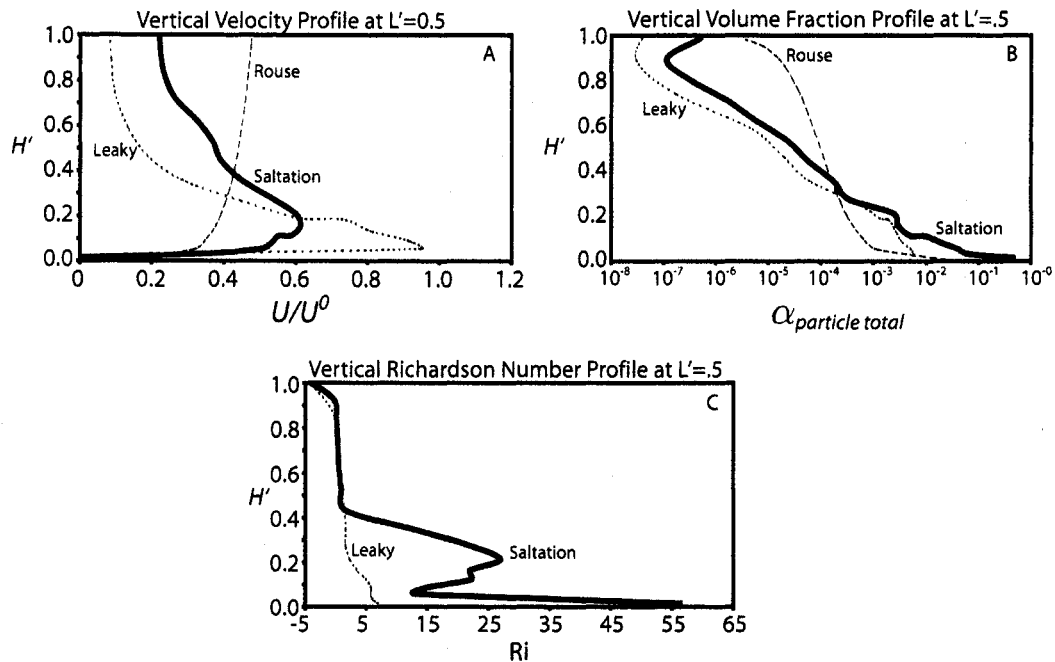


Figure 5.4: Vertical profiles of flow condition 1 at $L'=0.5$. A) The vertical velocity for leaky (small dashed line) is compared to the saltation (solid black line) and a Rousean profile (large dashed line). B) The vertical volume fraction profile of the saltation, leaky and Rousean profile is shown. The base of the saltation curve shows order of magnitude greater volume fraction in the region of bed-load transport.

5.5.2 Dynamics and Evolution of Bed-load

Although the flows are similar above $\sim 10\%$ the scale height of the flow, the boundary conditions provide the template for the transport capacity and energy of the bed-load region of the flow. As particles migrate to the base of the flow they are either sedimented through the leaky interface (simulations 1L-4L) or begin interacting through saltation (simulations 1S-4S). When considering the saltation boundary at $L'=1$, the temporally averaged bed-load comprises 40-50% of the total load of the flow, and the majority of the energy of the flow. However, the volume of particles in the bed-load increases with time as particles settle from the suspended load. For example after $t'=4$ greater than 80 % of the volume of particles is in the bed-load (Figure 5.5).

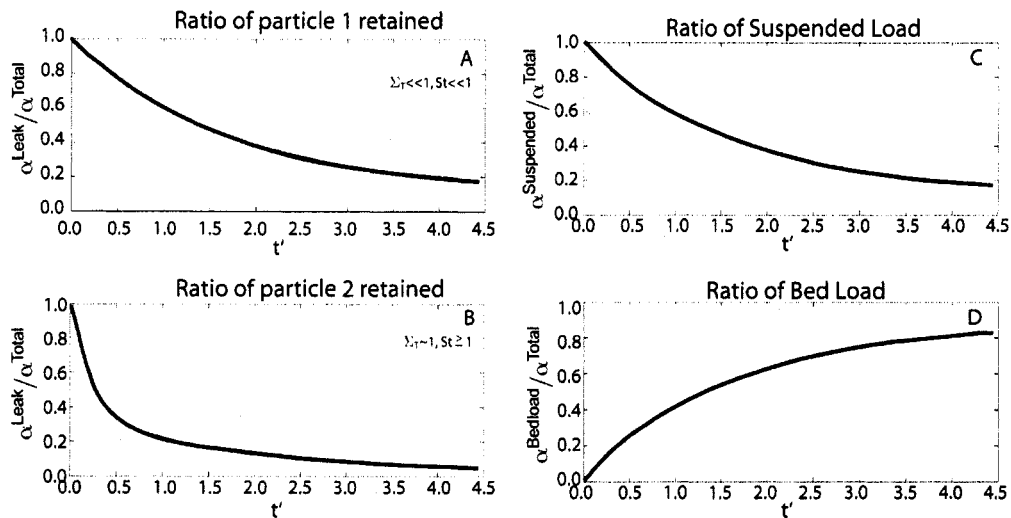


Figure 5.5: Rate of particle loss and rate of development of bed-load and suspended load for flow conditions 1. A) and B) give the rate of loss of particle 1 (small stability factor particles) and particle 2 (large stability factor particles), respectively. The rate of loss of the small stability factor particles is close to exponential (Table 5), whereas the rate of loss of the large stability factor particles shows a distinct inflection near $t' = .5$. C) and D) show the ratio of suspended and bed-load in the saltating boundary flows. Similar to the loss of small stability factor particles, the volume of material in the bed-load grows exponentially with time.

The rate at which particles enter the bed-load region of the flow is proportional to the settling velocity of the particles. The transfer rate of the small stability factor particles is close to exponential (Figure 5.5), and since these particles represent 95% of the original volume fraction of the particles, the growth of the bed-load layer is also exponential. However, the ($\Sigma_T \sim 1, St \geq 1$) particles have a distinct inflection in the rate at which they are transferred to the bed (Figure 5.5). Spatially, the $\Sigma_T \sim 1$ particles are transferred from the suspended load into the bed-load primarily from 0 - .5 L' regardless of the initial velocity of the gravity current. In contrast, the ($\Sigma_T \ll 1, St \ll 1$) particles are transferred to the bed over a much wider area and are more sensitive to the initial conditions of the flow (Figure 5.6). For instance, the small stability-factor (Table 5.3) particles remain in suspension more efficiently for the high Reynolds number flows and sediment over a greater distance.

As such a large fraction of the mass of the saltation flows are transported at the base of the flow with numerous particle-wall and particle-particle interactions, the multiphase flow differs markedly two-fluid homogeneous conservative gravity currents. The vertically average densimetric Froude number of the saltation boundary flows (including the front condition) is significantly lower than 1 and often below .5 (*Figure 5.7*). In contrast, the front of the leaky boundary flows varies between 1 and 1.4 similar to front conditions in well-mixed experimental particulate gravity currents (Britter & Simpson, 1978). Hence the suspended load portion of the simulated flows behave in a manner similar to other gravity currents. However, the saltation boundary flows in which particles at the base of the flow are not immediately sedimented behave as hybrid gravity currents and granular flows.

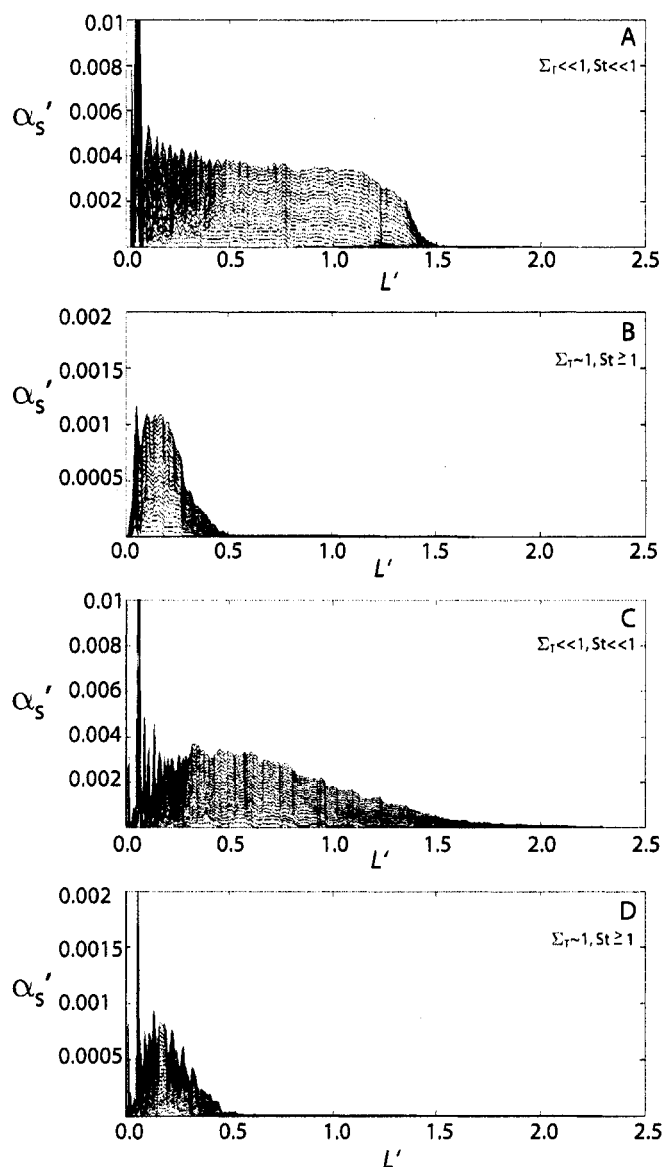


Figure 5.6: The progressive loss of particles for flow conditions 2 and 4. The individual lines represent the cumulative loss of material at different times (in $t' = .15$ intervals). A) and B) apply to flow conditions 2 and C) and D) refer to the more energetic flow conditions 4. Particle loss is normalized by the total volume of particles introduced in the flow. In panel A) the small stability factor particles leak through the basal boundary from 0-1.6 at which point the flow becomes more buoyant than its surroundings. Panel B) shows the particle loss of the large stability factor particles which are mostly confined to less than $L' = 0.5$. For the more energetic inlet conditions the small stability factor particles C) are distributed over a much wider area, but again the large stability factor particles D) are mostly confined to less than $L' = 0.5$.

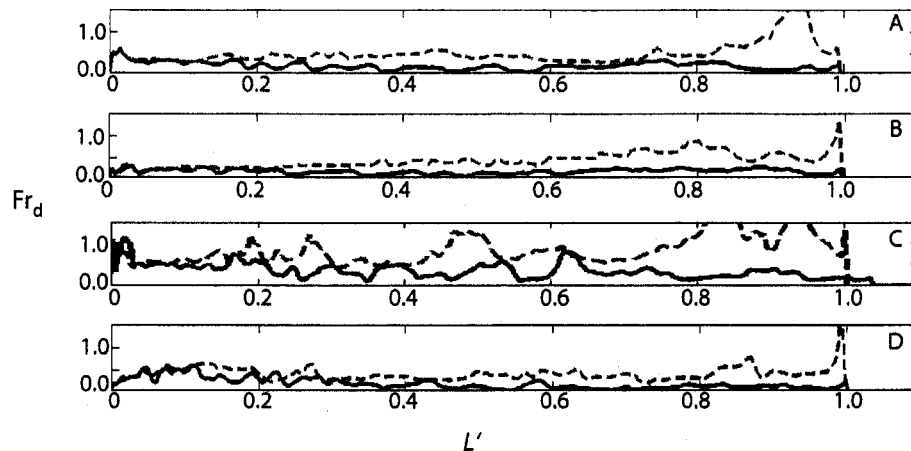


Figure 5.7: Vertically averaged denismetric Froude number when the flow front is at $L'=1$. Solid lines are the saltating boundary flows and the dashed lines represent leaky boundary flows. A)-D) correspond to flow conditions 1 – 4 (Table 5.3). The front of the leaky boundary flows are in the range 1 – 1.2 whereas the saltating boundary flows are less than 0.4 due to the development of bed-load.

5.5.3 Vertical and Lateral Particle Size Sorting in Transient Flows

The greater sedimentation rate of the $\Sigma_T \sim 1$ particles leads to a much greater proportion of the small stability-factor particles remaining in the flow for leaky boundary conditions. We compare sorting in these flows normalized to their initial proportions:

$$\gamma' = \frac{{}_2\alpha}{{}_1\alpha} \bigg/ \frac{{}_2\alpha^0}{{}_1\alpha^0}. \quad (24)$$

The sorting coefficient (γ') is greater than one if enriched in the larger grain size relative to the initial proportion and less than one if a greater amount of fine particles are present. In the negative log plots of Figure 5.8 and Figure 5.9, positive values correspond to an enrichment of fine material and negative values correspond to an enrichment of the coarse material. For leaky flow boundary conditions the sorting coefficient is almost always less than one, and on average the flow becomes progressively depleted in the large grain size with distance from the inlet. However,

there is significant structure to the sorting of particles at any single instant in time (*Figure 5.8*). The head of the current typically has regions where the sorting coefficient approaches (but rarely exceeds) unity for the leaky boundary flows.

In contrast, the bed-load region of the flow that develops in the saltation simulations has a sorting coefficient much greater than unity initially, becoming progressively more mixed with time due to the accumulation of small stability-factor particles. The front of these flows are also enriched in the large stability-factor component and is one of the few locations that has sorting coefficients greater than unity (*Figure 5.9*). This effect can be explained by the relative phase velocities of the two particle species. Strong vortices develop near the front of the flow exert drag on the particles. This non-steady forcing influences the small stability factor particles to a greater degree than the larger stability factor particles, and hence the larger grain sizes have a tendency to accumulate at the front of the granular flows. (Which may also explain why turbidites almost always have a clean and coarse Bouma A section.) Likewise, the elutriation rate of fine particles in buoyant plumes is much greater than the large particles and so dilution near the top of the current head will preferentially remove the fine component.

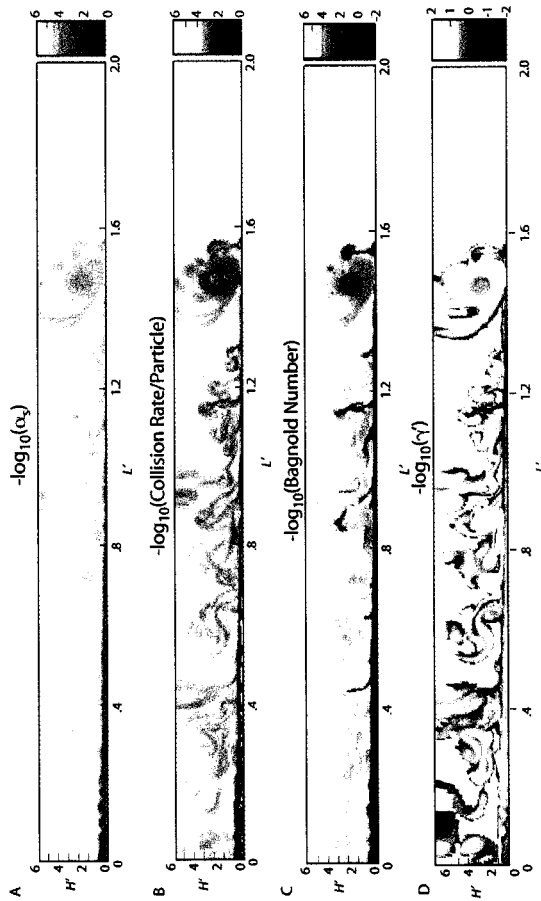


Figure 5.8: Flow traversing leaky boundary (flow conditions 1) and $t^* = 3$. A) The $-\log_{10}$ of the particle volume fraction, B) $-\log_{10}$ of the collision rate/particle, C) $-\log_{10}$ of the Bagnold number, D) $-\log_{10}$ of the sorting coefficient (positive values indicate enrichment of fine particles, negative values indicate enrichment of coarse material relative to the inlet values. Except near the inlet, the sorting coefficient remains positive (fine enriched) although portion of the head of the flow have near 0 values.

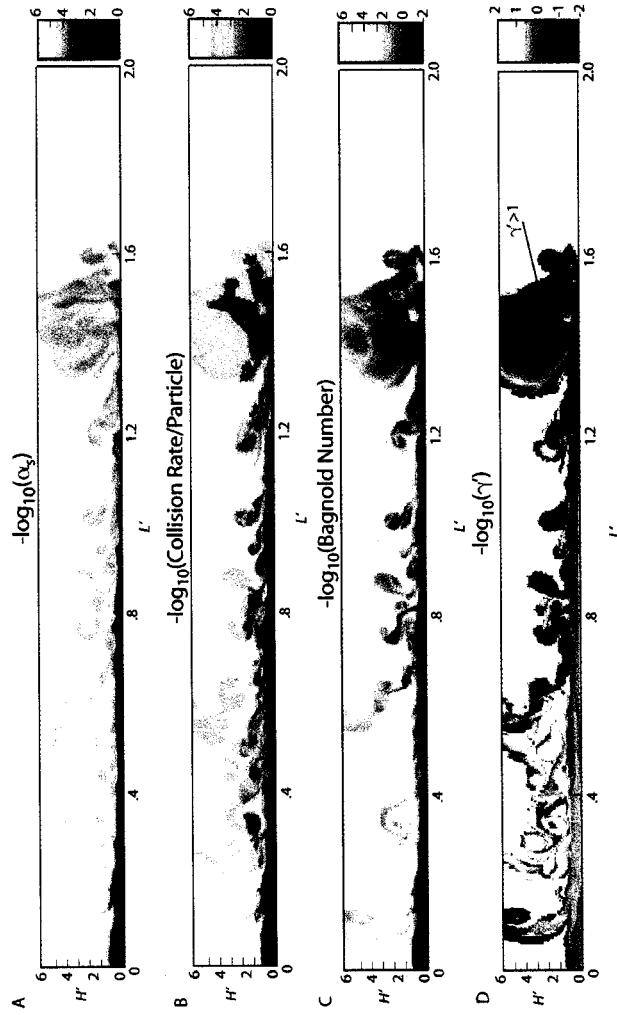


Figure 5.9: Flow traversing saltating boundary (flow conditions 1) and $t^* = 3$. A) The $-\log_{10}$ of the particle volume fraction, B) $-\log_{10}$ of the collision rate/particle, C) $-\log_{10}$ of the Bagnold number, D) $-\log_{10}$ of the sorting coefficient (positive values indicate enrichment of fine particles, negative values indicate enrichment of coarse material relative to the inlet values. Figure 9 shows that for the same inlet flow conditions the volume fraction and collision rate are much greater at the base of the saltating flows compared to the leaky boundary flows (Figure 5.8). The saltating flows are also more efficient at transporting the large stability factor particles (D) and near the front of the flow there are even regions where there is an enrichment of coarse material relative to inlet conditions (outlined in black).

In the leaky flows the elutriation rate is outpaced by sedimentation through the basal boundary (*Figure 5.6*). However for saltation boundary conditions the energetic front of the flow has sufficient shear such that little of the material is deposited. Hence the only major particle sink from the current head is elutriation that preferentially removes fine particles.

The vertically and temporally averaged sorting coefficient $\langle \gamma' \rangle$ at $L' = 1$ for the different flows is shown in *Figure 10* as a function of the densimetric Froude number. In general the sorting coefficient is higher for the saltation boundaries relative to leaky boundary flows. The fundamental differences in the sorting behavior between flows that have leaky or saltation boundaries is due to the longer residence time of particles in the saltation flows. In saltating flows, particles will have multiple encounters with the base and can be remobilized due to shear and particle collisions after encountering the base of the flows. This is modeled as a partial slip velocity (*Figure 5.4*). As larger particles can remain mobilized in the flow due to saltation, the downstream volume fraction is less diminished relative to leaky boundary flows. For the leaky flows the mean particle sorting at $L' = 1$ is largest for the highest initial kinetic energy. Vertically averaged sorting in saltation flows is much less sensitive to their initial kinetic energy, although *Figure 5.8* and *Figure 5.9* demonstrate that they are much more heterogenous in particle sorting vertically and laterally compared to leaky flows.

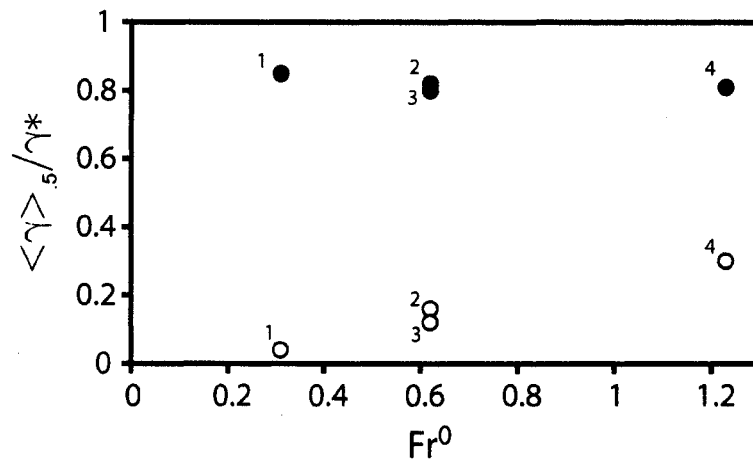


Figure 5.10: The vertically and temporally averaged sorting coefficient at $L'=0.5$ for flow conditions 1-4 and saltating (dark circles) and leaky (open circles) boundary conditions. The numbers to the right of the circles indicate the inlet conditions (Table 3). The sorting coefficients are plotted relative to their inlet Froude numbers. The leaky boundary sorting coefficient is sensitive to the inlet Froude number, whereas the inlet flow energy has little influence on the sorting coefficient for the saltating boundary flows.

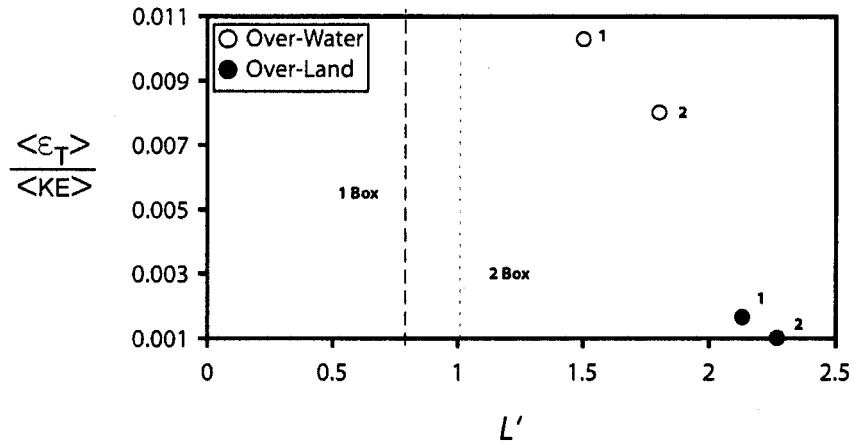


Figure 5.11: The dissipation rate of kinetic energy versus runout distance for flow conditions 1 and 2. Dissipation rate is normalized by the total kinetic energy of the flow. Again inlet conditions are indicated by the number near the circles and dark circles represent saltation boundaries. Box models using the same inlet conditions are plotted for comparison (although dissipation rate at boundary does not apply for these calculations). For both flow conditions 1 and 2 the run-out distance is greater for saltating flows than for leaky boundary flows.

5.5.4 The Influence of Bed Interaction on Run-Out Distance

The run-out distance and mean residence time of particles in a flow is controlled by the complex interplay of flow dilution and buoyancy and energy dissipation due to particle-particle and particle-boundary interactions. For the leaky boundary flows, run-out distance is ultimately a result of flow dilution and buoyancy reversal. While suspension and entrainment mechanism also operate in saltation boundary flows, frictional forces in the bedload determines the maximum run-out of the ground-hugging portion of the flow. Although basal friction and dilution due to particle loss are distinct physical mechanisms, they can both be described by energy dissipation relative to the total kinetic energy budget of the flow. In the case of leaky boundary conditions kinetic energy is removed from the flow due to mass loss (i.e. particles settling through the leaky boundary are removed from the flow). However, particles that reach the boundary in saltation flows lose only a portion of their energy for every particle-wall interaction. While it is true that after the particles have reached the base of the saltation flows they dissipate energy due to inelastic collisions with other particles and the wall, the rate at which this occurs is necessarily slower than if all energy from a particle is lost the instant it touches the bottom boundary as in the case of the leaky boundary. Particle-boundary energy dissipation was greater than any other mechanism. For a given period of time, the leaky boundary dissipates kinetic energy more efficiently than saltation and this correlates well with run-out distance (*Figure 5.11*).

For both flow conditions 1 and 2, the maximum run-out distance is greater for the saltation boundary flows rather than the leaky boundary flows. Similarly, the residence time of an average particle is much longer for all four flow conditions if saltation boundary flows are considered, although the differences are minimized for flows with the greatest initial kinetic energy (*Figure 5.4*). One measure of this is to examine the mean residence time of particles until the flow has decayed to 10% its initial volume flux normalized relative to the settling timescale of an average particle.

As the flows become more dilute (or have lower inlet energy) this measure of residence time approaches unity for the suspended load (*Figure 5.12*). As both Reynolds number and concentration increase the suspended load portion of the flow has a greater residence time due to turbulent suspension and to particle-particle collisions.

5.6 DISCUSSION

5.6.1 Dominant modes of momentum transfer

The development of bed-load in particle-laden flows alters the primary mechanism of momentum transfer from particle-fluid drag to particle-particle collisions. This is depicted in *Figures 5.8* and *5.9* where for $H' < 1$, the collision rate per particle is over an order of magnitude greater in the saltation boundary conditions. A conventional measure of the collisional redistribution of momentum relative to particle-fluid drag is given by the Bagnold number:

$$N_{Bag} = \frac{p\alpha\rho_s D^2 \eta}{(1-p\alpha)\mu}, \quad (5.25)$$

where η is the strain rate and μ is the viscosity of the interstitial fluid. Based on empirical observations, Iverson (Iverson, 1997) suggested that flows with Bagnold numbers greater than ~200 would have a greater momentum transfer due to particle collisions rather than particle-fluid drag. Although this transition is not rigorously defined, the saltation boundary flows clearly have regions of the flow with a Bagnold number greater than 200, whereas the densest portions of the leaky boundary flows are less than $N_{Bag} = 200$ (*Figure 5.8C* and *5.9C*).

One of the primary ways that the development of bed-load, and the resulting increase in particle-particle collisions, manifests itself is in the mixing of different particle species. In the suspended load portion of a flow, particles of different size and density, and hence with different stability-factors and Stokes numbers, will become segregated relative to each other. This is particularly relevant in situations similar to these simulations where the stability factor is much less than 1 in the case of the smallest particles and near to unity for the largest particles. As shown in Figure 3 the large stability factor particles are confined to the lower portions of the flow, and are nearly absent in the formation of meso-scale structures due to the development of shear and buoyancy instabilities. Hence, the leaky boundary flows that have only suspended load transport are efficient at unmixing different grain sizes and producing sorting that reflects energy of the flow (*Figure 5.10*). For instance, lower inlet Froude numbers produced smaller sorting coefficients (more poorly sorted) at the flow scale length ($L'=1$) for leaky boundary flows (*Figure 5.10*).

In contrast, the inlet kinetic energy (and inlet Froude number) and sorting number at $L'=1$ are poorly correlated for saltating flows (*Figure 5.10*). Particle-particle collisions and particle-boundary collisions can keep multiple grain sizes mobile, mixing particles with different stability factors. This result is consistent with the observation that in channel flow particle-wall and particle-particle collisions have a tendency to flatten the particle concentration across the channel (Yamamoto *et al.*, 2001; Sommerfeld, 2003). Once particles enter the bed-load region they are homogenized by the increased number of particle collisions, and meso-scale structure and fluctuations initially present in the suspended portion of the flow are subdued. The bed-load mixing mechanism likely plays a role in the development of massive, homogenous pyroclastic flow deposits and massive Bouma A units in turbidites. Changes in vertical grading in flows that have developed bed-load transport reflect the integrated upstream mean particle supply to the bed-load region, rather than local meso-scale turbulent structure of the flow.

5.6.2 The Role of Particle Stratification Compared to Homogeneous Flows

Particle-laden flows are manifestly heterogeneous in particle volume fraction and particle size sorting. A comparison between these simulated flows which track these heterogeneities and simplified approaches yields further insight in the relative importance of particle volume fraction heterogeneity on flow transport. Two common approaches to the treatment of particle laden gravity currents is to either assume homogeneity in particle volume fraction within the current or to assume particle volume fraction gradients based upon advection-diffusion of sediment (i.e. the Rouse approach).

For homogeneous transport, one approach at predicting the evolution of the current is to assume constant volume (no entrainment) and a front condition (usually $Fr_d \sim 1$). This approach is sometimes termed the 'box-model' approach due to the box shaped profiles produced with these assumptions (Dade & Huppert, 1995; Dade, 2003). Using a box-model approach, a run-out distance can be predicted at the point at which enough particles have sedimented to generate a buoyancy reversal. Key assumptions in this approach are that sedimentation rate is given by the settling velocity, once removed from the flow particles cannot become resuspended, and there is no cooling or entrainment (both of which would lower the interstitial gas density). Modifying the approach of Dade and Huppert (Dade & Huppert, 1995) to a 2-D current gives the following relation for current length:

$$R = \frac{-\ln\left(\frac{p\alpha}{p\alpha^0}\right)\dot{q}}{w_s}, \quad (5.26)$$

where \dot{q} is the constant volume flux ($u \cdot h$). When the mixture density equals the ambient fluid density $\sum_p \rho_p \epsilon_p + \rho_{int} \epsilon_g = \rho_{amb}$, the current will begin to ascend.

Run-out distances using the box modeling approach were less than predicted in the simulations (*Figure 5.11*) compared to either the saltating boundary flows or the leaky boundary flows. The assumptions used in developing the box-model approach emphasize suspended load conditions. For instance, the $Fr_d \sim 1$ front condition most clearly matches the results of the leaky boundary, suspended load flows (*Figure 5.7*). In contrast, the densimetric Froude number deviates significantly from unity when an interacting bed-load develops. The differences in run-out distance between the leaky boundary flows and the box model approach can principally be attributed to cooling and entrainment increasing the average gas density in the simulations. Hence neutral buoyancy is reached for a much more particle dilute flow that gives the flow a greater period of time to propagate. For example, the mean temperature below the scale height is 412 K at the maximum run-out distance for flow conditions 1 and leaky boundary conditions. The mean volume fraction below the scale height at this location is 1.6×10^{-4} . In contrast, without cooling or entrainment the interstitial gas density remains constant and the particle volume fraction at neutral buoyancy is 3.3×10^{-4} , or nearly 200 % greater particle volume fraction than when considering entrainment. Hence, if the interstitial fluid is less dense than the ambient fluid, run-out distance will be linked closely with entrainment efficiency. (In this case the box-model is a proxy for completely inefficient mixing). Particle sedimentation decreases the Richardson number (*Figure 5.4*) and lowers the required shear for efficient entrainment, and incorporating this effect will lead to run-out predictions of over a factor of 200 % different if vertical mixing does not occur.

Particle stratification models based upon mixing-length approximations to turbulent flow have been proposed in number of settings (Dingman, 1984; Ghosh *et al.*, 1986; Valentine, 1987). Using an eddy diffusivity proportional to the scale height of the flow (and assuming unidirectional, open-channel flow at equilibrium) yields a Rousean particle volume fraction profile:

$${}^p\alpha = \alpha_b \left(\frac{(H - H')/H'}{(H - b)/b} \right)^{Pn}, \quad (5.27)$$

where b is reference height near the base of the flow, α_b is the particle volume fraction at b , and Pn is the Rouse number ($Pn = \frac{w_s}{\kappa u_*}$, where w_s is the settling velocity, u_* is the shear velocity, and κ is the von Karman constant). Valentine (Valentine, 1987) applied this concept to pyroclastic flow transport, and predicted vertical gradients in the particle volume fraction. The Rousean particle volume fraction profile and open-channel velocity profiles using average shear velocity are compared to the volume fraction and velocity profile of these simulations at L₅ (Figure 5.4). As expected, the particle volume fraction in the Rousean profiles deviates significantly compared to the bed-load region of the saltation simulations due to the equilibrium assumption of balanced vertical particle flux inherent in the Rousean derivation. The vertical particle volume fraction gradients in the Rousean profile are also considerably smaller than leaky boundary condition simulations. The shear instabilities and entrainment at low Richardson numbers at the top of these currents helps to explain the differences between an equilibrium Rousean profile and the leaky gravity currents. The open-channel assumption of the velocity profile for the Rousean derivation predicts maximum velocity at the top of the current, whereas the simulations predict maximum velocities at approximately 1/3 the current scale height similar to experimental gravity currents (Parsons & Garcia, 1998; Choux & Druitt, 2002).

5.6.3 Development of bed-load and implications for changing boundary conditions

Bed-load material is continuously supplied from the suspended-load region, which suggests this layer can reform after changes in boundary conditions (i.e. from leaky to saltation boundaries). As an example, using inlet conditions 1 (*Table 5.4*) a simulation was conducted with leaky boundaries to $L'=1$ and saltating boundaries thereafter. By $L'=1.1$ scale length units a particle-rich bed-load region had developed after crossing the transition for leaky to saltating boundaries. This bed-load region was characterized by increased particle-particle collisions relative to its completely leaky flow counterpart and Bagnold numbers in excess of 1000. However, as most of the large stability factor particles had been removed during transit over the leaky boundary condition, the vertically averaged sorting coefficient of this bed-load region was $\sim .04$ at $L'=1.1$ and much less than a completely saltating boundary (*Figure 5.9*). These simulations provide an important caveat in the interpretation of well sorted deposits; they can imply particle capture upstream of deposition rather than locally dilute, suspended load conditions. Besides the transition from leaky to saltating boundaries, changes in topography may also alter the transition from suspended load to bed-load in particle-laden gravity currents if the bedload is removed after encountering particularly steep landscapes (Valentine, 1987; Branney & Kokelaar, 2002; Brown & Branney, 2004; Burgisser, 2004). Understanding the removal and formation of bed-load determines the amount of force that these currents supply to the near bed region and determines how hazardous a given flow will be to near-bed structures and populations.

5.7 CONCLUSIONS

The formation of bed-load transport in ground hugging particle-laden flows is a natural consequence of particle-bed interaction. The proportion of bed-load material is continuously evolving as particles that can no longer be suspended are transferred to the basal region of the flow. Saltation due to inelastic collisions at the bed results in increased particle volume fractions near the bed and a greater number of particle-particle collisions. These collisions homogenize the concentration of different size

particles and can result in greater residence time of particles in the flow. Entrainment and particle-fluid drag are capable of resuspending some material from the bed-load at the front of the current, and the preferential removal of fine material leaves portions of the bed-load at the front of the flow enriched in coarse material. This may be responsible for the lithic breccias observed in many pyroclastic flow deposits and massive units at the base of some turbidites. The increased mobility of particles at the base of the flow also results in greater run-out distance of these flows relative to completely leaky conditions by as much as 25%.

When flows encounter a leaky boundary (such as traversing water) bed-load formation is inhibited and a more dilute suspended load transport develops. Particles are organized into meso-scale structures due to particle-fluid interaction, and particles with different Stokes numbers are readily sorted relative to each other. The dilution in particle volume fraction that develops at the upper interface of these flows encourages shear instabilities and buoyancy reversal, and this results in entrainment of ambient fluid in the flow. Ultimately these flows become so dilute that they can no longer propagate as ground-hugging currents. Hence, the dichotomy of dense, bed-load transport and completely suspended load transport can be explained by particle-bed interaction and this interaction is one of the principle factors determining run-out length and order-disorder in deposits.

- Chapter 6 -

Closing Remarks and Future Directions

Magmatic and volcanic phenomena are time-dependent and contain structure and heterogeneity on multiple length-scales. The multiphase character of magmatic systems is responsible for much of the visible structure in deposits and outcrops, and can produce emergent rheological and chemical structures as discrete phases (crystals, bubbles, pyroclastic material) interact with the continuous fluid phases (magma or the atmosphere). In fact, a growing body of numerical, experimental and observational evidence from the natural sciences and engineering disciplines indicates that homogeneity in particle-fluid systems is the exception rather than the rule (Crowe, 1991; Squires & Eaton, 1991; Eaton & Fessler, 1994). This stands in contrast to previous conceptual approaches that have assumed magmatic systems to behave as steady, homogeneous entities. Due to the subsequent feedback in momentum and heat transfer the steady, homogeneous assumption can not only fail to predict the details of a flow field, but may also predict vastly different bulk flow and thermal fields as shown in previous chapters of this work.

The evolution of the lower crust in arc systems is dependent on the rate and intrusion configuration of mantle melts produced from flux melting in the mantle wedge. The generation and preservation of both crustal and mantle melts depends on the cumulative history of intrusions; the lower crustal system has both a chemical and thermal memory of previous events. However, both the compositional and thermal states of the crust at any one time can be produced by a non-unique combination of events. In order to examine the range of responses of the crust to magmatic intrusion a stochastic approach was adopted where a number of realizations of separate

intrusion histories were combined. Although individual realizations display a variety of behavior, a generalized evolutionary sequence of events can be deciphered provided that the average basalt flux remains near to constant. Shallow and young crust is a likely repository of residual mantle melts with melt fractions from .1 – .3 and dehydration crustal melts less than $\sim .15$, although interludes of transient higher melt fractions occur at the intersection of dike intrusions. The low melt fractions encountered in this sort of environment converge toward dacitic to rhyolitic composition and these pods of melt are often separated in time and space. Such conditions favor small scale heterogeneity and inhibit mixing of the distinct pockets of melt. The lower pressure conditions in the immature lower crust and low melt fractions result in garnet-poor and plagioclase-rich residual mineralogies that are positively buoyant relative to mantle peridotite. These conditions should favor crustal growth with continued intrusions from the mantle. This stands in contrast to thickened (>40 km) mature crust where continued intrusions promote greater melt fractions and the coalescence of melts in collapsing structures at the intersections of intrusions. These collapse structures promote mixing of both mantle and crustal melts which tend toward andesitic to basaltic andesite. The residual mineralogies have a dominant modes of pyroxene and garnet. If melt can be efficiently segregated from the residual mineralogy it will become denser than upper mantle peridotite and can initiate density instabilities that remove portions of the lower crust. While the criteria for the growth of these density instabilities is developed in this work, the fate of these drips as they descend into the mantle remains to be explored.

A problem closely related to the problem of lower crustal melt generation is the residence and transit times of these melts in the crustal column. Radioactive uranium-series nuclides provides a potentially useful chronometer of melting events in the crust and mantle, and previously it had been assumed that the only significant way to generate $(^{226}\text{Ra})/(^{230}\text{Th})$ disequilibria was through slab dehydration at depths of over 100 km in the mantle. As disequilibria will be undetectable after about five half lives of the ^{226}Ra nuclide ($\sim 10,000$ yrs), this hypothesis implies that disequilibria

measured at the surface is recording ultra-fast ascent from the slab to the surface. However, in this work a time-dependent model was developed that predicted that incongruent melting reactions in an amphibolite (as can occur in the lower crust) can also generate substantial $(^{226}\text{Ra})/(^{230}\text{Th})$ disequilibria. This model also predicted distinctive trace element signatures that could help distinguish these lower crustal melts from melts that are receiving $(^{226}\text{Ra})/(^{230}\text{Th})$ disequilibria from the slab. Now that the model framework has been developed to examine continuous, incongruent reactions in an amphibolite work remains to be done on testing whether other dehydration reactions impact other U-series nuclides at different levels in the crustal column.

Differentiated magmas that reach the near surface in arc systems often have highly polymerized SiO_2 compositions and high water contents, both contributing to the potentially explosive behavior of these systems when exposed to rapid depressurization events. Two problems related to the explosive eruption of dacites and rhyolites are considered in this work: conduit dynamics and pyroclastic flow transport. Both regimes involve multiphase flow and relative velocities between continuous and discrete phases. Following decompression in a magmatic conduit, bubbles begin to exsolve accelerating the magma and bubble mixture that can shear the magma or cause sufficient bubble over-pressure to fragment the magma brittly. This generates a turbulent particle and gas mixture, and one of the outstanding questions is how momentum is transferred in this mixture before it reaches the conduit vent into the atmosphere. Using a continuum multiphase model this work considered two end-members for momentum diffusion in the conduit: treating the particles as an inviscid (collisionless) continua or as continua with momentum transfer due to inelastic particle collisions. Particle collisions were found to have an important impact on the momentum transfer for larger (>1 cm) sized particles and resulted in larger relative motion between the gas and the particles as well as radial concentration variations. Few very large eruptions produce all fine material and this deviation from perfect fragmentation efficiency will result in mechanical non-

equilibrium of particles and gas exiting the vent. As the particle concentration and gas and particle velocities are extremely important in determining whether an eruptive column will collapse and form locally dangerous pyroclastic flows or ascend into the stratosphere and cause longer term climate impacts (Valentine & Wohletz, 1989), further work should be devoted to understanding the behavior of multiphase jets that are in mechanical non-equilibrium.

The internal structure of pyroclastic flows has long been debated (Branney & Kokelaar, 2002) due to the near impossibility of in-situ measurements. In particular, the relative amount of particles that are transported due to turbulent suspension compared to saltating particles is poorly understood. This work evaluated this effect by considering a leaky boundary (as might be encountered when a pyroclastic flow goes over water) and a saltating boundary (as would be encountered for flows that traverse land). This study revealed that the energy dissipation rate in pyroclastic flows is strongly controlled by the interactions at the base of these flows. Pyroclastic flows with leaky boundaries were better sorted and had shorter run-out distances compared to their saltating counterparts. The ultimate run-out distance of these flows was controlled by the interplay of dilution due to entrainment of ambient air and sedimentation and the basal interactions of particles. This work demonstrated that previous approaches that neglected entrainment dynamics and detailed examinations of boundary interactions could underpredict pyroclastic flow run-out by over 50%.

The development of the continuous multiphase model in this work is part of a continuing effort to develop an Eulerian-Eulerian-Lagrangian (EEL) model for eruptive flows. In this approach the smaller particle sizes are treated as continua and large particles are tracked explicitly. One of the benefits of this approach is that it enables model calculations and deposit data to be compared directly, and current and future work is planned to study the eruptive dynamics of the Kos Plateau Tuff using this technique. This work will also facilitate comparison to real-time observations and a future proposal is planned to use this technique in conjunction with in-situ

measurements made by UAV to better understand particle-size segregation in volcanic plumes. Further, the multiphase *EEL* approach is well suited to investigate the feedback between resuspension, entrainment, and reacting bedforms. In order to extend the *EEL* work to consider resuspension as a result of fluctuating particle and fluid motion a probabilistic subgrid approach to the ejection of particles at the bed will need to be developed based on statistical mechanics. The local velocity distribution for the fluid and particle phases is calculated in the *EEL* framework and makes this method particularly amenable to incorporating further statistical mechanics approaches. As sediment concentration contributes to the lateral pressure gradients that drive the dynamics of these flows, it can be surmised that the contribution of erosional material may significantly extend their run-out distance. The in-situ evolution of the grain-size distribution due to particle break up as a result of collisions will also be assessed. Numerical simulations based on the *EEL* approach can also be compared with field sites where resuspension has clearly occurred and where flows have been starved of erosion-provided sediment (such as flows that traverse bodies of water).

Although my previous research has focused on volcanic eruptions, the multiphase approach is general. Future research will delineate the dominant energy dissipation mechanism in particle-laden flow and quantify the transport capacity of flows that are evolving as a result of basal interactions and numerous particle collisions. The resulting modeling technology will have dual utility: it will be useful as a hazard assessment tool as well as provide key insight into many analogous self-organizing phenomena. Future applications of the numerical simulations include delineating potential scenarios for future eruptions, characterizing the dynamics associated with other volcanic deposits, examining the run-out and deposits of turbidity currents generated by large-island landslides (e.g. Canary or Hawaiian Islands) and understanding particle-laden flows in settings in which it is expensive or impossible to do exhaustive field work. For instance, evaluating the potential impact of pyroclastic and cryoclastic flows on other planetary bodies (with particular emphasis on

Mars) could be constrained by modeling, and missions to observe these deposits could be informed by the modeling process.

BIBLIOGRAPHY

- Agrawal, K., P. N. Loezos, M. Syamlal & S. Sundaresan (2001). The role of meso-scale structures in rapid gas-solid flows. *J. Fluid Mech* **445**, 151-185.
- Allen, S. R. & R. A. F. Cas (2001). Transport of pyroclastic flows across the sea during explosive, rhyolitic eruption of the Kos Plateau Tuff, Greece. *Bulletin of Volcanology* **62**, 441-456.
- Anderson, A. T. (1976). Magma mixing - Petrological process and volcanological tool. *Journal of Volcanology and Geothermal Research* **1**(1), 3-33.
- Anderson, A. T., A. M. Davis & F. Q. Lu (2000). Evolution of Bishop Tuff rhyolitic magma based on melt and magnetite inclusions and zoned phenocrysts. *Journal of Petrology* **41**(3), 449-473.
- Anderson, A. T., Jr., S. Newman, S. N. Williams, T. H. Druitt, C. Skirius & E. Stolper (1989). H₂O, CO₂, Cl and gas in Plinian and ash-flow Bishop rhyolite. *Geology* **17**, 221-225.
- Annen, C. & R. S. J. Sparks (2002). Effects of repetitive emplacement of basaltic intrusions on the thermal evolution and melt generation in the crust. *Earth and Planetary Science Letters* **203**(3-4), 937-955.
- Arth, J. G., F. Barker, Z. E. Peterman & I. Friedman (1978). Geochemistry of gabbro-diorite-tonalite-trondhjemitic suite of southwest Finland and its implications for origin of tonalitic and trondhjemitic magmas. *Journal of Petrology* **19**(2), 289-316.
- Bachmann, O., M. A. Dungan & P. W. Lipmann (2000). Voluminous lava-like precursor to a major ash-flow tuff: low-column pyroclastic eruption of the Pagosa Peak Dacite, San Juan volcanic field, Colorado. *Journal of Volcanology and Geothermal Research* **98**, 153-171.

- Bachmann, O., M. A. Dungan & P. W. Lipmann (2002). The Fish Canyon magma body, San Juan volcanic field, Colorado: Rejuvenation and eruption of an upper-crustal batholith. *Journal of Petrology* **43**(8), 1469-1503.
- Bachmann, O., M. A. Dungan & F. Bussy (2004). Insights into shallow magmatic processes in large silicic magma bodies: the trace element record in the Fish Canyon magma, Colorado. *Contributions to Mineralogy and Petrology* **In Press**.
- Barboza, S. A. & G. W. Bergantz (1996). Dynamic model of dehydration melting motivated by a natural analogue: applications to the Ivrea-Verbano zone, northern Italy. *Transactions of the Royal Society of Edinburgh* **87**, 23-31.
- Barboza, S. A. & G. W. Bergantz (1997). Melt productivity and rheology: complementary influences on the progress of melting. *Numerical Heat Transfer Part A-Applications* **31A**, 375-392.
- Barboza, S. A. & G. W. Bergantz (1998). Rheological transitions and the progress of melting of crustal rocks. *Earth and Planetary Science Letters* **158**, 19-29.
- Barboza, S. A., G. W. Bergantz & M. Brown (1999). Regional granulite facies metamorphism in the Ivrea zone: is the Mafic Complex the smoking gun or a red herring? *Geology* **27**, 447-450.
- Barboza, S. A. & G. W. Bergantz (2000). Metamorphism and anatexis in the mafic complex contact aureole, Ivrea Zone, Northern Italy. *Journal of Petrology* **41**(8), 1307-1327.
- Barth, M. G., S. F. Foley & I. Horn (2002). Partial melting in Archean subduction zones: constraints from experimentally determined trace element partition coefficients between eclogitic minerals and tonalitic melts under upper mantle conditions. *Precambrian Research* **113**, 323-340.

- Basaltic_Volcanism_Study_Project (1981). *Basaltic Volcanism of the Terrestrial Planets*. New York, Pergamon Press, Inc.
- Beard, J. S. & G. E. Lofgren (1991). Dehydration melting and water-saturated melting of basaltic and andesitic greenstones and amphibolites at 1, 3, and 6.9 kb. *Journal of Petrology* **32**, 365-401.
- Beattie, P. (1993). The generation of uranium series disequilibria by partial melting of spinel peridotite: Constraints from partitioning studies. *Earth and Planetary Science Letters* **117**, 379-391.
- Beattie, P. (2003). Uranium-thorium disequilibria and partitioning on melting of garnet peridotite. *Nature* **363**, 63-65.
- Benjamin, T. B. (1968). Gravity currents and related phenomena. *Journal of Fluid Mechanics* **31**(2), 209-248.
- Benyahia, S., M. Syamlal & T. J. O'Brien (2005). Evaluation of boundary conditions used to model dilute, turbulent gas/solids flows in a pipe. *Powder Technology* **156**(2-3), 62-72.
- Bergantz, G. W. (1989). Underplating and partial melting: Implications for melt generation and extraction. *Science* **245**, 1093-1095.
- Bergantz, G. W. (1990). Melt fraction diagrams: the link between chemical and transport models. In: J. Nicholls and J. K. Russell (ed.) *Modern Methods of Igneous Petrology: Understanding Magmatic Processes*: Mineralogical Society of America, **24**, 240-257.
- Bergantz, G. W. (1995). Changing paradigms and techniques for the evaluation of magmatic processes. *Journal of Geophysical Research* **100**(B9), 17,603-17,613.
- Berlo, K., S. Turner, J. Blundy & C. J. Hawkeswork (2004). The extent of U-series disequilibria produced during partial melting of the lower crust with

implications for the formation of Mount St. Helens dacites. *Contributions to Mineralogy and Petrology* **148**, 122-130.

Bindeman, I. N., A. M. Davis & M. J. Drake (1998). Ion microprobe study of plagioclase-basalt partition experiments at natural concentration levels of trace elements. *Geochimica Et Cosmochimica Acta* **62**(7), 1175-1193.

Bindeman, I. N. & A. M. Davis (2000). Trace element partitioning between plagioclase and melt; investigation of dopant influence on partition behavior. *Geochimica Et Cosmochimica Acta* **64**(16), 2863-2878.

Bird, P. (1979). Continental delamination and the Colorado Plateau. *Journal of Geophysical Research* **84**(B13), 7561-7571.

Bittner, D. & H. Schmeling (1995). Numerical modelling of melting processes and induced diapirisms in the lower crust. *Geophysical Journal International*, 59-70.

Blundy, J. & B. Wood (2003). Mineral-melt partitioning of uranium, thorium and their daughters. In: B. Bourdon, G. M. Henderson, C. C. Lundstrom and P. S. Turner (ed.) *Uranium-series geochemistry*. Washington, D.C.: Mineralogical Society of America and Geochemical Society, **52**, 59-123.

Bonnecaze, R. T., H. Huppert & J. R. Lister (1993). Particle-driven gravity currents. *Journal of Fluid Mechanics* **250**, 339-369.

Bourdon, B. & K. W. W. Sims (2003). U-series constraints on intraplate basaltic magmatism. In: (ed.) *Uranium-series geochemistry*, **52**, 215-254.

Branney, M. J. & P. Kokelaar (2002). *Pyroclastic density currents and the sedimentation of ignimbrites*. London, The Geological Society.

Brenan, J. M., H. F. Shaw, F. J. Ryerson & D. L. Phinney (1995). Experimental determination of trace-element partitioning between pargasite and a synthetic hydrous andesitic melt. *Earth and Planetary Science Letters* **135**, 1-11.

- Britter, R. E. & J. E. Simpson (1978). Experiments on the dynamics of gravity current head. *Journal of Fluid Mechanics* **88**(2), 223-240.
- Brown, R. J. & M. J. Branney (2004). Bypassing and diachronous deposition from density currents: Evidence from a giant regressive bed form in the Poris ignimbrite, Tenerife, Canary Islands. *Geology* **32**(5), 445-448.
- Bryan, W. B., G. Thompson & P. J. Michael (1979). Compositional variation in a steady-state zoned magma chamber: mid-Atlantic ridge at 36°50'N. *Tectonophysics* **55**, 63-85.
- Burgisser, A. & G. W. Bergantz (2002). Reconciling pyroclastic flow and surge: the multiphase physics of pyroclastic density currents. *Earth and Planetary Science Letters* **202**, 405-418.
- Burgisser, A. (2004). Physical volcanology of the 2050 BP caldera-forming eruption of Okmok Volcano, Alaska. *Bulletin of Volcanology* **67**(6), 497-525.
- Burgisser, A., G. W. Bergantz & R. E. Breidenthal (2005). Addressing complexity in laboratory experiments: the scaling of dilute multiphase flows in magmatic systems. *Journal of Volcanology and Geothermal Research* **141**(3-4), 245-265.
- Bursik, M. (1998). Tephra Dispersal. In: J. S. Gilbert and R. S. J. Sparks (ed.) *The Physics of Explosive Volcanic Eruptions*. London, UK: Geological Society Special Publication, 115-144.
- Cao, J. & G. Ahmadi (1995). Gas-particle 2-phase turbulent-flow in a vertical duct. *International Journal of Multiphase Flow* **21**(6), 1203-1228.
- Carey, S. & H. Sigurdsson (1989). The intensity of plinian eruptions. *Bull. Volcanology* **51**, 28-40.

- Carey, S., et al. (1996). Pyroclastic flows and surges over water: an example from the 1883 Krakatau eruption. *Bulletin of Volcanology* **57**, 493-511.
- Cervantes, P. & P. J. Wallace (2003). Role of H₂O in subduction-zone magmatism; new insights from melt inclusion in high-Mg basalts from central Mexico. *Geology* **31**(3), 235-238.
- Chapman, D. S. & K. P. Furlong (1992). Thermal state of the continental lower crust. In: D. M. Fountain, Arculus, R. and Kay, R.W. (ed.) *Continental Lower Crust*. Amsterdam: Elsevier.
- Choux, C. M. & T. H. Druitt (2002). Analogue study of particle segregation in pyroclastic density currents, with implications for the emplacement mechanisms of large ignimbrites. *Sedimentology* **49**, 907-928.
- Cole, J. W. (1982). Tonga-Kermadec-New Zealand. In: R. S. Thorpe (ed.) *Andesites; orogenic andesites and related rocks*. Chichester, UK: John Wiley and Sons, 245-258.
- Conrey, R. M., P. R. Hooper, P. B. Larson, J. T. Chesley & J. Ruiz (2001). Trace element and isotopic evidence for two types of crustal melting beneath a high Cascade volcanic center, Mt. Jefferson, Oregon. *Contributions to Mineralogy and Petrology* **142**, 261-283.
- Cooper, K. M. & M. R. Reid (2003). Re-examination of crystal ages in recent Mount St. Helens lavas: implications for magma reservoir processes. *Earth and Planetary Science Letters* **213**, 149-167.
- Costa, F., S. Chakraborty & R. Dohmen (2003). Diffusion coupling between trace and major elements and a model for calculation of magma residence times using plagioclase. *Geochim. Cosmochim. Acta.* **67**(12), 2189-2200.
- Crisp, J. A. (1984). Rates of magma emplacement and volcanic output. *Journal of Volcanology and Geothermal Research* **20**, 177-211.

- Crowe, C. T., R. A. Gore & T. R. Truitt (1985). Particle dispersion in free shear flows. *Part. Sci. Tech.* **3**, 149.
- Crowe, C. T. (1991). The state-of-the-art in the development of numerical models for dispersed phase flows. *Proc. First International Conference on Multiphase Flows* **3**, 49.
- Dade, W. B. & H. E. Huppert (1995). Runout and fine-sediment deposits of axisymmetric turbidity currents. *Journal of Geophysical Research* **100**, 18597-18609.
- Dade, W. B. (2003). The emplacement of low-aspect ratio ignimbrites. *Journal of Geophysical Research* **108**, 2211.
- Darteville, S., W. I. Rose, J. Stix, K. Kelfoun & J. W. Vallance (2004). Numerical modeling of geophysical granular flows: 2. Computer simulations of plinian clouds and pyroclastic flows and surges. *GEOCHEMISTRY GEOPHYSICS GEOSYSTEMS* **5**(8), 1-36.
- Davidson, J. P., J. M. Hora, J. M. Garrison & M. A. Dungan (2005). Crustal forensics in arc magmas. *Journal of Volcanology and Geothermal Research* **140**, 157-170.
- DeBari, S., S. Mahlburg Kay & K. R.W. (1987). Ultramafic xenoliths from Adagdak volcano, Adak, Aleutian Islands, Alaska: Deformed igneous cumulates from the mocho of an island arc. *Journal of Geology* **95**, 329-341.
- DeBari, S. M. & R. G. Coleman (1989). Examination of the deep levels of an island-arc: Evidence from the Tonsina ultramafic-mafic assemblage, Tonsina, Alaska. *Journal of Geophysical Research* **94**(4), 4373-4391.
- DePaolo, D. J., F. V. Perry & W. S. Baldrige (1992). Crustal versus mantle sources of granitic magmas: a two-parameter model based on Nd isotopic studies. *Transactions of the Royal Society of Edinburgh* **83**, 439-446.

- Dimalanta, C., A. Taira, G. P. J. Yumul, H. Tokuyama & K. Mochizuki (2002). New rates of western Pacific island arc magmatism from seismic and gravity data. *Earth and Planetary Science Letters* **202**, 105-115.
- Dingman, S. L. (1984). *Fluvial hydrology*. New York, WH Freeman and Co.
- Dingwell, D. B. (1996). Volcanic Dilemma: flow or blow? *Science* **273**, 1054-1055.
- Dobran, F. (1992). Nonequilibrium flow in volcanic conduits and application to the eruptions of Mt. St. Helens on May 18, 1980, and Vesuvius in AD 79. *Journal of Volcanology and Geothermal Research* **49**, 285-311.
- Dobran, F. (1993). *Global Volcanic Simulation of Vesuvius*, Giardini.
- Dobran, F., A. Neri & G. Macedonio (1993). Numerical simulation of collapsing volcanic columns. *JGR* **98**(B3), 4231-4259.
- Dobran, F. (2001). *Volcanic Processes, Mechanisms in Material Transport*, Kluwer Academic.
- Drew, D. A. (1983). Mathematical modeling of two-phase flow. *Ann. Rev. of Fluid Mech.* **15**, 261-291.
- Ducea, M. N. & J. B. Saleeby (1998). The age and origin of a thick mafic-ultramafic keel from beneath the Sierra Nevada batholith. *Contributions to Mineralogy and Petrology* **133**(1-2), 169-185.
- Ducea, M. N. (2002). Constraints on the bulk composition and root foundering rates of continental arcs: A California arc perspective. *Journal of Geophysical Research* **107**(B11), 2303.
- Ducea, M. N., S. Kidder & G. Zandt (2003). Arc composition at mid-crustal depths: Insights from the Coast Ridge Belt, Santa Lucia Mountains, California. *Geophysical Research Letters* **30**(13), Art. No. 1703.

- Dufek, J. D. & G. W. Bergantz (2005). Transient two-dimensional dynamics in the upper conduit of a rhyolitic eruption: A comparison of the closure models for the granular stress. *Journal of Volcanology and Geothermal Research* **143**, 113-132.
- Dufek, J. D. & G. W. Bergantz (2005). Lower Crustal Magma Genesis and Preservation: A Stochastic Framework for the Evaluation of Basalt-Crust Interaction. *Journal of Petrology* **46**, 2167-2195.
- Dungan, M. A. & J. Davidson (2004). Partial assimilative recycling of the mafic plutonic roots of arc volcanoes: An example from the Chilean Andes. *Geology* **32**(9), 773-776.
- Eaton, J. K. & J. R. Fessler (1994). Preferential Concentration of Particles in Turbulence. *Int. J. of Multiphase Flow* **20**(Suppl.), 169-209.
- Ewart, A. (1982). The mineralogy and petrology of Tertiary-Recent orogenic volcanic rocks: with special reference to the andesite-basaltic compositional range. In: R. S. Thorpe (ed.) *Andesites*. Great Britain: John Wiley and Sons, Ltd., 25-95.
- Fedors, R. F. & R. F. Landel (1979). An empirical method of estimating the void fraction in mixtures of uniform particles of different size. *Powder Technology* **23**, 225-231.
- Feeley, T. C., M. A. Cosca & C. R. Lindsay (2002). Petrogenesis and implications of cryptic hybrid magmas from Washburn Volcano, Absaroka Volcanic Province, U.S.A. *Journal of Petrology* **43**, 663-703.
- Fialko, Y. A. & A. M. Rubin (1999). Thermal and mechanical aspects of magma emplacement in giant dike swarms. *Journal of Geophysical Research* **104**(10), 23033-23049.
- Fisher, R. V. e. a. (1993). Mobility of a large-volume pyroclastic flow-emplacment of the Campanian ignimbrite, Italy. *J. Volc. Geotherm. Res.* **56**, 262-275.

- Fornelli, A., G. Piccarreta, A. Del Moro & P. Acquafredda (2002). Multi-stage melting in the lower crust of the Serre (southern Italy). *Journal of Petrology* **43**(12), 2191-2217.
- Freundt, A. (2003). Entrance of hot pyroclastic flows into the sea: experimental observation. *Bull. Volc.* **65**(144-164).
- Furlong, K. P. & D. M. Fountain (1986). Continental crustal underplating: Thermal considerations and seismic-petrologic consequences. *Journal of Geophysical Research* **91**(B8), 8285-8294.
- Gardner, J. E., R. M. E. Thomas, C. Jaupart & S. Tait (1996). Fragmentation of magma during Plinian volcanic eruptions. *Bull. Volcanology* **58**, 144-162.
- Gera, D., M. Syamlal & T. J. O'Brien (2004). Hydrodynamics of particle segregation in fluidized beds. *International Journal of Multiphase Flow* **30**, 419-428.
- Ghiorso, M. S. & R. O. Sack (1995). Chemical mass transfer in magmatic processes IV. A revised and internally consistent thermodynamic model for the interpolation and extrapolation of liquid-solid equilibria in magmatic systems at elevated temperatures and pressures. *Contributions to Mineralogy and Petrology* **119**, 197-212.
- Ghosh, J. K., B. S. Mazumder, M. R. Saha & S. Sengupta (1986). Deposition of sand by suspension currents: Experimental and theoretical studies. *Journal of Sedimentary Petrology* **56**, 57-66.
- Gidaspow, D. (1986). Hydrodynamics of Fluidization and Heat Transfer: Supercomputer Modeling. *Appl. Mech Rev* **39**(1), 1-23.
- Gidaspow, D. (1994). *Multiphase Flow and Fluidization: Continuum and Kinetic Theory Descriptions*, Academic Press.

- Gill, J. B. & R. W. Williams (1990). Th isotope and U-series studies of subduction-related volcanic rocks. *Geochimica Et Cosmochimica Acta* **54**, 1427-1442.
- Green, T. H. & A. E. Ringwood (1968). Genesis of the calc-alkaline igneous rock suite. *Contributions to Mineralogy and Petrology* **18**, 105-162.
- Green, T. H. (1972). Crystallization of calc-alkaline andesite under controlled high-pressure, hydrous conditions. *Contributions to Mineralogy and Petrology* **34**, 150-166.
- Green, T. H. (1982). Anatexis of mafic crust and high pressure crystallization of andesite. In: R. S. Thorpe (ed.) *Andesites; orogenic andesites and related rocks*. Chichester, U.K.: John Wiley and Sons, 465-487.
- Griffin, W. L., X. Wang, S. E. Jackson, N. J. Pearson, S. Y. O'Reilly, X. Xu & X. Zhou (2002). Zircon chemistry and magma mixing, SE China: In-situ analysis of Hf isotopes, Tonglu and Pingtan igneous complexes. *Lithos* **61**, 237-269.
- Grove, T. L., L. T. Elkins-Tanton, S. W. Parman, N. Chatterjee, O. Muntener & G. A. Gaetani (2003). Fractional crystallization and mantle-melting controls on calc-alkaline differentiation trends. *Contributions to Mineralogy and Petrology* **145**(5), 515-533.
- Grunder, A. L. (1995). Material and thermal roles of basalt in crustal magmatism: Case study from eastern Nevada. *Geology* **23**(10), 952-956.
- Gunn, D. J. (1978). Transfer of Heat or Mass to Particles in Fixed and Fluidized Beds. *International Journal of Heat and Mass Transfer* **21**, 467-476.
- Hannah, R. S., T. A. Vogel, L. C. Patino, G. E. Alvarado, W. Perez & D. R. Smith (2002). Origin of silicic volcanic rocks in central Costa Rica; a study of a chemically variable ash-flow sheet in the Tiribi Tuff. *Bulletin of Volcanology* **64**(2), 117-133.

- Harlow, F. H. & A. A. Amsden (1975). Numerical Calculation of Multiphase Flow. *J. Comput. Phys.* **17**, 19-52.
- Hart, G. L., C. M. Johnson, S. B. Shirey & M. A. Clynne (2002). Osmium isotope constraints on lower crustal recycling and pluton preservation at Lassen Volcanic Center, CA. *Earth and Planetary Science Letters* **199**, 269-285.
- Hartel, C., E. Meiburg & F. Necker (2000). Analysis and direct numerical simulation of the flow at a gravity current head. Part 1. Flow topology and front speed for slip and no-slip boundaries. *Journal of Fluid Mechanics* **418**, 189-212.
- Hazen, A. (1904). On Sedimentation. *Transactions of the American Society of Civil Engineering* **LIII**, 45-71.
- Hertogen, J. & R. Gijbels (1975). Calculation of trace element fractionation during partial melting. *Geochimica Et Cosmochimica Acta* **40**, 313-322.
- Hess, K. U. & D. B. Dingwell (1996). Viscosities of hydrous leucogranitic melts: a non-Arrhenian model. *Am mineral* **81**(9-10), 1297-1300.
- Hildreth, W. & S. Moorbath (1988). Crustal contributions to arc magmatism in the Andes of Central Chile. *Contributions to Mineralogy and Petrology* **98**, 455-489.
- Hirth, G. & D. L. Kohlstedt (1995). Experimental constraints on the dynamics of the partially molten upper mantle; deformation in the diffusion creep regime. *Journal of Geophysical Research* **100**(B8), 1981-2001.
- Hirth, G. & D. L. Kohlstedt (1996). Water in the oceanic upper mantle; implications for rheology, melt extraction and the evolution of the lithosphere. *Earth and Planetary Science Letters* **144**(1-2), 93-108.
- Holbrook, W. S., W. D. Mooney & N. I. Christensen (1992). The seismic velocity structure of the deep continental crust. In: D. M. Fountain, R. Arculus and R. W. Kay (ed.) *Continental Lower Crust*. Amsterdam: Elsevier, 1-34.

- Holland, T. J. B. & R. Powell (1998). An internally consistent thermodynamic data set for phases of petrological interest. *Journal of Metamorphic Geology* **16**(3), 309-343.
- Holloway, J. R. & C. W. Burnham (1972). Melting relations of basalt with equilibrium pressure less than total pressure. *Journal of Petrology* **14**, 1-29.
- Hopson, C. A. & J. M. Mattinson (1994). Chelan Migmatite Complex, Washington: Field evidence for mafic magmatism, crustal anatexis, mixing and protodiapiric emplacement. In: D. A. Swanson and R. A. Haugerud (ed.) *Geologic field trips in the Pacific Northwest: 1994 Geological Society of America Annual Meeting*. Seattle: Department of Geological Sciences, University of Washington, 1-21.
- Huppert, H. E. & R. S. J. Sparks (1988). The generation of granitic magmas by intrusion of basalt into continental crust. *Journal of Petrology* **29**(3), 599-624.
- Iverson, R. M. (1997). The physics of debris flows. *Rev. Geophysics* **35**(3), 245-296.
- Jackson, R. (1983). Some Mathematical and Physical Aspects of Continuum Models for the Motion of Granular Materials. In: R. E. Meyer (ed.) *Theory of Dispersed Multiphase Flow*. New York, NY: Academic Press, Inc.
- Jan, M. Q. & R. A. Howie (1981). The mineralogy and geochemistry of the metamorphosed basic and ultrabasic rocks of the Jijal complex, Kohistan, NW Pakistan. *Journal of Petrology* **22**, 85-126.
- Johnson, K. L. (1985). *Contact Mechanics*. Cambridge, UK, Cambridge University Press.
- Johnson, P. C. & R. Jackson (1987). Frictional-collisional constitutive relations for granular materials, with application to plane shearing. *Journal of Fluid Mechanics* **176**, 67-93.

- Jones, N. E. (2001). An experimental investigation of particle size distribution effects in dilute phase gas-solid flow, Purdue University.
- Jull, M. & P. B. Kelemen (2001). On the conditions for lower crustal convective instability. *Journal of Geophysical Research* **106**(B4), 6423-6446.
- Kay, R. W. & S. Mahlburg-Kay (1991). Creation and destruction of lower continental crust. *Geologische Rundschau* **80**, 259-278.
- Kay, R. W., S. Mahlburg Kay & R. J. Arculus (1992). Magma genesis and crustal processing. In: D. M. Fountain, R. Arculus and R. W. Kay (ed.) *Continental Lower Crust*. Amsterdam: Elsevier, 423-445.
- Kay, R. W. & S. M. Kay (1993). Delamination and delamination magmatism. *Tectonophysics* **219**, 177-189.
- Klein, M., H. G. Stosch & H. A. Seck (1997). Partitioning of high field-strength and rare-earth elements between amphibole and quartz-dioritic to tonalitic melts; an experimental study. *Chemical Geology* **138**(3-4), 257-271.
- Klein, M., H. G. Stosch, H. A. Seck & N. Shimizu (2000). Experimental partitioning of high field strength and rare earth elements between clinopyroxene and garnet in andesitic to tonalitic systems. *Geochimica Et Cosmochimica Acta* **64**(1), 99-115.
- Kobayashi, K. & E. Nakamura (2001). Geochemical evolution of Akagi volcano, NE Japan: Implications for interaction between island-arc magma and lower crust, and generation of isotopically various magmas. *Journal of Petrology* **42**(12), 2303-2331.
- Lange, R. A. & I. S. E. Carmichael (1987). Densities of Na₂O-K₂O-CaO-MgO-FeO-Fe₂O₃-Al₂O₃-TiO₂-SiO₂ liquids: New Measurements and derived partial molar properties. *Geochimica Et Cosmochimica Acta* **51**, 2931-2946.

- Lange, R. A. & A. Navrotsky (1992). Heat capacities of Fe₂O₃-bearing silicate liquids. *Contributions to Mineralogy and Petrology* **110**, 311-320.
- Lee, C. T., R. L. Rudnick & G. H. Brimhall (2001). Deep lithospheric dynamics beneath the Sierra Nevada during the Mesozoic and Cenozoic as inferred from xenolith petrology. *Geochemistry, Geophysics, Geosystems* **2**(Art. No. 2001GC000152).
- Lidiak, E. G. & W. T. Jolly (1996). Circum-Caribbean granitoids; characteristics and origin. *International Geology Review* **38**(12), 1098-1133.
- Lun, C. K. K., S. B. Savage, D. J. Jeffrey & N. Chepuniy (1984). Kinetic Theories for granular flow: inelastic particles in Couette flow and slightly inelastic particles in a general flow field. *J. Fluid Mech* **140**, 223-256.
- Lundstrom, C. C. (2003). Uranium-series disequilibria in mid-ocean ridge basalts: observations and models of basalt genesis. *Reviews in mineralogy and geochemistry* **52**, 175-214.
- Lyakhovskiy, V., S. Hurwitz & O. Navon (1996). Bubble Growth in rhyolitic melts: experimental and numerical investigation. *Bull. Volcanology* **58**, 19-32.
- Mader, H. M. (1998). Conduit Flow and Fragmentation. In: J. S. Gilbert and R. S. J. Sparks (ed.) *The Physics of Explosive Volcanic Eruptions*. London, UK: Geological Society Special Publication, 51-70.
- Marsh, B. D. (1981). On the crystallinity, probability of occurrence, and rheology of lava and magma. *Contributions to Mineralogy and Petrology* **78**, 85-98.
- Martin, D. & R. Nokes (1988). Crystal settling in a vigorously convecting magma chamber. *Nature* **332**, 534-536.
- Maxey, M. R. & J. J. Riley (1983). Equation of motion for a small rigid sphere in non-uniform flow. *Physics of Fluids* **26**(4), 883-889.

- McCarthy, T. C. & A. E. Patiño-Douce (1997). Experimental evidence for high-temperature felsic melts formed during basaltic intrusion of the deep crust. *Geology* **25**(5), 463-466.
- McDade, P., J. Blundy & B. Wood (2003). Trace element partitioning of the Tinaquillo Lherzolite solidus at 1.5 GPa. *Physics of the Earth and Planetary Interiors* **139**, 129-147.
- McKenzie, D. (1985). ²³⁰Th-²³⁸U disequilibrium and the melting processes beneath ridge axes. *Earth and Planetary Science Letters* **72**, 149-157.
- McKenzie, D. & M. J. Bickle (1988). The volume and composition of melt generated by extension of the lithosphere. *Journal of Petrology* **29**(3), 625-679.
- Meissner, R. & W. Mooney (1998). Weakness of the lower continental crust: a condition for delamination, uplift and escape. *Tectonophysics* **296**(1-2), 47-60.
- Melnik, O. E., A. A. Barmin & R. S. J. Sparks (2003). Conduit flow model for the case of high-viscous, gas-saturated magma. *Journal of Volcanology and Geothermal Research*.
- Middleton, G. V. (1966). Experiments on density and turbidity currents. *Canadian Journal of Earth Science* **3**, 523-637.
- Miller, A. & D. Gidaspow (1992). Dense, vertical gas-solid flow in a pipe. *American Institute of Chemical Engineers Journal* **38**(11), 1801-1815.
- Montgomery, D. R., G. Balco & S. D. Willet (2001). Climate, tectonics and the morphology of the Andes. *Geology* **29**(7), 579-582.
- Mukasa, S. B. & J. W. Shervais (1999). Growth of subcontinental lithosphere: evidence from repeated dike injections in the Balmuccia lherzolite massif, Italian Alps. *Lithos* **48**, 287-316.

- Muntener, O., P. B. Kelemen & T. L. Grove (2001). The role of H₂O during crystallization of primitive arc magmas under uppermost mantle conditions and genesis of igneous pyroxenites: an experimental study. *Contributions to Mineralogy and Petrology* **141**(6), 643-658.
- Necker, F., C. Hartel, L. Kleiser & E. Meiburg (2002). High-resolution simulations of particle-driven gravity currents. *International Journal of Heat and Mass Transfer* **28**(2), 279-300.
- Neri, A. & F. Dobran (1994). Influence of eruption parameters on the thermofluid dynamics of collapsing volcanic columns. *JGR* **99**(B6), 11,833-11,857.
- Neri, A. & G. Macedonio (1996). Numerical simulation of collapsing volcanic columns with particles of two sizes. *JGR* **101**(B4), 8153-8174.
- Neri, A. & D. Gidaspow (2000). Riser hydrodynamics: Simulation using kinetic theory. *Particle Technology and Fluidization* **46**(1), 52-67.
- Neri, A., A. Di Muro & M. Rosi (2002). Mass partition during collapsing and transitional columns by using numerical simulations. *JVGR* **115**, 1-18.
- O'Brien, T. J. & M. Syamlal (1991). Fossil Fuel Circulating Fluidized Bed: Simulation and Experiment. In: E. L. Gaden and A. W. Weimer (ed.) *Advances in Fluidized Systems: AIChE Symposium Series*, **281**, 127-136.
- Papale, P. & F. Dobran (1993). Magma flow along the volcanic conduit during the Plinian and pyroclastic flow phases of the May 18, 1980, Mount St. Helens eruption. *Journal of Geophysical Research* **99**, 4355-4373.
- Papale, P. & F. Dobran (1994). Magma flow along the volcanic conduit during the Plinian and pyroclastic flow phases of the May 18, 1980, Mt. St. Helens eruption. *JGR* **99**(B3), 4355-4373.

- Papale, P., A. Neri & G. Macedonio (1998). The role of magma composition and water content in explosive eruptions - 1. Conduit ascent dynamics. *JVGR* **87**(1-4), 75-93.
- Papale, P. (1999). Strain-induced magma fragmentation in explosive eruptions. *Nature* **397**, 425-428.
- Papale, P. & M. Polacci (1999). Role of carbon dioxide in the dynamics of magma ascent in explosive eruptions. *Bull. Volcanology* **60**(8), 583-594.
- Papale, P. (2001). Dynamics of magma flow in volcanic conduits with variable fragmentation efficiency and nonequilibrium pumice degassing. *JGR* **106**(B6), 11,043-11,065.
- Parsons, J. D. (1998). Mixing Mechanisms in Density Intrusions. Civil Engineering. Urbana-Champaign, University of Illinois, 258.
- Parsons, J. D. & M. H. Garcia (1998). Similarity of gravity current fronts. *Physics of Fluids* **10**(12), 3209-3213.
- Patankar, S. V. & D. B. Spalding (1972). A calculation procedure for heat, mass, and momentum transfer in three-dimensional parabolic flows. *International Journal of Heat and Mass Transfer* **15**, 1787.
- Patankar, S. V. (1980). *Numerical Heat Transfer and Fluid Flow*. New York, Hemisphere.
- Patiño-Douce, A. & J. Beard (1994). Dehydration-melting of biotite gneiss and quartz amphibolite from 3 to 15 kbar. *Journal of Petrology* **36**(3), 707-738.
- Patiño-Douce, A. E. & A. D. Johnston (1991). Phase equilibria and melt productivity in the pelitic system: implications for the origin of peraluminous granitoids and aluminous granulites. *Contributions to Mineralogy and Petrology* **107**, 202-218.

- Patiño-Douce, A. E. & J. Beard (1995). Dehydration-melting of biotite gneiss and quartz amphibolite from 3 to 15 kbar. *Journal of Petrology* **36**, 707-738.
- Pedersen, T., M. Heeremans & P. van der Beek (1998). Models of crustal anatexis in volcanic rifts: applications to southern Finland and the Oslo Graben, southeast Norway. *Geophysical Journal International* **132**(2), 239-255.
- Peirano, E. & B. Leckner (1998). Fundamentals of turbulent gas-solid flows applied to circulating fluidized bed combustion. *Prog. Energy Combust. Sci.* **24**, 259-296.
- Petford, N. & K. Gallagher (2001). Partial melting of mafic (amphibolitic) lower crust by periodic influx of basaltic magma. *Earth and Planetary Science Letters* **193**, 483-499.
- Pickett, D. A. & J. B. Saleeby (1993). Thermobarometric constraints on the depth of exposure and conditions of plutonism and metamorphism at deep levels of the Sierra-Nevada Batholith, Tehachapi Mountains, California. *Journal of Geophysical Research* **98**(B1), 609-629.
- Pinkerton, H. & R. J. Stevenson (1992). Methods of determining the rheological properties of magmas at sub-liquidus temperatures. *Journal of Volcanology and Geothermal Research* **53**(1-4), 47-66.
- Raia, F. & F. J. Spera (1997). Simulations of crustal anatexis: Implications for the growth and differentiation of continental crust. *Journal of Geophysical Research* **102**(B10), 22,629-22,648.
- Raju, N. & E. Meiburg (1995). The accumulation and dispersion of heavy particles in forced two-dimensional mixing layers. Part 2. The effect of gravity. *Physics Fluids* **7**, 1241-1264.
- Rapp, R. P. (1991). Origin of Archean granitoids and continental evolution. *EOS: Trans. AGU* **72**(No. 20), 225, 229.

- Rapp, R. P., E. B. Watson & C. F. Miller (1991). Partial melting of amphibolite/eclogite and the origin of Archean trondhjemites and tonalites. *Precambrian Research* **51**, 1-25.
- Rapp, R. P. & E. B. Watson (1995). Dehydration Melting of Metabasalt at 8-32 kbar: Implications for Continental Growth and Crust-Mantle Recycling. *Journal of Petrology* **36**(4), 891-931.
- Renner, J., B. Evans & G. Hirth (2000). On the rheologically critical melt fraction. *Earth and Planetary Science Letters* **181**, 585-594.
- Rudnick, R. L. & S. R. Taylor (1987). The composition and petrogenesis of the lower crust: A xenolith study. *Journal of Geophysical Research* **92**(B13), 13,981-14,005.
- Rudnick, R. L. (1990). Growing from below. *Nature* **347**, 711-712.
- Rushmer, T. (1991). Partial melting of two amphibolites: contrasting experimental results under fluid-absent conditions. *Contributions to Mineralogy and Petrology* **107**, 41-59.
- Rushmer, T. (1995). An experimental deformation of partially molten amphibolite: Application to low-melt fraction segregation. *Journal of Geophysical Research* **100**, 15,681-15,695.
- Saleeby, J., M. Ducea & D. Clemens-Knott (2003). Production and loss of high-density batholithic root, southern Sierra Nevada, California. *Tectonics* **22**(6), Art. No. 1064.
- Saleeby, J. & Z. Foster (2004). Topographic response to mantle lithosphere removal in the southern Sierra Nevada region, California. *Geology* **32**(3), 245-248.

- Savage, S. B. (1998). Analyses of slow high-concentration flows of granular materials. *JFM* **377**, 1-26.
- Scaillet, B., F. Holtz & M. Pichavant (1998). Phase equilibrium constraints on the viscosity of silicic magmas; 1. Volcanic-plutonic comparison. *Journal of Geophysical Research* **103**(B11), 27257-27266.
- Sen, C. & T. Dunn (1994). Dehydration melting of a basaltic composition amphibolite at 1.5 and 2.0 GPa: implications for the origin of adakites. *Contributions to Mineralogy and Petrology* **117**, 394-409.
- Shaw, H. R. (1972). Viscosities of magmatic liquids: an empirical method of prediction. *American Journal of Science* **272**, 870-893.
- Sims, K. W. W., D. J. DePaolo, M. T. Murrell, W. S. Baldrige, S. Goldstein, D. Clague & M. Jull (1999). Porosity of the melting zone and variations in the solid mantle upwelling rate beneath Hawaii: Inferences from ^{238}U - ^{230}Th - ^{226}Ra and ^{235}U - ^{231}Pa disequilibria. *Geochimica Et Cosmochimica Acta* **63**(23-24), 4119-4138.
- Sisson, T. W., K. Ratajeski, W. B. Hankins & A. F. Glazner (in press). Voluminous granitic magmas from common basaltic sources. *Contributions to Mineralogy and Petrology*.
- Slezin, Y. B. (2003). The mechanism of volcanic eruptions (a steady state approach). *Journal of Volcanology and Geothermal Research* **122**, 7-50.
- Sommerfeld, M. (2003). Analysis of collision effects for turbulent gas-particle flow in a horizontal channel: Part1. particle transport. *Int. J. of Multiphase Flow* **29**(4), 675-699.
- Sparks, R. J. S., L. Wilson & G. Hulme (1978). Theoretical modeling of the generation, movement and emplacement of pyroclastic flows by column collapse. *Journal of Volcanology and Geothermal Research* **83**, 1727-1739.

- Squires, K. D. & J. K. Eaton (1991). Preferential concentration of particles by turbulence. *Phys. Fluids A* **3**, 1169-1178.
- Sun, S. S. & W. F. McDonough (1989). Chemical and isotopic systematics of oceanic basalts; implication for mantle composition and processes. *Geological Society Special Publication* **42**(313-345).
- Syamlal, M. (1987). A Review of Granular Stress Constitutive Relations. Springfield, VA, National Technical Information Service.
- Syamlal, M. (1987). A review of granular stress constitutive relations. Springfield, VA, Department of Energy, 21353-2372.
- Syamlal, M., W. Rogers & T. J. O'Brien (1993). MFIIX Documentation: Theory Guide. Morgantown, WV, U.S. Department of Energy, 1-49.
- Thomas, N., C. Jaupart & S. Vergnolle (1994). On the vesicularity of pumice. *JGR* **99**, 15633-15644.
- Thomas, R. S., M. M. Hirshmann, H. Cheng, M. K. Reagan & R. L. Edwards (2002). (Pa-231/U-235)-(Th-230/U-238) of young mafic volcanic rocks from Nicaragua and Costa Rica and the influence of flux melting on U-series systematics of arc lavas. *Geochim. Cosmochim. Acta.* **66**(24), 4287-4309.
- Touloukian, Y. S., W. R. Judd & R. F. Roy, Eds. (1981). *Physical Properties of Rocks and Minerals*. New York, McGraw-Hill Book Co.
- Trumbull, R. B., R. Wittenbrink, K. Hahne, R. Emmermann, W. Busch, H. Gerstenberger & W. Siebel (1999). Evidence for late Miocene to recent contamination of arc andesites by crustal melts in the Chilean Andes (25-26 degrees) and its geodynamic implications. *Journal of South American Earth Sciences* **12**(2), 135-155.
- Tulloch, A. J. & D. L. Kimbrough (2003). Paired plutonic belts in convergent margins and the development of high Sr/Y magmatism: the Peninsular Ranges

Batholith of California and the Median Batholith of New Zealand. *Geological Society of America Special Paper* **374**, 275-295.

- Turner, S., B. Bourdon, C. Hawkesworth & P. Evans (2000). 226Ra-230Th evidence for multiple dehydration events, rapid melt ascent and the time scales of differentiation beneath the Tonga-Kermadec island arc. *Earth and Planetary Science Letters* **179**, 581-593.
- Turner, S., P. Evans & C. Hawkesworth (2001). Ultrafast source-to-surface movement of melt at island arcs from 226Ra-230Th systematics. *Science* **292**, 1363-1366.
- Turner, S., J. Foden, R. George, P. Evans, R. Varne, M. Elburg & G. Jenner (2003). Rates and process of potassic magma evolution beneath Sangeang Api Volcano, East Sunda Arc, Indonesia. *Journal of Petrology* **44**(3), 491-515.
- Turner, S., R. George, D. A. Jerram, N. Carpenter & C. Hawkesworth (2003). Case studies of plagioclase growth and residence times in island arc lavas from Tonga and the Lesser Antilles, and a model to reconcile discordant age information. *Earth and Planetary Science Letters* **214**(1-2), 279-294.
- Valentine, G. A. (1987). Stratified flow in pyroclastic surges. *Bulletin of Volcanology* **49**, 616-630.
- Valentine, G. A. & K. H. Wohletz (1989). Numerical models of Plinian eruption columns and pyroclastic flows. *JGR* **94**(B2), 1867-1887.
- van Westrenen, W., J. D. Blundy & B. J. Wood (2001). High field strength element/rare earth element fractionation during partial melting in the presence of garnet: Implications for identification of mantle heterogeneities. *Geochem. Geophys. Geosyst.* **2**, Paper number 2000GC000133.
- Versteeg, H. K. & W. Malalasekera (1995). *An introduction to computational fluid dynamics: the finite volume method*. Harlow, England, Pearson Education Limited.

- Vigneresse, J. L., P. Barbey & M. Cuney (1996). Rheological transitions during partial melting and crystallization with application to the felsic magma segregation and transfer. *Journal of Petrology* **37**, 1579-1600.
- Vigneresse, J. L. & B. Tikoff (1999). Strain partitioning during partial melting and crystallizing felsic magmas. *Tectonophysics* **312**, 117-132.
- Voller, V. R. & C. R. Swaminathan (1991). General source-based method for solidification phase change. *Numerical Heat Transfer* **19B**, 175-189.
- Wada, Y. (1994). On the relationship between dike width and magma viscosity. *Journal of Geophysical Research* **99**(9), 17743-17755.
- Wells, P. R. A. (1980). Thermal models for the magmatic accretion and subsequent metamorphism of continental crust. *Earth and Planetary Science Letters* **46**, 253-265.
- Williams, M. L., S. Hanmer, C. Kopf & M. Darrach (1995). Syntectonic generation and segregation of tonalitic melts from amphibolite dikes in the lower crust, Striding-Athabasca mylonite zone, northern Saskatchewan. *Journal of Geophysical Research* **100**(8), 15717-15734.
- Wilson, J. & J. W. Head III (1981). Ascent and eruption of basaltic magma on the earth and the moon. *Journal of Geophysical Research* **86**, 2971-3001.
- Wilson, L. (1976). Explosive volcanic eruptions, III. Plinian eruption columns. *Geophys. J. R. Astron. Soc.* **45**, 543-556.
- Wolf, M. B. & P. J. Wyllie (1994). Dehydration-melting of amphibolite at 10 kbar: the effects of temperature and time. *Contributions to Mineralogy and Petrology* **115**, 369-383.
- Yamamoto, Y., M. Potthoff, T. Tanaka, T. Kajishima & Y. Tsuji (2001). Large-eddy simulation of turbulent gas-particle flow in a vertical channel: effect of

considering inter-particle collisions. *Journal of Fluid Mechanics* **442**, 303-334.

Yunker, L. W. & T. A. Vogel (1976). Plutonism and plate tectonics: the origin of circum-Pacific batholiths. *Canadian Mineralogist* **14**, 238-244.

Zellmer, G. F., C. J. Hawkesworth, R. S. J. Sparks, L. E. Thomas, C. L. Harford, T. S. Brewer & S. C. Loughlin (2003). Geochemical evolution of the Soufriere Hills Volcano, Montserrat, Lesser Antilles Volcanic Arc. *Journal of Petrology* **44**(8), 1349-1374.

Zhang, Y. X. (1999). Exsolution enthalpy of water from silicate liquids. *JVGR* **88**(3), 201-207.

Zou, H. (1998). Trace element fractionation during modal and nonmodal dynamic melting and open-system melting: A mathematical treatment. *Geochimica Et Cosmochimica Acta* **62**(11), 1937-1945.

Zou, H. & A. Zindler (2000). Theoretical studies of ^{238}U - ^{230}Th - ^{226}Ra and ^{235}U - ^{231}Pa disequilibria in young lavas produced by mantle melting. *Geochimica Et Cosmochimica Acta* **64**(10), 1809-1817.

Zou, H. & M. Reid (2001). Quantitative modeling of trace element fractionation during incongruent melting. *Geochimica Et Cosmochimica Acta* **65**(1), 153-162.

APPENDIX A: Magma Properties

I. Mixture Properties

Both phase change and advection can result in mixtures of melt and solid and magmas of different composition residing in a control volume. A composition parameter (γ) describes the volume fraction of crustal material or intruded basalt residing at a particular location. If the γ equals one, the region is all crustal material, and if it equals zero it is all mantle-derived basalt. Intermediate values indicate relative proportions, and hence locally mixed material. The variable, f , denotes the local melt fraction. In the following nomenclature, the subscripts b and c will be used to refer to properties of the basalt and crust, respectively. Superscripts s and l refer to solid and melt. The mixture properties are defined as:

Mixture Density:

$$\rho_{\text{mix}} = \gamma f_c \rho_c^l + \gamma(1-f_c) \rho_c^s + (1-\gamma) f_b \rho_b^l + (1-\gamma)(1-f_b) \rho_b^s. \quad (\text{A.1})$$

Mixture Heat Capacity:

$$c_{\text{mix}} = \gamma f_c c_c^l + \gamma(1-f_c) c_c^s + (1-\gamma) f_b c_b^l + (1-\gamma)(1-f_b) c_b^s. \quad (\text{A.2})$$

Mixture Conductivity:

$$k_{\text{mix}} = \gamma f_c k_c^l + \gamma(1-f_c) k_c^s + (1-\gamma) f_b k_b^l + (1-\gamma)(1-f_b) k_b^s \quad (\text{A.3})$$

The rheology of solid/melt mixtures has been observed to deviate significantly from a simple linear mixing relationship as is depicted in *Appendix A Figure 1* (Vigneresse *et al.*, 1996; Barboza & Bergantz, 1998; Vigneresse & Tikoff, 1999; Renner *et al.*, 2000). Solid volume fractions that form an interlocking crystalline framework may greatly increase the mixture viscosity (Marsh, 1981). The critical melt fraction at this transition, CMF, is likely to be dependent on the strain rate of the material (Renner *et*

al., 2000) and may vary over a wide range of values (Barboza & Bergantz, 1998). A rapid drop in viscosity has not been observed in experiments with melt fractions reaching ~ 0.2 (Rushmer, 1995). We assume a critical melt fraction of .4 in order to link the bulk rheology of a melt supported crystal suspension to an interlocking crystal framework (Marsh, 1981). This is equivalent to the CMF suggested by Scaillet et al. (1998) for a monodisperse crystal size distribution.

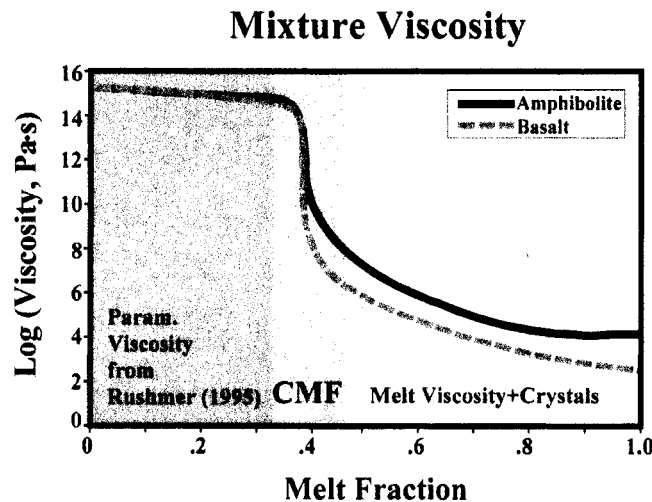


Figure A.1: Mixture viscosity as a function of melt fraction. The critical melt fraction (CMF) marks the transition from an interlocking crystalline framework and crystal-melt suspension. The CMF is assumed to equal 0.4 for mono-disperse crystal size distribution (Scaillet et al., 1998).

When the melt fraction is below the critical melt fraction, an empirically derived viscosity was used, motivated by the amphibolite deformation experiments of Rushmer (1995). The ductile rheology used here assumes a linear relationship between the applied stress and strain rate, and is a macroscopic manifestation of a process that has been shown to be a combination of brittle and plastic flow (Rushmer, 1995). This functional form is equivalent to an assumption of diffusion creep at low

melt fractions. For the subset of calculations that include the mantle interface, the diffusion creep of olivine was used as a proxy for mantle rheology (Hirth & Kohlstedt, 1995; Hirth & Kohlstedt, 1996; Jull & Kelemen, 2001). Above the critical melt fraction, the mixture viscosity is modified from the melt viscosity to account for the macroscopic effect of increased drag between crystals and melt (Marsh, 1981; Dobran, 1992; Pinkerton & Stevenson, 1992; Scaillet *et al.*, 1998). The mixture viscosity for melt fraction greater than the CMF becomes:

$$\mu_{\text{mix}} = \mu_{\text{m}}^i \left[1 + .75 \left(\frac{(1-f)/(1-\text{CMF})}{1-(1-f)/(1-\text{CMF})} \right) \right]^2. \quad (\text{A.4})$$

For melt fractions below the critical melt fraction the mixture rheology for the crust and mantle are given by:

$$\mu_{\text{mix}} = \mu_{\text{param}}, \quad (\text{A.5})$$

and

$$\mu_{\text{mantle}} = \frac{A^{-1/n} \exp\left(\frac{Q}{nRT}\right)}{2}, \quad (\text{A.6})$$

respectively. Here the parameters for the mantle rheology are,

$$\ln(A) = 15.4 \text{ MPa}^{-n} \text{ s}^{-1}, \quad Q = 515 \text{ kJ/mol}, \quad n = 3.5 \quad (\text{A.7})$$

(Hirth & Kohlstedt, 1996; Jull & Kelemen, 2001).

II. Numerical Method

The conservation equations were discretized using a finite volume numerical method (Patankar, 1980). The iterative procedure SIMPLER (Semi-Implicit Method for Pressure Linked Equations, Revised) was used to insure the pressure and velocity simultaneously satisfy both momentum and continuity (Patankar & Spalding, 1972; Patankar, 1980; Versteeg & Malalasekera, 1995). The power-law algorithm of Patankar (1980) was used in dynamic simulations and uses a hybrid of central

differencing and upwinding numerical schemes depending on the local Peclet number. Additionally, a predictor-corrector algorithm was used to compute the partitioning of energy into sensible and latent heat during phase change processes. Iteration and numerical under-relaxation was required for convergence given the non-linear melt fraction versus temperature relationships. The predictor-corrector phase change algorithm of Voller & Swaminathan (1991) has shown the best convergence and was used for the calculations presented.

III. Physical and Thermal Properties of Solid and Melt

The composition of the magma, and its volatile contents, determine the physical properties of the magma such as density and viscosity that are required to close equations A2-A5. The composition of the melts are projected from the amphibolite dehydration experiments of Wolf & Wyllie (1994) and the basaltic andesite crystallization experiments of Muntener et al. (2001) (*Appendix, Figures A.2 and A.3*). The experimentally determined compositions were parameterized with second-order polynomials in order to provide a relationship between the melt fraction and the composition of the magma.

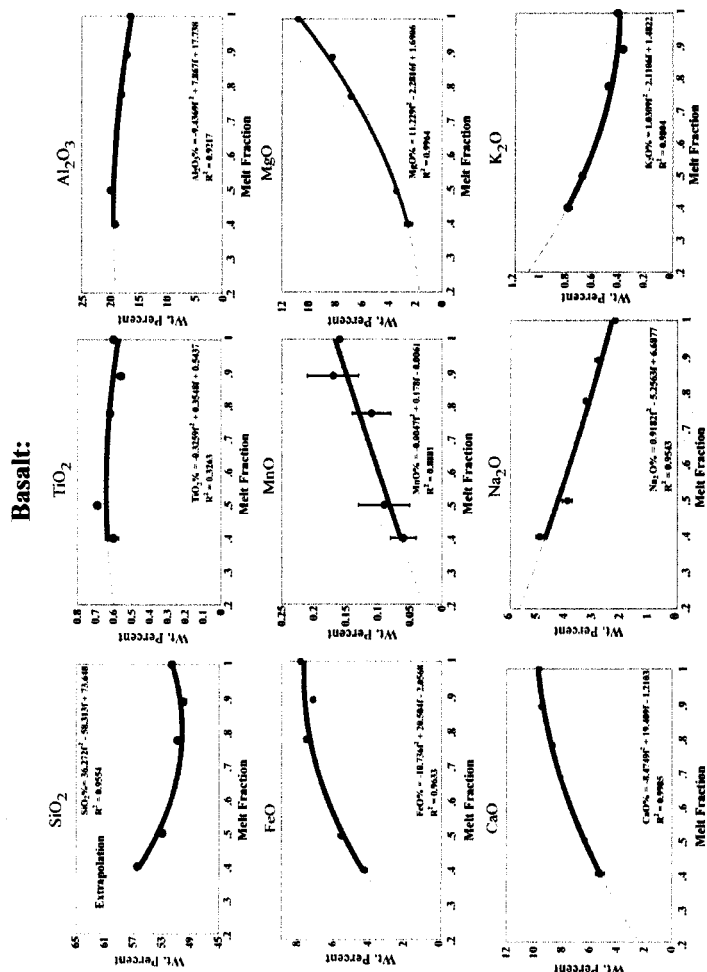


Figure A.2: Major element geochemical trends for the modeled intruded basalt versus melt fraction (Muntener *et al.*, 2001). Dashed line is an extrapolation of experimental values (circles). These experiments were performed on a basaltic andesite at 12 kbar with 3.8 wt. % water.

Amphibolite:

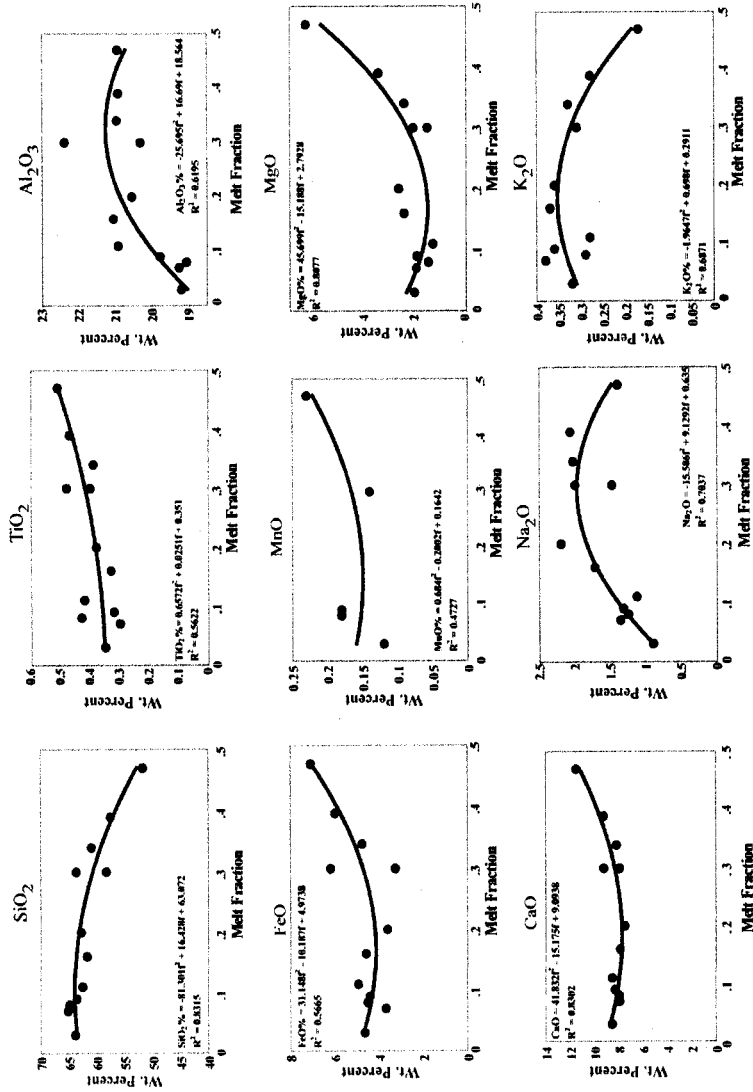


Figure A.3: Major element geochemical trends for the modeled amphibolitic crust versus melt fraction (Wolf & Wyllie, 1994). These experiments were performed on a high Mg # amphibolite at 10 kbar

The lowest melt fraction reported by Muntener et al. (2001) for the crystallizing basalt was .39. Extrapolation of the composition to melt fractions lower than .39 was accomplished with MELTS, with the acknowledgement that error is introduced by the uncertainty in the mode of the crystallizing phases outside of the experimental range due to the decreased range of amphibole stability in the thermodynamic calculations. The composite P-T diagram of a tholeiite with 5 wt. % water developed by Green (1982) indicates that the first appearance of plagioclase is at about $\sim 800^{\circ}\text{C}$ at 12 kbar which corresponds to a melt fraction between $\sim .1$ -.2. The MELTS calculations also reach plagioclase saturation at $\sim .2$ melt fraction.

IV. Transport Properties

Magmatic density, heat capacity, and viscosity can be determined using the correlations of Lange & Carmichael (1987), Lange & Navrotsky (1992), and Shaw (1972), respectively. Solid densities and heat capacities were determined using the experimental phase assemblages of Wolf & Wyllie (1994) and Muntener et al. (2001) and the thermodynamic database of Holland & Powell (1998). For the crystallizing basalt, the density was calculated at less than .39 melt fraction using MELTS (Ghiorso & Sack, 1995). These MELTS calculations reached amphibole saturation at .18 melt fraction compared to the first appearance of amphibole at $\sim .39$ for the same conditions in the experiments. This discrepancy is a likely consequence of the complexity of amphibole solid-solution. The difference in mode appears to be accounted for by clinopyroxene.

Garnet in the experiments and MELTS calculations crystallizes at approximately the same melt fraction and has a mode of 17% in the MELTS calculation and 15% in the experiments at a melt fraction of .39. The density of clinopyroxene and amphibole are very similar and so while the mode of the thermodynamic calculations did not exactly reproduce the experiments, the density was reasoned to be a good proxy. Other specified parameters used in the simulations

are included in *Table 2.3*. Mixture, melt and solid density of the residual melt from the intruding basalt and the amphibolite are compared as a function of melt fraction at 12 kbar in *Appendix Figure A.4* along with the density of a mantle peridotite at 800°C.

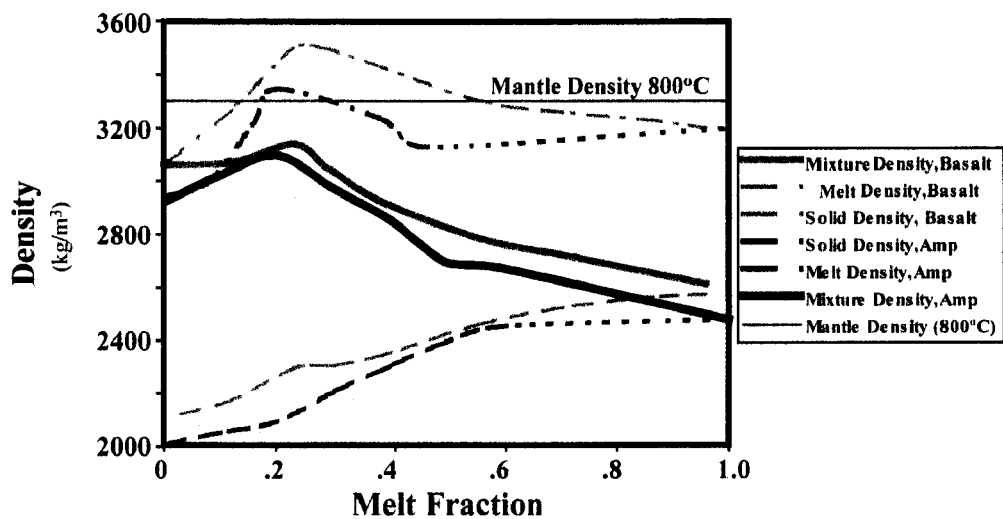


Figure A.4: Density of amphibolite and wet basalt as a function of melt fraction at 12 kbar (solid lines). Calculations are based off the dataset of Holland and Powell (1998) (crystals) and the algorithm of Lange and Carmichael (1987) (melt). Also shown are the cumulate and melt density as dashed lines.

**APPENDIX B:
Derivation of Collisionless Granular Transport**

As shown by Chapman and Cowling (1952) a general transport equation for a quantity γ is:

$$\frac{\partial n\langle\gamma\rangle}{\partial t} + \frac{\partial}{\partial \mathbf{x}_j} n\langle\gamma \mathbf{c}_i\rangle - n\mathbf{F}_i \left\langle \frac{\partial \gamma}{\partial \mathbf{c}_i} \right\rangle = \int \gamma \left(\frac{\partial f}{\partial t} \right)_{\text{coll}} d\mathbf{c}_i \quad (B1)$$

where f is the frequency distribution of velocities, \mathbf{F}_i is specific-force (N/kg), n is the number of particles in a control volume, $\left(\frac{\partial f}{\partial t} \right)_{\text{coll}}$ is the rate of change of the frequency distribution of particles as a result of collisions, and the average for a quantity is defined as:

$$n\langle\gamma\rangle = \int \gamma f d\mathbf{c}_i. \quad (B2)$$

If no collisions occur, the source term on the right hand side of equation (B1) goes to zero. To obtain an equation for the transport of momentum, let $\gamma = m\mathbf{c}_j$, where m is the mass of a particle. Using the fact that the product of the mass and number of particles is equal to the product of the density and volume fraction of particles ($m_p n = \rho_p \varepsilon_p$) and decomposing the velocity, \mathbf{c}_j , into its fluctuating component, \mathbf{C}_j , and its average \mathbf{u}_j gives:

$$\frac{\partial \rho \varepsilon \mathbf{u}_j}{\partial t} + \frac{\partial}{\partial \mathbf{x}_i} \rho \varepsilon \mathbf{u}_i \mathbf{u}_j + \frac{\partial}{\partial \mathbf{x}_i} \rho \varepsilon \langle \mathbf{C}_i \mathbf{C}_j \rangle - \rho \varepsilon \mathbf{F}_i \delta_{ij} = 0. \quad (B3)$$

To obtain this result note that:

$$\langle (\langle \mathbf{c}_i \rangle + \mathbf{C}_i) (\langle \mathbf{c}_j \rangle + \mathbf{C}_j) \rangle = \langle \mathbf{u}_i \mathbf{u}_j + \mathbf{C}_i \mathbf{u}_j + \mathbf{C}_j \mathbf{u}_i + \mathbf{C}_i \mathbf{C}_j \rangle = \mathbf{u}_i \mathbf{u}_j + \langle \mathbf{C}_i \mathbf{C}_j \rangle, \quad (B4)$$

$$\frac{\partial \mathbf{u}_j}{\partial \mathbf{u}_i} = 1 \text{ if } i = j, \quad (B5)$$

and

$$\frac{\partial \mathbf{u}_j}{\partial \mathbf{u}_i} = 0 \text{ if } i \neq j. \quad (B6)$$

A common first approximation of granular flows (Gidaspow, 1994; Chapman and Cowling, 1952) is that the velocity varies randomly about the mean velocity (i.e. it has a Maxwellian velocity distribution). Hence, it can be shown that the off diagonal terms of the $\langle \mathbf{C}_i \mathbf{C}_j \rangle$ tensor go to zero leaving the equation:

$$\frac{\partial \rho_p \varepsilon_p \mathbf{u}_j}{\partial t} + \frac{\partial}{\partial \mathbf{x}_i} \rho_p \varepsilon_p \mathbf{u}_i \mathbf{u}_j + \frac{\partial}{\partial \mathbf{x}_i} \rho_p \varepsilon_p \langle \mathbf{C}_i \mathbf{C}_j \rangle \delta_{ij} - \rho_p \varepsilon_p \mathbf{F}_i \delta_{ij} = 0, \quad (B7)$$

where the term $\rho_p \varepsilon_p \langle \mathbf{C}_i \mathbf{C}_j \rangle \delta_{ij}$ acts as the kinetic, or translational, stress in the equation. Equation (B7) is the equation of an inviscid granular material, and thus a good approximation is that a collision-less granular material is inviscid (Gidaspow, 1994).

**APPENDIX C:
Granular Constitutive Relations**

Momentum Equation Constitutive Relations

Stress Tensor

$${}^m\boldsymbol{\tau}_{ij} = 2{}^m\alpha{}^m\mu{}^m\mathbf{e}_{ij} + {}^m\alpha\left({}^m\lambda - \frac{2}{3}{}^m\mu\right)\frac{\partial{}^mU_i}{\partial x_i}\delta_{ij}, \quad (C1)$$

Rate of Strain

$${}^m\mathbf{e}_{ij} = \frac{1}{2}\left(\frac{\partial{}^mU_i}{\partial x_j} + \frac{\partial{}^mU_j}{\partial x_i}\right). \quad (C2)$$

Granular Phases

Total Granular Pressure

$${}^pP = {}^pP^f + {}^pP^{kc} \quad (C3)$$

Total Bulk Viscosity

$${}^p\lambda = {}^p\lambda^f + {}^p\lambda^{kc} \quad (C4)$$

Total Shear Viscosity

$${}^p\mu = {}^p\mu^f + {}^p\mu^{kc} \quad (C5)$$

Kinetic-Collisional Pressure

$${}^pP^{kc} = {}^p\alpha{}^p\rho{}^p\theta[1 + 2{}^p\alpha g_0(1 + e)] \quad (C6)$$

Total Kinetic-Collisional Viscosity

$${}^p\mu^{kc} = {}^p\alpha{}^p\rho({}^p\nu^{kin} + {}^p\nu^{coll}) \quad (C7)$$

Kinetic Shear Viscosity

$${}^p\nu^{kin} = \left[\frac{2}{3}k_{12}\eta_t + {}^p\theta(1 + \zeta_{c2}{}^p\alpha g_0)\right]\tau_p \quad (C8)$$

Collisional Shear Viscosity

$${}^p \nu^{coll} = \frac{8}{5} {}^p \alpha g_0 \frac{(1+e)}{2} \left({}^p \nu^{kin} + d \sqrt{\frac{{}^p \theta}{\pi}} \right) \quad (C9)$$

Collisional Bulk Viscosity

$${}^p \lambda = \frac{5}{3} {}^p \alpha {}^p \rho {}^p \nu^{coll} \quad (C10)$$

Frictional Pressure

$$P^f = a_{fs} \frac{({}^1 \alpha^{max} - {}^1 \alpha)^{b_{fs}}}{({}^1 \alpha - {}^1 \alpha^{min})^{b_{fs}}}, \text{ for } {}^1 \alpha^{min} < {}^1 \alpha < {}^1 \alpha^{max}, \text{ else } P^f = 0 \quad (C11)$$

Effective Viscosity Frictional Regime

$${}^p \mu^f = \frac{P^f \sin^2 {}^p \varphi}{\sqrt{4 \sin^2 {}^p \varphi I_{2D} + \left(\frac{\partial {}^p U_l}{\partial x_i} \right)^2}} \quad (C12)$$

Bulk Viscosity Frictional Regime

$${}^p \lambda^f = -\frac{2}{3} {}^p \mu^f \quad (C13)$$

Fluid Phase**Total Shear Viscosity**

$${}^1 \mu = {}^1 \mu^{mol} + {}^1 \mu^f \quad (C14)$$

Molecular Viscosity

$${}^1 \mu^{mol} = 1.7 \times 10^{-5} \left(\frac{{}^1 T}{273} \right)^{1.5} \left(\frac{383}{{}^1 T + 110} \right) \quad (C15)$$

Effective Turbulent Viscosity

$${}^1 \mu^t = {}^1 \rho C_\mu \frac{({}^1 k)^2}{{}^1 \varepsilon} \quad (C16)$$

Bulk Viscosity

$${}^1 \lambda = -\frac{2}{3} ({}^1 \mu) \quad (C17)$$

Particle-Gas Drag

$${}^1I_i = \frac{3^p \alpha^1 \alpha^1 \rho}{4V_r d} C_D^s |{}^1U_i - {}^pU_i| ({}^1U_i - {}^pU_i) - {}^p\alpha \frac{\partial}{\partial x_i} {}^1P \quad (C18)$$

Ratio of terminal velocity of a group of particles to the single particle terminal velocity

$$V_r = .5(A - .06Re_p + \sqrt{(.06Re_p)^2 + .12Re_p(2B - A) + A^2}) \quad (C19)$$

where:

$$A = {}^1\alpha^{4.14} \quad (C20)$$

$$B = \begin{cases} .8 {}^1\alpha^{1.28} & \text{if } {}^1\alpha \leq .85 \\ {}^1\alpha^{2.65} & \text{if } {}^1\alpha > .85 \end{cases} \quad (C21)$$

Drag Coefficient

$$C_D^s = \left[.63 + \frac{4.8}{\sqrt{Re_p}} \right]^2 \quad (C22)$$

Particle Reynolds Number

$$Re_p = \frac{d |{}^pU_i - {}^1U_i| {}^1\rho}{{}^1\mu} \quad (C23)$$

Momentum Transfer Between Particle Phases

$${}^pI_i = -F_{sp} ({}^pU_i - {}^sU_i), \quad s \neq p \quad (C24)$$

Coefficient of interphase force between particle phases

$$F_{sp} = \frac{3(1+e)\left(\frac{\pi}{2} + F_c \frac{\pi^2}{8}\right) ({}^2\alpha) ({}^2\rho) ({}^3\alpha) ({}^3\rho) ({}^2d + {}^3d)^2 g_0 ({}^2U_i - {}^3U_i)}{2\pi ({}^2\rho) ({}^2d)^3 + ({}^3\rho) ({}^3d)^3} + H_1 P^f \quad (C25)$$

Radial Distribution Function

$$g_0 = \frac{1}{{}^0\alpha} + \frac{3({}^1d)({}^2d)}{({}^0\alpha)^2 ({}^1d + {}^2d)} \left[\frac{{}^1\alpha}{{}^1d} + \frac{{}^2\alpha}{{}^2d} \right] \quad (C26)$$

Turbulence and Pseudo-Thermal Energy Closure Equations

Granular Energy Conductivity

$${}^p\kappa = {}^p\alpha {}^p\rho ({}^p\kappa^{kin} + {}^p\kappa^{coll}) \quad (C27)$$

Kinetic Component of Granular Energy Conductivity

$${}^p\kappa^{kin} = \left(\frac{9}{10} k_{12} \eta_t + \frac{3}{2} {}^p\theta (1 + \nu_c ({}^p\alpha) g_0) \right) \left(\frac{9}{5 t_{12}^x} + \frac{\xi_c}{p t^c} \right)^{-1} \quad (C28)$$

Collisional Component of Granular Energy Conductivity

$${}^p\kappa^{coll} = \frac{18}{5} ({}^p\alpha) g_0 \frac{(1+e)}{2} \left({}^p\kappa^{kin} + \frac{5}{9} ({}^p d) \sqrt{\frac{{}^p\theta}{\pi}} \right) \quad (C29)$$

Dissipation of Particle Fluctuating Energy

$${}^p\varepsilon = 12(1-e^2) ({}^p\alpha)^2 ({}^p\rho) g_0 \frac{{}^p\theta^{3/2}}{{}^p d} \quad (C30)$$

Turbulence Exchange Terms

$$\Pi_{k1} = \beta (k_{12} - 2({}^1k)) \quad (C31)$$

$$\Pi_{\varepsilon 1} = C_{3\varepsilon} \left(\frac{{}^1\varepsilon}{{}^1k} \right) \Pi_{k1} \quad (C32)$$

$$\Pi_{k2} = \beta (k_{12} - 3({}^p\theta)) \quad (C33)$$

$$k_{12} = \frac{\eta_t}{1 + (1 + X_{p1}) \eta_t} (2({}^p k) + 3X_{21} {}^p\theta) \quad (C34)$$

Particle Relaxation Timescale

$$t_{12}^x = \frac{{}^p\alpha {}^p\rho}{\beta} \quad (C35)$$

Energetic Eddies times scales

$${}^1t^t = \frac{3}{2} C_\mu \frac{{}^1k}{{}^1\varepsilon} \quad (C36)$$

Fluid Lagrangian integral time-scale

$$t'_{l2} = \frac{t'_l}{\sqrt{1 + C_\beta \xi_r^2}} \quad (C37)$$

where:

$$\xi_r^p = \frac{3|U_r|^2}{2({}^1k)} \quad (C38)$$

$$C_\beta = 1.8 - 1.35 \cos^2(\theta) \quad (C39)$$

Collisional time-scale

$${}^p t^c = \frac{{}^p d}{6({}^p \alpha) g_0 \sqrt{16{}^p \theta / \pi}} \quad (C40)$$

$$\frac{1}{{}^p t} = \frac{2}{{}^p t_{12}^x} + \frac{\sigma_c}{{}^p t^c} \quad (C41)$$

Collisional Constants

$$\zeta_{e2} = \frac{2}{5}(1+e)(3e-1) \quad (C42)$$

$$v_e = (1+e)^2(2e-1)/100 \quad (C43)$$

$$\zeta_e = (1+e)(49-33e)/100 \quad (C44)$$

$$\sigma_e = (1+e)(3-e)/5 \quad (C45)$$

$$X_{p1} = \frac{{}^p \alpha^p \rho}{{}^1 \alpha^1 \rho} \quad (C46)$$

Thermal Energy Constitutive Relations**Thermal Conductivity**

$${}^m k = {}^m k^{\text{eff}} + {}^m k^t \quad (C47)$$

Effectivity Conductivity of the gas phase

$${}^1 k^{\text{eff}} = (1 - \sqrt{1 - {}^1 \alpha}) \left(.025 \sqrt{\frac{{}^1 T}{300}} \right) \quad (C48)$$

Turbulent Conductivity of Gas Phase

$${}^1k^t = \frac{({}^1\alpha)({}^1c_p)({}^1\mu^t)}{Pr} \quad (C49)$$

Effective Conductivity of the particle phases

$${}^p k^{\text{eff}} = {}_{\text{Th}}{}^1k \left[\frac{\varphi_k R_{\text{km}} + (1 + \varphi_k) \lambda_{\text{gm}}}{\sqrt{1 - {}^1\alpha}} \right] \quad (C50)$$

Where:

$$\lambda_{\text{gm}} = \frac{-2}{(1 - b/R_{\text{km}})} \left[\frac{(R_{\text{km}} - 1)b/R_{\text{km}}}{(1 - b/R_{\text{km}})^2} \ln \left(\frac{b}{R_{\text{km}}} \right) + \frac{b-1}{(1 - b/R_{\text{km}})} + \frac{b+1}{2} \right] \quad (C51)$$

$$b = 1.25 \left[\frac{1 - {}^1\alpha}{{}^1\alpha} \right]^{10/9} \quad (C52)$$

$$R_{\text{km}} = \frac{{}^p k}{{}^1 k} \quad (C53)$$

Interphase Heat Transfer

$$H_{\text{gp}} = -\gamma_{\text{gp}} ({}^p T - {}^1 T) \quad (C54)$$

where:

$$\gamma_{\text{gp}} = \frac{{}^1 C_p R_{\text{gm}}}{\exp[{}^1 C_p R_{\text{gm}} / \gamma_{\text{gp}}^0] - 1} \quad (C55)$$

$$\gamma_{\text{gp}}^0 = \frac{6({}_{\text{Th}}{}^1 k)(1 - {}^1\alpha)Nu}{({}^p d)^2} \quad (C56)$$

Nusselt Number Correlation

$$Nu = \left[7 - 10({}^1\alpha) + 5({}^1\alpha)^2 \right] \left[1 + 0.7(Re_p)^2 (Pr)^{.33} \right] + \left[\frac{1.33 - 2.4({}^1\alpha)}{+1.2({}^1\alpha)^2} \right] (Re_p)^7 (Pr)^{.33} \quad (C57)$$

Curriculum Vitae

Josef D. Dufek

Education:

University of Chicago, Chicago, IL 1996-2000

B.Sc. (6/2000) with Honors in Geophysical Science and Student Marshal

University of Washington, Seattle, WA 2001 -2006

MS in Geological Sciences, 2004

Ph.D. in Earth and Space Sciences, 2006

Josef (Joe) Dufek grew up in Lander, Wyoming and graduated from Lander Valley High School in 1996. He attended the University of Chicago on a college honors scholarship and majored in Geophysical Sciences. While at the University of Chicago he had the opportunity to work with Prof. Ray Pierrehumbert on Mars glacier-climate interaction and with Prof. Fred Anderson on pre-eruptive volatile contents of the Bishop Tuff magma. In 2001 he started his graduate work at the University of Washington working with Prof. George W. Bergantz, and has worked on lower crustal magma dynamics and the eruptive dynamics of explosive volcanic eruptions. He has accepted a Miller postdoctoral fellowship at the University of California, Berkeley where he will continue to examine the multiphase dynamics of volcanic eruptions.

Awards and Honors

- AGU student paper award, Fall Meeting 2004.
- Johnston Award recognizing graduate student research (University of Washington), 2004.
- NASA Earth Systems Science Fellowship (2004 - current).
- Received National Defense Science and Engineering Graduate Fellowship, 2001-2004
- Received NSF Graduate Fellowship but declined to receive National Defense Fellowship
- Received Achievement Rewards for College Scientists (ARCS) Fellowship, 2001.
- Inducted into Phi Beta Kappa Honor Society, 1999.
- University of Chicago Student Marshal, Academic Honor, 2000.
- University of Chicago College Honors Scholarship, 1996-2000.

- National Merit Scholarship, 1996.
- United States Senate Youth Scholarship (program sponsored by William Randolph Hearst Foundation and U.S. Senate).
- Robert C. Byrd Honors Scholarship, 1996-2000.

Publications

Dufek, J.D. and Bergantz, G.W. *Lower Crustal Magma Genesis and Preservation: A Stochastic Framework for the Evaluation of Basalt-Crust Interaction*, *J. Petrology*, **46**, 2167-2195.

Dufek, J.D. and Bergantz, G.W. *Transient two-dimensional dynamics in the upper conduit of a rhyolitic eruption: A comparison of closure models for the granular stress*, *J. Volc. Geothermal Res.*, **143**, 113-132, 2005.

Dufek, J.D. and Cooper, K.M. *(²²⁶Ra)/(²³⁰Th) excess generated in the upper mantle and lower crust: Implications for magma transport and storage time scales*. *Geology*, **33** (10), 833-836, 2005.

Dufek, J.D. and Bergantz, G.W. *The suspended-load and bed-load transport of particle laden gravity currents: Insight from pyroclastic flows that traverse water*, Submitted, *Theoretical and Computational Fluid Dynamics*, Nov. 2005.

Herrick, R.R., Dufek, J.D. and P.J. McGovern. *The Evolution of Large Shield Volcanoes on Venus*. *JGR*. Vol. 110. (EO1002), 1-19, 2005.

Petcovic, H.L. and Dufek, J.D. *Modeling of Magma Flow and Cooling Dikes: Implications for Emplacement of Columbia River Flood Basalts*. *JGR*, Vol. 110 (B10201), 1-15, 2005.

Wallace, P.J., Dufek, J.D., Anderson, A.T., and Zhang, X.Y. *Cooling rates of Plinian-fall and pyroclastic-flow deposits in the Bishop Tuff: inferences from water speciation in quartz hosted glass inclusion*, *Bull. Of Volcanology*, **65** (3), 105-123, 2003.

Invited Talks

Colloquia Talk at Arizona State University (Nov., 2004): *The Over-Water Mobility of Pyroclastic Flows: Linking the Physics at the Flow-Sea Interface with the Depositional Record*.

Colloquia Talk at University of British Columbia (Nov., 2005): *Catastrophic sedimentation: Using numerical simulations and deposits to decipher the eruptive dynamics of volcanoes.*

Colloquia Talk at Caltech (Jan., 2006): *Catastrophic sedimentation: Using numerical simulations and deposits to decipher the eruptive dynamics of volcanoes.*

Dufek, J.D. and Bergantz, G.W. *Physical and Temporal Controls on Lower Crustal Melting and Mixing: Mass and Enthalpy Transport in Actively Growing Arcs.* Eos Trans. AGU, 85(47), Fall Meet. Suppl., Abstract V51E-03, Invited Talk, 2004.

Dufek, J.D. and Bergantz, G.W. *The Over-Water Transport of Pyroclastic Flows: A Coupled Grain Size Distribution and Multi-fluid Numerical Approach.* A keynote talk in Modelling Volcanism Section, IAVCEI, 2004.

Dufek, J.D. and Bergantz, G.W. *The Multiphase Characterization of Volcanic Phenomena: A Comparison of Numerical and Experimental Approaches.* Fall AGU, 2005

Meeting Presentations

Dufek, J. D. and Herrick, R. *Comparison of Extinct and Active Large Shield Volcanoes on Venus*, Lunar and Planetary Science Conference XXXI, abstract # 1447, 1999.

Dufek, J. D. and Pierrehumbert, R. T. *A Coupled Dynamic Glacier-Atmosphere Model of the Climate of Early Mars.* Eos Trans. AGU, 81 (48), Fall Meet. Suppl., 2000.

Dufek, J.D., Wallace, P.J. and Anderson, A.T. *Hydrous Speciation Cooling Rates in the Bishop Tuff: Application of Heat Conduction Modeling to Constrain Emplacement Conditions*, Eos Trans. AGU, 82(47), Fall Meet. Suppl., 2001.

Davis, A.M., Dufek, J.D. and Wadhwa, M. *Euhedral phosphate grains in vugs and vesicles in ordinary chondrites, lunar samples, and the Ibitira eucrite; implications for trace element transport processes*, Meteoritics and Planetary Science. 36 (9), Suppl., 2001.

Dufek, J.D. and G.W. Bergantz. *A stochastic evaluation of the dynamical and thermal response of the lower crust to progressive basaltic input: Applications to MASH zone dynamics.* EOS Trans. AGU, 83 (47), Fall Meet. Suppl., Abstract V61A-1346. 2002.

Dufek, J.D., Bergantz, G.W. and S. Dartevelle. *Comparing the performance of differing approaches to modeling volcanic conduit conditions: Eulerian-Eulerian multiphase algorithm and hyperbolic methods*. Geophysical Research Abstracts, Vol. 5, 13864, 2003.

Dufek, J.D. and G.W. Bergantz. *Thermal and rheological constraints on lower crustal melting and mixing: A stochastic evaluation of basaltic intrusion by progressive dikeing*. Fall GSA, Abstracts with Programs – Geological Society of America. 35; 6, Page 632. 2003.

Petcovic, H.L., Dufek, J.D. Grunder, A. and Bergantz, G.W. *Field and modeling constraints on the thermal history of a swarm of Columbia River Basalt dikes, Cornucopia Stock*. Fall GSA, Abstracts with Programs – Geological Society of America. 35; 6, Page 550. 2003.

Dufek, J.D. and Bergantz, G.W. *Applications of a Unifying Computational and Theoretical Framework to Multi-Scale Eruption Processes*. Society of Industrial and Applied Mathematics (SIAM) Annual Meeting, 2004.

Dufek, J.D. and Cooper, K.M. *(^{226}Ra)/(^{230}Th) Excess Generated in the Lower Crust: Implications for Magma Transport Rates in Arc Settings*. Eos Trans. AGU, 85(47), Fall Meet. Suppl., AbstractV53A-0614, 2004.

Dufek, J.D. and Bergantz, G.W. *Applications of a hybrid multiphase theoretical and numerical framework to naturally occurring gravity currents*. Modeling of Turbidity Currents and Related Gravity Currents, Santa Barbara, 2005.